

University of Alberta

**Design and Fabrication of Fractal Photoconductive Terahertz Emitters and
Antenna Coupled Tunnel Diode Terahertz Detectors**

by

Pouya Maraghechi

A thesis submitted to the Faculty of Graduate Studies and Research
in partial fulfillment of the requirements for the degree of

Doctor of Philosophy

in

Photonics and Plasmas

Department of Electrical and Computer Engineering

©Pouya Maraghechi

Fall 2012

Edmonton, Alberta

Permission is hereby granted to the University of Alberta Libraries to reproduce single copies of this thesis and to lend or sell such copies for private, scholarly or scientific research purposes only. Where the thesis is converted to, or otherwise made available in digital form, the University of Alberta will advise potential users of the thesis of these terms.

The author reserves all other publication and other rights in association with the copyright in the thesis and, except as herein before provided, neither the thesis nor any substantial portion thereof may be printed or otherwise reproduced in any material form whatsoever without the author's prior written permission.

*This work is dedicated to my wife, Sahar and my parents, for their
unconditional support and love.*

Abstract

Improved terahertz (THz) photoconductive antennas that are able to both emit higher THz radiation power and detect lower THz radiation signal levels than the traditional THz photoconductive antennas are presented. Also, different classes of fractals are investigated to realize whether the enhanced THz radiation properties of fractal photoconductive THz emitters are universal to all fractals. Finally, the effect of self-similarity of the antenna structure on its performance is studied.

New classes of metal-insulator-metal (MIM) junctions that possess extreme asymmetry and nonlinearity in their current-voltage (I-V) characteristics are investigated. Metal-insulator-insulator-metal (MIIM) diodes incorporating different electron tunneling mechanisms under forward and reverse bias are implemented through the introduction of a cascaded potential barrier. A high I-V nonlinearity, up to 10 times that of a conventional MIM, was obtained for identical metal electrodes. As the next step, the tunneling mechanism is further altered. For this, resonant tunneling transport is incorporated into a metal-insulator-insulator-insulator-metal (MIIM) diode. This is analogous to a tunnel diode (normal tunneling) with the mechanism of a resonant tunneling device. It is envisioned that high speed THz rectifiers, ultrahigh bandwidth frequency mixers, diodes, and electron tunnel transistors having extraordinary I-V nonlinearity can be realized.

Next, the tunnel diodes are integrated into the antenna-coupled detectors for detecting free space THz radiation. The fabrication process for the MIIM, and MIIM diodes having an integrated antenna has been presented. To accomplish this, the knowledge gained from designing and fabricating optimized THz fractal antennas and

highly nonlinear MIIM and MIIIM diodes is utilized for fabricating ultrafast THz detectors.

Finally, the capabilities of THz spectroscopy for characterizing and studying the time dynamics of devices and complicated systems were investigated. To accomplish these tasks, a versatile optical setup for all-THz time resolved pump-probe spectroscopy was designed and tested. This THz setup is used to potentially characterize the temporal and spectral response of the fabricated antenna coupled MIIM and MIIIM diodes. Importantly, utilizing this setup and conventional THz time-domain spectroscopy (THz-TDS), the interaction of THz waves with complex media such as metal-dielectric composites was investigated. This was to expand the utilization of THz imaging from imaging inside dielectric materials into imaging more complex materials largely composed of highly opaque substances. The knowledge gained through a series of experiments was applied in utilizing THz-TDS for imaging dielectric objects embedded inside metallic media. This advancement of THz-TDS was successfully accomplished.

Acknowledgement

First and foremost, I would like to graciously thank my supervisor, Professor Abdulhakem Y. Elezzabi, for his unwavering help and support over the course of this degree. The countless hours that Dr. Elezzabi has spent discussing problems, debating interpretations, and making suggestions have helped shape both the contents of this thesis and my development as a scientist. His endless encouragement, helpful criticisms and passion for science have greatly helped me develop as a researcher.

Secondly, I would like to extend my appreciation to Prof. Ken Cadien for providing access to his laboratory and deposition equipment and specially his guidance in device fabrication process. In particular, I would like to thank Ali Forough-Abari for taking time out of his busy schedule to help me make samples on countless occasions.

The technicians and staff at University of Alberta, NanoFab, and machine shop are well appreciated for providing laboratory resources and services.

I thank my peers in the lab Cameron Straatsma, Shawn Sederberg, Mike Startsev, Corey Baron, and Michael Quong for interesting discussions and making my experience more fun throughout this program. They would always lend me a hand if I asked and I am grateful for their help.

My life in Edmonton has been enlightened by the presence of kind and caring friends, *Alireza Karimipour*, *Vahid Jalili*, *Babak Asghari*, *Farshid Vejahati*, *Omid Movahhedi*, and many others. Their help and companionship will never be forgotten.

Finally, I would like to thank my family and specially my wife for their continued support throughout the course of my studies.

Table of Contents

1.	CHAPTER 1 Introduction to THz Radiation	1
1.1	Photoconductive THz emitters.....	3
1.2	THz radiation detection.....	6
1.3	THz time domain spectroscopy	10
1.4	Research Objectives.....	12
1.5	Thesis outline	13
2.	CHAPTER 2 Fractal photoconductive terahertz radiation emitters	16
2.1	Introduction.....	16
2.2	Fractal geometry and antenna	19
2.3	Sierpinski's antenna at Microwave frequencies.....	20
2.4	Design and fabrication of PC THz emitters	25
2.4.1	Experimental methods.....	27
2.4.2	Results and discussion	27
2.5	Sierpinski fractal PC THz emitter.....	30
2.5.1	Results and discussion	33
2.6	Apollonian PC THz emitter	41
2.6.1	Results and discussion	44
2.7	Effect of self-similarity	51
2.7.1	Results and discussion	53
2.7.2	Summary	56
3.	CHAPTER 3 Terahertz electron tunnel devices.....	58
3.1	Introduction.....	58
3.2	Review of electron tunnel devices	59
3.2.1	Tunnel diodes.....	59
3.2.2	Resonant Tunneling diodes.....	61
3.2.3	Metal-insulator-metal diodes	64
3.3	Fabrication of metal-insulator-metal diodes	67
3.3.1	MIM fabrication via PVD oxide deposition.....	69

3.3.2	MIM fabrication via ALD oxide deposition	73
3.4	Metal-insulator-insulator-metal diodes	78
3.5	Metal-insulator-insulator-insulator-metal diodes.....	83
3.6	Summary	91
4.	CHAPTER 4 MIM detector design, fabrication, and characterization.....	92
4.1	Introduction.....	92
4.2	Square-law detectors and mixers	96
4.3	Circuit design	97
4.4	Fabrication	100
4.4.1	Phase one	100
4.4.2	Phase two	106
4.4.3	Phase three	107
4.4.4	Final device fabrication and characterization	111
4.5	A Novel Nanofabrication Damascene Lift-off Technique.....	114
4.5.1	Experimental Details.....	116
4.5.2	Results and discussions.....	119
4.6	Summary	125
5.	CHAPTER 5 THz spectroscopy for characterization and imaging	126
5.1	Introduction.....	126
5.2	All THz pump, THz probe characterization setup	128
5.2.1	Setup design	131
5.2.2	Results and discussions.....	134
5.3	Time-resolved study of THz particle plasmons	139
5.3.1	Experimental details.....	140
5.3.2	Results and discussions.....	141
5.7	Characterizing a plasmonic random composite	147
5.7.1	Results and discussion	148
5.8	Terahertz imaging inside metal-filled media	155
5.8.1	Results and discussion	157
5.9	Summary	166
6.	CHAPTER 6 Conclusions	168

6.1	Future work.....	171
	References.....	172
	APPENDIX A Allowed energy levels in potential wells	182
	APPENDIX B MIM cut-off frequency.....	184
	APPENDIX C The design of a reversible wafer holder for uniform photoresist coating of deeply etched cavities	186
	C1. Design of the wafer holder.....	188
	C2. Photoresist coating procedure	190
	C3. Results.....	192

List of Tables

Table 4-1 Summary of the properties of the fabricated MIM detectors. 112

Table C-1 Process flow of the photoresist coating procedure. 191

List of Figures

Figure 1-1 Schematic of THz generation via PC THz emitter.....	3
Figure 1-2 Dipole radiation for a PC THz emitter.....	4
Figure 1-3 Schematic of the PC THz emitter having: (a) stripline, (b) dipole, and (c) bow-tie antenna.....	6
Figure 1-4 Schematic of the EO detection setup, which consists of an EO crystal (EO), quarter wave-plate ($\lambda/4$), and Wollaston prism (WP). The polarization state of the optical probe pulse is illustrated at the bottom of the figure.....	8
Figure 1-5 Schematic of PC THz detection.....	9
Figure 1-6 Top view schematic of the THz-TDS system. In this image the optical probe pulse has a temporal delay of Δt with respect to the pump pulse.....	11
Figure 2-1 Schematic of: (a) a bow-tie, (b) Sierpinski's first order fractal, and (c) Sierpinski's second order fractal, antenna.....	21
Figure 2-2 Schematic of a Sierpinski gasket antenna with five iterations at the right. (a) Input reflection coefficient, (b) input resistance, and (c) input reactance of the antenna [49].	22
Figure 2-3 Current density distribution of the Sierpinski antenna surface at difference resonant frequencies [46].....	23
Figure 2-4 The five-iteration fractal Koch monopole [46].	24
Figure 2-5 Time domain terahertz waveforms emitted from the bow-tie PC THz emitters for $L= 190 \mu\text{m}$ (black), $105 \mu\text{m}$ (light blue) and $80 \mu\text{m}$ (red). The inset depicts the SEM image of the fabricated bow-tie THz PC emitters.....	28
Figure 2-6 Spectral power for bow-tie PC THz emitters for $L= 190 \mu\text{m}$ (black), $105 \mu\text{m}$ (light blue) and $80 \mu\text{m}$ (red).	29
Figure 2-7 Complementary of (a) bow-tie, (b) first order, (c) second order, and (d) third order Sierpinski PC THz emitters.	31
Figure 2-8 PC emitters of (a) the bow-tie, (b) first order, (c) second order, and (d) third order PC THz emitters.....	32
Figure 2-9 Spectral power for the complementary bow-tie and Sierpinski PC THz emitters orders one to three and the bow-tie PC THz emitters.....	33

Figure 2-10 Spectral power for the bow-tie and Sierpinski PC THz emitters orders one to three. Note that the scale is normalized to the complementary THz PC emitters.....	34
Figure 2-11 Normalized power plots of the (a) complimentary Sierpinski PC THz emitter and (b) Sierpinski PC THz emitter. The amount of frequency shift (Δf) is shown on the top right corner of the figures.	35
Figure 2-12 Directivity plot for the (a) Bow-tie and Sierpinski Fractal emitters and (b) Complementary bow-tie and Sierpinski fractal emitters. The dashed line represents the location of substrate-air interface.....	36
Figure 2-13 The spatial distribution of the surface plasmon current density, $J_x(x,y)$, in logarithmic scale along the axis of the Sierpinski PC THz emitters of (a) the bow-tie, (b) first order, (c) second order, and (d) third order, acquired at an intermediate peak emission frequency of 0.55 THz.	38
Figure 2-14 The spatial distribution of the surface plasmon current density, $J_x(x,y)$, in logarithmic scale along the axis of the complementary Sierpinski PC THz emitters of (a) the bow-tie, (b) first order, (c) second order, and (d) third order, acquired at an intermediate peak emission frequency of 0.55 THz.	39
Figure 2-15 SEM images of the fractal-like geometries iteration orders (a) two, and (b) three applied only to one side of the antenna. The spatial distribution of the surface plasmon current density of the, $J_x(x,y)$, in logarithmic scale along the axis of the fractal-like geometries iteration orders (a) two, and (b) three applied only to one side of the antenna, acquired at an intermediate peak emission frequency of 0.55 THz.	40
Figure 2-16 Schematic of: (a) a circular, (b) first order Apollonian fractal, and (c) second order Apollonian fractal, antenna.	43
Figure 2-17 SEM images of (a) circular dipole, (b) first order Apollonian, (c) second order Apollonian, (d) complementary circular dipole, (e) complementary first order Apollonian, and (f) complementary second order Apollonian emitter.	44
Figure 2-18 Spectral power for PC THz emitters.	45
Figure 2-19 FDTD results for (a) the frequency response of the Circular, Apollonian order one (Apol. 1), and Apollonian order two (Apol. 2) PC THz emitter, and (b) the	

radiation patten on the above mentioned emitters ($ E_{\theta} $ is the magnitude of azimuthal component of the THz electric field).....	47
Figure 2-20 A plot of E_x versus E_y for duration of 2.6 ps demonstrating the polarization purity of the transmitted THz electric field. The arrow in (d) indicates the evolution direction of electric field.....	48
Figure 2-21 The spatial distribution of the surface plasmon electric field $E_x(x,y)$, for (a) circular dipole, (b) first order Apollonian, (c) second order Apollonian, (d) complementary circular dipole, (e) complementary first order Apollonian, and (f) complementary second order Apollonian emitter.....	50
Figure 2-22 (a) bow-tie, (b) first order Sierpinski PC THz emitter, (c) second order Sierpinski PC THz emitters, (d) modified non-fractal PC THz emitter of order one, and (e) modified non-fractal PC THz emitter of order two.	52
Figure 2-23 Spectral power for first order Sierpinski (dark blue), bow-tie (light blue) and first order modified (red) PC THz emitter.	53
Figure 2-24 Spectral power for second order Sierpinski (dark blue), bow-tie (light blue) and second order modified (red) PC THz emitter.	54
Figure 2-25 The spatial distribution of the surface current density, $J_x(x,y)$, in logarithmic scale along the axis of the Sierpinski PC THz emitters of (a) the bow-tie, (b) first order, (c) second order, (d) second order modified, and (e) second order modified PC THz emitter.....	56
Figure 3-1 Energy band diagram of a tunnel diode in thermal equilibrium	60
Figure 3-2 (a) static I-V characteristic curve of a tunnel diode at different bias voltages. Energy band diagrams of devices under biasing conditions (V_1 - V_5) are plotted in (b)-(f). The direction of arrow shows the direction of electron tunneling.	60
Figure 3-3 Structural schematic of a GaAs/AlGaAs RTD. The energy band diagram is drawn on the left.....	62
Figure 3-4 I-V characteristic curve for a GaAs/AlGaAs RTD. The specific features on the I-V curve are labeled as (a)-(e).	62
Figure 3-5 Energy band diagram of a RTD under various bias voltages. (a) zero bias, (b) resonance tunneling through E_1 , (c) first negative resistance region, (d) resonance tunneling through E_2 , and (e) second negative resistance region.	63

Figure 3-6 Energy diagram of two similar metallic layers (M1 and M2) spaced by an insulating layer. a) When there is no bias applied, b) bias $-V$ is applied to metal M2, and c) bias $+V$ is applied to metal M2. In this figure, W is the work function of the metal, ξ is the electron affinity of the oxide material, ϕ is the barrier height, d is the barrier width and V is the applied bias.	65
Figure 3-7 I-V characteristic curve for Cr-SiO ₂ -Cr MIM having a 3.3 nm of oxide deposited at Micralyne. The third order polynomial fit is shown in the Figure. To check if the device is stable, several voltage sweeps were performed on the same spots.	71
Figure 3-8 I-V characteristic curve for Cr-SiO ₂ -Cr with oxide thickness of 3.0 nm deposited in the NanoFab facility.	72
Figure 3-9 An image of the MIM devices on the substrate and the shadow mask used for fabricating the MIM diodes.....	74
Figure 3-10 Schematic of the layout of the MIM device. Here, I_1 is the insulating layers corresponding to either an Al ₂ O ₃ or aHfO ₂ layer.	75
Figure 3-11 Current versus voltage characteristic curves for the Cr/HfO ₂ /Cr and Cr/Al ₂ O ₃ /Cr devices . The data for Al ₂ O ₃ was magnified 10 times for illustrative purpose. The higher tunneling current observed from the Cr-HfO ₂ -Cr diode is attributed to the lower barrier height associated with HfO ₂ compared to that of Al ₂ O ₃ . The insets depict the logarithm of the current versus the voltage for each device.	75
Figure 3-12 Plots of: (a) asymmetry, (b) nonlinearity, and (c) curvature coefficient of the Cr/Al ₂ O ₃ /Cr and Cr/Al ₂ O ₃ /Cr devices.	77
Figure 3-13 Schematic of the energy band diagram for devices having a cascaded potential barrier at (a) zero, (b) forward, and (c) reverse bias. Here M1 and M2 are the electrodes of two sides of the device, d_1 and d_2 are the oxide thickness of the two insulators, and ϕ_1 and ϕ_2 are potential barrier heights formed at the interface of M1 and M2 with their corresponding insulators, respectively.	79
Figure 3-14 Schematic of: (a) the layout of the MIIM device and (b) the energy band diagram. Here, I_1 , and I_2 are the insulating layers corresponding to Al ₂ O ₃ and HfO ₂ layers, respectively. Φ_{b1} , and Φ_{b2} are the potential barrier for Al ₂ O ₃ and HfO ₂ layers, respectively.	80

Figure 3-15 Current versus voltage characteristic curves for the Cr/Al₂O₃-HfO₂/Cr device. The inset depicts the logarithm of the current versus the voltage..... 80

Figure 3-16 Plots of: (a) asymmetry, (b) nonlinearity, and (c) curvature coefficient of the Cr/Al₂O₃/Cr, Cr/Al₂O₃/Cr and Cr/Al₂O₃/Cr devices..... 82

Figure 3-17 Cross-sectional views of the MIIM tunnel device. (a) A schematic diagram depicting a fabricated MIIM device having a 2nm thick Al₂O₃ layer, a 2nm thick HfO₂ layer, and a 2nm thick Cr₂O₃ layer. (b) The Cross-sectional transmission electron microscope (TEM) image of a Cr/Cr₂O₃-HfO₂-Al₂O₃/Cr MIIM device. The layers are grown on a 550nm thick SiO₂ film on top of a 500μm thick Si substrate. Each oxide layer is 2nm thick. The oxides are grown sequentially in accordance to their ascending potential barrier values (i.e. 0.64eV, 0.75eV and 2.62eV, for Cr₂O₃, HfO₂, and Al₂O₃, respectively), thus forming a cascading potential barrier profile. .. 84

Figure 3-18 I-V experimental results and energy band diagram model of the MIIM device having a cascaded potential barrier profile. (a) Current versus voltage characteristic curves for the Cr/Cr₂O₃-HfO₂-Al₂O₃/Cr device. (b) Energy band diagram of the M1/Cr₂O₃-HfO₂-Al₂O₃/M1 device having a cascaded potential barrier profile at zero voltage. Here, M1 represents the Cr electrodes, Φ_{b1} (2.62 eV) and Φ_{b4} (0.64 eV) are the potential barrier heights for Al₂O₃ and Cr₂O₃ layers, respectively. Φ_{b2} (0.87 eV) and Φ_{b3} (1.1 eV) are the potential barrier heights between Al₂O₃-HfO₂ and between HfO₂-Cr₂O₃ interfaces, respectively. Energy band diagram¹⁸ of the Cr/Cr₂O₃-HfO₂-Al₂O₃/Cr device at: (c) -3.0 V, (d) +1.2 V, and (e) +2.7 V. The arrows depict the electron tunneling direction..... 86

Figure 3-19 I-V experimental results and energy band diagram model of the MIIM device having a non-cascaded potential barrier profile. (a) I-V characteristic curves for the Cr/Cr₂O₃-Al₂O₃-HfO₂/Cr device. The features in the I-V characteristic curves of the MIIM device have been marked as (iv), (v) and (vi). (b) Energy band diagram of the M1/Cr₂O₃-Al₂O₃-HfO₂/M2 device having a non-cascaded potential barrier profile at zero voltage. Here, M1 represents the Cr electrodes, Φ_{b1} (1.75 eV) and Φ_{b4} (0.64 eV) are the potential barrier heights for Al₂O₃ and Cr₂O₃ layers, respectively. Φ_{b2} (0.87 eV) and Φ_{b3} (1.98 eV) are the potential barrier heights between HfO₂-Al₂O₃ and between Al₂O₃-Cr₂O₃, respectively. The energy band diagram¹⁸ of the Cr/Cr₂O₃-

Al ₂ O ₃ -HfO ₂ /Cr device at: (c) -1.2 V, (d) +3.0 V, and (e) +3.8 V. The arrows depict the electron tunneling direction.	89
Figure 3-20. Figures of merit used to characterize the efficiency and performance of electron tunneling devices. (a) Logarithmic plot of asymmetry of Cr/Cr ₂ O ₃ -HfO ₂ -Al ₂ O ₃ /Cr and Cr/Cr ₂ O ₃ -Al ₂ O ₃ -HfO ₂ /Cr devices. In both devices, the asymmetry peaks when the current in the negative bias polarity becomes significantly small. For this, the data in the vicinity of these regions were removed within ±100 mV from the peaks. (b) Nonlinearity of the Cr/Cr ₂ O ₃ -HfO ₂ -Al ₂ O ₃ /Cr and Cr/Cr ₂ O ₃ -Al ₂ O ₃ -HfO ₂ /Cr devices.....	90
Figure 4-1 Schematic of a point contact MIM is shown.....	93
Figure 4-2 Schematic of a MIM diode having an integrated antenna being illuminated by an incident electromagnetic wave. The antenna captures and focuses the electric field of the radiation across the MIM diode. The MIM diode rectifies the electric field to provide power to the load.	97
Figure 4-3 Circuit representation of the overall system of a MIM with an integrated antenna connected to a load (RL).	97
Figure 4-4 Design pattern for the MIM devices. (a) The overall design consists of a 4×4 array of MIMs. (b) The junction area and the antenna is placed in one write field area. The junction dimensions in this design are 200 nm × 200 nm.....	100
Figure 4-5 SEM image of Cr/Al ₂ O ₃ /Cr junction having 5 nm of oxide deposited using plasma ALD. The roughness of the first electrode is clearly visible in the image.....	103
Figure 4-6 SEM image of Cr/Al ₂ O ₃ /Cr junction having 8 nm of oxide deposited using plasma ALD.	103
Figure 4-7 Optical image of the chip after 5 nm of Al ₂ O ₃ oxide is deposited by ALD using thermal oxidation at 150°C. The cracks are visible at the corners of the pads.	104
Figure 4-8 SEM image of Cr/Al ₂ O ₃ /Cr junction having 3 nm of oxide deposited using ALD. The first Cr electrode was deposited by evaporation technique.	106
Figure 4-9 Process steps for the fabrication of MIM diodes: (a) first electrode is deposited and the second electrode is patterned; (b) oxide deposition via ALD; (c)	

metal deposition; (d) lift-off. Revised process flow: (e) first electrode is deposited; (f) oxide deposition via ALD; (g) resist coated, EBL patterned, and material depiction of second electrode; (h) lift-off.	108
Figure 4-10 SEM images of diode junctions of: (a) chip #1, and (c) chip #2 at 10Kx magnification. Zoomed in (30×10^3 times) SEM images of (b) chip#1, and (d) chip#2.	109
Figure 4-11 Current versus volatge characteristic curves for the Cr/Al ₂ O ₃ /Cr devices having junction areas of 400nm×400nm (chip #1) and 150nm×150nm (chip #2). ..	110
Figure 4-12 SEM image of two devices on chip #3.....	111
Figure 4-13 Design pattern for the final MIM diodes having integrated antennas. (a) The overall design consists of a 5x1 array of MIMs. (b) Zoomed in image of (a). The junction geometry is identical to that illustrated in section 4.3.1. The design areas in purple and green are electrode 1 and 2 respectively.	111
Figure 4-14 SEM image of an MIIM diode having an integrated fractal antenna....	113
Figure 4-15 Current versus volatge characteristic curves for the chip #5 and chip #4. The curve for chip#4 is multiplied by 10^{-4}	113
Figure 4-16 Process steps for the damascene lift-off process: (a) surface of the substrate is coated by resist; (b) after pattern transfer and development; (c) etching of pattern; (d) metal deposition; (e) final result after lift-off.	117
Figure 4-17 SEM images of various features resulting from the damascene lift-off process (a), (c) and (e). The same features fabricated using a conventional lift-off process are shown in panels (b), (d) and (f). Note that the conventional lift-off process results in rougher edges as indicated by the bright borders around the perimeter of the structures.	120
Figure 4-18 Zoomed-in SEM images of the same features resulting from: (a) damascene lift-off process and (b) conventional lift-off process. It is clearly visible that the edges of the deposited Cr are much smoother in comparison to the conventional lift-off process when the damascene lift-off process is utilized.....	121
Figure 4-19 AFM images of the cross-shaped feature (a,b). Sequentially zooming in on the top arm (c,d & e,f). Results of the conventional lift-off process are shown in	

(a), (c) and (e). The same feature fabricated using the innovative lift-off process is shown in panels (b), (d) and (f).....	122
Figure 4-20 Cross-sectional topographic representation of the edges obtained from: (a) the damascene lift-off process, showing three cross-sections, and (b) the conventional lift-off process, showing four cross-sections, at different locations along the edge. The lines in the inset image show the location and direction of the cross-section on the edge.....	123
Figure 4-21 Schematic representation for: (a) the conventional lift-off process after metal deposition, (b) the damascene lift-off process after metal deposition, (c) conventional process after lift-off, and (d) damascene process after lift-off. L1 is the thickness of the resist and L2 is the thickness of the exposed material in contact with the resist.	124
Figure 5-1 First THz pump-probe setup that was operated by splitting the THz radiation pulses.	130
Figure 5-2 (a) Schematic of the THz-PP-TDS system. The 10 fs, 800 nm laser pulse train is split into three pulse trains: An optical probe (20 mW), an optical pump 1(60 mW, generating THz pump pulse) and an optical pump 2 (30 mW, generating THz probe pulse). The THz-PP-TDS system consists of four 90° off-axis gold-coated parabolic mirrors, two PC THz emitters, and an electro-optic sampling setup. The generated THz radiation pump pulse and TH radiation probe pulse were collected and co-linearly focused along with the optical probe pulse onto a 500 μm thick <111> ZnSe electro-optic crystal. The THz radiation-induced polarization modulation of the optical probe was extracted via a balanced detection arrangement, and lock-in detection was carried out at the bias voltage modulation frequency. (b) Schematic of the THz emitters. The two PC THz emitters were placed near each other at a separation of 200 μm. The bias voltages of the PC THz emitters 1 and 2 were modulated at frequencies f_1 and f_2 , respectively. Through phase-locking at the modulation frequency of the biasing voltage, this configuration allows locking at and detecting the THz radiation due to the THz pump signal, or the THz probe signal, or both.	132

Figure 5-3 Electric fields of the THz radiation pump and probe pulses as generated and detected by the abovementioned THz-PP-TDS system. The THz probe pulse is delayed by 5.5 ps with respect to the THz pump pulse. The modulating frequencies (f_1 and f_2) of bias voltages applied to both PC THz emitters were set to 81 KHz. The ratio of the THz pump to THz probe was set to 3:1 in this experiment..... 135

Figure 5-4 The spot sizes of both the THz radiation pump and probe pulses were mapped out using the knife edge technique in the (a) x - direction and (b) y - direction. The FWHM spatial extent of the THz radiation focal region was found to be 510 μm and 740 μm along the x - and y -directions, respectively. In the x -direction, both the THz radiation pump pulse and the THz radiation probe pulse overlapped and along the y -direction, the centers of the focal spots were displaced by 200 μm with a 90% overlap. The x - and y - directions are depicted in the inset of (b)..... 136

Figure 5-5 Electric fields of the THz radiation pump and probe pulses where the polarity of the THz probe pulse is reversed by 180° with respect to the THz pump pulse. The THz probe pulse is delayed by 5.5 ps with respect to the THz pump pulse and the modulating frequencies (f_1 and f_2) of bias voltages applied to both PC THz emitters were set to 81 KHz. The ratio of the THz pump to THz probe was set to 3:1 in this experiment..... 137

Figure 5-6 The THz-TDS probe signal pulse acquired at 40.5 kHz . Here, the PC THz emitter generating the THz radiation pump pulse was modulated at $f_1=81$ kHz while the PC THz emitter generating the THz radiation probe pulse was modulated at $f_2=40.5$ kHz..... 138

Figure 5-7 Schematic of the proposed THz-PP experiment on Au sub-wavelength particles. 140

Figure 5-8 (a) Time-domain THz probe signals transmitted through Au particle sample at various delay times (Δt), and (b) their corresponding spectral power plots. 141

Figure 5-9 (a) Time-domain THz probe signals transmitted through Au particle sample at various delay times (Δt), and (b) their corresponding spectral power plots. The THz probe pulse electric field is out-of-phase with respect to the THz pump pulse. 142

Figure 5-10 The percent change of the total integrated spectral power for the transmitted THz probe pulse compared to the transmitted THz probe when the THz pump pulse is blocked. P-P states for pump-probe in the legend. The solid lines in the figure are fitted curves. 143

Figure 5-11 Schematic of the situation when the THz pump pulse has been coupled into THz particle plasmons and the THz probe pulse is been illuminated onto the Au ensemble at a later time..... 144

Figure 5-12 Phase of the transmitted THz probe electric field for $\Delta t=0, 1, 2$ ps of when pump-probe are: (a) in-phase, and (b) out-of-phase..... 146

Figure 5-13 (a) Schematic diagram illustrating the random composite consisting of polydispersed metallic and dielectric particles. The circled images depict scanning electron microscope images of the dielectric and metal particles and an optical image of the composite. (b) Time-domain terahertz waveforms transmitted through an empty sample cell (reference) and 4.0 mm thick Co/sapphire particle mixtures for Co particles volume fraction, f , varying from 0.0 % to 100 %..... 148

Figure 5-14 (a) Illustrative diagram depicting the THz electric field (E_{THz}) transmitted through the random metallic-dielectric composite with components polarized parallel (E_{\parallel}) and perpendicular (E_{\perp}) to the incident polarization and temporal position shifted by a time T relative to the transmission through a dielectric particle sample (upper left). (b) Time-dependent THz pulse intensity envelopes through a 4.0 mm thick sample having various f values for both parallel and perpendicular polarization states. Here, the time axis is measured relative to a 4.0 mm thick pure dielectric ensemble. (c) Power spectra of a THz pulse transmitted through mixtures of metallic and dielectric particles for varying f . The band marks the frequency range which is shared among all the samples of different f 150

Figure 5-15 (a) Plot of the change (relative to a dielectric ensemble) of the effective refractive index of the random composite as a function of f and frequency. (b) Effective refractive index of the random metallic-dielectric composite measured at 0.23 THz and various f . Notably, within the atypic range the refractive index is larger than either the dielectric (n_{eff}^d) or metallic (n_{eff}^m) ensembles refractive indices..... 152

Figure 5-16 Group velocity (normalized to c) versus the average optical separation between metallic particles. The inset illustrates the average optical separation of metallic particles immersed in a background of a dielectric particle ensemble, where r_{ave} is the average radius occupied by a single metallic particle in a volume V_{ave} and a is the average diameter of a metallic particle.....	153
Figure 5-17 Transmitted THz electric field through the metallic ensemble. (blue) free space time domain signal, (light blue) time domain signal through the Cu and (purple) time domain signal through Cu and Teflon.	158
Figure 5-18 (a,b) Pictures of the Teflon objects used in the experiment. (c) An illustration depicting the THz electric field (E_{THz}) transmitted through the samples.	158
Figure 5-19 Acquired raw transmitted instantaneous power images of the embedded integrated over the duration of the pulse (a) 0.8 mm thick triangular-shaped object at a resolution of (16×13) pixels and (b) 1.1 mm thick polygon-shaped object at a resolution of (10×12) pixels. The dashed lines indicate the location of the embedded object.....	160
Figure 5-20 The super-resolved images of those presented in Fig. 3. The high-resolution images are based on total transmitted instantaneous power with a 9-fold increase in spatial resolution for the original (a) (16×13) pixel triangular-shaped and (b) (10×12) pixel polygon-shaped Teflon objects. The dashed lines indicate the location of the embedded object.	161
Figure 5-21 Acquired raw 2D maps of the THz pulse arrival time of (a) 0.8 mm thick triangular-shaped object at a resolution of (16×13) pixels and (b) 1.1 mm thick polygon-shaped object at a resolution of (10×12) pixels. The dashed lines indicate the location of the embedded object.	162
Figure 5-22 Acquired raw 2D maps of the phase magnitude taken at 0.15 THz for the (a) 0.8 mm thick triangular-shaped object at a resolution of (16×13) pixels and (b) 1.1 mm thick polygon-shaped object at a resolution of (10×12) pixels.....	164
Figure 5-23 The super-resolved images with a 9-fold increase in resolution for the acquired (a,c) pulse arrival time images and for (b,d) phase magnitude images. The dashed lines indicate the location of the embedded object.	165

Figure A-1 Energy band diagram of the Cr/Cr ₂ O ₃ -HfO ₂ -Al ₂ O ₃ /Cr device. The solid black lines depict the potential well. The inset on top depicts the approximated potential well profile (the dashed black line).....	182
Figure B-1 The equivalent circuit for the MIM diode with an integrated antenna...	184
Figure C-1 (a) A schematic of the wafer holder with a mounted wafer showing a face up mounting arrangement. (b) Side view of the wafer holder used in the photoresist coating.....	189
Figure C -2 Image of the Teflon wafer holder in the bowl.....	191
Figure C-3 Cross-sectional SEM images (500×) near the edge of a 110 μm deep cavity and photoresist coating using: (a) the face up spin coating process. Here, the photoresist accumulation extends to a distance of 145 μm, followed by a sloping region that monotonically increases in thickness, starting at 2.2 μm at a position 145 μm away from the corner point. (b) The face down/face up spin coating process. This process produces a photoresist layer of uniform thickness beyond a distance of 107 μm.	192
Figure C-4 A cross-sectional SEM image (1700×) of a photoresist layer at the bottom of a 110 μm cavity. A uniform thickness of 1.7 μm was achieved using the face down/face up spin coating process beyond a distance of 107 μm.	193
Figure C-5 Cross-sectional SEM images (500×) near the edge of a 300 μm deep cavity and photoresist coating using (a) the face up spin coating process. Here, the photoresist accumulation extends to a distance of 166 μm, followed by a sloping region that monotonically increases in thickness, starting at 1 μm at a position 166 μm away from the corner point. (b) The face down/face up spin coating process. This process produces a photoresist layer of uniform thickness beyond a distance of 104 μm.	194
Figure C-6 An illustration (not to scale) of a cross-sectional view of a rotating wafer having a cavity etched on the left side. Due to centrifugal force, the accumulation of photoresist at the opposite edges of this cavity is asymmetric.	195

List of Abbreviations

AFM	atomic force microscopy
ALD	atomic layer deposition
a.u.	arbitrary units
CW	continuous wave
EBL	electron beam lithography
EO	electro-optic
FDTD	finite-difference time-domain
GHz	gigahertz
MBE	molecular beam epitaxy
MIM	metal-insulator-metal
MIIM	metal-insulator-insulator-metal
MIIM	metal-insulator-insulator-insulator-metal
PC	photoconductive
P-P	pump-probe
QW	quantum well
RIE	reactive ion etching
RTD	resonant tunneling diode
SEM	scanning electron microscopy
SNR	signal to noise
STM	scanning tunneling microscopy
THz	terahertz
TDS	time domain spectroscopy
WKB	Wentzel, Kramers, and Brillouin
WP	Wollaston prism

1. CHAPTER 1

Introduction to THz Radiation

The terahertz (THz) radiation band is associated with electromagnetic frequencies falling in the range of 0.1-30 THz [1, 2]. At 1 THz (1000 GHz) electromagnetic radiation has a free-space wavelength of 300 μm , a period of 1 ps and a photon energy of 4.1 meV. In comparison to other electromagnetic spectral regions, THz has been the least investigated radiation band. This is mainly due to the technical difficulties involved in fabricating compact and, more importantly, efficient THz sources and detectors. It is only in the past two decades that extensive attention has been devoted to the study of this frequency region. To date, both pulsed and continuous wave (CW) THz sources have been realized in two different schemes either using nonlinear optical media or accelerating electrons. In parallel, various coherent detection techniques have been created for detecting pulsed and CW THz radiation. While electro-optic sampling and photoconductive switching have been the technique of choice for detecting pulsed THz radiation, photomixing and heterodyne detection have been primarily used for detecting CW THz radiation.

It is the unique characteristics of THz radiation that initially stimulated research for its many applications [2-4]. A list of unique properties of THz radiation is as follows:

1. Wavelength: The wavelength of THz radiation is longer than that of visible and IR radiation. Thus, for imaging and sensing purposes THz radiation scattered less by the Mie scattering effect. In addition, most dielectric materials such as clothes, paper, wood and plastic are transparent to THz radiation. Nondestructive evaluation applications are one of the most important applications of THz waves.

2. Photon energy: The low photon energies of THz radiation cause THz waves to be of a non-ionizing nature. This preserves biological tissues when exposed to THz radiation in contrast to X-ray radiation.
3. Spectral fingerprint: Many molecules have spectral absorption signatures at THz frequencies. This is because of the rotational and vibrational transitions energies in the meV range.
4. Time-domain spectroscopy: The radiation absorptivity and electromagnetic dispersion of materials are directly accessible from the temporal profile of the THz electric field acquired via THz time domain spectroscopy (THz-TDS).

It is these unique properties of THz radiation that provides applications of THz waves in many research fields ranging from astronomy, atmospheric [5-7] and biological sciences [8-10] all the way to security and nondestructive testing [4, 11-13]. However, there exist some fundamental concerns that cause problems for future development of THz applications: (1) The attenuation of THz waves is high as it propagates in air; (2) The THz signal is very weak as it is transmitted through thick samples; (3) Due to the low efficiency of the present THz pulse sources, a lock-in detector with milliseconds time constant is needed for increasing the SNR of the detection setup. This greatly reduces the data acquisition speed, which is one of the most critical disadvantages of current THz systems.

Clearly, THz systems having high SNR are vitally important for improving the application of THz imaging, sensing and spectroscopy systems. As a result, the main motivations for this thesis are: (1) Investigation of more efficient THz sources and more sensitive detectors. Not only would the required scanning time be reduced, but also long-distance spectroscopy and imaging becomes more feasible. (2) Develop a fabrication process for making arrays of THz detectors. To date, most THz detection is performed by a single detector, which requires raster scanning the sample and thus significantly decreases the acquisition speed. With the availability of a 2D THz detector array, most of the issues of conventional THz imaging and sensing systems (acquisition speed and complexity) would be eliminated. This would ultimately result in the construction of a THz camera. (3) Investigation of the

interaction of THz waves with complex media such as metal-dielectric composites. This would be favorable in expanding the utilization of THz imaging from imaging inside dielectric materials (such as scanning envelopes) into imaging more complex materials largely composed of highly opaque substances (i.e. metals).

1.1 Photoconductive THz emitters

Since the first demonstration of terahertz (THz) generation via photoconductive (PC) excitation of a semiconductor surface by Auston et al. [14], this method has become very popular for producing ultra-short THz pulses for various applications [4]. A schematic of THz pulse generation using a PC THz emitter is illustrated in Figure 1-1.

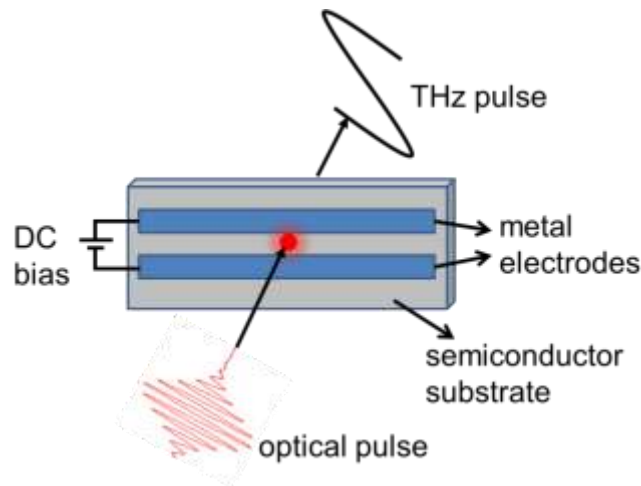


Figure 1-1 Schematic of THz generation via PC THz emitter.

In the PC generation scheme, free carriers are excited in a semiconductor material by an ultrashort pulse of above band-gap radiation (i.e. fs pulse in Figure 1-1). These transient carriers are then accelerated by means of a bias electric field to generate a broadband THz pulse [1, 15, 16]. To apply this DC bias, two metallic electrodes are deposited on the semiconductor substrate. The bipolar THz pulse is produced by the acceleration and decay of the free carriers in the substrate. In order

for the PC switch to produce broadband THz radiation, the switching action should be on the order of a picosecond. PC switch turn on time is determined by the laser pulse duration while its turn off time is governed by the photoexcited carrier lifetime in the semiconductor substrate. While laser pulses having duration of femtoseconds are utilized for illuminating the PC switch, the upper limit of the PC switching time is constrained by the carrier lifetime of the substrate material. For this, a semiconductor having short carrier life time is vital. Low-temperature grown gallium arsenide (LT-GaAs) and radiation-damaged silicon-on-sapphire (RD-SOS) have been utilized as suitable PC substrates. The carrier lifetimes of these materials are ultra-short (~0.2 ps) due to the high concentrations of defects, which enhance the trapping and recombination of the photoexcited carriers in the substrate.

Figure 1-2 illustrates the dipole radiation of the THz pulse from a PC THz emitter.

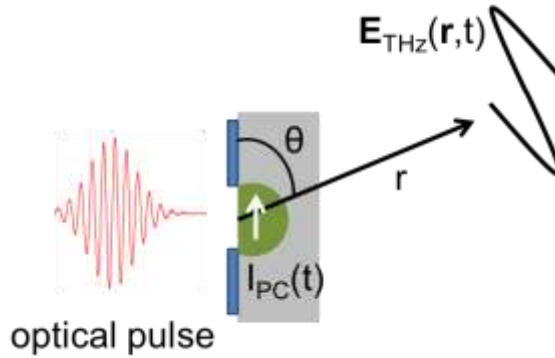


Figure 1-2 Dipole radiation for a PC THz emitter

Considering the radiation source of the PC switch as a point-like Hertzian dipole antenna [14], the radiated THz electric field can be written as:

$$E_{THz}(t) = \frac{\mu_0 L_0}{4\pi} \frac{\sin\theta}{r} \frac{d}{dt_r} [I_{PC}(t_r)] \propto \frac{dI_{PC}(t)}{dt} \quad (1.1)$$

where L_0 is the laser spot size, I_{PC} is the generated photocurrent, θ is the angle between the dipole moment vector and the direction of observation, and $t_r = t - r/c$ is the retarded time [17, 18]. This expression indicates that the radiated THz

electric field is proportional to the time derivative of the photocurrent produced in the PC switch. As the next step, the dependence of I_{PC} to various experimental parameters is calculated.

It has been shown that the convolution of the optical intensity profile and the impulse response of the photocurrent is given by:

$$I_{PC}(t) = \int I_{opt}(t-t') [en(t')v(t')] dt' \quad (1.2)$$

where $I_{opt}(t)$ is the intensity profile of the optical pulse, e is the electron charge, $n(t)$ is the carrier density, and $v(t)$ is the average electron velocity. The dynamics of the carrier density under an impulsive excitation is:

$$\frac{dn(t)}{dt} = -\frac{n(t)}{\tau_c} + G(t), \quad n(t) = \begin{cases} e^{-t/\tau_c} & \text{for } t > 0 \\ 0 & \text{for } t < 0 \end{cases} \quad (1.3)$$

where τ_c is the carrier lifetime and $G(t)$ is the carrier generation rate due to optical excitation ($G(t)$ has the form of a $\delta(t)$ which is the Dirac delta function). The equation of motion of electrons is expressed by the Drude-Lorentz model and is:

$$\frac{dv(t)}{dt} = -\frac{v(t)}{\tau_s} + \frac{e}{m} E_{DC}, \quad v(t) = \begin{cases} \mu_e E_{DC} [1 - e^{-t/\tau_c}] & \text{for } t > 0 \\ 0 & \text{for } t < 0 \end{cases} \quad (1.4)$$

where τ_s is the momentum relaxation time, m is the effective electron mass, E_{DC} is the DC bias electric field, and μ_e is the electron mobility, $\mu_e = e\tau_s/m$. Consider the laser pulse to be $I_{opt}(t) = I_{opt}^0 e^{-t^2/\tau_p^2}$, where τ_p is the pulse duration and I_{opt}^0 is the maximum intensity. Substituting for $n(t)$ and $v(t)$ from equations (1.3) and (1.4) into (1.2) and performing the integration leads to:

$$I_{PC}(t) \propto \mu_e E_{DC} I_{opt}^0 \quad (1.5)$$

Using this relation it is evident that the output of a PC switch depends on the bias voltage and the optical pump laser intensity. However, experimentally it is found that the THz output power is limited. (1) The E_{DC} is limited by the breakdown voltage of the vacuum [1], and (2) high optical pump powers saturate the THz radiation emission power due to the screening of the biasing field by excess photocarriers [19].

The metallic electrodes in this configuration also act as an emitting antenna by coupling the generated THz from the substrate into free space (i.e. impedance matching). Different geometries such as the stripline (Figure 1-3 (a)), dipole (Figure 1-3 (b)) and bow-tie (Figure 1-3 (c)) electrodes have been utilized as emitting THz antennas.

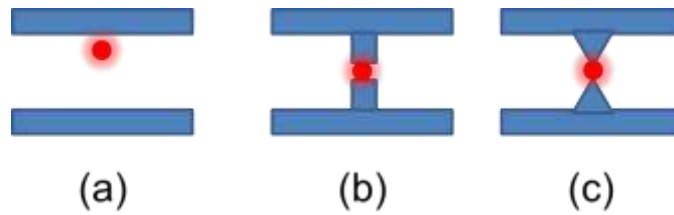


Figure 1-3 Schematic of the PC THz emitter having: (a) stripline, (b) dipole, and (c) bow-tie antenna.

It has been shown that the geometry of the emitting antenna influences the bandwidth as well as the amplitude of the generated THz electric field [19, 20]. A more detailed discussion of the effect of antenna design on performance of THz PC emitters is presented Chapter 2.

1.2 THz radiation detection

There are two major categories of detection schemes for detecting THz radiation: (1) coherent and (2) incoherent techniques [17]. In the coherent detection scheme, both the amplitude, as well as, the phase of the field is measured. However, for incoherent detection only the intensity of the field is measured. As a result, more radiation properties can be acquired by means of the coherent detection scheme.

Coherent detectors also possess higher sensitivity and spectral resolution when compared to incoherent detectors.

Most incoherent THz detectors are thermal sensors and they include bolometers [21], Goley cells [22], pyroelectric devices, Schottky diodes [23], superconductor-tunnel-junction (STJ) detectors [24], and Kinetic inductance detectors (KIDS) [25]. The principle of operation of all these detectors is based on absorbing THz radiation through a radiation absorber used in the detector. The bolometer consists of an electrical resistance thermometer (such as heavily doped Si or Ge) in which the resistance of the absorbing element changes as its temperature changes. Commonly, bolometers are operated under cryogenic temperatures. A Goley cell consists of an absorbing element behind a sealed gas chamber. The incident radiation heats the absorber and the volume of the sealed gas is modified, and by measuring this volume change the average power of the incident radiation is found. In pyroelectric detectors the change in the material temperature (due to the incident radiation) produces an electric polarization, which can be further measured, as it is proportional to the power of the incident radiation. An important property of thermal detectors is their inherent broad wavelength range of operation. To provide frequency selectivity appropriate filters are typically employed. In all the thermal detectors the absorbing materials need to reach a thermal equilibrium before a measurement is taken, so the response time of such detectors are inherently slow in the range of 0.1-0.001 s. In addition, the operation of these detectors is limited by thermal background noise. Thus, the threshold of the incident radiation power is higher compared to a coherent detector. The other class of incoherent detectors is high speed rectifying diodes. Schottky diodes are one example of these detectors where the output signal of the diode is the rectified input signal and the output voltage is proportional to the input power. It has been shown that Schottky diode based detectors are capable of detecting radiation up to 0.8 THz.

The common coherent detection techniques for THz pulses are electro optic (EO) and PC detection [26, 27]. For EO detection, the nonlinear Pockels effect is utilized. In this technique, the THz radiation and an optical probe pulse are

collinearly propagated in the EO crystal. A schematic of a common EO sampling setup is illustrated in Figure 1-4.

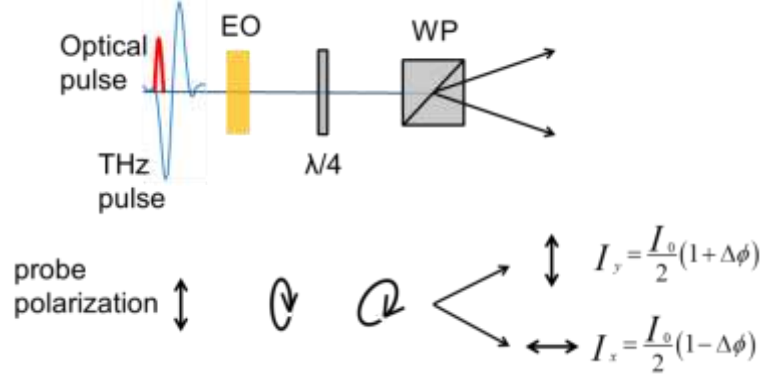


Figure 1-4 Schematic of the EO detection setup, which consists of an EO crystal (EO), quarter wave-plate ($\lambda/4$), and Wollaston prism (WP). The polarization state of the optical probe pulse is illustrated at the bottom of the figure.

The principle of the EO mechanism is as follows: the presence of a THz electric field induces birefringence in the EO crystal effectively changing the polarization state of the optical probe pulse as it propagates through the EO crystal. The evolution of the polarization state of the optical probe pulse is depicted at the bottom of Figure 1-4. Note that the initial state of polarization of the probe pulse is linear. The magnitude of the birefringence in the EO crystal is proportional to the amplitude of the THz electric field while the direction of the polarization is proportional to the sign of the THz electric field. Thus, the probe pulse possesses an elliptical polarization after passing through the EO crystal and the quarter wave-plate. Using a Wollaston prism, the probe beam is split into two orthogonal components, which are then guided to a balanced photodiode. Through this technique the difference in intensity of the two polarization components, $I_s = I_y - I_x$ of the probe pulse is measured. By considering the differential phase retardation, $\Delta\Phi$, introduced by the EO crystal to each component of the probe pulse, the measured signal I_s can be written as:

$$I_s = I_y - I_x = I_0 \Delta\phi \propto I_0 n_o r_{41} E_{THz} \quad (1.6)$$

where n_o is the refractive index of EO at optical frequency, r_{41} is the EO coefficient and I_0 is the intensity of the probe pulse. Thus the signal detected by the balanced photodiode is directly proportional to the amplitude of the THz electric field. The complete profile of the THz electric field is obtained by varying the time delay between the optical and THz pulses and measuring I_s . For a more detailed treatment of EO sampling in zinc-blende crystals see the thesis work of Jonathan Holzman [28].

The other technique for coherent detection of THz pulses is PC detection [1, 14]. The detection mechanism in this technique is similar to that of a PC THz emitter. The schematic of the PC THz detection scheme is illustrated in Figure 1-5.

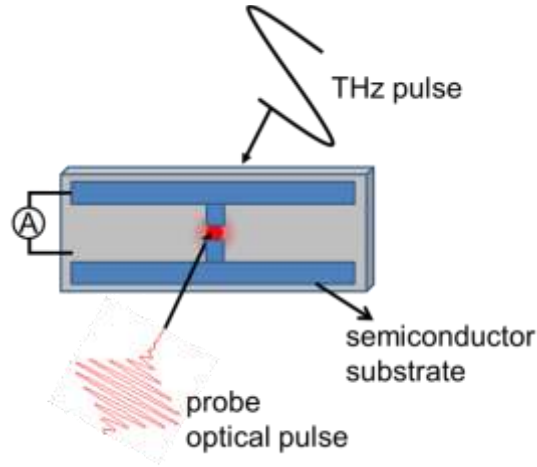


Figure 1-5 Schematic of PC THz detection.

In this setup, the electrodes are not biased. Instead, the incident THz radiation induces charges on the antenna when photocarriers are liberated by the probe pulse. The induced charges result in photocurrent, $I(t)$, that is measured by an ammeter. In this technique, $I(t) \propto E_{THz}(t)$. In this detection scheme, the antenna plays a critical role in coupling the incident THz radiation into the ammeter. Thus, through utilizing more efficient THz antennas the performance of the PC THz detector can be improved significantly. High performance THz antennas are expansively studied in Chapter 2.

It should be mentioned that these coherent detection schemes have advantages over the incoherent detection schemes [29]. (1) The sensitivity of the coherent

detection technique is substantially higher than that of incoherent detection. It has been shown that the sensitivity of coherent detection is 1000 times than that of incoherent liquid-helium-cooled bolometers; (2) Due to temporal gating during coherent detection, the thermal noise is eliminated in this technique. Both of the coherent detection schemes mentioned above are utilized in conventional THz-TDS systems.

1.3 THz time domain spectroscopy

Terahertz time-domain spectroscopy (THz-TDS) has been widely used as a technique for investigating material properties of thin films, polymers, and even metamaterials. Due to the unique properties of THz radiation, THz-TDS systems have found considerable utilization in many applications such as characterization, imaging and sensing [1]. In THz-TDS the electric field of the incident THz radiation is directly measured such that through the transmission/reflection of THz radiation through/from material targets, the absorptive as well as dispersive properties of the target material can be obtained.

The description of the THz-TDS system that was used in the course of this study is presented in Figure 1-6. The THz radiation generation and detection in this system is by mean of the PC THz emission (section 1.1) and EO detection technique (section 1.2), respectively.

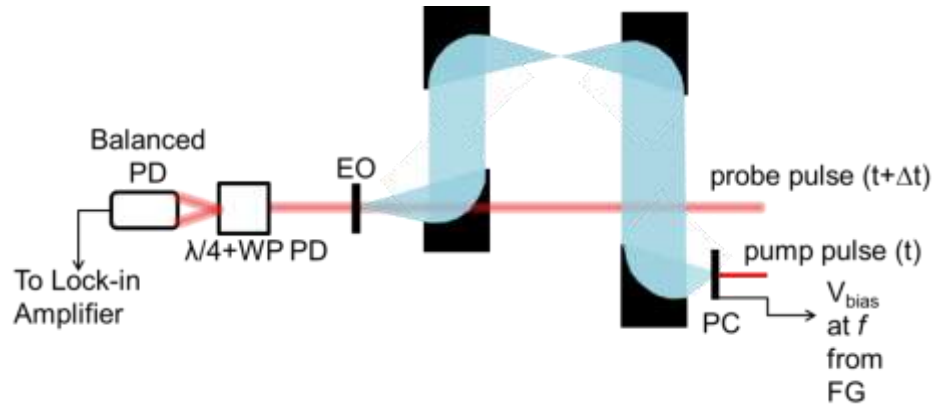


Figure 1-6 Top view schematic of the THz-TDS system. In this image the optical probe pulse has a temporal delay of Δt with respect to the pump pulse.

In this THz-TDS system, a mode-locked Ti:Sapphire laser generating ~ 20 fs laser pulses centered at 800 nm with a repetition rate of 80 MHz is used. The fs laser pulses are split into two portions using a broadband beam splitter to provide a pump and a probe pulse. Using a mechanical stepper motor a temporal delay is introduced to the pump beam with a temporal resolution of 80 fs. For the generation of THz pulses, the pump beam (60 mW) is focused onto a 20 V_{p-p} biased PC THz emitter, which is fabricated on a 500 μm thick semi-insulating (100) GaAs substrate having a resistivity of $2.5 \times 10^7 \Omega \text{ cm}$. The generated THz pulses are collimated and focused by a pair of 2inch diameter off-axis parabolic mirrors. This configuration enables the positioning of desired samples at the focus of the THz field. Using a similar parabolic mirror set, the THz pulse is collimated and refocused onto the EO crystal. For the THz detection, the fs optical probe beam (20 mW) is collinearly focused with the THz pulse onto a 0.5mm thick $\langle 111 \rangle$ ZnSe crystal. After propagating through the EO crystal, quarter wave-plate, and Wollaston prism a balanced photodiode converts the intensity difference of the two orthogonal polarization components of the probe beam into voltage. This voltage is proportional to the strength of the THz electric field as indicated in equation (1.6). This voltage signal is then amplified using a low-noise preamplifier and finally passed to a lock-in amplifier. The reference signal of the lock-in is synchronized with the signal from the function generator used for biasing the PC THz emitter (f , shown in Figure 1-6). In this THz-

TDS configuration, through modulation of the bias of the PC THz emitter at 54 KHz and locking at that modulating frequency, the low frequency noises are filtered out resulting in a high signal to noise ratio (SNR). The time-domain THz electric field is reconstructed by varying the time delay between the probe and the pump pulse while acquiring the voltage signal. This system results in a ~1 ps single-cycle THz pulses. Although the generated THz radiation is of the order of 10 nW, due to the coherent detection mechanism the SNR of the THz-TDS system is $\sim 10^4$. The properties of the generated THz pulse further depend on the emitting PC switch characteristics. By utilizing PC THz switches having various emitting antenna designs, this dependence is extensively investigated in Chapter 2.

1.4 Research Objectives

The main objectives of this thesis are:

1. To develop improved THz antenna designs that are able to emit higher THz radiation power and detect lower THz radiation signal levels than traditional THz PC antennas.
2. To develop electron tunnel diodes as high-speed rectifiers and mixers. Thus, metal-insulator-insulator-metal (MIIM) diodes have been studied for this purpose.
3. Investigate the incorporation of resonant tunneling into electron tunneling diodes. This is to research rectifying devices having improved I-V characteristics. Thus, metal-insulator-insulator-insulator-metal (MIIMM) diodes have been studied for this purpose.
4. Investigate the optimum process flow for fabricating planar antenna coupled MIM diodes for terahertz radiation detection applications.

5. To integrate the knowledge gained in designing and fabricating optimized THz antenna designs and high-speed tunnel rectifying diodes having maximum nonlinearity and asymmetry for fabricating ultrafast THz detectors.
6. To develop a versatile optical setup for all-THz time resolved pump-probe spectroscopy. This is for potentially characterizing the temporal and spectral response of the fabricated antenna coupled MIIM, and MIIIM diodes.
7. To research the interaction and effect of induced surface charges on the propagation of THz radiation. For this, THz pump-probe and THz-TDS were utilized to study the properties of transmitted THz pulses through composite and metallic material media.
8. To test for expanding the utilization of THz imaging from imaging inside dielectric materials into imaging more complex materials. THz-TDS is used for imaging dielectric objects embedded inside metallic media.

1.5 Thesis outline

The thesis consists of six chapters and is organized as follows:

- **Chapter 2: Fractal photoconductive terahertz radiation emitters** - In this chapter a comprehensive study of improved THz antenna designs that are able to emit higher THz radiation power and detect lower THz radiation signal levels than the traditional THz PC antennas is performed. A new class of plasmonic PC THz emitters based on fractal geometries is discovered. It is illustrated that this concept is applicable to all fractal geometries such as Sierpinski and Apollonian fractals. In addition, the

effect of self-similar geometry on radiation properties of PC THz emitters is investigated.

- **Chapter 3: THz electron tunnel devices** - This chapter presents a review of electron tunnel devices and in particular metal-insulator-metal diodes. A metal-insulator-insulator-metal quantum electronic tunneling device suitable for high-speed rectifiers is presented. Through the introduction of the resonant tunneling mechanism in a metal-insulator-insulator-insulator-metal diode, tunnel devices having enhanced nonlinearity and asymmetry I-V characteristics were achieved. It is envisioned that these high-speed rectifiers and mixers are suitable as diodes for THz radiation detectors as well as high-speed mixers.
- **Chapter 4: THz detector design, fabrication, and characterization**— In this chapter, the design, fabrication and characterization of antenna coupled MIM diodes are presented. The motivation behind fabricating these devices is to present a fast response THz detector to replace current THz detectors, which suffer from an inherently poor response time. The knowledge gained from designing and fabricating optimized THz antennas and fast response and highly nonlinear MIIM and MIIIM diodes will be integrated for fabricating ultrafast THz detectors.
- **Chapter 5: THz spectroscopy for characterization and imaging** – This chapter presents the capabilities of THz spectroscopy for characterizing and studying the time dynamics of devices and complicated systems. A versatile optical setup for all-THz time resolved pump-probe spectroscopy was designed and tested. This THz setup will be used to potentially characterize the temporal and spectral response of the fabricated antenna coupled MIIM, and MIIIM diodes. The knowledge gained through a series of experiments was applied in utilizing THz-TDS for imaging dielectric objects embedded inside metallic media. It is

envisioned that through the utilization of the fabricated fractal THz emitters and the rectifying THz detectors, more sensitive and higher speed THz imaging systems can be realized.

Chapter 6: Conclusions– The contributions of this research are summarized in this chapter. Some recommendations and plans for future work also suggested.

2. CHAPTER 2

Fractal photoconductive terahertz radiation emitters¹

2.1 Introduction

There has been an increasing interest in utilizing terahertz (THz) radiation for imaging, spectroscopy, and sensing [2, 4, 30]. Properties such as low attenuation through common dielectrics; being of shorter wavelengths compared to microwaves, which results in higher resolution imaging; and, the non-ionizing nature of the radiation at these frequencies (3 meV at 1 THz) makes THz radiation a suitable candidate for the above mentioned novel applications among others. With such attractive characteristics, research for optimized THz emitters, in particular photoconductive (PC) switch emitters, has gained considerable attention within the THz community. To date, investigation of producing high-field THz radiation via PC emitters involved the implementation of various THz PC configurations, such as bowtie, strip line, log-periodic, as well as dipole antenna emitters, all utilizing photoconductively-driven excitation schemes [19, 31, 32]. Nonetheless, the common theme of such designs is the excitation of free carriers in a semiconductor gap and then coupling the THz radiation to free-space by means of the surrounding metallic electrodes, which act as an emitting antenna. The emission properties of these THz sources have been explored both in terms of radiation spectrum bandwidth and the total radiation power emitted [31, 32]. In this regard, there have been reports on increasing the intensity of the THz radiation by optimizing the photoconductive antenna's design [33, 34]. By utilizing more complex photoconductive antenna designs better radiation directivity [35] and multiband THz emission were reported [36]. While much progress has been made in this area, to date there has not been any

¹ This work has been published by P. Maraghechi and A. Y. Elezzabi in, *Journal of Infrared, Millimeter, and Terahertz Waves*, **32** (7), 2011, *Optics Express*, **18** (26), 2010, and *Journal of Infrared, Millimeter, and Terahertz Waves*, **32** (11), 2011. Part of this work will appear in *IEEE Journal of Selected Topics in Quantum Electronics*, 2012.

investigations on antenna surface engineering to improve the emission characteristics of the photoconductive antennas by means of sub-wavelength control of THz surface plasmon currents.

It is well known that the magnitude and orientation of transient surface currents on a PC THz antenna govern the amount of the emitted THz power and the polarization purity of the emitted radiation. Thus, modifying the surface current flow pattern on the radiating element (antenna arms or transmission line), the radiation characteristics of the emitter can be configured to provide a particular resonance frequency, bandwidth, gain, efficiency, and polarization selectivity. In the microwave regime, this task is often achieved by utilizing spatial patterning of the antenna patch surface in the form of a fractal arrangement.

Fractal-shaped antennas are becoming very attractive in designing innovative antennas for communication systems. This stems from their self-similar and space filling geometrical arrangement that map into unique electromagnetic radiation properties. Due to these unique properties, advanced antennas with capabilities of being miniature, operating at multi-frequencies and possessing high directivity have been realized [37, 38]. In THz frequency range, implementation of multiband emission has been illustrated by Miyamaru et al. [37] via an H-fractal antenna on Si-GaAs substrate. In this chapter, a new class of plasmonic PC THz emitters based on a fractal geometries (Sierpinski and Apollonian). Comprehensive investigation of the radiation characteristics of the *complementary* fractal PC THz emitters is also introduced and explored at various fractal orders. By utilizing the unique aforementioned self-similar space filling of the tailored fractal surface and the plasmonic surface current spatial distribution, PC THz emitters exhibiting improved performance to conventional bow-tie THz emitters are demonstrated.

Due to their higher radiation power and better signal to noise (S/N) ratio, PC THz emitters based on fractal configuration are expected to be ideal for situations when higher THz signals are required, such as in THz-TDS systems. In parallel, these the THz fractal –based antennas can be utilized in THz PC detection schemes for sensitive detection schemes. Due to their improved receiving characters, it is

envisioned that a THz detection system capable of detecting lower levels of THz radiation than traditional detectors is a reality.

The goal of this chapter is to research improved THz antenna designs that are able to emit higher THz radiation power and accordingly able to detect low THz radiation signal levels than the traditional THz PC antennas. Also, different classes of fractals are investigated to realize whether the enhanced THz radiation properties of fractal PC THz emitters are universal to all fractals. Finally, the effect of self-similarity present on the antenna structure is studied.

This chapter is outlined as follows: the first section introduces the fractal geometries under investigation and their distinguishing characteristics. In the second section, the application of fractal geometries in designing microwave antennas is discussed. Particularly, the characteristics of fractal antennas in the GHz frequency range are reviewed. The third section is devoted to the design and fabrication process of the PC THz emitters where the effect of the overall length of the emitting antenna on the antenna emission properties is extensively studied. In the fourth section, by utilizing the unique self-similar and space filling of the tailored fractal surface and the plasmonic surface current spatial distribution, PC THz emitters exhibiting improved performance (~80% increase in the emitted THz radiation power) to conventional bow-tie and Sierpinski gasket THz emitters are demonstrated. The fifth section discusses a special class of PC THz dipole emitters based on the Apollonian fractal geometry. A comprehensive investigation of the radiation characteristics of the Apollonian fractal PC THz emitter as well as its quasi-complementary geometry is introduced and explored for various fractal orders. Finally, the effect of self-similarity in fractal PC THz emitters is studied. The performance of fractal THz PC emitters are compared to those of non-fractal emitters, and their radiation properties are studied. It is demonstrated that the THz radiation emission enhancement results not only from the sub-wavelength apertures pattern present on the antenna's surface, but also from the inherent self-similarity of the fractal geometry.

2.2 Fractal geometry and antenna

The term fractal, meaning broken or irregular fragments, was initially introduced by Mandelbrot [39] as “a shape made of parts similar to the whole in some way”. Many of the patterns in nature such as galaxies, snowflakes, mountain ranges, trees and leaves possess self-similar pattern that seem complex. It was the study of such patterns that initiated the advance of fractal geometry.

Two most important properties that characterize fractal geometry are fractal self-similarity and fractal dimension.

Self-similarity: An object is said to be self-similar when it is composed of smaller copies of itself. A more detailed definition for self-similarity is presented in [40]. It is noteworthy that only ideal mathematical objects possess infinite number of self-similar copies, and this is in contrast with the fractal structures in real world. The fractals deviating from the ideal fractal geometry are often called band-limited fractal shapes [41]. One of the unique properties of fractal geometries is that such structures do not have characteristic size which is direct consequence of self-similarity.

Dimension: The most intuitive definition of the dimension of an object is the number of coordinates required to describe that object. For example, a line has a dimension of one while a cube has a dimension of three. However, this definition of dimension fails to describe the dimensions of fractal objects. For fractal dimension, there are almost ten different definitions [40] all having some properties in common, but each with its own unique properties. For the purpose of the work that follows, the Hausdorff dimension is used for the definition of fractal dimension [40].

Since their earliest stage, fractals have found various applications in many branches of science and engineering. Through the combination of fractal geometries with electromagnetic theory, fractal electrodynamics, which investigates new classes of radiators, surfaces, propagators and scatterers, has evolved. One of the major applications of fractal in electrodynamics is in antenna theory and design. Designing antennas with properties of being: compact size, low profile, conformal and broadband has been an ever-growing demand. The reason fractal antenna design has

gained a lot of attention is the possibility of [42]designing improved antennas by incorporating fractal properties into conventional antenna design and applications.

Jaggard et al. [43, 44] during 1986-1992, studied the interaction of electromagnetic radiation with fractal structures. It was the results from these experiments that triggered the idea of utilizing fractal geometries as an antenna. The most unique property of fractal geometry that was utilized was the scale independence of structures that would be suitable for designing wavelength-independent antennas. The term fractal antenna, which involves fractal-shaped antennas, was first introduced by Werner [45] in 1994. However, there is an evidence of fractal antenna in 1993 in a final term project by Punete [45]. Sierpinski's antenna was the first fractal antenna that was illustrated to possess multiband frequency behavior. Other classes of fractals that were utilized as emitters are Minkowski dipole, Hilbert curve, Koch curves and fractal trees [46].

2.3 Sierpinski's antenna at Microwave frequencies

The Sierpinski fractal is the most classical fractal shape and its properties have been vastly studied in antenna design and applications. This multi-band fractal antenna was first introduced by Puentre et al. [47, 48]. The geometrical construction of the Sierpinski fractal starts with an equilateral triangle (Figure 2-1(a)). Next, a central triangle with vertices that are located at the midpoints of the side of the original triangle is removed from the initial structure resulting in Sierpinski's first order fractal (Figure 2-1(b)).

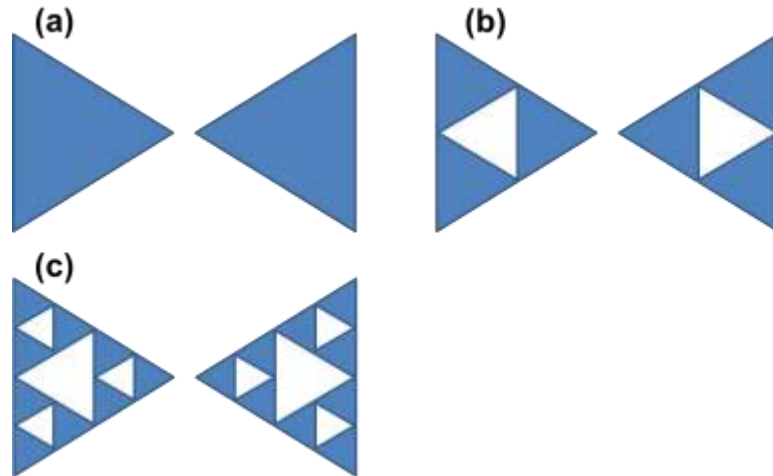


Figure 2-1 Schematic of: (a) a bow-tie, (b) Sierpinski's first order fractal, and (c) Sierpinski's second order fractal, antenna.

This process is continued until the desired fractal level is achieved (e.g. Sierpinski's second order fractal as shown in Figure 2-1(c)). The fractal dimension of the Sierpinski gasket of module 1 is 1.585 and the ideal structure has three copies of the whole structure scaled down by a factor of 2. On the second iteration, 3^2 exact copies of the triangular shapes are scaled down by a factor of 2^2 and so on. Due to this construction scheme, the Sierpinski gasket is considered a self-similar structure. A Sierpinski antenna having five fractal iterations is shown in Figure 2-2.

There are two reasons why Sierpinski gaskets have received the attention of the antenna design community: (1) their antenna characteristics can be easily compared to the well know traditional bow-tie antenna and (2) due to the presence of an apex in the gasket structure, the antenna has a well-defined feeding point. Several Sierpinski monopoles were constructed and tested by Puentre et al. [47, 48]. The investigated fractal antenna was the structure shown in Figure 2-2 and it consisted of thin triangular copper plates properly attached together. The antenna was placed over an 80×80 cm aluminum ground plate and fed through a 50 Ω coaxial probe.

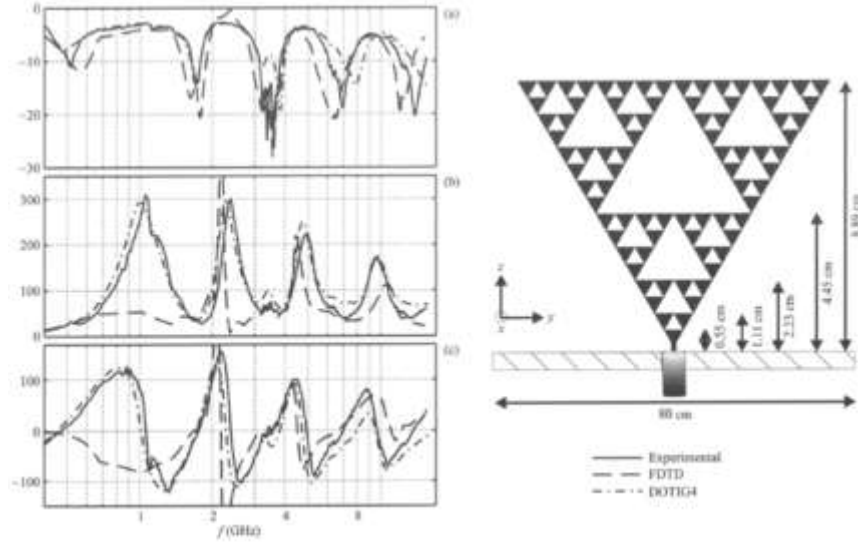


Figure 2-2 Schematic of a Sierpinski gasket antenna with five iterations at the right. (a) Input reflection coefficient, (b) input resistance, and (c) input reactance of the antenna [49].

The fractal antenna was tested in the frequency range of 0.05 GHz to 16 GHz [49]. The input resistance, reactance and magnitude of the input return loss are plotted versus frequency in Figure 2-2 (a-c). The multiband characteristic of the fractal antenna is evident from the plots. The input reflection coefficient plot clearly depicts five log-periodically spaced bands that are in good agreement with the numerical results. The resonant frequencies occur at 0.52, 1.74, 3.51, 6.95, and 13.89 GHz. The resonant frequencies are log-periodically spaced by a factor of $\delta=2$, which is the characteristic scaling factor of the Sierpinski design. In addition, the number of resonant frequencies follows the iteration number of the fractal structure. An empirical design equation has been derived for calculating the resonant frequencies of the Sierpinski monopole:

$$f_n \approx 0.26 \frac{c}{h} \delta^n \quad (2.1)$$

where c is the speed of light, h is the height of the largest gasket, and δ is the log-period.

To gain a deeper understanding into the operation of a Sierpinski antenna, Gonzalez et al. [50] studied the current density distribution over the fractal surface via

finite-difference time-domain (FDTD) simulations. Figure 2-3 illustrates the magnitude $|\vec{j}|$ of the current density vector. The figures on the right are the zoomed in plots of the circled area.

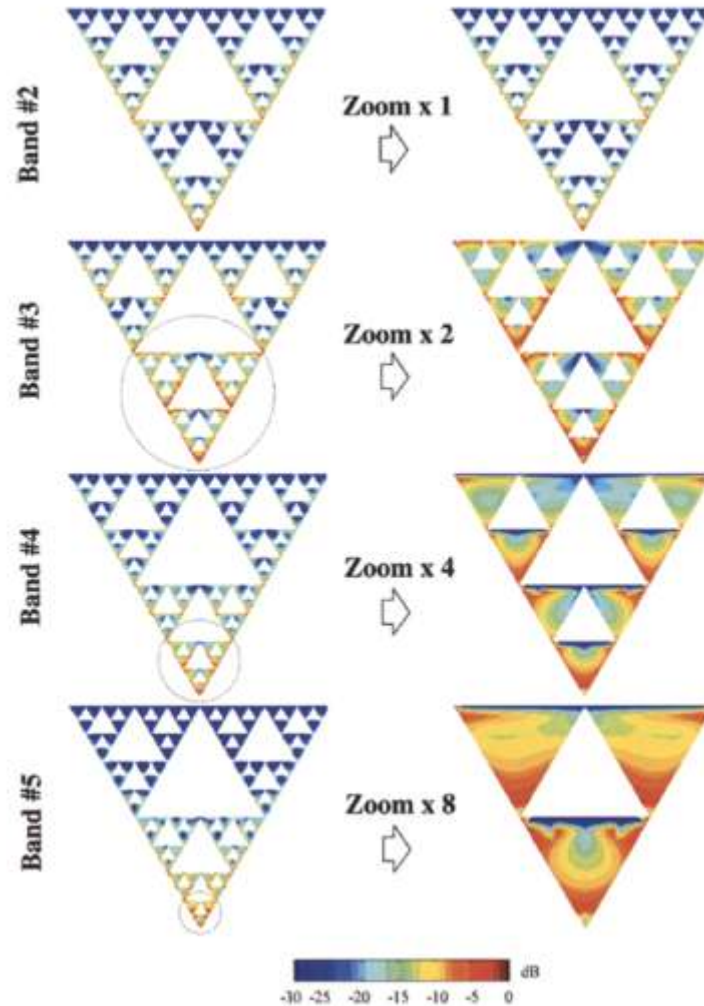


Figure 2-3 Current density distribution of the Sierpinski antenna surface at difference resonant frequencies [46].

It is evident that the current density distribution shows a self-similar pattern on the surface of the antenna. This investigation has been further verified experimentally by mean of infrared thermographs [50] showing the hot spots due to resistive lose in the Sierpinski antenna.

Another important and practical class of fractals is the Koch curve, which was named after the Swedish mathematician Helge von Koch. The Koch curve is

constructed by iteratively replacing the central segment of the unit interval by two segments of length $1/3$, both forming the upper part of an equilateral triangle. The Koch curve is a self-similar object and the overall object consists of many rescaled copies of the structure. Puente et al. [51] showed both numerically and experimentally that the Koch monopole can improve the antenna characteristics of the small monopole antennas. This antenna is illustrated in Figure 2-4.

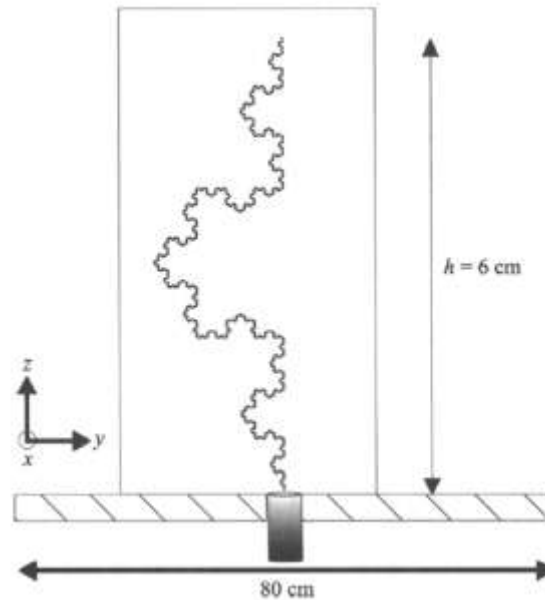


Figure 2-4 The five-iteration fractal Koch monopole [46].

Furthermore, Breden and Lagley [52] illustrated that a Koch fractal antenna also possesses multi-band characteristics. This study covered a frequency range of 1GHz to 10 GHz. Finally, Liu et al. [53] investigated the relationship between Sierpinski gasket and Apollonian packing monopole antennas. They concluded that the Apollonian monopole antenna possesses a multi-band characteristic in the frequency range of 1 -10 GHz.

2.4 Design and fabrication of PC THz emitters

Generating THz radiation via photoconductive (PC) excitation of a semiconductor surface has become a popular method for producing ultrashort THz pulses for various applications [4]. In this technique, broadband THz pulses are produced by accelerating the transient carriers by means of a bias electric field. For efficient coupling of the generated THz radiation from substrate into free space, integrated antennas were introduced to the PC switches. To date, significant attention has been given to utilizing various antenna designs, such as bow-tie [54], strip line [19, 55], strip line dipole [31, 56] as well as fractal based [20, 37] antennas for better generation and detection of THz radiation. Consequently, there have been investigations of the relationship between the geometric design parameters of strip line dipole antennas and their emitted THz radiation properties [19, 31, 57]. For example, Smith et al. investigated the spectral response of THz strip line dipole antennas of different lengths [57]. More recently, Miyamaru et al. reported on the relationship between the geometric parameters of a strip line dipole antenna design and the temporal characteristics of the transient THz radiation emission [31]. However, despite their high emission characteristics and broadband capability, there has been no experimental investigation on the relationship between the THz radiation emitted from a bow-tie antenna and its geometrical scale.

Bow-tie antennas, which are well known for their broadband response, have been vastly utilized for emitting and detecting THz radiation [54]. Similar to a strip line antenna, at a given operating frequency the length of the bow-tie antenna dictates its resonant frequency response. However, this resonant frequency is shifted due to the influence of the semiconductor substrate of the PC emitter. To account for this, empirical methods for calculating the appropriate antenna length for a predetermined resonant frequency response have been utilized. By utilizing the quasi-static [58], high-frequency [59] and Brown and Woodward [60] approximations for calculating the effective antenna length, various bow-tie antennas having different lengths were fabricated and tested. In order to better design a bow-tie PC THz emitter, we set forth to test the validity of these approximations.

Since an integrated surface antenna is fabricated directly on a dielectric substrate having permittivity ϵ_{sub} , the current induced on the antenna's surface propagates at a velocity of $c/\sqrt{\epsilon_{eff}}$, where c is the speed of light and ϵ_{eff} is the effective permittivity of the antenna in the half free-space, half dielectric substrate. It has been shown by Rutledge et al. [58] that ϵ_{eff} can be approximated by the quasi-static equation:

$$\epsilon_{eff} = \frac{\epsilon_{sub} + 1}{2} \quad (2.2)$$

At higher frequencies; however, the frequency dependence of the effective permittivity must be considered. In this approach, a bow-tie antenna can be transformed into a coplanar transmission line through the application of conformal mapping techniques [61]. Thus, the well-known dispersion characteristics of the coplanar transmission line can be exploited in the antenna design. Here, the analytical expression for the frequency-dependent effective permittivity for a coplanar transmission line is given by:

$$\epsilon_{eff}(f) = \left(\sqrt{\frac{\epsilon_{sub} + 1}{2}} + \frac{\left(\sqrt{\epsilon_{sub}} - \sqrt{\frac{\epsilon_{sub} + 1}{2}} \right)}{1 + a \left(\frac{f}{f_{te}} \right)} \right)^{1/2} \quad (2.3)$$

where a is related to the transmission line geometry and f_{te} is the surface wave cut-off frequency, defined by Frankel et al. [59].

Finally, Brown and Woodward [60] empirically demonstrated a calculation method for arriving with the appropriate resonant frequency length scale for the bow-tie antenna. They showed that for a bow-tie antenna having a 60° flare angle three resonant antenna lengths can be deduced by finding the zeros of the antenna reactance. These measurements were performed at a frequency of 500 MHz; however, their extrapolation to the THz frequencies is uncertain.

2.4.1 Experimental methods

The basic design of the PC THz emitter antenna was an equilateral bow-tie. The PC THz emitters were fabricated by means of photolithography on a 500 μm thick semi-insulating (100) GaAs substrate having a resistivity of $2.5 \times 10^7 \Omega \text{ cm}$. Following a photolithography patterning step, thin layers (20nm/100nm) of Cr/Au were sputtered and the metallic fractal pattern is transferred to the substrate using a lift-off process. In order to apply a bias voltage to the antenna arms, two 10 μm wide transmission lines were attached to the fractal antenna elements. The half-wavelength bow-tie antennas were designed for a resonance frequency of 0.53 THz, thus, the effective antenna lengths were calculated using the three different approximation techniques noted above. Three bow-tie antennas of end-to-end length L (see inset Figure 2-5) were fabricated, where $L=105 \mu\text{m}$ corresponds to the quasi-static length, $L=190 \mu\text{m}$ corresponds to Brown and Woodward's third resonance length, and $L=80 \mu\text{m}$ corresponds to the high-frequency approximation length.

It should be noted that according to Brown and Woodward's experiments, three resonant antenna lengths are present for a bow-tie antenna having a 60° flare angle. At the design frequency of 0.53 THz, these lengths are 46 μm , 107 μm and 190 μm . Only a bow-tie emitter having an antenna length of 190 μm was fabricated considering that the 107 μm antenna length is nearly identical to that of the quasi-static approach. Furthermore, since the THz radiation emission from the $L=46 \mu\text{m}$ strip line dipole antenna was shown to be very weak, its bow-tie counterpart was not considered in this experiment [57]. For all three antennas a 5 μm gap is used as the feed point.

2.4.2 Results and discussion

The PC THz emitters were illuminated by 60 mW Ti:sapphire laser pulses having durations of 20 fs, a central wavelength of 800 nm and a repetition rate of 80 MHz. The laser pulse was focused onto the 5 μm gap between the two antenna arms,

which are biased at 12 V_{pp}. The radiated THz and optical probe pulses were focused collinearly onto a 500 μm thick <111> ZnSe electro-optic crystal where complete information of the time-domain THz electric field was obtained. Since the biasing electric field of 2.4×10⁴ V/cm across the 5 μm gap is the same for all emitters, the spectral response of the three antennas having different lengths can be directly compared. Time domain terahertz waveforms emitted from the three different PC THz bow-tie emitters are shown in Figure 2-5 [62].

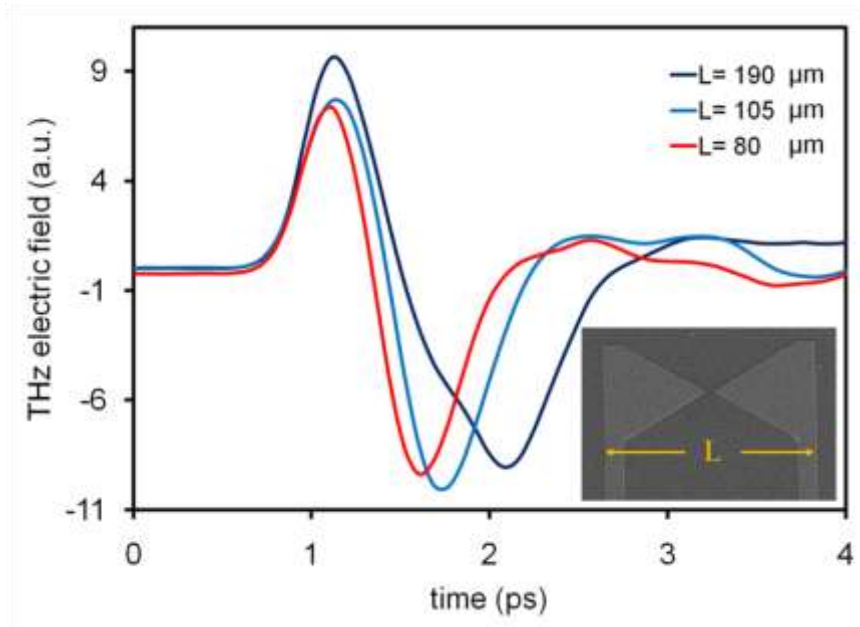


Figure 2-5 Time domain terahertz waveforms emitted from the bow-tie PC THz emitters for L= 190 μm (black), 105 μm (light blue) and 80 μm (red). The inset depicts the SEM image of the fabricated bow-tie THz PC emitters.

It is observed that the PC THz bow-tie emitter having its antenna length calculated using the quasi-static approach exhibits the shortest temporal duration (FWHM=0.7 ps). However, as the antenna length is increased, the full width half maximum (FWHM) of the emitted THz pulses are broadened, where the 190 μm bow-tie length emitter exhibits a FWHM duration of 1.4 ps. It is also observed that the peak-to-peak of the emitted THz electric field decreases with decreasing antenna length. This result is in good agreement with the results reported for dipole PC THz

emitters [31, 57]. To shed light on the frequency content of these emitters, the spectral power of the time-domain signals are depicted in Figure 2-6.

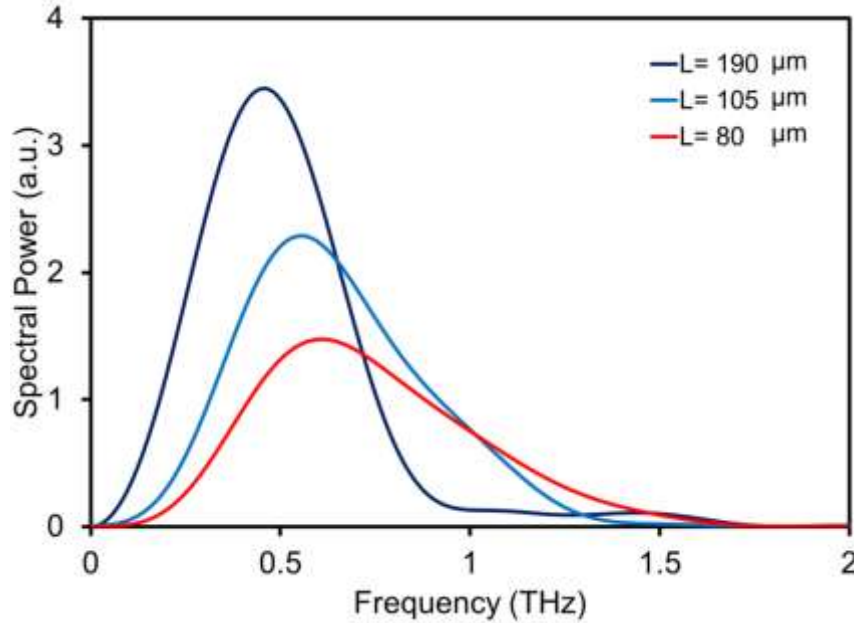


Figure 2-6 Spectral power for bow-tie PC THz emitters for $L=190\ \mu\text{m}$ (black), $105\ \mu\text{m}$ (light blue) and $80\ \mu\text{m}$ (red).

In a similar fashion to strip line dipole THz emitters, the THz radiation power emitted from the bow-tie PC emitter increases with antenna length. For $L=190\ \mu\text{m}$ (designed according to Brown and Woodward's scale length) exhibits a peak frequency of 0.46 THz. This antenna emits up to a maximum frequency of 0.8 THz, with a bandwidth of 0.4 THz FWHM. Furthermore, the $L=105\ \mu\text{m}$ bow-tie THz emitter, designed using the quasi-static approximation length, emits at a peak frequency of 0.55 THz. This THz PC emitter supports higher frequencies up to ~ 1.6 THz and possess a wider bandwidth (~ 0.55 THz FWHM). As the length of the antenna is decreased from $190\ \mu\text{m}$ to $105\ \mu\text{m}$, the intensity of the peak frequency is reduced by a factor of 1.5. Interestingly, the THz PC emitter designed using the high-frequency approximation results in a peak frequency of 0.62 THz, but with much lower THz radiation intensity when compared to the other bow-tie emitters. Such a bow-tie THz emitter exhibits a similar THz emission bandwidth (~ 0.6 THz FWHM) to that obtained using the quasi-static approximation. It is evident that the quasi-static

approximation for the bow-tie THz emitters provides the best match (within 5% deviation) between the design peak frequency and the measured one.

The above mentioned fabrication method and the quasi-static approximation was utilized to design and fabricate the fractal PC THz emitters in the following sections.

2.5 Sierpinski fractal PC THz emitter

In this section, we present a new class of plasmonic PC THz emitters based on a Sierpinski gasket fractal geometry [20]. Comprehensive investigation of the radiation characteristics of the *complementary* Sierpinski fractal PC THz emitters is introduced and explored for various fractal orders. By utilizing the unique aforementioned self-similar and space filling of the tailored fractal surface and the plasmonic surface current spatial distribution, we show that these PC THz emitters exhibit improved performance to conventional bow-tie and Sierpinski gasket THz emitters.

The PC THz antenna architecture follows that of the common Sierpinski fractal. Here, one starts with a simple 60° equilateral triangle as basic bow-tie antenna. For the first iteration the middle of each sides are connected and that surface is cut out of the solid bow-tie antenna surface. The iteration process is repeated for different orders, i , such that any triangular portion is an exact replica of the whole gasket, or the gasket is perfectly self-similar. As the number of iterations increases, self-similar smaller triangular apertures are formed on the surface of the antenna. The dimension of the Sierpinski gasket is $\log(3/2) = 1.5849$ and the total solid area of the antenna surface, A_i , at each iteration is given by $A_i = 1 - \sum_{i=1}^N (3/4)^i$. The basic design of the PC THz emitter antenna structure is a complementary bow-tie Sierpinski gasket fractal. These emitter antennas were fabricated using an inverted pattern of a regular Sierpinski gasket fractal pattern, where the total solid area of the antenna surface, $A_{Ci} = I - A_i$, at each iteration. However, in order to maintain a constant photoconductive area (optically-excited antenna feed point) for the complementary

Sierpinski gasket fractal antennas, a 2 μm wide strip frame circumscribed the inverted Sierpinski gasket fractal units. Notably, with such reconfiguration, the electric field applied to the photocurrents is kept the same for all types of fractal antennas under study.

It should be noted that throughout the investigation the antennas' shape and length are kept fixed and only the sub-wavelength features within the antenna are altered in a self-similar manner to form the Sierpinski gasket fractal. This ensures that at the optically-excited antenna feed point the biasing electric field is the same for all of the THz emitters.

Figure 2-7(a-d) illustrates scanning electron microscope (SEM) images of the fabricated complementary bow-tie PC THz emitter and the complementary Sierpinski PC THz emitters for the first three orders ($i = 1, 2$ and 3). Overall, it can be stated that the PC THz emitters encompass triangles of lengths $\sim 52 \mu\text{m}$ for the complementary bow-tie emitter down to $\sim 1.5 \mu\text{m}$ for the complementary third-order Sierpinski PC THz emitter.

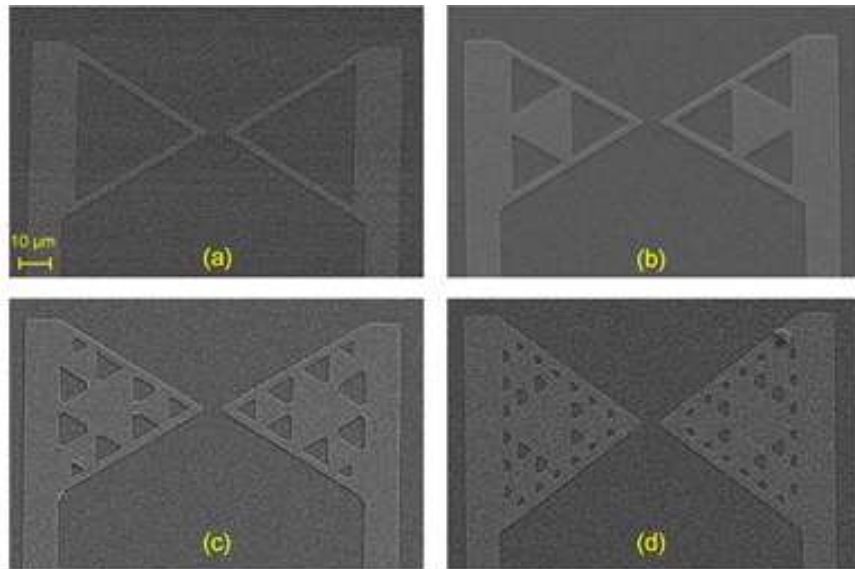


Figure 2-7 Complementary of (a) bow-tie, (b) first order, (c) second order, and (d) third order Sierpinski PC THz emitters.

These sub-wavelength features of the antenna are vital to the operation of the PC THz emitters as they enable the emitters to access the THz plasmonic regime. For

comparison, a traditional bow-tie antenna was fabricated along with three ($i = 1, 2$ and 3) Sierpinski PC THz emitters. SEM images of these emitters are shown in Figure 2-8.

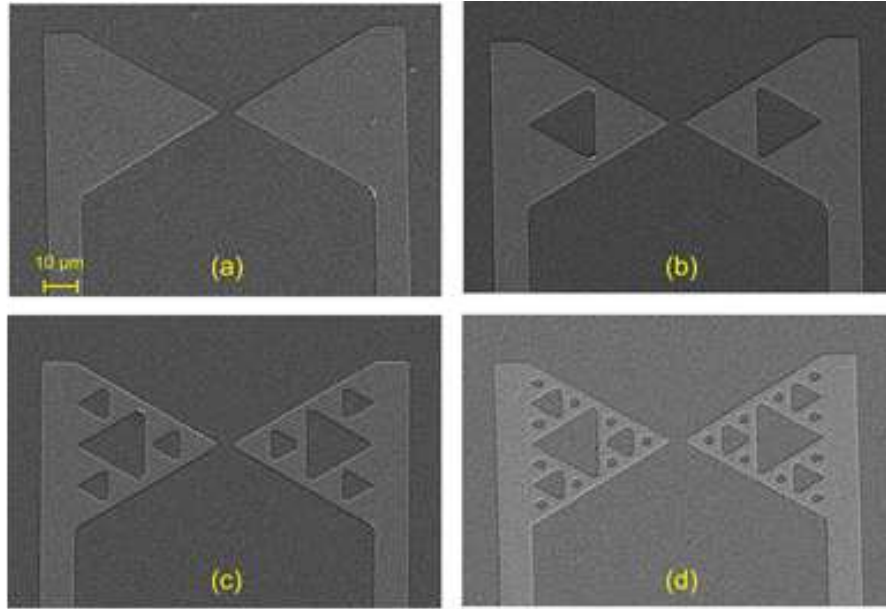


Figure 2-8 PC emitters of (a) the bow-tie, (b) first order, (c) second order, and (d) third order PC THz emitters.

The most crucial step is the alignment of the PC THz antenna with the focused laser beam. For minimizing any misalignment issues when different PC THz emitters are compared, two alignment steps have been taken. First, the focal spot of the laser is located at the 5 μm gap via a coarse visual microscope. Second, for fine alignment, the DC resistance of the photoconductive switch was monitored while the emitter's gap was illuminated. To ensure that all PC emitters have the same DC resistance (5 ΩK) prior to any THZ-TDS measurements, the location of the PC THz emitter was fine-tuned correspondingly. This is important in finding an absolute reference measurement of power.

2.5.1 Results and discussion

The effect of the sub-wavelength fractal openings present in the complementary Sierpinski PC THz emitters on the radiation properties of such emitters is investigated using time-domain THz spectroscopy. To isolate this effect, the electric field across the PC junctions was kept fixed for all fractal emitter having various orders. The spectral powers of the emitted radiation for complimentary Sierpinski PC THz emitter are illustrated in Figure 2-9 along with the spectral power of a conventional bow-tie PC THz emitter.

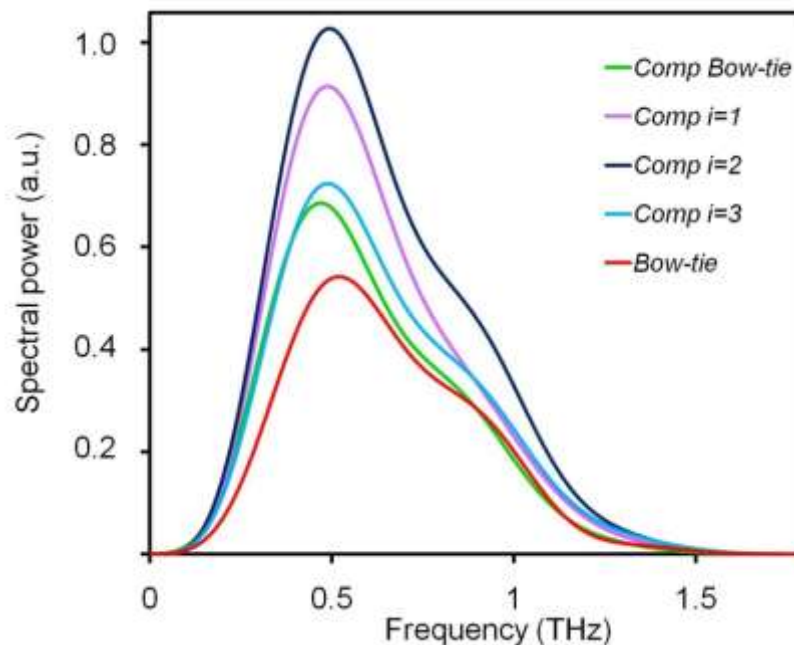


Figure 2-9 Spectral power for the complementary bow-tie and Sierpinski PC THz emitters orders one to three and the bow-tie PC THz emitters.

Interestingly, the THz radiated power of the complementary Sierpinski PC THz emitters increases as the fractal order is increased up to the second-order, after which it starts to decrease. It is worth noting that one finds a 20% increase in the radiation power when using the first order complimentary Sierpinski PC THz emitter compared to the bow-tie emitter. The highest emitted THz radiation enhancement was observed from the second-order complementary Sierpinski PC THz emitter;

which, when compared to a bow-tie emitter of the same dimension, exhibits an ~80% increase in the emitted THz radiation power. Furthermore, this enhanced THz emission does not come at the expense of loss in the radiated THz bandwidth, as the detected bandwidth is almost identical (within 10%) to that of the bow-tie PC emitter of similar dimensions. Clearly, this power enhancement cannot be attributed to the biasing electric field distribution since the optically-injected electrons and holes in the GaAs substrate in all of the emitters experience the same electric field of 2.4×10^8 V/cm at the 5 μm gap.

To shed light into the origin of the enhanced THz emission from the complementary Sierpinski PC THz emitters, radiation from Sierpinski PC THz emitters, which includes the bow-tie antenna, have been studied. The spectral powers of the emitted radiation from the Sierpinski PC THz emitter are illustrated in Figure 2-10 along with the spectral power of a bow-tie PC THz emitter having the same dimensions.

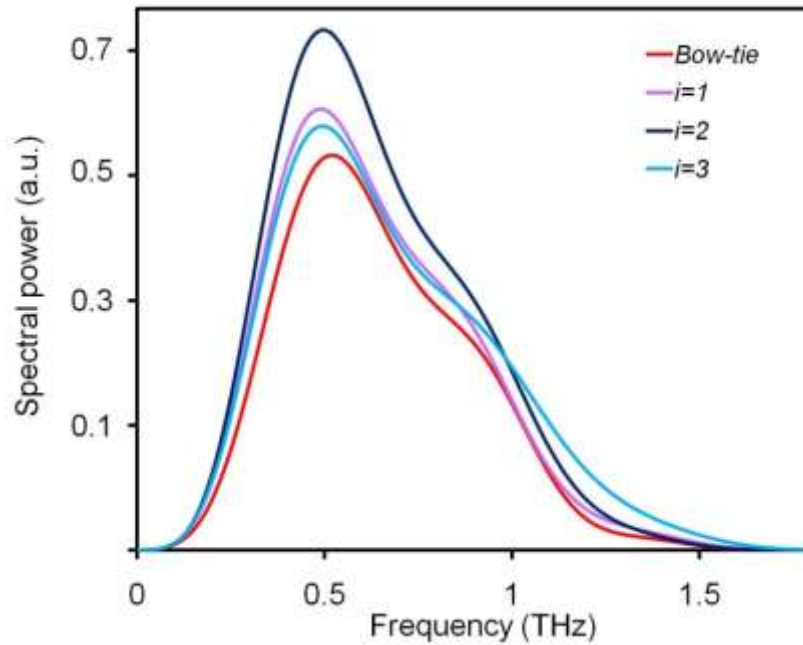


Figure 2-10 Spectral power for the bow-tie and Sierpinski PC THz emitters orders one to three. Note that the scale is normalized to the complementary THz PC emitters.

A similar trend is observed for the different orders of the Sierpinski PC THz emitters. All the Sierpinski PC THz emitters of different orders emit higher THz

radiation compared to the bow-tie emitter, albeit lower than the complementary ones. The radiated power of the Sierpinski PC THz emitters increases as the fractal order is increased up to the second-order, after which it starts to decrease similar to the complementary ones. The presences of multi-resonances are expected for fractal surfaces when illuminated by a broadband electromagnetic radiation. For the second order Sierpinski antenna when illuminated by a broadband source (4 THz bandwidth), the 3D-FDTD simulations show the presence of two resonance frequencies at ~ 0.6 and ~ 2.1 THz. Not surprisingly, the first resonance frequency of the second order Sierpinski PC THz emitter was ~ 0.6 THz when the emitted radiation was acquired by the THz-TDS system. However, since the maximum frequency emission of the GaAs-PC switch is 1.5 THz, the second resonance at 2.1 THz is not excited by the PC switch.

While both complementary Sierpinski and Sierpinski PC THz emitters exhibit higher THz emission characteristics with the former being of higher THz emission, it is imperative to pay close attention to their spectral peak. Figure 2-11 (a,b) depicts a plot of the normalized spectral power of both complementary Sierpinski and Sierpinski PC THz emitters along with their corresponding bow-tie emitters.

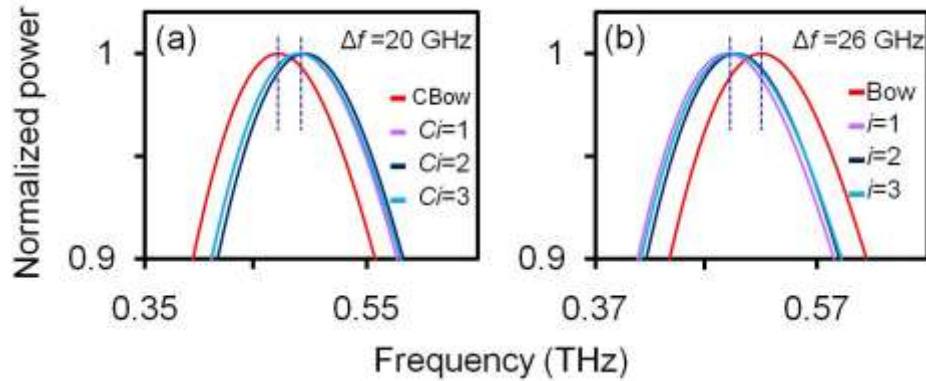


Figure 2-11 Normalized power plots of the (a) complimentary Sierpinski PC THz emitter and (b) Sierpinski PC THz emitter. The amount of frequency shift (Δf) is shown on the top right corner of the figures.

It is evident that the central frequency of the emitted radiation from the higher order complementary Sierpinski PC THz emitters are blue shifted by 20 GHz compared to the complementary of the bow-tie PC THz emitter (Figure 2-11 (a)). In

contrast, the Sierpinski PC THz emitters have undergone a red shift by 26 GHz compared to the bow-tie emitter (Figure 2-11 (b)). The observed frequency shifting is attributed to the slight change of the impedance of the higher order antennas relative to their bow-tie counterparts. A similar effect has been observed at the microwave frequencies, where higher order Sierpinski's fractal antennas show a red frequency shift [38]. This increase in THz emitted radiation power is not due to change in the antennas directivity. Electromagnetic simulations indicated that there is no directivity change associated with the different orders of fractals as well as the complementary bow-tie PC emitter (Figure 2-12 (a, b)).

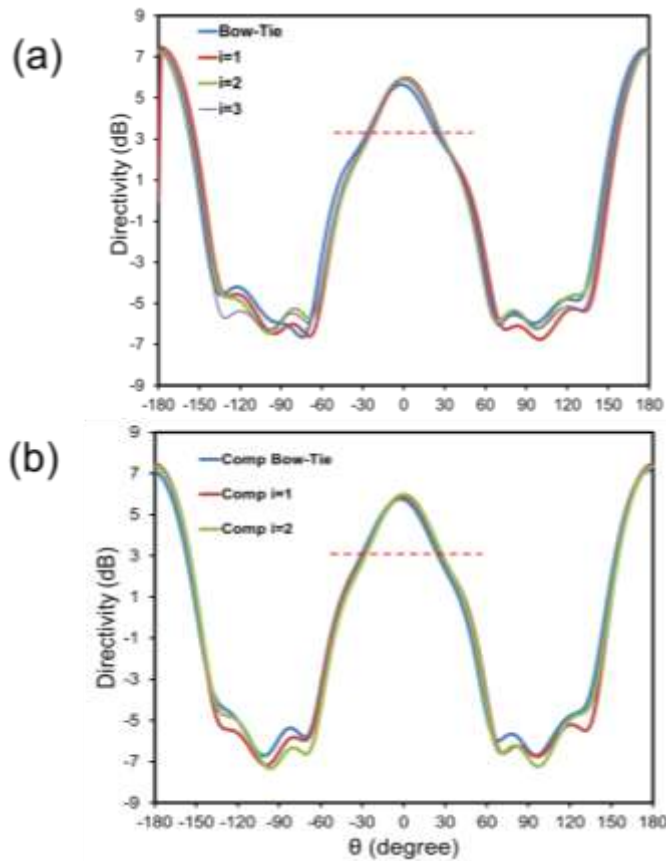


Figure 2-12 Directivity plot for the (a) Bow-tie and Sierpinski Fractal emitters and (b) Complementary bow-tie and Sierpinski fractal emitters. The dashed line represents the location of substrate-air interface.

Since the surface's sub-wavelength restructuring is responsible for this enhanced THz emission, it is only natural to examine what is occurring on the surface

of the fractal emitters. A key lead is to examine the spatial distribution of the surface plasmon current density. Finite difference time domain (FDTD) numerical simulation was performed to obtain the plasmonic surface current densities on all the fractal PC THz emitters. The emitters' dimensions and parameters are chosen to match the experimental ones including the antenna material (Au), transmission line, and the antenna substrate (GaAs). Figure 2-13 illustrates the spatial distribution of the surface plasmon current density, $J_x(x,y)$, along the axis of the Sierpinski emitters acquired at an intermediate peak emission frequency of 0.55 THz.

It is well-known that the incorporation of antenna architecture into a PC THz emitter improves the coupling efficiency of the THz radiation from the semiconductor substrate to free-space. However, this coupling efficiency can be further enhanced by introducing an antenna operating in the plasmonic regime. Unlike the interaction with a smooth antenna surface, the THz electric field residing inside the semiconductor can interact with the antenna's overall surface via coupling through collective electronic excitations at the antenna's metallic surface (surface plasmons) provided that this surface satisfies the conservation of energy E and momentum \mathbf{k} of the incident THz field. By engineering the antenna surface to have perforations of dimensions that are much less than the wavelength of the excited radiation, the THz generated from the PC gap is coupled to the sub-wavelength structures by means of inducing surface charges. The charge depolarization at these metallic features is assigned to the induced THz surface plasmon currents.

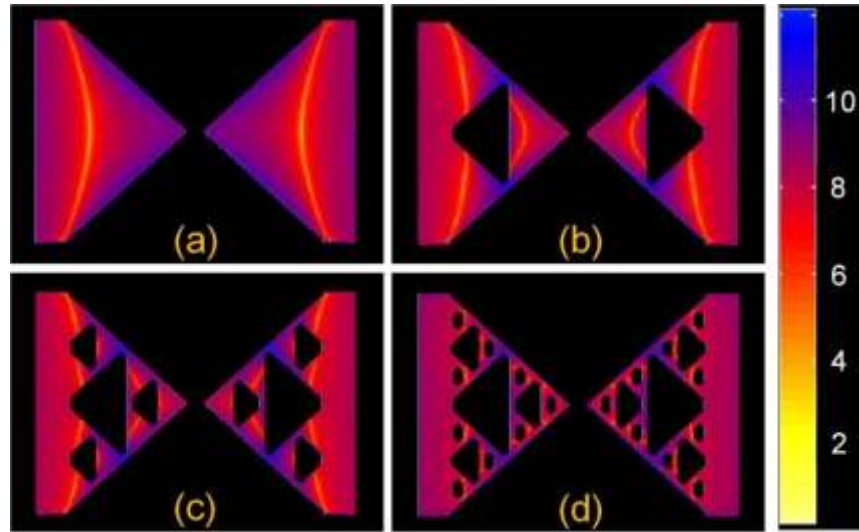


Figure 2-13 The spatial distribution of the surface plasmon current density, $J_x(x,y)$, in logarithmic scale along the axis of the Sierpinski PC THz emitters of (a) the bow-tie, (b) first order, (c) second order, and (d) third order, acquired at an intermediate peak emission frequency of 0.55 THz.

As shown in Figure 2-13 (a), the bow-tie PC THz emitter, the surface plasmon current is distributed in such a way that the current density increases along the sides of the structure. However, in the Sierpinski PC THz emitters $i = 1, 2$ and 3 , the sub-wavelength perforations present on the fractal antennas redistribute these currents more towards the nodes on the side of the antenna (Figure 2-13 (b-d)). Furthermore, in Figure 2-13 (b-d) one clearly observes the self-similar current pattern on the sub-units of the fractal antenna. In these structures, the antenna surface behaves as a collection of individual sub-wavelength radiators that are coherently coupled to each other. It is the radiation resulting from these coherent and self-similarly-distributed currents that in the far-field augment the THz radiation emission.

An exact complementary Sierpinski PC THz emitter also produces a self-similar current pattern; however, in the present complementary Sierpinski PC THz emitters, the $2 \mu\text{m}$ wide circumscribing strip acts to steer $J_x(x,y)$ towards the outer edges of the antenna, specifically near the antenna gap (as shown in Figure 2-14).

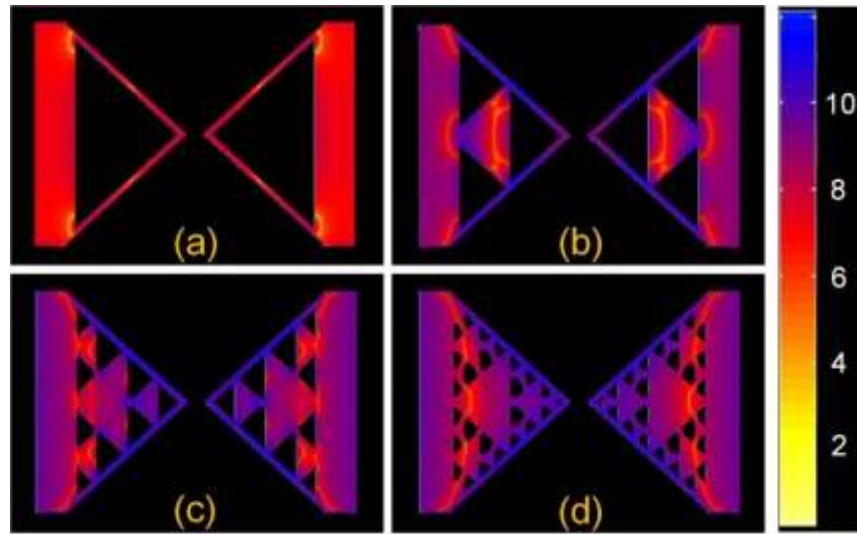


Figure 2-14 The spatial distribution of the surface plasmon current density, $J_x(x,y)$, in logarithmic scale along the axis of the complementary Sierpinski PC THz emitters of (a) the bow-tie, (b) first order, (c) second order, and (d) third order, acquired at an intermediate peak emission frequency of 0.55 THz.

This modification in the surface plasmon currents within the triangular fractal units is responsible for improving the emission properties of the complimentary antenna compared to the bow-tie (Figure 2-13 (a)), its complementary (Figure 2-14 (a)), and Sierpinski PC THz emitters (Fig. 6 (b-d)). As the complementary Sierpinski PC THz emitters order is increased, the perforations' dimension present on the antenna surface shrinks as $\sim \lambda/10$, $\lambda/22$, and $\lambda/200$ for the first, second, and third fractal orders, respectively. For $i = 3$ (Figure 2-14 (d)), the dimensions of the apertures become much smaller than the wavelength ($\lambda/200$) and the characteristics of the antenna plasmon surface current distribution resembles that of the solid surface bow tie antenna (Figure 2-13 (a)). Here, the small fractal perforations do not participate in coupling of the surface plasmon to the antenna and thus, the THz emission power decreases.

The THz radiation power for both the Sierpinski PC THz emitters and their complementary geometries increases from the first-order up to the second-order. This has been attributed to the self-similarity of the fractal architecture. To investigate the role of the fractal's self-similarity on the enhanced THz emission, two THz PC emitters having fractal-like geometries were introduced as shown in Figure 2-15. In

these geometries, the fractal iteration was introduced to only one side of the triangle of the first order Sierpinski PC THz emitter. These THz PC emitters do not possess the self-similar characteristics inherent to the Sierpinski gasket fractals. However, their metallic filled areas relative to the bow-tie shown in Figure 2-13 (a) are 69% and 67% for the structures shown in Figure 2-15 (a) and Figure 2-15 (b), respectively. This falls between that for the first-order (75%) and second-order (56%) Sierpinski PC THz emitters.

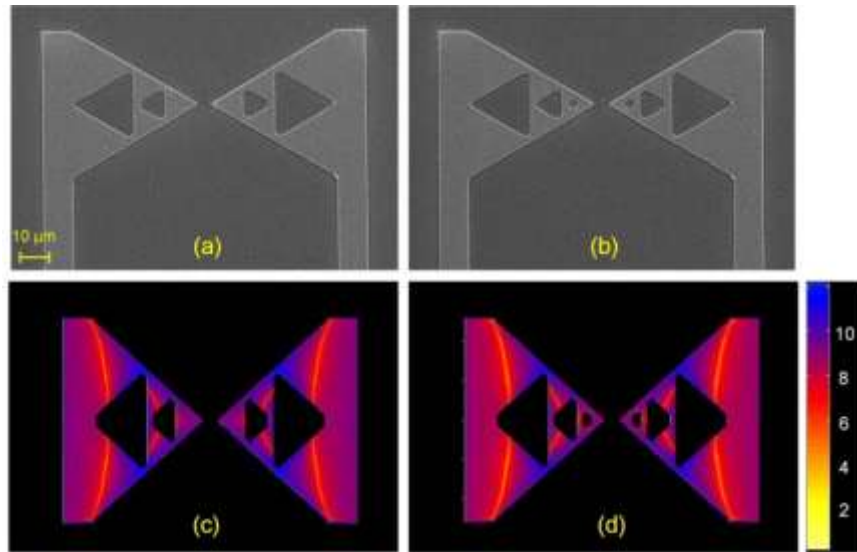


Figure 2-15 SEM images of the fractal-like geometries iteration orders (a) two, and (b) three applied only to one side of the antenna. The spatial distribution of the surface plasmon current density of the, $J_x(x,y)$, in logarithmic scale along the axis of the fractal-like geometries iteration orders (a) two, and (b) three applied only to one side of the antenna, acquired at an intermediate peak emission frequency of 0.55 THz.

The Sierpinski fractals PC emitters have been chosen for this investigation since the complementary fractal PC emitters used in this experiment are not truly exact complementary fractals. This is because; the $2\mu\text{m}$ wide circumscribing strip lines were needed to have the same electric field concentration at the antenna's gap. This is the reason why the self-similar surface plasmon current distribution is not obvious in the Figure 2-14. For the purpose of comparison, we chose to investigate an exact fractal (Sierpinski fractal) to shed light on the current distribution on the surface. From Figure 2-15 (c, d), it is observed that the surface plasmon current

density maps of these emitters do not show the self-similar patterns. Both THz PC emitters showed equal THz radiation emission power to the bow-tie PC THz emitter which is 18% and 30% lower than those obtained from the $i = 1$ and $i = 2$ Sierpinski PC THz emitters, respectively. In these PC THz emitters, the lack of self-similarity reveals itself by lowering the coherent interference and coupling of the generated PC THz radiation by the perforations to free-space. This finding supports the fact that the self-similar current distribution is the key in the observed enhanced THz emission. The self-similar geometry can be thought of as an intermediate configuration between periodic and non-periodic geometry. As shown in Figure 2-13 (b-d), the apertures present on the Sierpinski's fractal antennas are configured in a self-similar fashion. If the apertures on the antenna surface were configured in a periodic manner, the output emission would show a resonance radiation at specific frequencies governed by the periodicity parameters. On the other hand, if the apertures were distributed in a non-periodic fashion, the emitted radiation would not result in optimal constructive interference at the far-fields. For a self-similar surface structure, each segment of the antenna is a replica of the whole antenna, with its size being scaled down according to the fractal order. In such a configuration, the radiation emitted by each segment will be added coherently to result in the overall radiation pattern. That is, the overall radiation pattern of the fractal antenna is the summation of all the individual radiators that are configured in a self-similar architecture.

2.6 Apollonian PC THz emitter

Considering the concept of introducing fractal architecture into PC THz emitters, an unanswered question is whether this enhancement is intrinsic to other fractal types besides the well-studied Sierpinski fractal. Having ultra-wideband characteristics is a vital antenna property for investigation of new classes of THz PC emitters. It is known from microwave antenna theory that thickening the arms of the dipole results in an increased bandwidth. The reason for this is that for a thick dipole, the current distribution no longer varies sinusoidal across the dipole arms. This

clearly makes a bow-tie dipole a better emitter than a simple planar dipole. However, a typical integrated wire dipole antenna and a bow-tie antenna are just simple 2D manifestations of their 3D counterparts which are a cylindrical dipole and biconical dipole, respectively (both of which possess even wider bandwidth). In the same fashion, a circular dipole antenna is just a 2D planar version of the spherical dipole antenna.

To generalize the concept of fractal PC THz emitters, we investigate a special class of plasmonic PC THz dipole emitters based on circular-Apollonian fractal geometry. A circular dipole antenna is studied as a unique dipole (2D version of a spherical dipole antenna) that has been shown to exhibit interesting electromagnetic characteristics at microwave frequency range. Only recently circular dipole antenna has been explored [63]. This antenna exhibits distortion-free ultra-wideband characteristics, an omnidirectional radiation pattern, and a linear phase response. Its self-similar family belongs to the circular-Apollonian fractal family. A comprehensive investigation of the radiation characteristics of the Apollonian fractal THz emitter, as well as its quasi-complementary geometry, is introduced and explored for various fractal orders.

The basic design of the PC THz emitter antenna is an Apollonian gasket fractal [64]. The geometrical construction of the Apollonian fractal starts with a circle (Figure 2-16(a)). Next, three identical circular holes tangent to the circumference of the initial circle are removed from the solid surface resulting in first order Apollonian fractal (Figure 2-16(b)).

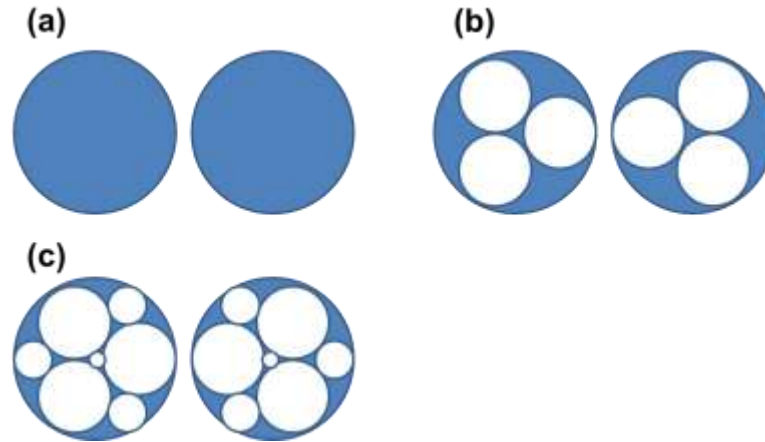


Figure 2-16 Schematic of: (a) a circular, (b) first order Apollonian fractal, and (c) second order Apollonian fractal, antenna.

Finally, by iteratively removing the largest possible circular holes (still tangent to the circumference of the structure features) this process is continued until the desired fractal level is achieved (e.g. second order Apollonian fractal as shown in Figure 2-16(c)). The fractal dimension of the Apollonian fractal is 1.305. Due to this construction scheme, the Apollonian fractal is considered a self-similar structure.

The complementary fractal antennas were fabricated using an inverted pattern of a regular Apollonian fractal pattern. However, in order to maintain the same photoexcitation area (optically-excited antenna feed point) for the complementary Apollonian fractal antennas in comparison to the Apollonian gasket counterpart, a 2 μm wide strip border is made to circumscribe the complementary Apollonian fractal units. Therefore, the complementary fractals presented here are not exact fractals but rather quasi-fractals. Hence, they will be addressed as complementary fractals. In addition, three 2 μm wide lines have been added to the design to ensure that the inner circles are connected. Notably, with such configurations, the electric field applied to the photocurrents is kept the same for all types of fractal antennas under study. The THz emitters were fabricated using the procedure described in 2.4.1.

Scanning electron microscopy (SEM) images of the fabricated circular, Apollonian fractal orders one and two, complementary circular and complementary Apollonian fractal orders one and two THz emitters are shown in Figure 2-17.

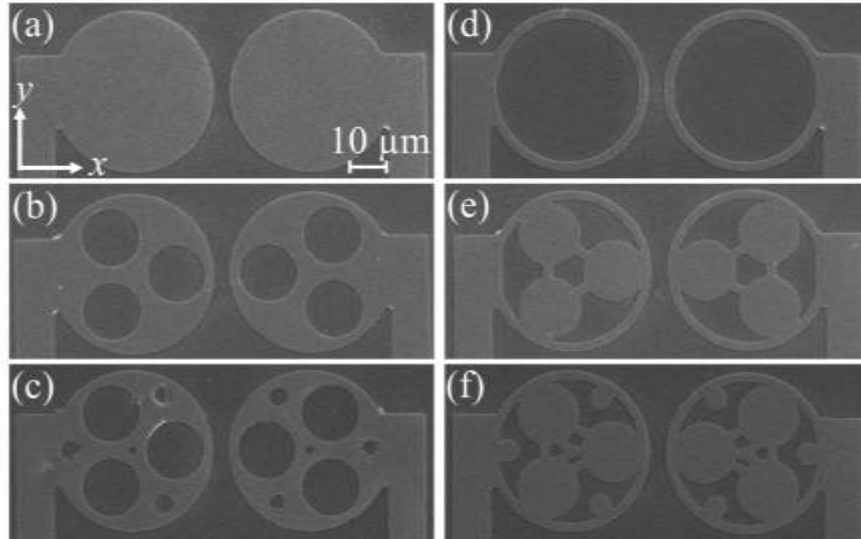


Figure 2-17 SEM images of (a) circular dipole, (b) first order Apollonian, (c) second order Apollonian, (d) complementary circular dipole, (e) complementary first order Apollonian, and (f) complementary second order Apollonian emitter.

Clearly, the fractal spatial pattern and the size of the sub-wavelength apertures present on the emitter's surface are different for various fractal orders. By applying the same biasing electric field (2.4×10^4 V/cm) across the $5 \mu\text{m}$ gap, and since the overall outer edge shape of the Apollonian dipole emitters is identically circular for all PC THz emitters, the role of the sub-wavelength apertures can be clearly isolated from the elementary circular dipole antenna (shown is Figure 2-17(a)).

2.6.1 Results and discussion

The spectral powers of the emitted radiation for the Apollonian fractal emitters, the complementary Apollonian fractal emitters, as well as the circular emitter are presented in Figure 2-18.

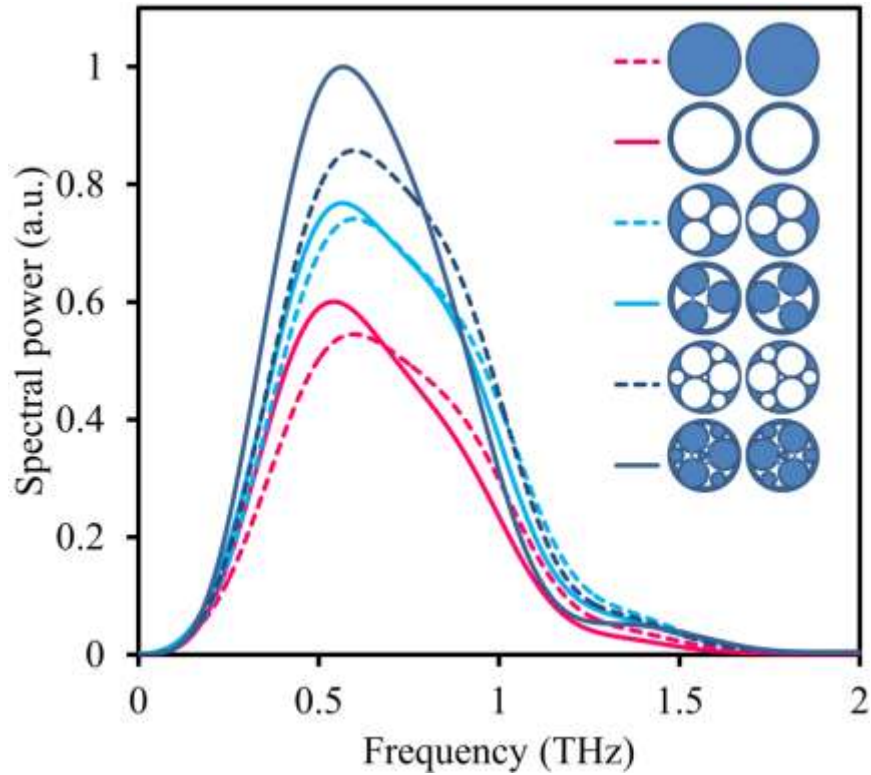


Figure 2-18 Spectral power for PC THz emitters.

As the order of the fractal is increased, it is observed that the THz radiation power emitted by the Apollonian fractals is enhanced compared to the circular dipole emitter. Specifically, the Apollonian emitters of orders one and two show a 40% and a 50% increase in the emitted radiation power, respectively. Furthermore, a similar trend is observed for the complementary Apollonian fractal THz PC emitters as compared to both the complementary circular dipole emitter and the circular dipole emitter. Interestingly, every order of the complementary Apollonian PC emitters exhibits higher THz radiation emission compared to its Apollonian counterpart. Here, the second order complementary exhibits up to 60% and 40% increase in the radiated THz power when compared to the circular and complementary dipole PC emitter, respectively. The emitted THz radiation power of a circular dipole emitter at the same bias is 50% less than that of a bow-tie emitter. However, when the Apollonian architecture is introduced, the emitted THz radiation power is 10% higher than that of the bow-tie emitter. When the Apollonian PC emitter antenna is biased to ~ 21 V, the

THz radiation power emitted is 97% higher than that from bow-tie PC THz emitter biased at 12 volts. Unfortunately, the bow-tie PC THz emitter damages for voltages higher 13 V. It is noteworthy that this is not an absolute comparison since the feed point of the Apollonian emitter compared to the bow-tie emitter is different. While the former is confined between the apexes of the bow-tie, the latter is spread out since it is formed by the adjacent edge of two circles. This causes the effect of the biasing field to be higher for the bow-tie antenna emitter in comparison to the circular-dipole antenna emitter. Thus, one can operate the circular dipole emitter at higher biases than the bow-tie to obtain even higher THz radiation power without breakdown. While it is well known that fractal antennas radiate in multiband modes for various orders, in this case, no resonant bands were observed.

As for the Sierpinski fractals PC emitters, this enhanced THz emission does not come at the expense of loss in the radiated THz bandwidth, as the detected bandwidth is almost identical (within 11%) to that of the circular dipole emitter of similar dimensions. To support this fact, finite-difference time-domain (FDTD) simulations were performed on the circular, as well as on Apollonian order one and two emitters. The spectral responses of the emitters obtained from the antennas present on the substrate are shown in Figure 2-19(a). It is calculated that the operational bandwidth of the antennas are indeed identical (within 6%). Furthermore, the total radiation power from the Apollonian emitters order one and two are identical and are enhanced from that of the circular emitter by only 6%. This suggests that the observed radiated power enhancement of the Apollonian PC THz emitters is not solely related to the antenna characteristics as the antenna-like characteristics are not fully verified by the experimental results.

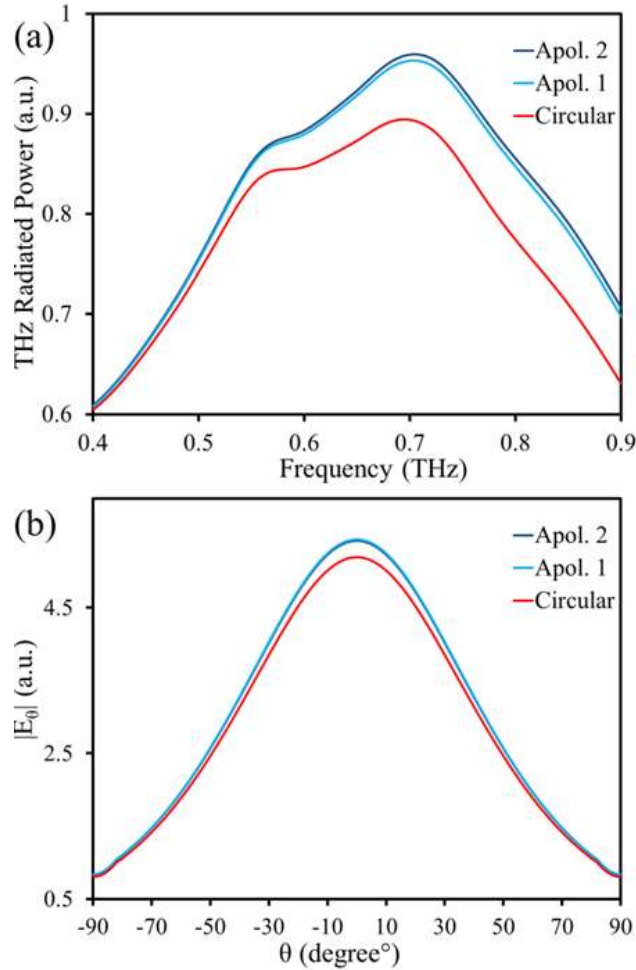


Figure 2-19 FDTD results for (a) the frequency response of the Circular, Apollonian order one (Apol. 1), and Apollonian order two (Apol. 2) PC THz emitter, and (b) the radiation patter on the above mentioned emitters ($|E_{\theta}|$ is the magnitude of azimuthal component of the THz electric field).

Electromagnetic simulations also show that this THz power enhancement is not as a result of altering the radiation pattern of the PC THz emitters. As illustrated in Figure 2-19 (b) the radiation power ($|E_{\theta}|$, the magnitude of azimuthal component of the THz electric field) for the Apollonian emitters of order one and two only increase by 5 % compared to that of the circular emitter. In addition, the directivity of all three emitters is shown to be identical. Evidently, this THz radiation power enhancement with an increasing fractal order is associated with the presence of the sub-wavelength fractal patterns. Such a trend has been also observed for the Sierpinski's fractal-based THz emitters [20].

To shed light onto the radiation characteristics of the Apollonian fractal emitters as well as their complementary counterparts, the polarization state of the radiated THz field is measured as shown in Figure 2-20.

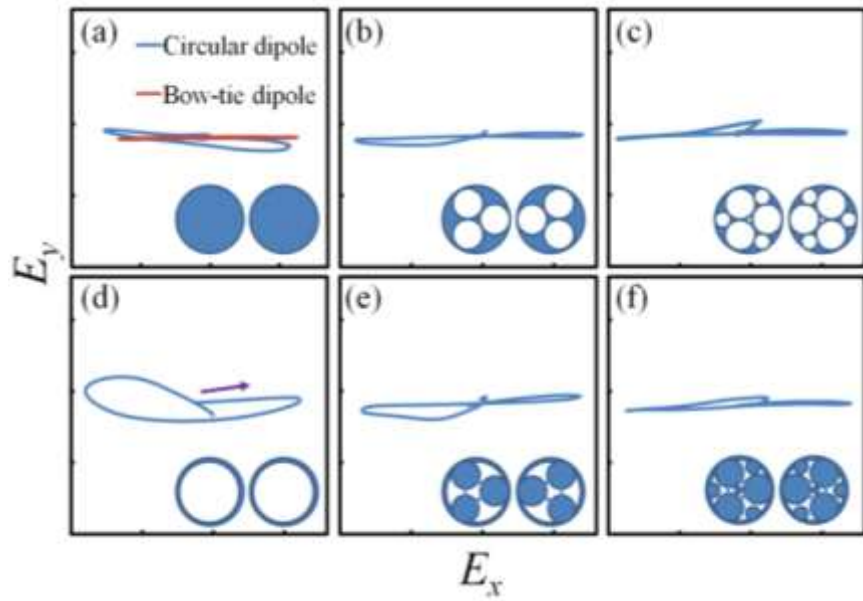


Figure 2-20 A plot of E_x versus E_y for duration of 2.6 ps demonstrating the polarization purity of the transmitted THz electric field. The arrow in (d) indicates the evolution direction of electric field.

The co-polarized, $E_x(t)$, and cross-polarized, $E_y(t)$, components of the radiated THz fields were acquired. Thus, the trajectories of the tip of the electric field vector, $\mathbf{E}(t) = E_x(t) \mathbf{i} + E_y(t) \mathbf{j}$, of the radiated THz field is plotted for the duration of 2.6 ps. It is observed from Figure 2-20 (a) that the polarization of the THz field from the circular dipole emitter is mainly directed along the x-direction (i.e. direction of the biasing field) with the presence of a minor field component along the y-direction. The polarization purity is comparable to that of a conventional bow-tie THz emitter of similar dimensions. Apollonian fractal orders one (Figure 2-20(b)) and two (Figure 2-20(c)) exhibit a similar polarization map. Interestingly, as shown in Figure 2-20(d), the electric field polarization map of the complementary of the circular dipole emitter reveals an appreciable $E_y(t)$.

The origin of this polarization component is due to the fact that the current on the emitter surface is confined to flow along the circumference of a circular border. Thus, resulting in an emitted radiation field possessing both $E_x(t)$ and $E_y(t)$ components. However, as the order of the Apollonian complementary fractal is increased (Figure 2-20(e,f)), the polarization of the THz field becomes similar to the corresponding Apollonian emitters, exhibiting a major $E_x(t)$ component. The introduction of the sub-wavelength metallic features by the complementary Apollonian configuration to the circular ring, combined with the addition of the interconnecting lines, result in providing a more direct path for the current to flow along the axis of the emitting dipole. This indicates that these new classes of PC THz emitters are capable of emitting highly-polarized THz radiation having higher powers.

Since the sub-wavelength restructuring introduced to the surface of the fractal emitters is associated with the enhanced THz emission, it is insightful to examine the field distribution on the surface of the emitters. Having a PC THz emitter improves the coupling efficiency of the THz radiation from the semiconductor substrate to free-space. It was realized that the efficiency can be enhanced for an antenna operating in the plasmonic regime [20]. By engineering the antenna surface to have perforations of dimensions that are much less than the wavelength, the THz generated from the PC gap is coupled to the sub-wavelength structures by means of surface charges. The charge depolarization at these metallic features is assigned to the induced THz surface plasmon currents.

Finite-difference time-domain simulations were performed to obtain the plasmonic electric field, $E_x(x,y)$, for the fractal PC THz emitters. Figure 2-21 illustrates the spatial distribution of $E_x(x,y)$ at the peak emission frequency of 0.7 THz, in the plane of the Apollonian fractal structures and their complementaries. As shown in Figure 2-21, the maximum field is present at the antenna feed point for all the structures. In Figure 2-21(a), the THz surface plasmon $E_x(x,y)$, is uniformly distributed on the surface of the circular dipole antenna.

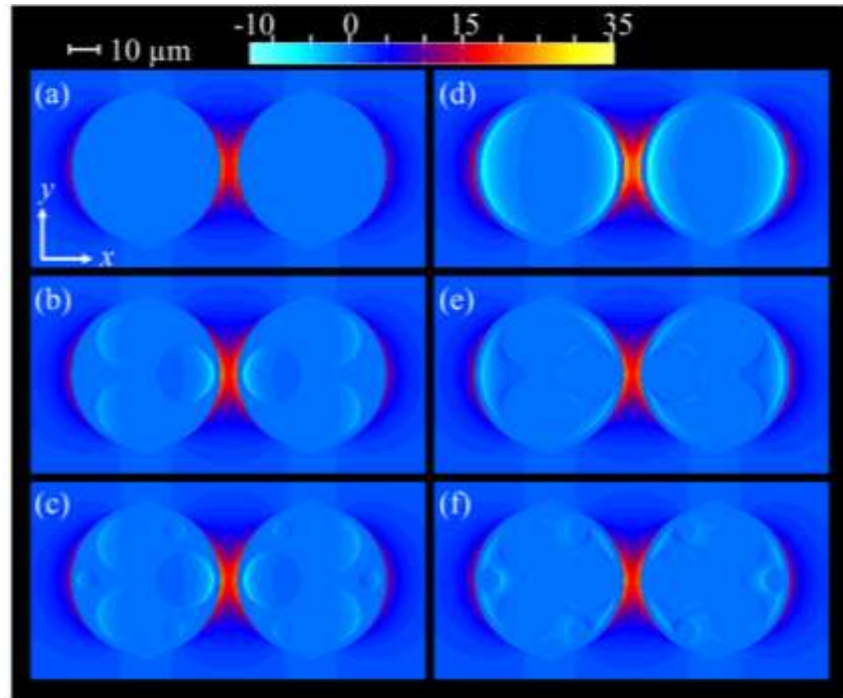


Figure 2-21 The spatial distribution of the surface plasmon electric field $E_x(x,y)$, for (a) circular dipole, (b) first order Apollonian, (c) second order Apollonian, (d) complementary circular dipole, (e) complementary first order Apollonian, and (f) complementary second order Apollonian emitter.

However, due to the presence of sub-wavelength apertures on the Apollonian orders one and two, the plasmon electric field is distributed such that the apertures are polarized along the x-direction (Figure 2-21(b,c)). One clearly observes the self-similar field pattern on the apertures present on the surface of the fractal antennas. The sub-wavelength perforations can be viewed as coherently coupled THz radiators, where THz radiation emissions from the self-similar currents add up coherently in the far-field. Spatially altering the THz surface plasmon fields within the circular fractal units is responsible for improving the surface emission characteristics of the Apollonian fractal emitters. The distribution of the $E_x(x,y)$ on the complementary circular and Apollonian emitters are shown in Figure 2-21(d-f). While a true complementary Apollonian structure shows a self-similar distribution of the $E_x(x,y)$, the self-similarity in the plasmonic field distribution is not as clear due to the presence of the circumscribing $2\mu\text{m}$ ring and the three $2\mu\text{m}$ wide interconnecting

lines, which render the structure to be slightly different for an ideal complementary Apollonian fractal.

To conclude, it has been shown here that the emission properties of PC THz emitters can be further enhanced if: (1) sub-wavelength perforations are introduced on the surface of the antenna and (2) these perforations are constructed in fractal architecture. To further investigate this statement, the true effect of self-similarity on the emission properties of PC THz emitters is comprehensively investigated in the next section.

2.7 Effect of self-similarity

The enhanced performance is attributed to the fractal configuration self-similarity of the surface plasmon current spatial distribution present on the antenna's surface. However, a question that remains to be answered is whether the THz radiation emission enhancement results from the inherent fractal self-similarity, or is it due to the sub-wavelength apertures pattern present on the antenna's surface? That is, can a sub-wavelength pattern other than a fractal pattern meet the THz radiation power enhancement requirement? To answer these questions, we investigate the role of self-similarity in the THz radiation emission characteristics from Sierpinski fractal PC THz bow-tie emitters. By studying various orders of Sierpinski fractal bow-tie emitters and their non-fractal patterned counterparts, we show that self-similarity is indeed solely responsible for the observed enhance of THz radiation emission from such PC emitters [65].

The PC THz antenna design follows that of a Sierpinski fractal triangle forming a 60° equilateral triangle as basic bow-tie antenna structure. For comparison purposes, a conventional bow-tie THz PC emitter was fabricated as well (Figure 2-22(a)). For all antennas, a $5\ \mu\text{m}$ gap is used as the feed point. The THz fractal antenna pattern consists of self-similar triangular apertures, as shown in Figure 2-22(b,c). In a similar fashion, the non-fractal PC THz bow-tie emitters are designed to have circular apertures. Here, the spatial distribution of the Sierpinski fractal

pattern is kept the same; however, at the locations of the Sierpinski triangles, circular apertures are formed instead (as shown in Figure 2-22 (d) and 1(e)). Thus, the self-similar architecture present in the Sierpinski emitters is destroyed because the perforations on the emitter surface are circular and the overall shape of the emitter is triangular.

For the fractal Sierpinski THz emitters, the triangular apexes are inherently located at the perimeter of the basic triangular antenna surface, thus resulting in an electrically discontinuous fractal pattern in the overall pattern of the antenna. To overcome such an issue, $2\mu\text{m}$ wide contact lines were placed on the perimeters of the structures as shown in Figure 2-22 (b,c). A similar procedure was applied to circular features in the modified non-fractal THz emitters (shown in Figure 2-22 (d,e)).

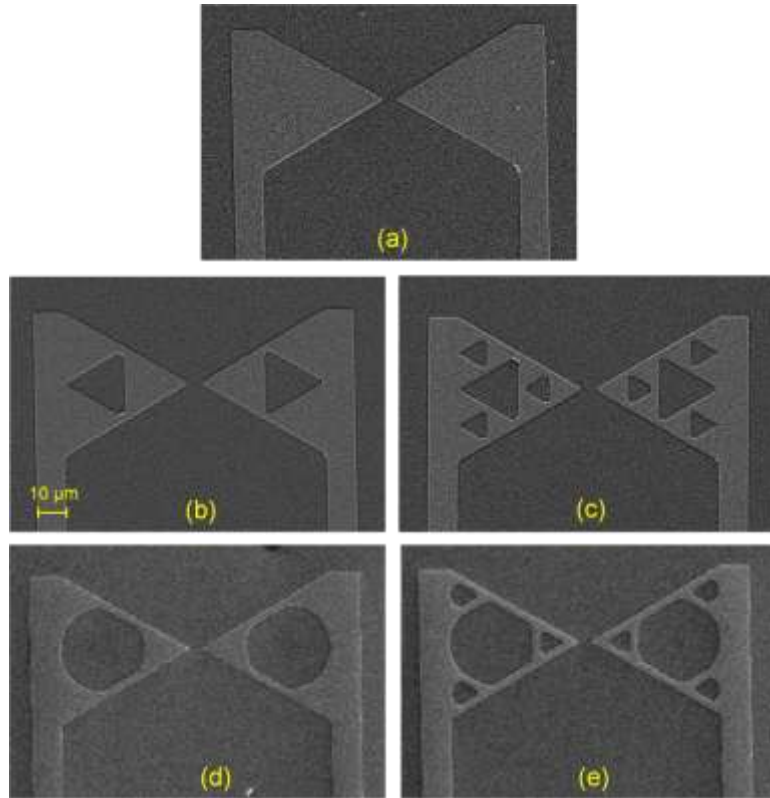


Figure 2-22 (a) bow-tie, (b) first order Sierpinski PC THz emitter, (c) second order Sierpinski PC THz emitters, (d) modified non-fractal PC THz emitter of order one, and (e) modified non-fractal PC THz emitter of order two.

To ensure that at the optically-excited antenna feed point the biasing electric field is the same for the THz emitters under study, the overall antenna dimensions and

shape are kept fixed. This way, one can isolate the effect of the self-similarity of the fractal from that of a circularly-patterned non-fractal antenna surface. The alignment procedure is identical to what was discussed in previous sections.

2.7.1 Results and discussion

As mentioned earlier, the goal of this study was to investigate the effect of the self-similar sub-wavelength perforations on the radiation properties. In particular, openings that are designed and distributed in a fractal configuration are compared to those designed distributed in a non-fractal manner. To further isolate the effect of distribution of the perforation, the electric field across the $5\mu\text{m}$ gap was fixed for all emitters, and all the emitters were excited at the same laser power. Illustrated in Figure 2-23 are the THz spectral powers of the emitted radiation for bow-tie PC emitter, a corresponding fractal structure (first order Sierpinski THz emitter), and a non-fractal structure (first order modified THz emitter).

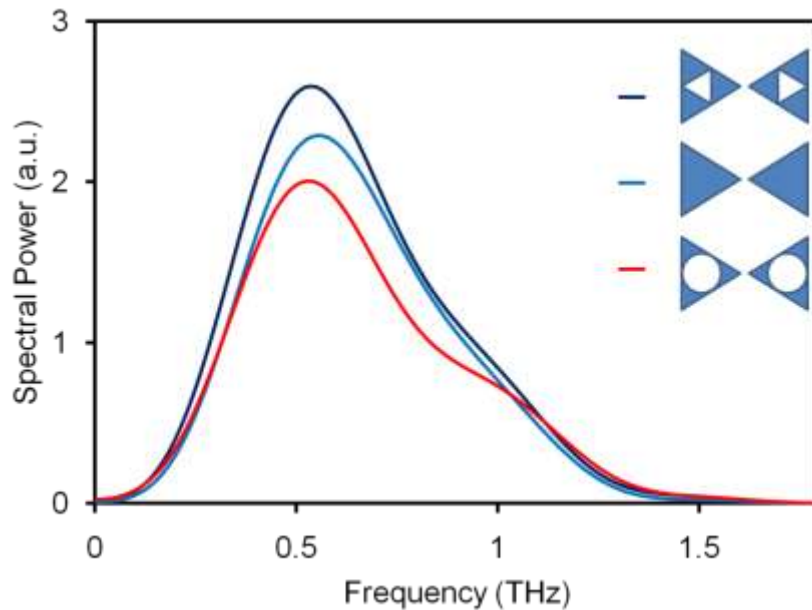


Figure 2-23 Spectral power for first order Sierpinski (dark blue), bow-tie (light blue) and first order modified (red) PC THz emitter.

It is evident that the first order Sierpinski PC THz emitter delivers higher THz radiation power when compared to the bow-tie THz emitter. Clearly, the self-similarity present in the first order Sierpinski PC THz is responsible for this enhancement in the THz radiation power. To demonstrate the role of self-similarity on the emitted THz radiation, we investigated the THz radiation emitted from the modified THz emitter in which the fractal architecture has been destroyed (Figure 2-22 (d)). Upon examining Figure 2-23, it is clear that the emitted THz radiation power for this modified THz emitter is 20% and 10% less than that from the first order Sierpinski THz emitter and the bow-tie THz emitter, respectively. To further investigate the influence of self-similarity in such THz emitters, a second order Sierpinski PC THz emitter (Figure 2-22(c)) and the second order modified emitter (Figure 2-22(e)) were studied. The spectral powers of the emitted THz radiation for the aforementioned emitters as well as the bow-tie PC THz emitter are illustrated in Figure 2-24.

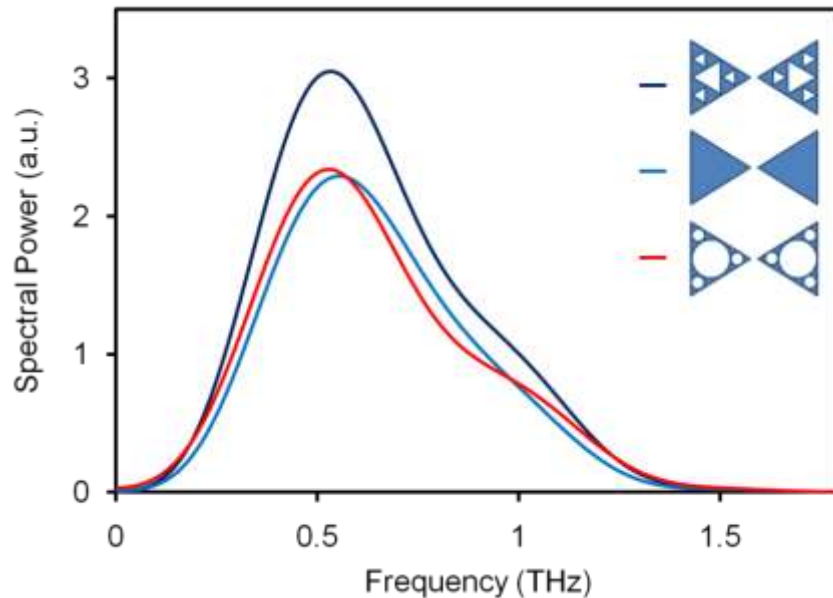


Figure 2-24 Spectral power for second order Sierpinski (dark blue), bow-tie (light blue) and second order modified (red) PC THz emitter.

Undoubtedly, further increase of self-similarity in the second order Sierpinski PC THz emitter results in a 30% increase of the emitted THz radiation power compared to that from the bow-tie THz emitter. Interestingly, the emitted THz

radiation for the second order modified non-fractal THz emitter is 20% less than the second order Sierpinski PC THz emitter. It is observed that in all cases the non-fractal structures emit considerably lower THz radiation when compared to the fractal architecture (Sierpinski THz emitters).

There is strong evidence correlating the enhancement of the THz emitted power and the fractal configuration of the THz emitters. The distribution of the size and perforation must follow an exact fractal architecture for such an emitter to exhibit a higher THz emission efficiency. This can be explained as follows: When the THz radiation couples to the antenna, it induces surface charge oscillations, known as THz surface plasmons, on the antenna's surface. Since the emitted THz radiation which is collected in the far-field is due to the radiating surface currents, the orientation and spatial distribution of the surface currents determine the magnitude of the emitted THz radiation. The presence of a self-similar pattern on the surface of the antenna causes the surface plasmon currents to distribute themselves accordingly in a self-similar fashion. The far-field THz radiations, due to the fractally-distributed currents interfere constructively, and this manifests itself in an enhancement of the emitted THz radiation power. However, in the modified non-fractal THz emitters, since the overall self-similarity is destroyed, the far-field THz radiation interference is not as effective, and, thus, these emitters do not exhibit the THz radiation power enhancement compared to the Sierpinski THz emitters. This conclusion is further supported by the fact the THz radiation power emitted from the second order modified emitter is increased from its first order counterpart by 15% as the circular perforations are self-similar, but do not belong to a fractal class.

Since the surface's sub-wavelength restructuring is responsible for this enhanced THz emission, the spatial distribution of the surface current density is further examined. Finite difference time domain (FDTD) numerical simulation was performed to obtain the surface current densities on all the fractal as well as non-fractal PC THz emitters. Figure 2-25 illustrates the spatial distribution of the surface current density, $J_x(x,y)$, acquired at an intermediate peak emission frequency of 0.6 THz.

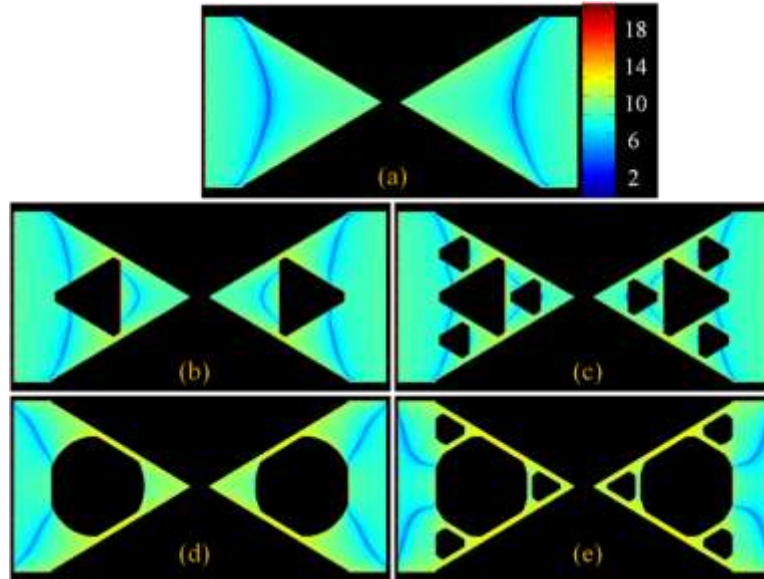


Figure 2-25 The spatial distribution of the surface current density, $J_x(x,y)$, in logarithmic scale along the axis of the Sierpinski PC THz emitters of (a) the bow-tie, (b) first order, (c) second order, (d) second order modified, and (e) second order modified PC THz emitter.

As shown in Figure 2-25(a), the bow-tie PC THz emitter, the surface plasmon current is distributed in such a way that there exists a low current density at the center of the bow-tie emitter. On the other hand, in the Sierpinski PC THz emitters orders one and two, one clearly observes the self-similar current pattern on the sub-units of the fractal antenna (Figure 2-25(b,c)). However, this self-similar surface current distribution on the surface of the antenna is destroyed for the first and second order modified PC THz emitter (Figure 2-25(d,e)).

2.7.2 Summary

In this chapter, a new class of PC THz emitters using fractal geometry has been presented and thoroughly investigated. The characteristics of fractal antennas at GHz frequencies have been explored. In this chapter a new class of plasmonic photoconductive THz emitters based on a complementary Sierpinski gasket fractal geometry is presented. Due to the presence of sub-wavelength perforations on the surface of the antenna, these antennas operate in the plasmonic regime. By utilizing

the unique self-similar and space filling of the tailored fractal surface and the plasmonic surface current spatial distribution, photoconductive THz emitters exhibiting improved performance (~80% increase in the emitted THz radiation power) to conventional bow-tie and Sierpinski gasket THz emitters are demonstrated. It is shown that the self-similarity of the surface plasmon current present on the antenna surface is responsible for this emission enhancement.

In addition, we presented on a special class of photoconductive (PC) THz dipole emitters based on Apollonian fractal geometry. A comprehensive investigation of the radiation characteristics of the Apollonian fractal PC THz emitter as well as its quasi-complementary geometry was introduced and explored for various fractal orders. By utilizing the plasmonic surface current through the Apollonian spatial distribution, higher order fractal PC THz emitters exhibit improved performance to their lower fractal order counterparts. It was found that the complementary of the second-order Apollonian fractal resulted in up to ~ 60% increase in the radiated power when compared to the circular dipole emitter.

Finally, the effect of self-similarity in fractal photoconductive THz emitters is presented. The performance of fractal THz PC emitters are compared to those of non-fractal emitters, and their radiation properties are studied. It is demonstrated that the THz radiation emission enhancement results from the inherent fractal self-similarity and not only from the subwavelength apertures pattern present on the antenna's surface. Through the application of this concept, photoconductive THz emitters having higher THz radiation power could be designed and fabricated. Due to their higher radiation power and better signal to noise (S/N) ratios, these emitters are ideal for situations when higher THz signals (S/N) are required such as in THz-TDS systems.

3. CHAPTER 3

Terahertz electron tunnel devices²

3.1 Introduction

Electron tunneling devices have been widely utilized in key semiconductor, spintronic, and superconductor device technologies. Semiconductor resonant tunneling devices have gained attention due to their high-speed response, room temperature operation, as well as an inherent compatibility with many technologies, such as high electron mobility transistors and metal oxide field effect transistors [66]. Spintronic tunnel magnetoresistance junctions are the heart of magnetic random access memories and transpinnors [67], whereas superconductor tunnel junctions are central for applications to quantum computing [68], millimeter and terahertz wave detectors [69], superconducting quantum interference devices, and ultrafast logic circuits [70].

The goal of this chapter is to research superior metal-insulator-metal junctions that possess extreme asymmetry and nonlinearity characteristics making them suitable as high speed rectifiers and mixers. These diodes will be integrated into the antenna-coupled detectors for detecting free space THz radiation.

This chapter is outlined as follows: The first section introduces the concepts of electron tunnel devices. The principle of operation and some of the applications of tunnel diodes, resonant tunneling diodes, and metal-insulator-metal (MIM) diodes is described in detail. In the second section, the fabrication process of MIM diodes is presented. Particularly, the characteristics of the fabricated MIM devices are investigated. The third section is devoted to fabrication and characterization of a metal-insulator-insulator-metal quantum electronic tunneling device suitable for high

² This work has been published by P. Maraghechi et al. in, *Applied Physics Letters*, **99**, 2011 and in, *Applied Physics Letters*, **100**, 2012.

frequency rectification. The unique potential barrier profile of this novel device manifests itself in highly nonlinear and asymmetric current-voltage (I-V) characteristics which are far superior to that of conventional MIM diodes.

Finally, the incorporation of resonant tunneling phenomenon through multi-stepped potential barriers of metal-insulator-insulator-insulator-metal (MIIM) diodes is presented. It is shown that such electron tunneling diodes exhibit extreme asymmetry and high non-linearity due to resonant electron tunneling via multiple quantum well formation at the insulators interfaces. The presented MIIM devices are shown to have the maximum asymmetry ever presented in the literature.

3.2 Review of electron tunnel devices

In this section, three types of devices (tunnel diodes, resonant tunnel diodes, and metal-insulator-metal diodes) operating with the quantum tunneling phenomenon is discussed.

3.2.1 Tunnel diodes

The first evidence of an electron tunneling device, known as the Esaki diode, was introduced by L. Esaki in 1958 [71]. In the course of investigating the internal field emission in a degenerate germanium p-n junction, Esaki discovered an “anomalous” I-V characteristic (e.g. negative resistance region) under forward bias operation. He explained this behavior using the concept of quantum tunneling, and found reasonable agreement between tunneling theory and his experimental results.

A tunnel diode consists of a p-n junction where the semiconductor materials are very highly doped (degenerate). Figure 3-1 illustrates the energy band diagram of such diode at thermal equilibrium.

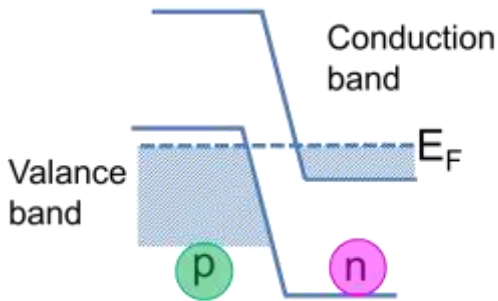


Figure 3-1 Energy band diagram of a tunnel diode in thermal equilibrium

Since the semiconductors in this case are highly doped, the Fermi level, E_F , of each semiconductor is located within an allowed energy band. In addition, the depletion region in this diode is considerably thin ($\sim 100\text{\AA}$) compared to that of a normal p-n junction [23]. A typical, static I-V characteristic of a tunnel diode is shown in Figure 3-2 (a).

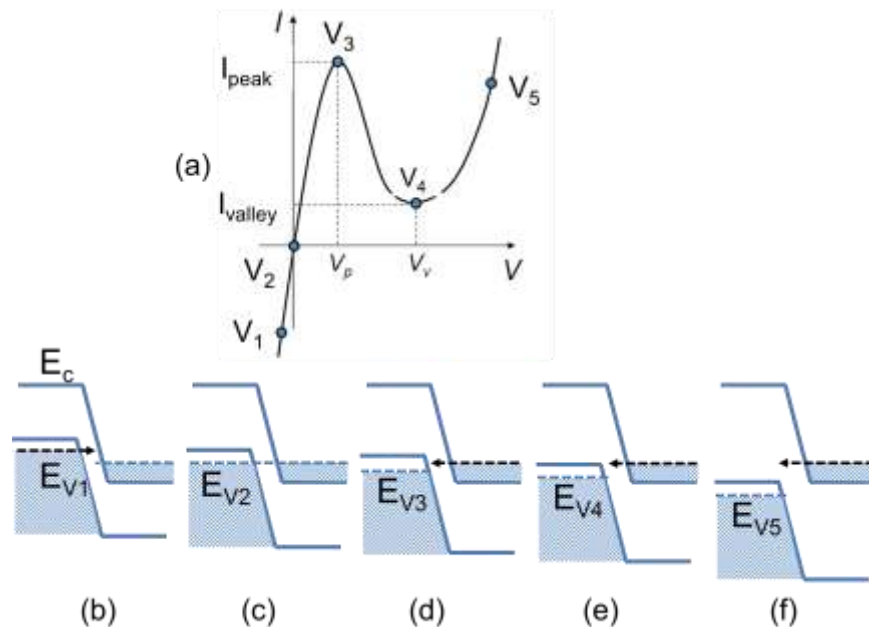


Figure 3-2 (a) static I-V characteristic curve of a tunnel diode at different bias voltages. Energy band diagrams of devices under biasing conditions (V_1 - V_5) are plotted in (b)-(f). The direction of arrow shows the direction of electron tunneling.

The prominent features of this I-V characteristic curve are: (1) The sharp rise in current at small forward bias, (2) the peak current, I_{peak} , at V_p , (3) the decrease of

current with increasing forward bias, (4) the minimum (valley) current, I_{valley} , at V_V , and (4) a normal exponential increase in current with increasing forward bias. To discuss the features (V_1 - V_2) present on the I-V characteristic of the tunnel diode, energy band diagrams of the device under those biasing conditions have been plotted in Figure 3-2 (b)-(f). At zero bias voltage (Figure 3-2 (c)), since the Fermi levels of the two semiconductors are at the same level there is no current flow. Figure 3-2 (b) illustrates that the current under reverse bias voltage is due to electrons tunneling from the valance band into the conduction band. When a small forward bias voltage is applied, electrons can tunnel from the n-side to the p-side of the device due to the narrow thickness of the depletion region. This tunneling current reaches a maximum value ((Figure 3-2 (d))) where there is a maximum number of unoccupied states for the electrons to tunnel into. As the bias voltage is further increased, there are less unoccupied states available, and the tunneling current starts to decrease. At a voltage value of V_V (Figure 3-2 (e)), the edge of the conduction band for the n-type region reaches the maximum of the valance band of the p-type region. Therefore, there are a minimum number of unoccupied states present for the electrons to tunnel into and the tunneling current reaches a minimum value, I_{valley} . By further increasing the biasing voltage, the electrons possess sufficient energy to penetrate the barrier and the resultant current flow is the same as that which occurs in a normal p-n junction (Figure 3-2 (f)). This current is referred to as injection current as opposed to tunneling current. It has been proposed by Moagar-Poladian [72] that this class of tunnel diodes can operate at frequencies up to 40 GHz and the spectral domain of detectable photon energy covers an interval of the order of 0.05–0.2 eV.

3.2.2 Resonant Tunneling diodes

The resonant tunneling diode (RTD) was first introduced by Tsu and Esaki in 1973 [73] who also studied the device's I-V characteristic in detail. This was followed by an experimental demonstration of the RTD done by Chang et al. in 1974 [74]. The research on RTDs gained a significant of attention, particularly due to the

progresses semiconductor epitaxial growing techniques, such as molecular beam epitaxy (MBE) and metalorganic chemical vapour deposition (MOCVD) technologies. It was in 1985 that the operation of RTD was demonstrated at room temperature by Shewchuk et al. [75].

Figure 3-3 illustrates the most popular structure of a RTD which consists of GaAs/AlGaAs layers [76]. This type of RTD is also referred to as a double barrier diode because of the presence of two quantum wells in the structure.

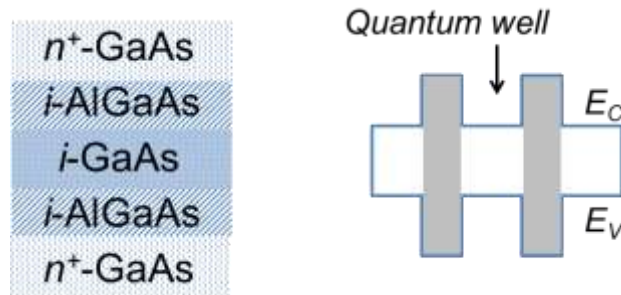


Figure 3-3 Structural schematic of a GaAs/AlGaAs RTD. The energy band diagram is drawn on the left.

In the above mentioned GaAs/AlGaAs RTD structure, the middle quantum-well thickness is typically $\sim 50 \text{ \AA}$ and the barrier layers are $15\text{-}50 \text{ \AA}$ in thickness. The need for epitaxial deposition of layers and abrupt doping profiles in the fabrication of RTDs necessitates the use of MBE, and in some cases MOCVD technologies. An I-V characteristic for a RTD having a single quantum-well is shown in Figure 3-4.

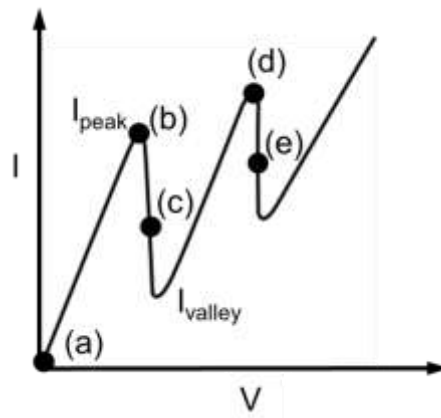


Figure 3-4 I-V characteristic curve for a GaAs/AlGaAs RTD. The specific features on the I-V curve are labeled as (a)-(e).

As illustrated above, the I-V characteristic curve of a RTD possesses peaks and valleys. Certain points on the I-V characteristic have been labeled as (a)-(e) and the energy band diagrams of the structure at these bias voltages are plotted in Figure 3-5 [76].

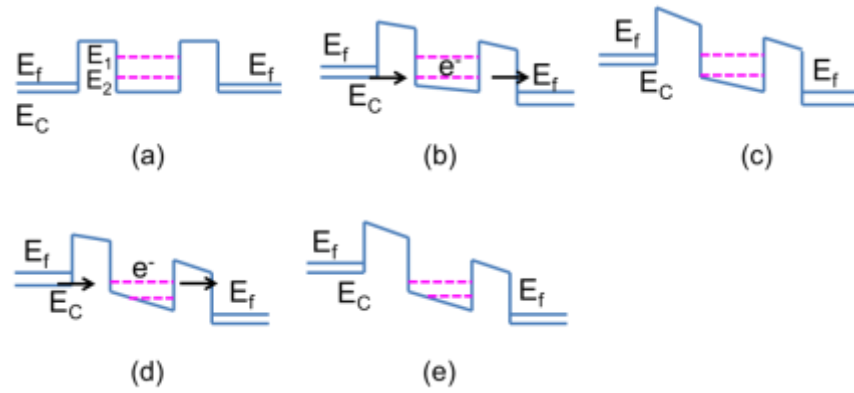


Figure 3-5 Energy band diagram of a RTD under various bias voltages. (a) zero bias, (b) resonance tunneling through E_1 , (c) first negative resistance region, (d) resonance tunneling through E_2 , and (e) second negative resistance region.

The energy band diagram of the RTD at equilibrium is shown in Figure 3-5 (a). Quantum mechanics states that in a quantum well of width W , there exists discrete sub-bands, n , at which an electron is allowed to occupy at energy E_n according to,

$$E_n = \frac{h^2 n^2}{8m^* W^2}, \quad n = 1, 2, 3, \dots \quad (3.1)$$

Where h is Planck's constant, m^* is the effective mass of the electron, and W is the width of the well. In this case we have considered two states (E_1 and E_2) for the above mentioned well. Quantum mechanics also states that there exists a certain probability for the tunneling of electrons from the left electrode to the right electrode. However, this tunneling probability can be significant only if there exists an empty state in the quantum well at the same energy level of the emitted electron. This is called a resonant tunneling phenomena and RTDs utilize this mechanism for their operation.

Due to the presence of tunneling phenomena, the rise in the current for RTD devices is high even at low bias. The tunneling current increases up to a peak value of I_{peak} as shown in Figure 3-4 (b). The energy band diagram at this bias voltage is shown in Figure 3-5 (b). It is clear that the electrons at this bias voltage have the same level of energy as the first allowed energy state of the QW (E_1) and resonant tunneling becomes the governing electron transport mechanism. As the bias is further increased, the energy of the emitted electrons become slightly larger than E_1 (Figure 3-4 (c)) and the tunneling current reduces (Figure 3-5 (c)). Due to the presence of two QW states, the resonant tunneling phenomenon is repeated once again (Figure 3-4 (d)). This feature of negative differential conductivity is the key factor of utilizing RTDs as functional devices such as amplifiers, oscillators, and pulse generators [76].

Tunneling is inherently an ultrafast phenomenon (10^{-15} - 10^{-16} s) because it is not transit-time limited; thus, a RTD is considered to be among the fastest devices ever made. RTDs as mixers have been demonstrated to detect radiation up to 2.5 THz, and as oscillators they can generate 700 GHz signals [77].

3.2.3 Metal-insulator-metal diodes

A metal-insulator-metal (MIM) diode is a quantum tunneling device whose electron transport characteristics are governed by the metal-insulator interfaces [61, 78-80]. This class of rectifying elements is currently the center of attention for the development of improved antenna-coupled infrared detectors [81-83], high frequency mixers [61, 84], and optical rectennas [85]. The interest is driven by the diode's unique attributes, such as its nanoscale footprint, room temperature operation, zero bias voltage requirement and ease of integration with complementary metal-oxide-semiconductor (CMOS) technology [82, 86]. In addition, an important key advantage of an MIM diode over a semiconductor-based diode is its ultrafast response time and broad bandwidth characteristics. For example, the response time of a typical MIM diode having a nanoscale dimension is on the order of the quantum mechanical electron tunneling time, which can be as fast as $\sim 10^{-16}$ s [87]. Furthermore, since the

electron tunneling phenomenon is a highly nonlinear process, it permits rectification and mixing of ultrahigh frequency electromagnetic radiation. These unique attributes of metal-insulator interface(s) merit further investigation.

When two metallic electrodes are separated by a thin insulating layer, a potential barrier is formed which acts to prevent electron flow. This can be better explained using the energy band diagram shown in Figure 3-6. For simplicity, the case where the two electrodes are similar metals is considered. By applying a voltage difference between the electrodes, electrons can tunnel through this barrier and appear in the opposing metallic layer. The direction and magnitude of the current flow depend on the voltage polarity and potential barrier height (ϕ), respectively.

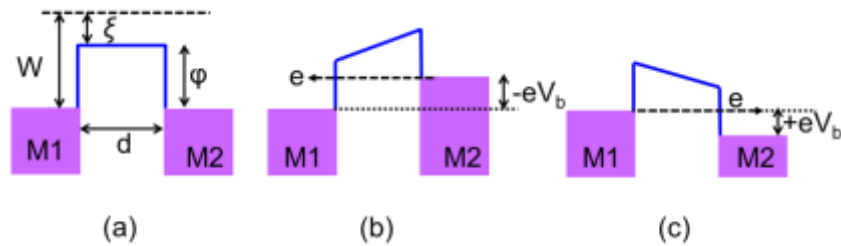


Figure 3-6 Energy diagram of two similar metallic layers (M1 and M2) spaced by an insulating layer. a) When there is no bias applied, b) bias $-V$ is applied to metal M2, and c) bias $+V$ is applied to metal M2. In this figure, W is the work function of the metal, ξ is the electron affinity of the oxide material, ϕ is the barrier height, d is the barrier width and V is the applied bias.

The theory for the operation of MIM devices has been discussed in detail as a Fowler-Nordheim tunneling phenomenon and is well described by Simmons [88, 89]. Figure 3-6(a) illustrates the case when there is no bias applied to the MIM junction. In this case the Fermi levels of the two metals are equal and the barrier has a rectangular shape. When a bias ($-V_b$) is applied across the MIM, the Fermi level of the metals shift correspondingly and the barrier holds the shape of a trapezoid as shown in Figure 3-6(b). Here, there is a net flow of electrons through the barrier due to tunneling from one electrode to the other. Under dc conditions, where the bias is not modulated, Simmons [88] has shown that by using the Wentzel, Kramers, Brillouin (WKB) approximation, the tunneling current density (J) as a function of bias voltage (V) for a trapezoidal barrier is given by:

$$J = J_0 \left\{ \bar{\varphi} \exp\left(-A \bar{\varphi}^{-\frac{1}{2}}\right) - \left(\bar{\varphi} + eV\right) \exp\left(-A \left(\bar{\varphi} + eV\right)^{\frac{1}{2}}\right) \right\} \quad (3.2)$$

where

$$J_0 = \frac{2}{2\pi h} \frac{1}{(\beta\Delta s)^2},$$

$$A = \frac{4\pi\beta\Delta s}{h} (2m)^{\frac{1}{2}},$$

$$\beta \approx 1$$

In these relations, $\bar{\varphi}$ is the mean barrier height, e is the charge of the electron, m is the mass of the electron, and h is Planck's constant. Furthermore, it has been shown that by introducing an image potential, the corners of the trapezoidal barrier become round and therefore the effective barrier width (Δs) is reduced. It can be observed from this relation that the tunneling current (J) and the applied bias (V) have a nonlinear relation; therefore, providing a physical explanation for the rectifying and mixing capabilities of MIM diodes. The nonlinear relation depends on the barrier height and width as well as the dielectric permittivity of the oxide layer.

Alternative electron transport mechanisms in MIM junctions are: (1) photon-assisted tunneling, (2) thermally assisted tunneling, and (3) field-assisted tunneling. When the MIM junction is illuminated by photons of energy $h\nu$, they can interact and excite the electrons within the metal. The electrons residing at the Fermi level of the metal near the barrier can gain enough energy to increase their transmission probability and therefore tunnel through the barrier to the other metal. This conduction mechanism is regarded as photon-assisted tunneling. In parallel, the incident photons can cause lattice vibrations in the material, which correspondingly introduces heat to the material. Electrons close to the Fermi level gain $k\Delta T$ energy by the incident photons, where k is the Boltzmann constant and ΔT is the change in temperature. Because of this energy rise, these electrons are able to tunnel through the barrier and appear on the other electrode. Such a tunneling process is referred to as a thermally-assisted tunneling. It should be noted that the thermal effects are inherently slow ($\sim\mu s$) and are limited by the thermal constant and geometry of the

MIM junction [90]. This effect can contribute to the response time of the detector for dc detection, but it is too slow to influence the mixing process beyond a certain cut-off frequency (determined by the thermal time constant of the device structure [91]).

Field-assisted tunneling or Fermi-level modulation tunneling occurs when the MIM device is introduced to a voltage oscillation. In this process, the barrier height will also be modulated at the oscillating frequency. Therefore, the tunneling current will be modulated at the oscillating frequency, and the tunneling signal can be thought of as an AC current component in addition to the existing dc current (both resulting from tunneling transport mechanism).

3.3 Fabrication of metal-insulator-metal diodes

Many different metals have been used as electrodes in the fabrication of MIM devices. Examples of junction materials are Al-Al₂O₃-Al, Cr-CrO-Au, Nb-NbO_x-Au, and Ni-NiO-Ni. The first point contact MIM was Al-Al₂O₃-Al fabricated by Dees [92]. Many materials have been studied as a choice for electrode materials in point contact MIM. It was shown that W-NiO-Ni was the best candidate among others for detecting and mixing high frequencies. In the thin film MIM fabrication, Gustafson et al. [93], Elchinger et al. [94] and Wiesendanger et al. [95] fabricated and tested Al-Al₂O₃-Ni, Al-Al₂O₃-Al and Cr-CrO-Au, respectively. As mentioned by Wilke et al. [79] all these devices were inferior to Ni-NiO-Ni MIMs. Heiblum et al. [90] states that silver, copper and chromium are not good candidates as they oxidize too readily and silver films deteriorate over time. Chromium, in addition to oxidizing too easily, has a high dc resistance. Although gold has a low resistance it cannot be oxidized. Ni-NiO-Al and Ni-NiO-Au were tested and shown to be electrically unstable due to ion electromigration between the different metals.

The most critical material element of any electron tunneling device is the quality of the ultra-thin oxide layer since the electron tunneling mechanism is highly dependent on the oxide thickness, d , and the potential barrier height. Clearly, d must not exceed a few nanometers, otherwise the tunneling current drastically diminishes

[61]. Furthermore, for high I-V nonlinearity, the oxide layer must be able to withstand an extremely high electric field ($\sim 10^9$ V/m). However, material breakdown voltage is proportional to d and a compromise must be reached on the maximum electric field strength attainable. There have been approaches for fabricating thin oxide layers, such as *in-situ* oxidization [81], plasma oxidization of crystalline metallic electrodes [96], and sputtering of the oxide [61].

Here, a brief literature review on recently fabricated thin film MIM diodes and the method of oxide fabrication used is presented. Fumeaux et al. [61] fabricated $100 \text{ nm} \times 100 \text{ nm}$ Ni-NiO-Ni MIMs with a zero bias resistance of $\sim 100 \text{ } \Omega$. This device successfully operated up to 30 THz. The barrier in this device, NiO, was deposited using a sputtering technique. Berland et al. [97] was successful in fabricating $500 \text{ nm} \times 500 \text{ nm}$ Nb-NbO_x-Nb MIM diodes, and, by utilizing a plasma oxidation process, they were able to reduce the zero bias resistance down to 0.5-2.5 k Ω from 70 k Ω -20 M Ω . When devices with junction areas on the order of $100 \text{ nm} \times 100 \text{ nm}$ and $200 \text{ nm} \times 200 \text{ nm}$ were fabricated, the value of the zero bias resistance was reported as $\sim 25 \text{ k}\Omega$. Hobbs et al. [83] reported on the fabrication of $600 \text{ nm} \times 600 \text{ nm}$ Ni-NiO-Ni MIMs having $150 \text{ } \Omega$ of zero bias resistance. Here, the oxide barrier was formed using an oxygen plasma technique. It is mentioned by this group that ambient or thermal oxidation produces unstable MIM junctions. Krishnan et al. [98] reported on fabricating Ni-NiO-Cr MIMs having $1 \mu\text{m} \times 1 \mu\text{m}$ junctions with a zero bias resistance of 500 k Ω . The oxide in this case was fabricated by means of reactive sputtering at low powers. Tiwari et al. [81] fabricated $50 \text{ nm} \times 80 \text{ nm}$ Al-AlO_x-Pt MIMs operating at 30 THz. In their study it is shown that MIM junctions are produced by etching the native oxide formed on the first electrode and re-oxidizing it prior to the deposition of the second electrode. A zero bias resistance of 1.6 k Ω was achieved for the fabricated MIM, and it was shown that this value is a function of the oxygen dosage introduced to the chamber during the oxidation stage [81].

However, the primary limitation of these techniques is the inability to create, and more importantly, precisely control of the formation of the ultra-thin oxide across the entire surface area of the device's tunnel junction. As such, the tunnel devices suffer from low yield and low reliability. Only recently Cowell et al. [99]

demonstrated that atomic layer deposition (ALD) can be employed in the fabrication of MIM diodes. Certainly, it is highly desirable to material-engineer the potential barrier layer to be thick enough to withstand the high electric field and yet would ‘*quantum mechanically behave*’ as a thin potential barrier.

In the following sections, the procedure for fabrication of MIMs at the University of Alberta NanoFab is described in detail. This investigation is divided into two sections: (1) MIM fabrication via physical vapour deposition (PVD) oxide deposition, and (2) MIM fabrication via ALD oxide deposition.

3.3.1 MIM fabrication via PVD oxide deposition

The fabrication of the MIM diodes was initiated by incorporating Al as the first electrode layer for the MIM diode. However, due to occasional failure of the lift off process, which was caused by the low adhesion of Al to the surface, discontinuities were present on the electrode especially at the 200 nm wide line. Cr was then picked as the next candidate since it is used as an adhesion layer in the thin film industry and its native oxide has a thickness of ~2nm [100]. The first layer of Cr was sputter deposited then oxidized in atmosphere and then a second Cr layer was sputtered on top. The fabricated Cr/CrO₂/Cr devices showed an ohmic I-V relationship and did not exhibit any noticeable nonlinearity. This behavior was attributed to the low quality of the oxide formed on Cr in atmosphere. It should be mentioned that oxidizing the freshly deposited Cr film by exposing it to pure oxygen before venting the chamber was not possible in the sputtering equipment used. In order to overcome such limitation, SiO₂ was suggested as the oxide layer since it possesses high electric field breakdown (~8-11 MV/cm).

To check the quality of the deposited SiO₂, millimeter size junctions were fabricated by means of a shadow mask technique. The MIM devices were grown on a 550nm thick SiO₂ film on top of a 500µm Si substrate. The first electrode was a 100nm thick Cr layer deposited through a shadow mask having circular (5mm diameter) openings on a SiO₂ substrate using magnetron sputtering. The sample was

then brought out of the sputtering chamber, and was transferred to the evaporation chamber for the deposition of SiO₂ oxide layer. Finally, the sample was transferred back to the sputtering chamber for the deposition of the second 100nm thick Cr electrode. The thickness of the deposited SiO₂ was tested on a witness sample using a variable-angle ellipsometer. MIM devices having oxide thicknesses of 1, 2, 3 and 4 nm were fabricated and the I-V characteristics of these samples were measured using a KEITHLEY 4200-SCS semiconductor parametric analyzer. This device is capable of sweeping voltage across a given interval while monitoring the current. Again, all of the junctions exhibited an ohmic I-V characteristic. This behavior was attributed to the size of the MIM electrodes as the junction areas were too large for ensuring the growth of nanometer thick continuous SiO₂ films.

As the next step, the MIM junction area was reduced to 200 nm × 200 nm. By reducing the deposition area, the probability of obtaining continuous ultra-thin oxide films is increased. For this, the electron beam lithography (EBL) technique was utilized since the design consisted of sub-micron (200 nm wide) lines. In the first lithography step, the bottom electrode was patterned followed by a metallization step via sputter deposition. After depositing the oxide layer (in this case, SiO₂), the chip underwent a second EBL step for patterning the second electrode. This was followed by another metallization step, which would then fabricate the second electrode having the desired material. Samples for accurate thickness deposition of SiO₂ were prepared and sent to Micralyne Inc. since they host a very accurate SiO₂ evaporator system. SiO₂ with thicknesses of 2.0, 2.5 and 3.3 nm were deposited on three different samples. The samples having a 2.0 and 2.5 nanometer thick oxide showed ohmic I-V characteristics, while the other sample (oxide thickness of 3.3 nm) was not. The nonlinear I-V characteristic curve acquired from the sample having the 3.3 nm thick oxide is shown in Figure 3-7.

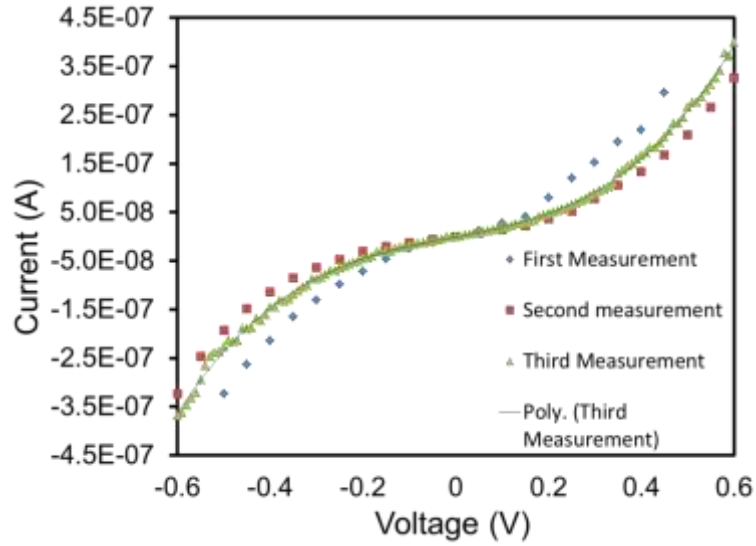


Figure 3-7 I-V characteristic curve for Cr-SiO₂-Cr MIM having a 3.3 nm of oxide deposited at Micralyne. The third order polynomial fit is shown in the Figure. To check if the device is stable, several voltage sweeps were performed on the same spots.

By fitting the experimental data using a cubic polynomial function, one can find that the zero bias resistance of the 3.3 nm is 5 MΩ. This zero bias resistance is too high for such a tunneling device. This high resistance was assigned to the uncertainty in the thickness of the oxide, and, unfortunately, there was no direct method of measuring such thin layers. For comparison, deposition of the SiO₂ was performed in the NanoFab for oxide thickness of 3.0 nm. The I-V characteristic curve for this sample is shown in Figure 3-8.

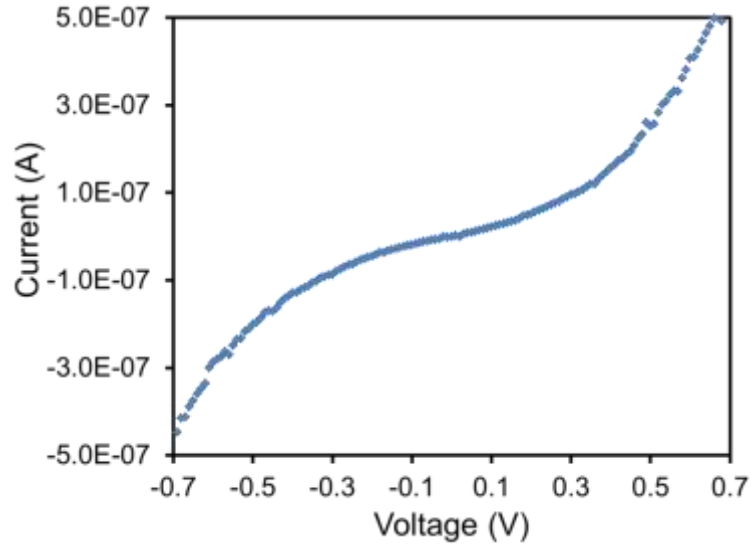


Figure 3-8 I-V characteristic curve for Cr-SiO₂-Cr with oxide thickness of 3.0 nm deposited in the NanoFab facility.

The zero bias resistance for this device was 5 MΩ as calculated from the fitted cubic equation. Using SiO₂ as the oxide layer had two disadvantages: (1) Since the first electrode is introduced to atmosphere before the deposition of the SiO₂ there exists an ~2.5 nm layer of low quality native oxide (CrO₂). This suggests that the SiO₂ layer was in fact deposited on the CrO₂ layer and therefore the thickness of the overall oxide is ~ 5.5 nm. (2) Unlike other oxides, accurately depositing 2-3 nm of oxide is a very challenging process. This brought us to conclude that the SiO₂ is not a good choice for the oxide layer. Using high quality native oxides (formed in situ) as the insulating layer, was the approach taken for future devices.

It has been reported that the thickness and quality of the native oxide formed on the deposited metal depends on the humidity of the laboratory and the partial pressure of oxygen in the air [81]. In this new approach, good control of the grown native oxide on the freshly deposited metal is achieved by briefly exposing the metal to oxygen prior to venting the deposition chamber. This way, since oxygen is the only gas reacting with the metal surface, a high quality native oxide is expected to form. It was after this that it was decided to deposit the oxide layer in situ. Attempts were made to add an oxygen source to the sputtering chamber in the NanoFab but it was unsuccessful. On another sputtering equipment, the NanoFab had an oxygen

source connected. This option was needed since the goal was to sputter etch the native oxide formed on the first electrode and then introduce the bare electrode to oxygen to form a controlled oxide (high quality oxide). Finally, the second electrode would be sputtered in situ without breaking the vacuum. Unfortunately, the sputtering rate of this machine would change due to reactive oxidation by many other users, thus, coating the chamber with various dielectric materials (oxide), which degraded the quality of the grown oxide. In addition, while attempting to perform the sputter etching the matching circuit for the RF source was frequently in need of repair. It was after this stage that the ALD system was installed in Dr. Cadien's lab in the Department of Chemical and Material Engineering and hence after, the deposition of oxide was performed by ALD.

3.3.2 MIM fabrication via ALD oxide deposition

Since the most critical component of the MIM and MIIM devices is the ultrathin ($d \leq 40 \text{ \AA}$) oxide layer(s), the desired oxide layers are deposited, in-situ via a load-lock, by means of atomic layer deposition (ALD). Since the ALD process is a surface reaction driven process, it guarantees the formation of high quality, pinhole free and uniform oxide layers[101]. Clearly, the modification to these ultrathin oxides layers changes the form of the barrier, and thus alters the conduction of electrons across the junction.

The ALD system installed in Dr. Cadien's lab is a Kurt J. Lesker ALD-150L, which is a combination of a sputtering chamber and an ALD chamber connected thorough a load-lock. The sputtering chamber is equipped with a sputtering gun capable of sputtering at variable substrate temperatures, an ion source for ion bombardment processes and a residual gas analyzer (RGA). The ALD chamber is capable of performing both thermal and plasma-assisted ALD deposition of oxides at variable substrate temperatures.

ALD of aluminum and hafnium oxide layers were grown in the Kurt J. Lesker ALD-150L system in plasma enhanced mode at 300°C using trimethylaluminum (TMA) and tetrakis (dimethylamido) hafnium (TDMAH), as metallic precursors and

oxygen plasma as oxygen source. Growth per cycle (GPC) was $1.12 \pm 0.04 \text{ \AA/cycle}$ for the Al_2O_3 and $1.83 \pm 0.09 \text{ \AA/cycle}$ for the HfO_2 , as measured by in-situ spectroscopic ellipsometry. Each ALD cycle included 20-40 ms of precursor dose followed by 5s of argon gas purge and 1s of oxygen plasma exposure followed by 2s of purging. The roughness of the ALD layered oxide stacks was measured using an atomic force microscope (AFM). The oxide layers thicknesses were measured in-situ using a J. A. Woollam M-2000DI ellipsometer configured for a 70° angle of incidence.

The MIM devices were grown on a 550nm thick SiO_2 film on top of a $500\mu\text{m}$ Si substrate. The fabrication of the MIM devices was performed by means of a shadow mask technique. To isolate the effect of the potential barrier shape on the device performance from the potential barrier offset (i.e. δ), Cr was used for all device electrodes. The first electrode was a 100nm thick Cr layer deposited on a SiO_2 substrate using magnetron sputtering. Next, a shadow mask having 0.5mm diameter circular openings was placed on the substrate to facilitate the deposition of the oxide layers. ALD was employed for the deposition of oxide layers. For the fabrication of the MIM devices, desired layers of Al_2O_3 or HfO_2 were deposited. Finally, the sample was transferred back to the sputtering chamber in-situ via a load-lock for the deposition of the second 100nm thick Cr electrode. An image of the shadow mask and the final devices are shown in Figure 3-9.

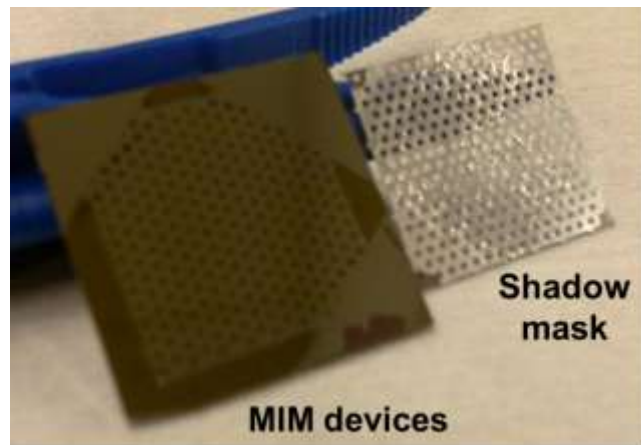


Figure 3-9 An image of the MIM devices on the substrate and the shadow mask used for fabricating the MIM diodes.

Using the abovementioned fabrication method, MIM diodes consisting of Cr/Al₂O₃/Cr and Cr/HfO₂/Cr were fabricated [102]. The schematic of a fabricated MIM device is illustrated in Figure 3-10. Here, I₁ represents the oxide layer (Al₂O₃ or HfO₂ layer).

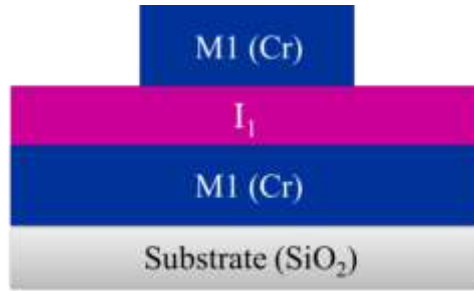


Figure 3-10 Schematic of the layout of the MIM device. Here, I₁ is the insulating layers corresponding to either an Al₂O₃ or aHfO₂ layer.

The oxide layer for the fabricated Cr/Al₂O₃/Cr and Cr/HfO₂/Cr is 4nm thick. The I-V curves for Cr/Al₂O₃/Cr and Cr/HfO₂/Cr are illustrated in Figure 3-11.

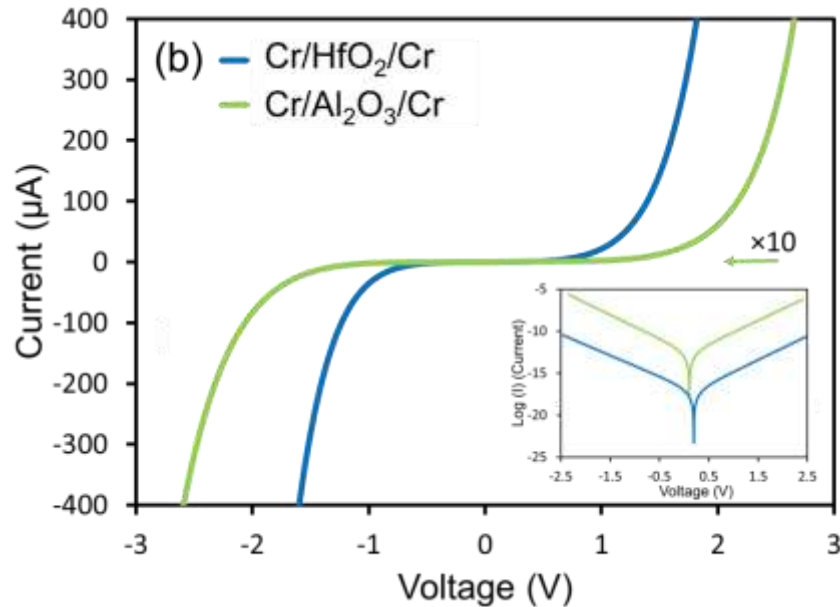


Figure 3-11 Current versus voltage characteristic curves for the Cr/HfO₂/Cr and Cr/Al₂O₃/Cr devices. The data for Al₂O₃ was magnified 10 times for illustrative purpose. The higher tunneling current observed from the Cr-HfO₂-Cr diode is attributed to the lower barrier height

associated with HfO₂ compared to that of Al₂O₃. The insets depict the logarithm of the current versus the voltage for each device.

Clearly, both MIM diodes exhibit a symmetric I-V behavior over the same voltage range. Since the top and bottom electrodes in the MIM devices are similar metals (i.e. Cr), their energy band diagram is the same as shown in Figure 3-6. In addition, the higher tunneling current observed from the Cr-HfO₂-Cr diode is attributed to the lower barrier height associated with HfO₂ (1.75 eV) compared to that of Al₂O₃ (3.05 eV). If the device consists of two similar electrodes, with a work function W , and the voltage polarity is reversed on its electrodes, Φ remains symmetric around the zero voltage. This results in a symmetric I-V response as electrons encounter the same potential barrier height δ ($= \Phi - W$), and shape regardless of the voltage polarity. However, utilizing dissimilar metallic electrodes breaks the potential barrier's symmetry. In such a configuration, since the electrodes have different W , the amount of δ encountered by the electrons depends on the electrodes' voltage polarity. Through this model, a variety of MIM diodes have been realized [103]. However, the degree of the I-V asymmetry is limited by the amount of δ offset, and it is restricted to few selections of metals.

In order to utilize the electron tunneling phenomenon for device applications, the degrees of asymmetry η ($= \left| \frac{I_p}{I_n} \right|$) and non-linearity χ ($= \frac{dI}{dV} / \frac{I}{V}$) along with the curvature coefficient, γ ($= \frac{d^2I}{dV^2} / \frac{dI}{dV}$) are essential. Here, I_p and I_n are the current under positive and negative voltages, respectively. Both χ and η are key figures of merit used to characterize the efficiency and performance of electron tunneling devices. The resulting I-V behavior of Cr/Al₂O₃/Cr, and Cr/HfO₂/Cr were quantified by examining χ , γ and η , as shown in Figure 3-12(a-c). As illustrated in Figure 3-11, the Cr/Al₂O₃/Cr, and Cr/HfO₂/Cr diodes possess highly symmetric I-V curves thus, $\eta \sim 1$ over the whole voltage range. The nonlinearity present in the two MIM devices is similar and ranges from 2 to 8. The curvature coefficients of the Cr/Al₂O₃/Cr, and Cr/HfO₂/Cr MIM devices reach a value of ~ 2.8 beyond 0.6V.

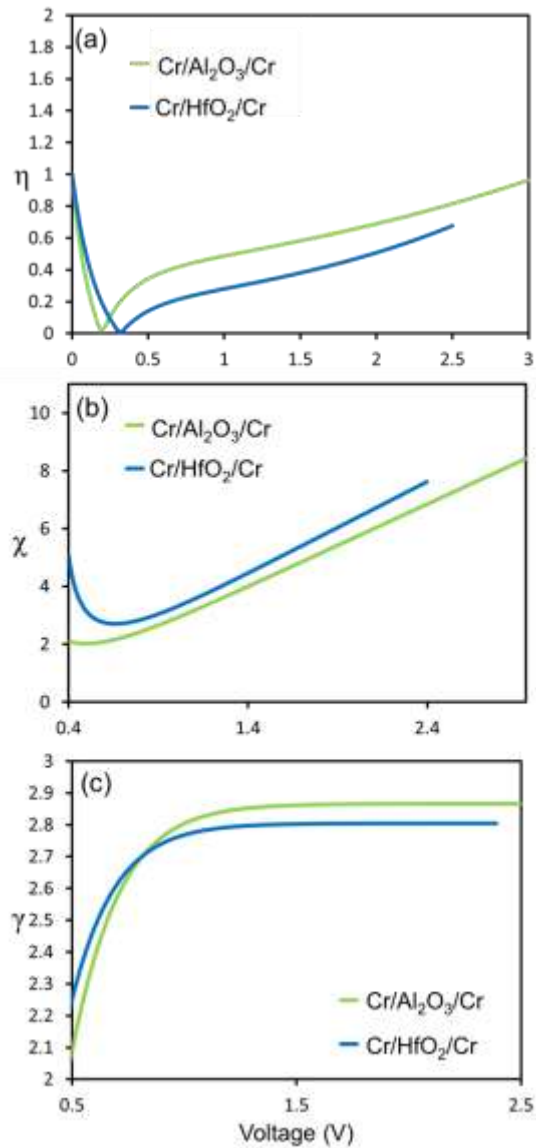


Figure 3-12 Plots of: (a) asymmetry, (b) nonlinearity, and (c) curvature coefficient of the Cr/Al₂O₃/Cr and Cr/Al₂O₃/Cr devices.

For efficient rectification purposes, the degree of nonlinearity, χ , curvature coefficient, γ , and asymmetry, η , in the current-voltage (I-V) characteristic of the conventional MIM diode need to be increased. As mentioned earlier, these factors are constrained by the work function of metallic electrode, W , materials and the electron affinity, ζ , of the sandwiched insulator. Indeed, it would be advantageous to engineer a tunnel barrier in a fashion such that the device characteristics of the

investigated metal-insulator-insulator-metal (MIIM) diode (χ , γ and η) are enhanced (>10) beyond that of a conventional MIM (i.e. $\chi \approx 2$ and $\eta \approx 1$).

3.4 Metal-insulator-insulator-metal diodes

Since the electron tunneling probability depends on the insulator thickness, d , and ϕ , the mechanism by which electrons traverse the barrier under forward bias should be different from that under reverse bias in order to increase the I-V asymmetry. Furthermore, for the MIM diode to operate on a femtosecond time scale, the electron conduction mechanism must be of the tunneling type. An electron tunnelling device consisting of a series of laterally indented barriers, which were sandwiched between metallic electrodes, was initially proposed by DiVentra et al. [104]. Depending on the polarity of the electrodes, it was postulated that such a class of devices would exhibit two different tunneling mechanisms for electron conduction: resonant and direct tunneling. Thus, an electron tunnelling device consisting of a MIIM is expected to exhibit enhanced χ and η compared to those of a conventional MIM device. However, to date no operational MIIM devices having highly nonlinear I-V characteristics have been demonstrated.

Figure 3-13 depicts a schematic representation of the ideal energy band diagram for a cascaded potential barrier MIIM diode at zero, forward, and reverse bias. In general, the two metal electrodes, (M1 and M2) are chosen to have different work functions ($W1$ and $W2$, respectively) and the oxides could have different thicknesses ($d1$ and $d2$, respectively). As illustrated in Figure 3-13(a), the cascaded potential barrier profile is asymmetric at zero bias voltage. Above a certain forward bias voltage, the electron energy level (M2 Fermi level) can reach or even surpass the edge of the second oxide's potential barrier height (Figure 3-13(b)). Here, the electrons traverse the potential barrier height at a high tunneling probability as the *effective* potential barrier thickness appears to be less than the actual thickness of the two oxide layers. On the other hand, when a reverse bias voltage is applied, the electrons' tunneling probability drops drastically since they have to traverse across

the whole barrier, as shown in Figure 3-13(c). This alteration of tunneling mechanism in forward and reverse bias voltages is attributed to the enhanced nonlinearity present in the MIIM diode presented here.

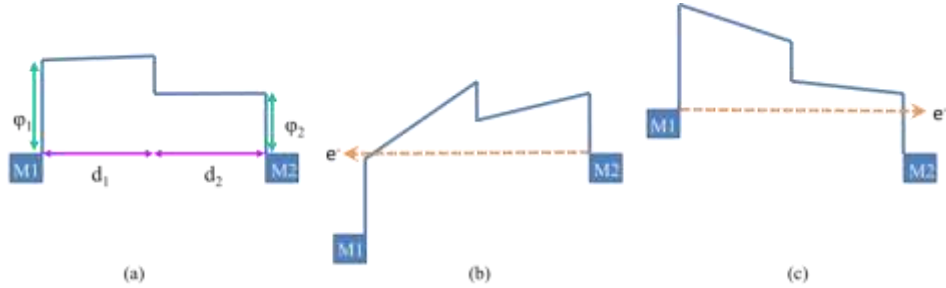


Figure 3-13 Schematic of the energy band diagram for devices having a cascaded potential barrier at (a) zero, (b) forward, and (c) reverse bias. Here M1 and M2 are the electrodes of two sides of the device, d_1 and d_2 are the oxide thickness of the two insulators, and ϕ_1 and ϕ_2 are potential barrier heights formed at the interface of M1 and M2 with their corresponding insulators, respectively.

The MIIM were fabricated by the ALD process described in the previous section. Similarly, to isolate the effect of the barrier engineering in the nonlinear I-V characteristics of the devices, both electrodes were selected to be of the same metal (M1, M2 \equiv Cr). Clearly, the modification to these ultrathin oxides layers changes the form of the barrier, and thus alters the conduction of electrons across the junction. The tunnel barrier is engineered in such a fashion as to have a cascading form where $\Phi_{b1} = 3.05$ eV (corresponding to Al_2O_3) and $\Phi_{b2} = 1.75$ eV (corresponding to HfO_2). For this section, MIIM diodes consisting of $\text{Cr}/\text{Al}_2\text{O}_3\text{-HfO}_2/\text{Cr}$ and were fabricated and compared to the previous MIM diodes consisting of $\text{Cr}/\text{Al}_2\text{O}_3/\text{Cr}$ and $\text{Cr}/\text{HfO}_2/\text{Cr}$.

The schematic of a fabricated MIIM device and its energy band diagram are illustrated in Figure 3-14(a) and (b), respectively. Here, I_1 represents the Al_2O_3 layer and I_2 represents the HfO_2 layer [102].

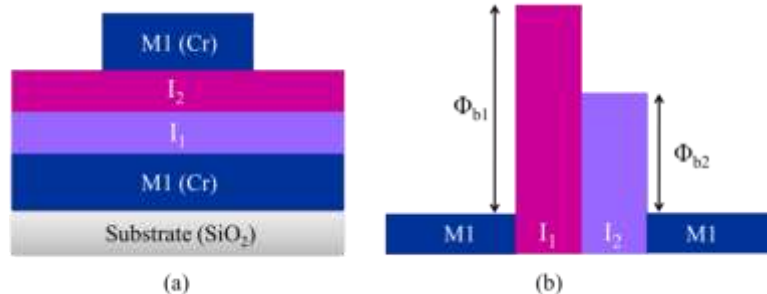


Figure 3-14 Schematic of: (a) the layout of the MIIM device and (b) the energy band diagram. Here, I_1 , and I_2 are the insulating layers corresponding to Al_2O_3 and HfO_2 layers, respectively. Φ_{b1} , and Φ_{b2} are the potential barrier for Al_2O_3 and HfO_2 layers, respectively.

The fabricated $Cr/Al_2O_3-HfO_2/Cr$ diode insulating potential barrier is made up of a 2nm Al_2O_3 layer and a 2nm HfO_2 layer, which provides an overall thickness of 4nm. To isolate the effect of the cascaded potential barrier of the $Cr/Al_2O_3-HfO_2/Cr$ diode on the I-V characteristics, this device was compared to a 4 nm thick single potential barriers devices made from $Cr/Al_2O_3/Cr$ and $Cr/HfO_2/Cr$ layers. The I-V characteristic of the fabricated $Cr/Al_2O_3-HfO_2/Cr$ diode is depicted in Figure 3-15.

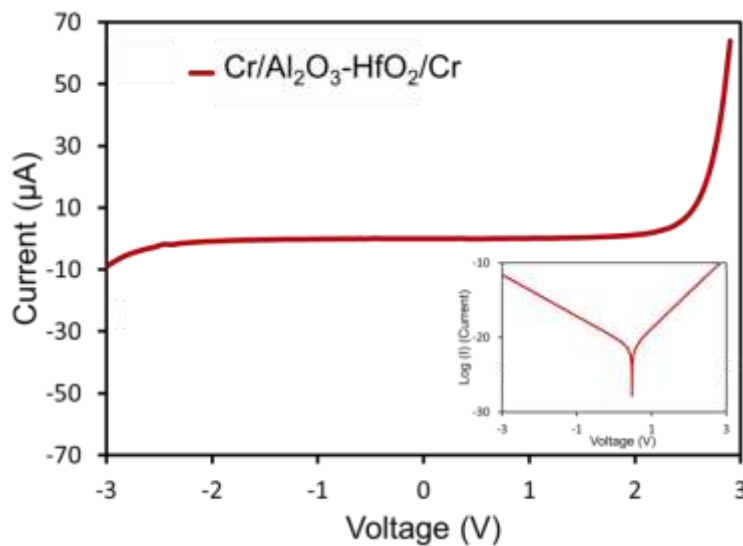


Figure 3-15 Current versus voltage characteristic curves for the $Cr/Al_2O_3-HfO_2/Cr$ device. The inset depicts the logarithm of the current versus the voltage.

It is evident that the I-V curve for the $Cr/Al_2O_3-HfO_2/Cr$ diode is highly asymmetric around $V=0$, where in the forward direction ($V>0$) the current reaches

64 μ A (at V=3V) and in the reverse direction (V<0) is only 7 μ A (at V= -3V). This high degree of asymmetry is observed by comparing the I-V curve of the MIIM (Figure 3-15) with that of a MIM diode shown in Figure 3-11. It should be stressed that this asymmetry is inherently due to the MIIM cascaded potential barrier and not due to the metallic electrodes as both electrodes are made from the same metal (i.e. Cr). Evidently, the MIIM device depicts superior nonlinearity in comparison to MIM devices having the same oxide thickness.

The resulting I-V behavior of Cr/Al₂O₃-HfO₂/Cr, Cr/Al₂O₃/Cr, and Cr/HfO₂/Cr were quantified by examining the asymmetry, η , nonlinearity, χ , and curvature coefficient, γ , as shown in Figure 3-16 (a-c). As illustrated in Figure 3-16 (a), the Cr/Al₂O₃/Cr, and Cr/HfO₂/Cr diodes possess highly symmetric I-V curves where $\eta \sim 0.8$ over the whole voltage range. This behavior is expected since the utilized metallic electrodes are identical on the opposite sides of the oxide potential barrier. On the other hand, when the oxide layer is modified to form a cascaded potential barrier layer, the barrier height symmetry is broken and asymmetric I-V behavior is observed. Figure 3-16 (b) depicts the degree of χ of the fabricated diodes. Clearly, the rate of change of the nonlinearity over the voltage range for the Cr/Al₂O₃-HfO₂/Cr diode is 5.5 V⁻¹ which is 2.8 times higher than the 2.8 V⁻¹ obtained from the Cr/HfO₂/Cr and Cr/Al₂O₃/Cr devices. Furthermore, Figure 3-16 (c) illustrates that the value of the curvature coefficient for the MIIM device is 1.7 times that of the MIM devices. Due to the enhanced nonlinearity, curvature coefficient, and asymmetric characteristics, these diodes are advantageous to MIM diodes when utilized as rectifiers and mixers.

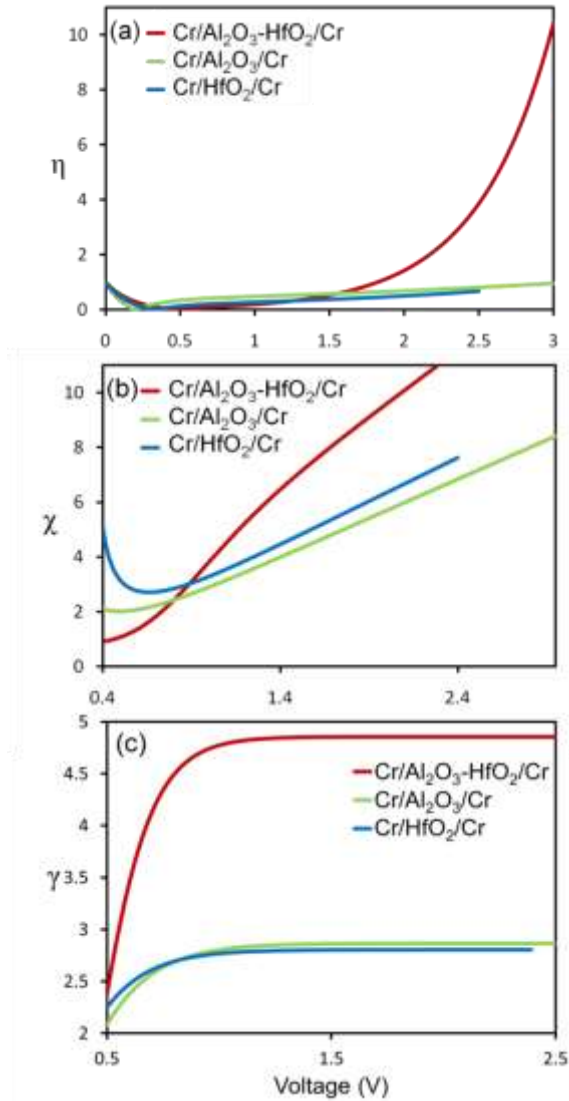


Figure 3-16 Plots of: (a) asymmetry, (b) nonlinearity, and (c) curvature coefficient of the Cr/Al₂O₃/Cr, Cr/Al₂O₃/Cr and Cr/Al₂O₃/Cr devices.

Through the introduction of a cascaded potential barrier, different mechanisms for electron tunneling under forward and reverse voltage biases were realized. A high I-V nonlinearity, up to 10 times that of a conventional MIM, was obtained for identical metal electrodes. As the next step, the tunneling mechanism is further altered. For this, resonant tunneling transport is incorporated into a metal-insulator-metal diode. This would be analogous to a tunnel diode (normal tunneling) with the mechanism of a RTD (resonant tunneling) device. It is envisioned that high speed rectifiers, ultrahigh bandwidth frequency mixers, diodes, and electron tunnel

transistors having extraordinary I-V nonlinearity can be realized through the incorporation of the resonant tunneling phenomenon with the MIM device architecture.

3.5 Metal-insulator-insulator-insulator-metal diodes

The next task of the investigation is the demonstration of electron resonant tunneling phenomenon through multi-stepped potential barriers of metal-insulator-insulator-insulator-metal (MIIM) diodes [105]. Through selection of oxide materials and atomically multilayering the potential barrier profile design, MIIM devices consisting of Cr/Cr₂O₃-HfO₂-Al₂O₃/Cr and Cr/Cr₂O₃-Al₂O₃-HfO₂/Cr were fabricated and characterized. Due to electron resonant tunneling, via multiple quantum wells formation at the oxides interfaces, it is expected that such electron tunneling diodes would exhibit extreme asymmetry and high non-linearity. As explained, both χ and η are key figures of merit used to characterize the efficiency and performance of electron tunneling devices. To augment the performance of a typical MIM tunnel diode, designing the shape of tunneling potential barrier offers a valuable degree of freedom for enhancing both χ and η .

An electron tunnelling device consisting of a series of laterally indented potential barriers was first proposed by DiVentra *et al.* [104, 106]. It was postulated that such a configuration would exhibit two distinct electron tunneling mechanisms: resonant tunneling and direct tunneling. In analogy, an electron tunneling device consisting of a metal-insulator-insulator-insulator-metal (MIIM) is envisaged to exhibit extreme asymmetry and high non-linearity. Through material selection of appropriate oxide materials, potential barriers having cascaded (Cr₂O₃-HfO₂-Al₂O₃) and non-cascaded (Cr₂O₃-Al₂O₃-HfO₂) profiles were fabricated and tested.

The fabrication of the MIIM devices was similar to the fabrication of MIM devices and a shadow mask technique was utilized. Here again, to isolate the effect of the potential barrier shape on the device performance from the potential barrier offset (i.e. δ), Cr was used for all device electrodes. The first electrode was a 100nm

thick Cr layer deposited on a SiO₂ substrate using magnetron sputtering. This was followed by the growth of a ~2nm thick Cr₂O₃ layer through the introduction of oxygen to the deposited Cr film. Next, a shadow was placed on the substrate to facilitate the deposition of the other oxide layers. For the fabrication of the MIIM devices, 2 nm thick layers of Al₂O₃ and HfO₂ were deposited in a desired order. Finally, the sample was transferred back to the sputtering chamber in-situ via a load-lock for the deposition of the second 100nm thick Cr electrode.

Figure 3-17 illustrates a cross-sectional schematic and transmission electron microscope cross-sectional image of a Cr/Cr₂O₃-HfO₂-Al₂O₃/Cr MIIM structure.

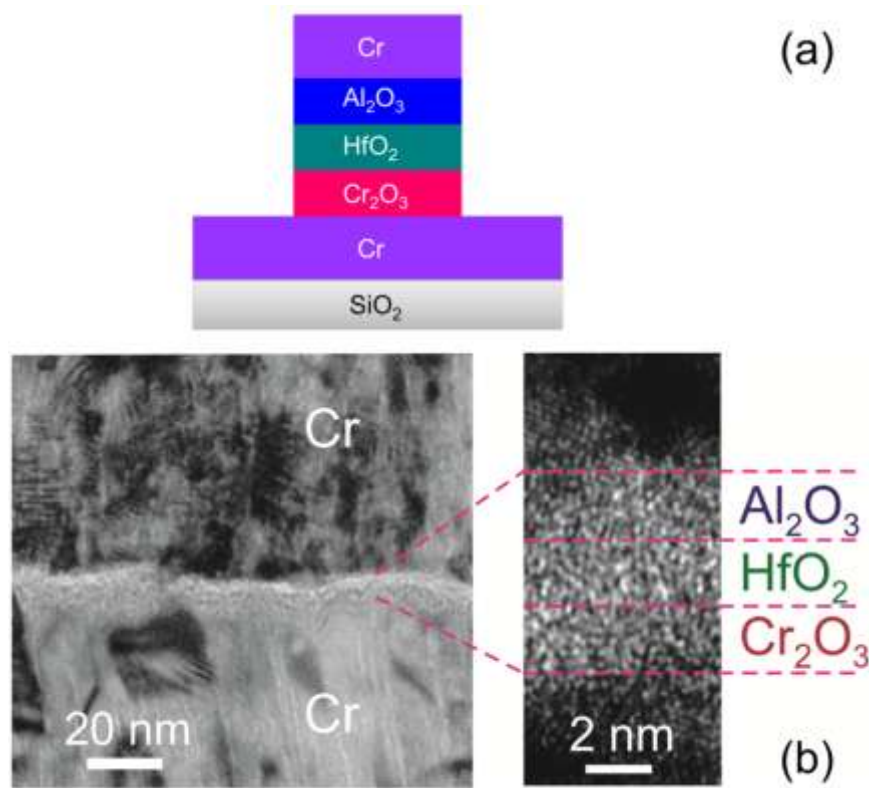


Figure 3-17 Cross-sectional views of the MIIM tunnel device. (a) A schematic diagram depicting a fabricated MIIM device having a 2nm thick Al₂O₃ layer, a 2nm thick HfO₂ layer, and a 2nm thick Cr₂O₃ layer. (b) The Cross-sectional transmission electron microscope (TEM) image of a Cr/Cr₂O₃-HfO₂-Al₂O₃/Cr MIIM device. The layers are grown on a 550nm thick SiO₂ film on top of a 500μm thick Si substrate. Each oxide layer is 2nm thick. The oxides are grown sequentially in accordance to their ascending potential barrier values (i.e. 0.64eV, 0.75eV and 2.62eV, for Cr₂O₃, HfO₂, and Al₂O₃, respectively), thus forming a cascading potential barrier profile.

Figure 3-18(a) displays the I-V characteristic of this MIIIM cascaded potential barrier. It is evident that such a potential barrier profile results in I-V characteristic possessing considerably large degrees of asymmetry ($\eta = 10^4$) and nonlinearity ($\chi = 6$). A closer examination of Figure 3-18 (a) shows that the Cr/Cr₂O₃-HfO₂-Al₂O₃/Cr diode I-V curve exhibits features (labeled as ‘i’, ‘ii’ and ‘iii’) which occur at specific voltage values (-3.0V, +1.2V, and +2.7V, respectively). Such features are the hallmark of the engineered energy band structure imprinted on the tunneling current via the cascaded potential. An illustrative energy band diagram of a Cr/Al₂O₃- HfO₂-Cr₂O₃/Cr MIIIM device is shown in Figure 3-18 (b). Where $\Phi_{b1} = 2.62$ eV , $\Phi_{b2} = 0.87$ eV, $\Phi_{b3} = 1.1$ eV, and $\Phi_{b4} = 0.64$ eV. The mechanism responsible for the abrupt increase in the current at -3.0V (at ‘i’) is illustrated in Figure 3-18 (c). At -3.0 V, the potential barrier profile tilts such that electrons tunneling from the left electrode have energy surpassing that of the Cr₂O₃ layer potential barrier and exactly matching the edge of the HfO₂ potential barrier. Further increase in the bias voltage results in a decrease in the HfO₂ potential barrier height. Consequently, a small increase in the voltage, results in a significant enhancement of the tunnel current. At this negative bias polarity arrangement, direct electron tunneling is the dominant electron transport mechanism. By reversing the voltage polarity, current starts to rise when the voltage reaches +1.2V (at ‘ii’). Figure 3-18 (d) shows that a narrow quantum well begins to form between the Cr₂O₃ and the HfO₂ layers at +1.2V. As described by quantum mechanics, there are allowed energy levels associated with this potential well. A sharp turn-on of the diode’s current occurs in a situation when the energy of the electrons (associated with the Fermi level of the positively biased electrode) matches an allowed energy level of the potential well. At +1.2V, a shallow potential well forms at the interface between the Cr₂O₃ and HfO₂ layers. As the voltage increases, both the width and the depth of the potential well increase, causing the bound energy states to shift to lower energies.

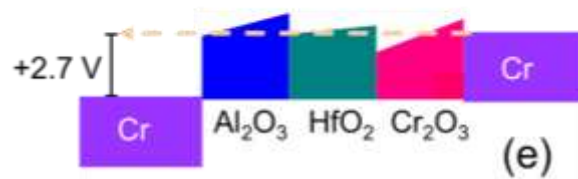
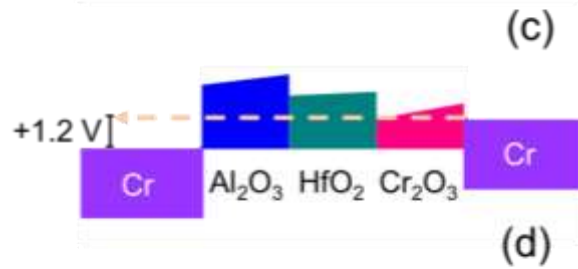
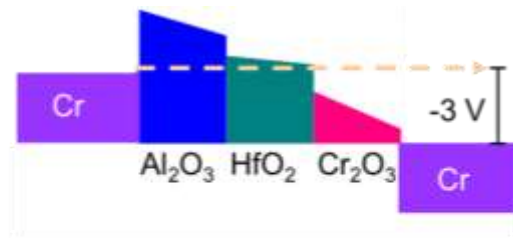
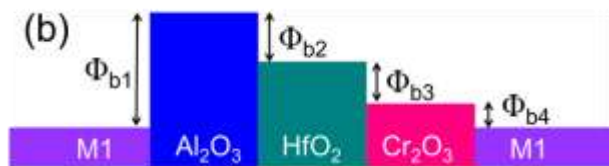
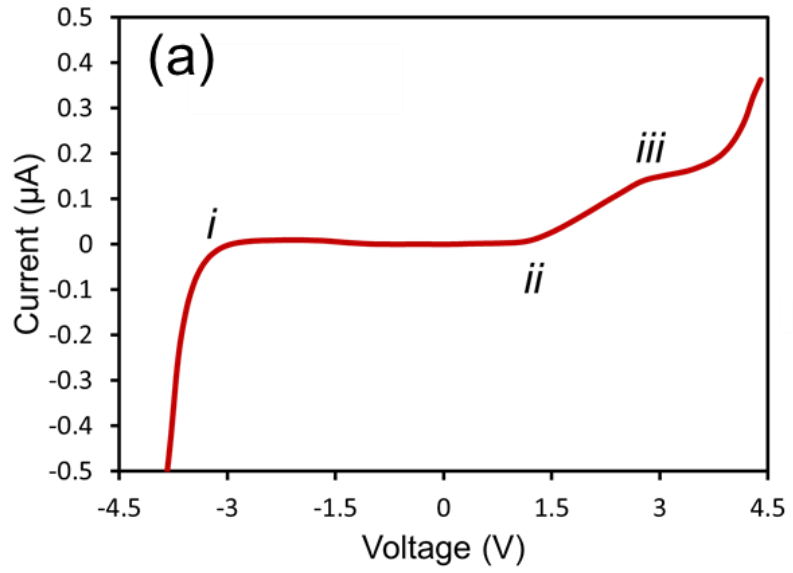


Figure 3-18 I-V experimental results and energy band diagram model of the MIIM device having a cascaded potential barrier profile. (a) Current versus voltage characteristic curves for

the Cr/Cr₂O₃-HfO₂-Al₂O₃/Cr device. (b) Energy band diagram of the M1/Cr₂O₃-HfO₂-Al₂O₃/M1 device having a cascaded potential barrier profile at zero voltage. Here, M1 represents the Cr electrodes, Φ_{b1} (2.62 eV) and Φ_{b4} (0.64 eV) are the potential barrier heights for Al₂O₃ and Cr₂O₃ layers, respectively. Φ_{b2} (0.87 eV) and Φ_{b3} (1.1 eV) are the potential barrier heights between Al₂O₃-HfO₂ and between HfO₂-Cr₂O₃ interfaces, respectively. Energy band diagram¹⁸ of the Cr/Cr₂O₃-HfO₂-Al₂O₃/Cr device at: (c) -3.0 V, (d) +1.2 V, and (e) +2.7 V. The arrows depict the electron tunneling direction.

Over the +1.5V to +2.7V voltage range, the width is estimated to vary from 0.5nm to 1nm, with a corresponding potential well depth of 0.1eV to 0.8eV, respectively. The MIIM potential profile constrains each well to possess only one allowed state. At +1.3V, there is a resonant state ~17meV below the Fermi level of the injecting Cr electrode, and thus at room temperature, electron resonant tunneling becomes dominant (See Appendix A for calculations). Further increase in the voltage does not lead to abrupt increase in the current since the bound state shifts further below the Cr Fermi level (effectively reducing the current). However, at the same time, the potential barrier height is lowered. The tradeoff between the two mechanisms leads to a monotonic rise in the tunneling current.

The feature labeled ‘*iii*’ occurring at +2.7 V (Figure 3-18 (e)) reveals the start of the formation of a second potential well between the HfO₂ and Al₂O₃ layers. Again, there is only one resonant state residing near the bottom of the second potential well. At 2.8 V a shallow potential well forms in which the bound energy state resides near the Fermi level injecting Cr electrode. However, by increasing the voltage, this well deepens and, thus, shifts the bound energy state far from the energy of the electrons that participate in the tunneling mechanism. The voltage increase also results in a reduction of the effective potential barrier height of the Al₂O₃ and the overall tunnel current plateaus beyond +2.7 V. Further increase in the voltage raises the energy of the electrons to overcome the HfO₂ potential barrier and significantly increases the current. Clearly, through introduction of different electron tunneling mechanism at opposite voltage polarities, it is possible to make this type of device having similar electrodes, to operate in different electron tunneling regimes: direct tunneling and resonant tunneling. It is only through potential barrier design of the

oxide layer that significant enhancement of I-V asymmetry and non-linearly has been achieved.

Since the engineered oxide layer is responsible for the observed enhanced performance, we show that rearranging the order of the oxide layers (i.e. the potential barrier profile) in a non-cascading fashion, where the HfO₂ and the Al₂O₃ oxide layers are exchanged, results in entirely different I-V characteristics (Figure 3-19 (a)), asymmetry and nonlinearity. An illustrative diagram depicting a non-cascaded potential barrier profile of a Cr/Cr₂O₃-Al₂O₃-HfO₂/Cr MIIIM device is shown in Figure 3-19 (b). Where $\Phi_{b1} = 1.75$ eV , $\Phi_{b2} = 0.87$ eV, $\Phi_{b3} = 1.98$ eV, and $\Phi_{b4} = 0.64$ eV. The rearrangement of the potential barrier profile, to have a higher magnitude barrier at the middle of the energy gap, results in a positive tunneling current magnitude that surpasses the negative current. There is a clear difference between the I-V curves of the MIIIM device having a cascaded potential barrier profile to that of a non-cascaded profile. While the former is turned on at -3V at reverse bias, the latter stays off at all reverse voltage biases up to the breakdown voltage value. To shed light on the features observed and labeled ‘*iv*’ at +1.2V, ‘*v*’ at +3V and ‘*vi*’ at 3.8V, in Figure 3-19 (a), we refer to the energy band diagram (Figure 3-19 (c-e)).

As the voltage is scanned from -5V toward 0V, the tunneling current is highly suppressed since electrons must tunnel through the whole potential barrier of Figure 3-19(b). At ‘*iv*’ the shape of the I-V curve is attributed to the voltage where a quantum well is formed between Cr₂O₃ and Al₂O₃ layers (Figure 3-19(c)). Beyond the +1.2V voltage value, the tunneling current monotonically increases through a similar mechanism for the cascaded potential barrier. However, at a voltage of + 3.0 V (at ‘*v*’) a distinct feature becomes evident.

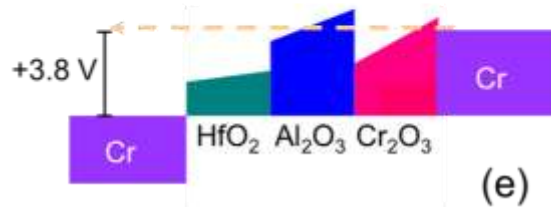
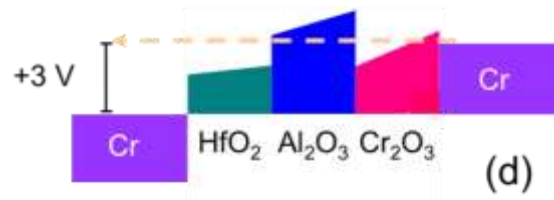
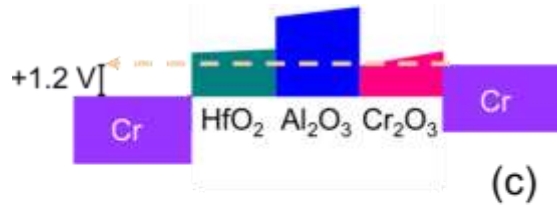
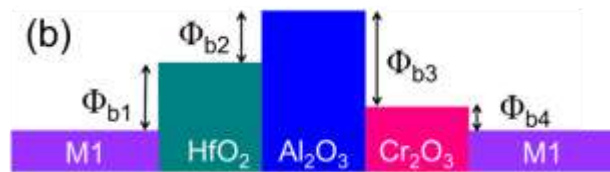
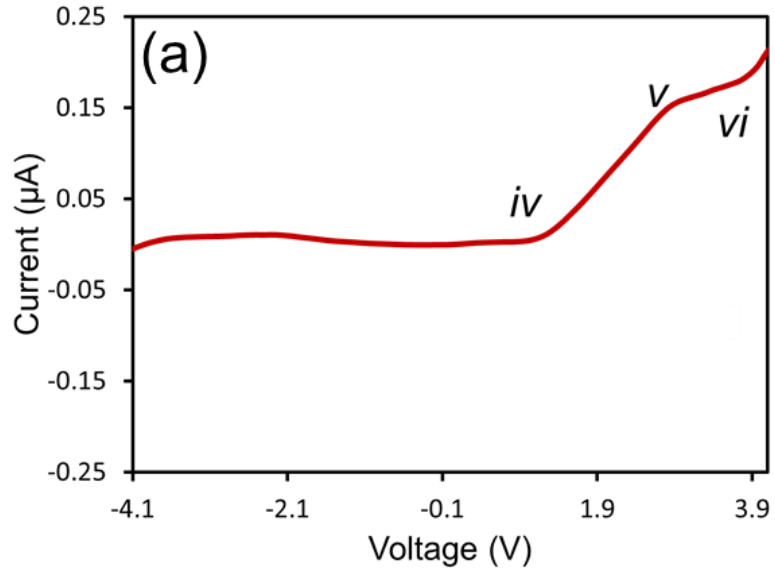


Figure 3-19 I-V experimental results and energy band diagram model of the MIIM device having a non-cascaded potential barrier profile. (a) I-V characteristic curves for the Cr/Cr₂O₃-

$\text{Al}_2\text{O}_3\text{-HfO}_2/\text{Cr}$ device. The features in the I-V characteristic curves of the MIIM device have been marked as (iv), (v) and (vi). (b) Energy band diagram of the M1/ $\text{Cr}_2\text{O}_3\text{-Al}_2\text{O}_3\text{-HfO}_2$ /M2 device having a non-cascaded potential barrier profile at zero voltage. Here, M1 represents the Cr electrodes, Φ_{b1} (1.75 eV) and Φ_{b4} (0.64 eV) are the potential barrier heights for Al_2O_3 and Cr_2O_3 layers, respectively. Φ_{b2} (0.87 eV) and Φ_{b3} (1.98 eV) are the potential barrier heights between $\text{HfO}_2\text{-Al}_2\text{O}_3$ and between $\text{Al}_2\text{O}_3\text{-Cr}_2\text{O}_3$, respectively. The energy band diagram¹⁸ of the Cr/ $\text{Cr}_2\text{O}_3\text{-Al}_2\text{O}_3\text{-HfO}_2$ /Cr device at: (c) -1.2 V, (d) +3.0 V, and (e) +3.8 V. The arrows depict the electron tunneling direction.

Examining the energy band diagram at this bias voltage (Figure 3-19(d)) reveals that the electrons' energy is high enough to reach the left edge of the Al_2O_3 potential barrier. At 3.8V (at 'vi'), the current increases due to the decrease of the effective potential barrier thickness (Figure 3-19(e)). At this bias voltage, electrons have enough energy to be in the vicinity of the Al_2O_3 potential barrier. It is beyond this biasing voltage value that the electrons go beyond the potential barrier height of the Al_2O_3 oxide and, thus, the I-V characteristic curve illustrates a significant tunnel current increase.

The effect of oxide material architecture on operational specifications (e.g. η and χ) of the electron tunnel devices is further investigated and presented in Figure 3-20 (a,b) for both cascaded and non-cascaded potential barrier profiles.

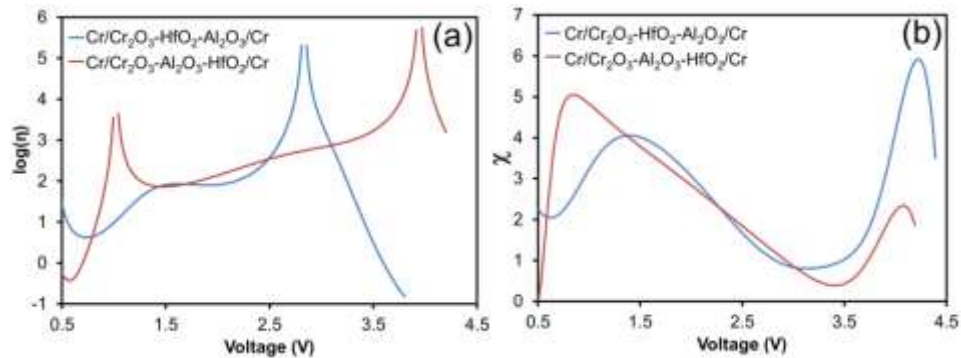


Figure 3-20. Figures of merit used to characterize the efficiency and performance of electron tunneling devices. (a) Logarithmic plot of asymmetry of Cr/ $\text{Cr}_2\text{O}_3\text{-HfO}_2\text{-Al}_2\text{O}_3/\text{Cr}$ and Cr/ $\text{Cr}_2\text{O}_3\text{-Al}_2\text{O}_3\text{-HfO}_2/\text{Cr}$ devices. In both devices, the asymmetry peaks when the current in the negative bias polarity becomes significantly small. For this, the data in the vicinity of these regions were removed within ± 100 mV from the peaks. (b) Nonlinearity of the Cr/ $\text{Cr}_2\text{O}_3\text{-HfO}_2\text{-Al}_2\text{O}_3/\text{Cr}$ and Cr/ $\text{Cr}_2\text{O}_3\text{-Al}_2\text{O}_3\text{-HfO}_2/\text{Cr}$ devices.

In both devices, the asymmetry peaks when the current in the negative bias polarity becomes significantly small. For this, the data in the vicinity of these regions were removed within ± 100 mV from the peaks. (b) Nonlinearity of the Cr/Cr₂O₃-HfO₂-Al₂O₃/Cr and Cr/Cr₂O₃-Al₂O₃-HfO₂/Cr devices.

It is interesting to note that the two devices can be operated in different regimes depending on the voltage level. For the non-cascaded potential barrier device operating at low voltage around 1V, η can be as high as $10^{3.5}$ compared to 10 for a cascaded potential barrier device. However, at 2.8 V, the device having a cascaded potential barrier shows $\eta \approx 10^5$, after which it decreases with increasing voltage. On the other hand, the non-cascaded potential barrier device shows $\eta \approx 10^5$ at 3.8 V. The η values are more than two orders of magnitude than those reported for Nb/Nb₂O₅/Pt MIM diode [103]. Similarly, the value of χ in Figure 4b, show $\chi = 5$ around 1V for the non-cascaded potential barrier device compared to 2.5 for the cascaded potential barrier device at the same voltage. At 4.2V, the cascaded potential barrier device exhibits higher nonlinearity ($\chi = 6$), whereas, $\chi = 2.3$ at 4 V for the non-cascaded potential barrier device. The devices' low or high operating voltage selectivity is determined by its potential barrier design rather than material electrical properties.

3.6 Summary

In this chapter, the concepts and principle of operation and some of the applications of electron tunnel devices such as tunnel diodes, resonant tunneling diodes, and metal-insulator-metal (MIM) diodes is described in detail. While the characteristics of MIMs have been vastly studied, little is known about the effect of potential barrier engineering on the characteristics of these tunneling diodes. In this chapter, the improved metal-insulator-metal diodes, MIIM and MIIM diodes, have been presented and thoroughly investigated. It is shown that the asymmetry and nonlinearity characteristics of these rectifiers outperform the conventional MIM design. It is envisioned that these novel electron tunnel diodes are suitable for detecting THz radiation.

4. CHAPTER 4

MIM detector design, fabrication, and characterization³

4.1 Introduction

Metal-insulator-metal (MIM) devices have been used in detecting and mixing of microwave radiation since 1966 [92]. This is due to the nonlinearity present in the I-V characteristic (diode-like characteristic) of these devices. In MIM devices, the radiation is coupled to the diode via an antenna and electrons flow across the diode junction due to the quantum mechanical tunneling phenomenon. While the electron tunneling probability is low, it has shown to be effective in the operation of such quantum-based electron transport devices. The early designs of MIM diodes were point contact MIM junctions. They consisted of a fine-etched tungsten tip, which was brought in close contact with an oxidized metallic surface. A schematic of the point contact MIM is illustrated in Figure 4-1. In this design, the diode junction was formed by a thin native oxide layer sandwiched between two metallic layers (i.e. the tip and the surface). Since the contact area (junction area) is on the order of $0.01 \mu\text{m}^2$, it possesses inherently low capacitance. This feature has been used to demonstrate the performance of MIM diodes at high-frequencies [82]. In addition, the tip also acts as a long wire antenna which couples the electromagnetic radiation to the diode.

³ Part of this work has been published in, *IEEE Transactions in Nanotechnology*, **10**, 2011.

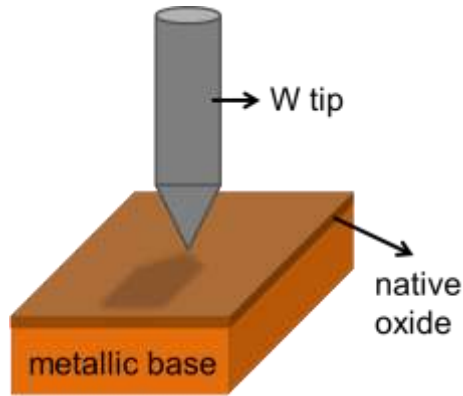


Figure 4-1 Schematic of a point contact MIM is shown.

Due to their high speed response, point contact MIM diodes have been used in absolute frequency measurements required for time and frequency standards [107]. Although these devices were shown to be promising mixers and rectifiers, there exist certain drawbacks inherent to point contact MIMs:

1. **Reproducibility:** Precise control of the junction area (the area of the tip in near contact with the metallic substrate) in these devices is a very challenging task. It will be discussed later that the response time (or bandwidth) of an MIM device is sensitive to its junction area.
2. **Mechanical instability:** In these devices, the tip-metal separation is in the order of tens of angstroms, thus making these devices delicate and unstable for long term operation.

In order to eliminate the above mentioned drawbacks, researchers attempted to fabricate these devices on planar substrates. Thin-film MIMs with integrated antennas rectifying in the 10 μm region were first fabricated and tested by Small et al. [108] and Wang et al. [109]. These thin film MIM diodes were fabricated using standard photolithographic methods. Due to the resolution limitation of photolithography, the junction area in such devices was $\sim 1 \mu\text{m}^2$ (100 times the area of the point contact type), thus leading to a much larger inherent capacitance. In this experiment the MIM diodes were illuminated by $\sim 1 \text{ W}$ of laser radiation at 10.6 μm focused to a 200 μm diameter spot. Utilizing electron beam lithography (EBL), the

limitations of photolithography can be eliminated and features as small as 10 nm can be fabricated.

To obtain devices with faster response, Wilke et al. [79, 84] reported the first thin film MIM fabricated using EBL having a contact area of $0.056 \mu\text{m}^2$. These devices were integrated with dipole antennas that could detect CO_2 laser radiation $10.6 \mu\text{m}$. In order to obtain faster response, and to perform mixing experiments at 28 THz (far infrared radiation), Fumeaux et al. [61] fabricated MIM diodes with a junction area of $\sim 100\text{nm} \times 100\text{nm}$ ($0.012 \mu\text{m}^2$) which are comparable to the contact area of the point contact MIMs. A 200 mW CO_2 laser radiation at $10.6 \mu\text{m}$ focused to a $100 \mu\text{m}$ diameter spot was utilized in this experiment. These MIMs were integrated with a bow-tie antenna to couple infrared (IR) radiation to the diode. Krishnan et al. [96] studied the effects of dielectric thickness and contact area on I-V characteristics of thin film MIM diodes having a junction area from $1 \mu\text{m}^2$ to $100 \mu\text{m}^2$. The same group reported on the fabrication of a prototype rectifying antenna element operating at 2.5 GHz using MIM diodes with a junction area of $1 \mu\text{m}^2$ in conjunction with a microstrip slot antenna [98]. Hobbs et al. [83] investigated the tunnel barrier parameters for a Ni-NiO-Ni tunnel junction having a $0.4 \mu\text{m}^2$ junction area. Recently, Tiwari et al. [81] reported on fabrication of a Al- Al_2O_3 -Pt MIM having a junction area of $50 \text{ nm} \times 80 \text{ nm}$ which was capable of rectifying 30 THz laser radiation. The MIMs were illuminated by 25 W of CO_2 laser radiation at $10.6 \mu\text{m}$.

The goal of this chapter is to research the fabrication and characterization of MIM diodes having an integrated antenna to be utilized as THz radiation detectors. The motivation behind fabricating these devices is to present a fast response THz detector to replace current THz detectors which suffer from an inherently poor response time. To accomplish this, the knowledge gained from designing and fabricating optimized THz antenna designs (chapter 2) and highly nonlinear MIIM and MIIIM diodes (chapter3) will be integrated for fabricating ultrafast THz detectors.

As mentioned in the introduction, due to the inherently slow response of conventional THz detectors, they cannot be used for detecting ultrahigh THz

frequencies. Sensitivity of thermal detectors can be increased by thermally isolating them from their surroundings, but this comes at the expense of slowing the detectors' response time. In addition, these detectors suffer from low detectivity. MIM and MIIM detectors with an integrated antenna overcome these limitations. Due to the electron tunneling effect, MIM and MIIM diodes are inherently fast detectors and can be operated at room temperature. The incorporation of an integrated antenna allows frequency selectivity, as well as, polarization selectivity can be performed without the requirements for bulky and expensive filters (which are required for existing THz detectors, such as bolometers and Golay cells). The proposed detector can be used in these imaging and sensing applications while having all the advantages of an MIM diode, such as fast and broadband detection as well as room temperature operation. However, the fabrication of such diodes is very delicate as it requires the deposition of a few nanometers of an oxide layer that is sandwiched between two metallic electrodes. The surface/edge roughness and step coverage involved in this fabrication process are not straightforward and require an elaborate and complicated fabrication procedure. This includes detailed research on lithography and deposition as well as pattern transfer of the diode component.

This chapter is outlined as follows: the first section introduces the equivalent circuit of the MIM diode having an integrated antenna. From there, the design parameters related to the response of the detector are determined. In the second section, the fabrication of the THz detector is discussed. Three phases at which the fabrication process flow was modified to achieve the final fabrication recipe is comprehensively described. In addition, the final device fabrication process along with the final detector characterization is illustrated. Finally, a modified lift-off technique required for the fabrication of the detectors is demonstrated.

4.2 Square-law detectors and mixers

MIM, MIIM, and MIIIM diodes are considered as square-law detectors since their rectified signal is proportional to the square of the amplitude of the input signal [110]. This is a direct result of their nonlinear I-V characteristic. To show this one can expand the output current of the junction in a Taylor series and terminate it at the squared term, resulting in:

$$I(V) = I(V_b) + \left(\frac{dI}{dV} \right)_{V_b} \delta V + \frac{1}{2!} \left(\frac{d^2I}{dV^2} \right)_{V_b} (\delta V)^2 \quad (4.1)$$

where V_b is the bias voltage and δV is the small input signal. It can be observed that the output, in addition to having a dc value, is proportional to the square of the amplitude of the input signal as long as the second derivative of the I-V characteristic of the device is non-zero. By looking at this equation it is observed that the rectified signal is proportional to the second derivative of the I-V characteristic of the MIM diode for a defined input signal. In other words, when comparing different MIM diodes the diode which has a larger $\left(\frac{d^2I}{dV^2} \right)$ component compared to others will produce a larger rectified signal. As an example, if the input signal is

$\delta V = V_0 \sin(\omega t)$ the output signal will have $V_{rec} = \frac{1}{4} \left(\frac{d^2I}{dV^2} \right)_{V_b} V_0^2$ as the rectified portion in

addition to frequency components of ω and 2ω . Due to the proportionality of the output signal to the square of the input signal, a detector of this type is called a “square-law” detector. By expanding the output signal to higher orders, higher harmonics appear in the expression. Nonlinear characteristics of MIM diodes make them an ideal candidate as mixers as well as rectifiers. Consider the input signal as the summation of two frequencies $\delta V = V_0 (\sin(\omega_1 t) + \sin(\omega_2 t))$, since this input signal is squared, it produces an output consisting of a rectified signal and the beat signal at a frequency of $(\omega_2 - \omega_1)$. Due to the very fast response time and nonlinear current-voltage characteristics of tunneling phenomena, the MIM, MIIM, and MIIIM diodes can be used as mixers in heterodyne detection [107].

4.3 Circuit design

The schematic of a MIM diode having an integrated antenna under illumination of electromagnetic radiation is illustrated in Figure 4-2.

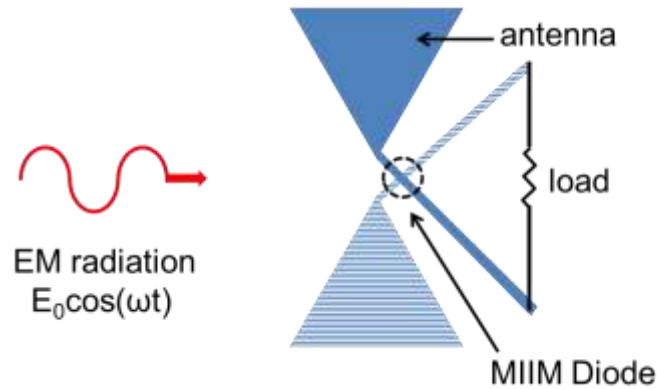


Figure 4-2 Schematic of a MIM diode having an integrated antenna being illuminated by an incident electromagnetic wave. The antenna captures and focuses the electric field of the radiation across the MIM diode. The MIM diode rectifies the electric field to provide power to the load.

The circuit representation for the above mentioned device is shown in Figure 4-3. In this schematic, the antenna is modeled as an alternating voltage source (V_s) and a resistor (R_a). The MIM diode is modeled as a resistor ($R_d(V)$) and a capacitor (C_d) connected in parallel to each other. Finally, two series resistances (R_t and R_L) represent the transmission line resistance and the load, respectively.

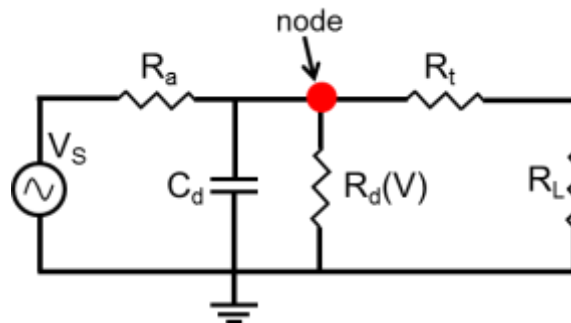


Figure 4-3 Circuit representation of the overall system of a MIM with an integrated antenna connected to a load (RL).

In this Figure, R_a is the antenna resistance, C_d is the junction capacitance, R_t is the transmission line resistance and R_L is the load resistance. In addition, here, R_d is the resistance of the diode at the operating voltage, and it is given by

$$R_d = \left(\frac{dI}{dV} \right)^{-1} \text{ where } I(V) \text{ is calculated from the function fitted to the I-V}$$

characteristic of the fabricated diode. To obtain the voltage across the diode, the Kirchoff current law (KCL) relation for the diode node is written as:

$$C_d \frac{dV}{dt} + V \left(\frac{1}{R_a} + \frac{1}{R_d(V)} + \frac{1}{R_t + R_L} \right) = \frac{V_s}{R_a} \quad (4.2)$$

Using this expression, the voltage across the load can be calculated using a simple voltage divider relation.

As mentioned earlier, different groups have used MIM diodes and have illustrated mixing processes for frequencies up to 128 THz. This indicates that the tunneling mechanism must have a very fast response time. In order to understand the parameters limiting this response, once again, the equivalent circuit of the junction is studied. For this, only the circuit components regarding the MIM diode ($R_d(V)$ and C_d) and the integrated antenna (V_s, R_a) are considered. As shown in Appendix B the cut-off frequency of this circuit is defined as

$$\nu_c = \frac{1}{2\pi R_a C_d} \quad (4.3)$$

Clearly, the cut-off frequency is inversely proportional to the junction capacitance. To place the cut-off frequency at larger values for a defined antenna resistance, junction capacitance must be decreased. Considering the junction as two parallel metallic plates with the oxide in between, C_d is defined as

$$C_d = \epsilon \epsilon_0 \frac{A}{d} \quad (4.4)$$

where A is the junction area, d is the oxide thickness and ϵ is the relative permittivity of the oxide. In order to decrease the junction capacitance (for a specific oxide material) one can decrease the junction area and/or increase the oxide thickness. However, tunneling current decreases exponentially for increasing oxide thickness as shown experimentally by Fisher et al. [111]. In other words, tunneling devices require extremely thin oxide layers having thicknesses on the order of tens of Angstroms. Therefore, to increase the cut-off frequency one needs to fabricate MIM diodes having a small junction area. As mentioned in the introduction, junction areas in point contact MIM diodes were on the order of $0.01 \mu\text{m}^2$. In early days of fabricating thin film MIMs [108] the junction area was limited to the ability of photolithography at that time ($1 \mu\text{m}^2$). To overcome this limitation the “Edge-MIM” was introduced with junction areas on the order of $(1 \mu\text{m} \times 100 \text{ nm})$ [90]. It was not until after the introduction of EBL that junction areas on the order of $100 \text{ nm} \times 100 \text{ nm}$ became possible [61]. However, MIM devices were demonstrated to operate as rectifiers and mixers above the cut-off frequency, [78]; however, the current amplitude decreases as $\omega^{-3/2}$.

A cut-off frequency of 3.0 THz is desired for our detector since it is far from the central frequency of 0.6 THz of our THz pulse. Considering equation (4.3) for the cut-off frequency and assuming that $R_A \approx 100 \Omega$ one finds that $C_d \sim 0.5 \text{ fF}$. Considering the oxide barrier to be 3.0 nm thick Al_2O_3 ($\epsilon_r=8.6-10$), then, the corresponding junction area must be $17 \times 10^{-15} \text{ m}^2$. Therefore, in our design the junction can be fabricated by overlapping two 150 nm wide transmission lines, where the MIM structure can be sandwiched between them.

Utilizing the design parameters for: (1) the integrated antenna dimensions (from chapter 2), (2) the potential barrier profile (from chapter 3), and (3) the diode junction area from the circuits model above, the procedure for the fabrication of MIM detectors at the University of Alberta NanoFab is described in the next section.

4.4 Fabrication

In this section, the path taken for finding a suitable fabrication procedure of MIM diodes having an integrated antenna is described. The investigation was divided into three phases where over 40 MIM diodes were fabricated and tested. In the course of this investigation, a novel lift-off technique required for the fabrication of MIM detectors was developed [112] and presented in section 4.3.4. Moreover, a reversible spin holder [113] was developed for uniform resist coating of deep trenches which is presented in Appendix C.

4.4.1 Phase one

To fabricate the Cr-Al₂O₃-Cr MIM diodes and the integrated bow-tie antenna the design pattern shown in Figure 4-4 was used.

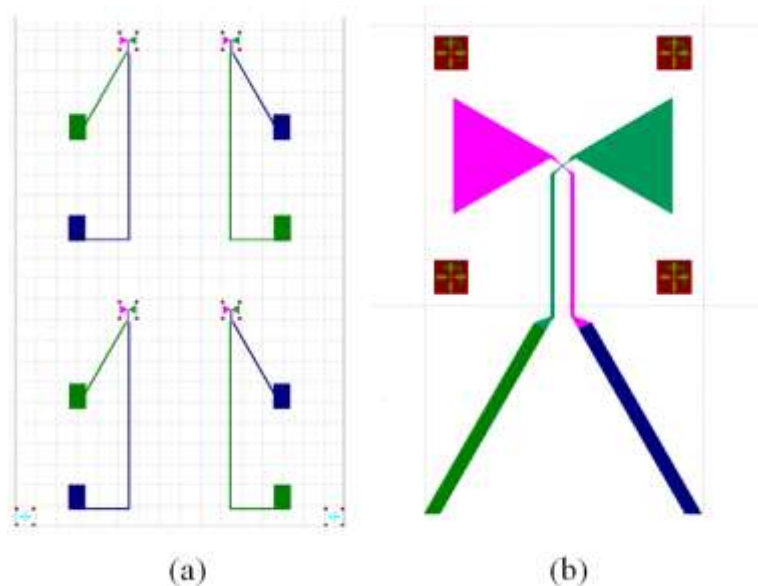


Figure 4-4 Design pattern for the MIM devices. (a) The overall design consists of a 4×4 array of MIMs. (b) The junction area and the antenna is placed in one write field area. The junction dimensions in this design are 200 nm × 200 nm.

To pattern this design the electron beam lithography (EBL) system was utilized since the design consists of few hundred nm wide lines. In the first

lithography step, the red and blue sections were patterned and metal deposition for the first Cr electrode was performed by sputtering. A comprehensive description of the EBL lithography step and development is described in section 4.4.1. After depositing the oxide layer using ALD the chip underwent the second layer of EBL patterning. The fine alignment marks located on the corners of the write fields at which each diode is placed are used to align the chip for patterning the second layer (green layer).

A bi-layer Poly methyl methacrylate (PMMA) A2 was used as the lithography resist. The resist thickness was 180 nm as measured using the ellipsometry technique. In this fabrication process, the resist was used as both a lithography resist as well as an etch mask. In order to deposit 80 nm of Cr and have a successful lift-off, the sample was reactive ion etching (RIE) etched ~50 nm after lithography and prior to the first electrode deposition. The purpose of the etching process was to etch a few nanometers of the substrate material within the pattern resulting in cleaning and nano-scale roughening of the substrate pattern. By employing this novel method, a high yield (>95%) lift-off process is achieved and the required resist thickness for a successful lift-off process is reduced from that used in conventional processes (refer to section 4.4 for more details) [114].

After the lift-off process, 30 nm of Cr was left standing out from the substrate. EBL resist was once again coated on the chip and the second layer was patterned and developed. In order to increase the yield of the lift-off process for the second electrode deposition, the sample undergoes another short etch (~20 nm) process prior to the oxide deposition. The desired thickness of the oxide layer was deposited on the sample using the ALD technique. The sample was then moved to the sputtering machine and the deposition of the second Cr layer (~80 nm) was performed. The excess material is lifted-off by placing the chip in acetone for a short period of time. Unfortunately, the MIM diodes fabricated using this procedure had either an ohmic characteristics or a disconnected contacts. IT was later revealed that the device failure was due to sputter deposition of the first electrode, and performing RIE on the first electrode prior to ALD deposition of the oxide.

Next, some alterations to the above mentioned process were introduced.

1. The bi-layer PMMA thickness was changed to 250 nm by changing the coating parameters.
2. A 70 nm layer of Cr is deposited at 3 mTorr of Ar for the first electrode making only 20 nm of Cr stand out of the substrate.
3. The recess for the second electrode is eliminated to minimize the complexity of the process since the reactions of the first layer of Cr to the RIE etch is presently unknown.
4. After the second electrode is lithographed, the sample is ion-gunned at 100 eV for 3 minutes. This process eliminates the native oxide on the first layer Cr electrode and prepares fresh Cr for the ALD process.
5. The ion-gunned sample is transferred to the ALD chamber *in-situ* and Al₂O₃ is deposited at the desired thickness.
6. The sample is then transferred to the sputtering chamber *in-situ* and 65 nm of Cr is deposited on the chip and the final lift-off is performed on the sample.

Using this approach, the connectivity of the first electrode is tested before and after the deposition of the second electrode. As a start, MIMs having oxides with thicknesses of 5 and 8 nm were fabricated through plasma ALD using 49 and 79 cycles, respectively. After the ALD process, the surface of the PMMA was rough and it was concluded that the plasma in the ALD system was the source for this roughness. After the deposition of the second layer and the lift-off process, no problems were observed at the chip surface due to the roughness of the PMMA. However, it was apparent that the first electrode of these devices was not electrically connected. The samples were observed using SEM and no visible disconnection was observed at the junction or along the transmission line. An SEM micrograph of a diode with 5 nm of oxide is shown in Figure 4-5.

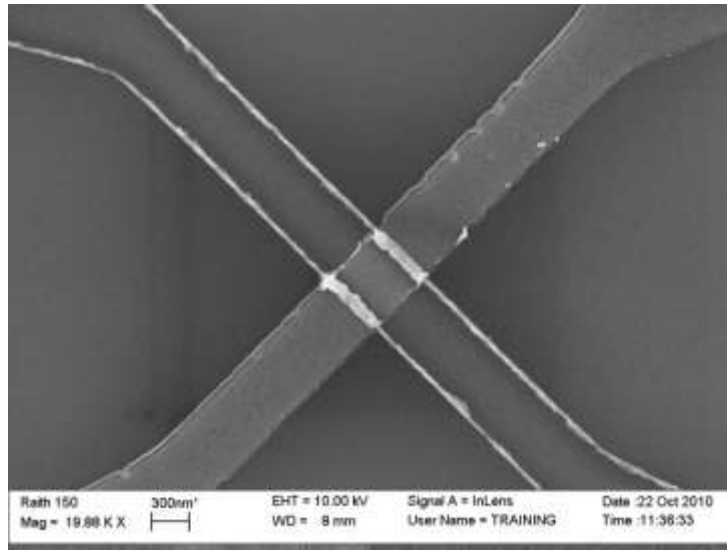


Figure 4-5 SEM image of Cr/Al₂O₃/Cr junction having 5 nm of oxide deposited using plasma ALD. The roughness of the first electrode is clearly visible in the image.

It can be observed that there were no visible cracks or discontinuity on the two electrodes. After observing the junction for the MIM having 8 nm of oxide it was concluded that the plasma presence in the ALD chamber causes the bottom electrode to be severely damaged. Figure 4-6 is the SEM micrograph of the MIM with 8 nm of Al₂O₃.

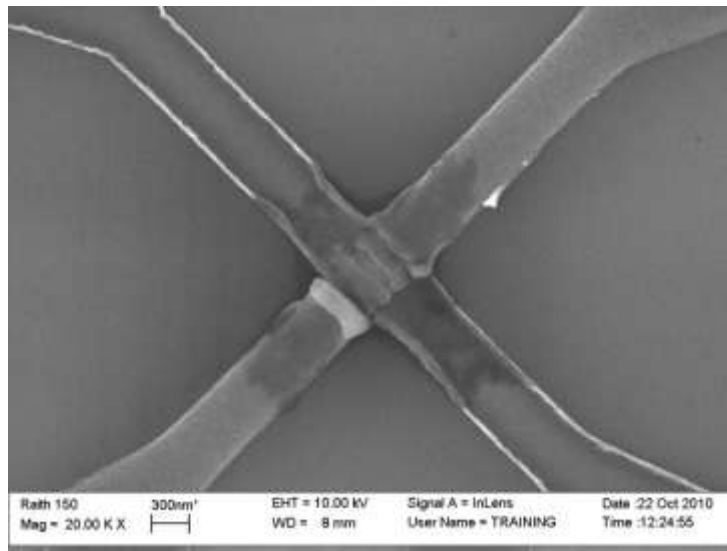


Figure 4-6 SEM image of Cr/Al₂O₃/Cr junction having 8 nm of oxide deposited using plasma ALD.

This deformation of the junction at longer cycles was attributed to the O₂ plasma causing the first electrode to become disconnected due to charging effect. It was then decided to eliminate the plasma in the ALD process and proceed with thermal ALD of Al₂O₃. The thermal ALD was performed on a sample at 150 °C and after the lift-off all the electrodes were shorted to each other due to cracking of the PMMA and deposition of Cr through these cracks onto the substrate. An optical image of this chip is shown in Figure 4-7. It was observed that the edges of the pads have been cracked and the cracks have propagated until they come to a discontinuity. The thermal ALD process was performed on another chip at 100 °C since the plasma ALD was performed at the same temperature and no cracking was observed.

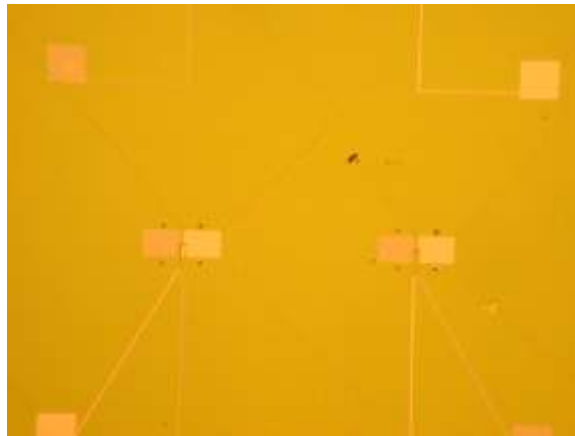


Figure 4-7 Optical image of the chip after 5 nm of Al₂O₃ oxide is deposited by ALD using thermal oxidation at 150°C. The cracks are visible at the corners of the pads.

A sample with 5 nm (84 cycles, 0.9 Å/cycle) of thermal Al₂O₃ was fabricated and tested. Surprisingly, the first electrode was still electrically disconnected. At this point, two hypotheses were investigated to troubleshoot the problem. (1) The heating of the chip to ~180 °C for 1 hour during the prebake of the PMMA coating process required for the second electrode lithography might cause cracking of the electrode at the junction trench. (2) The second electrode might apply significant stress to the bottom electrode causing it to fracture.

To check the heating effect described in (1), a sample having only the first electrode was checked for electrical connectivity and was then heated to ~180 °C for

1 hour. After this baking process, a second electrical connectivity test was performed. It was observed that three out of four diodes on the chip were open circuited. The sample was then exposed to the ion gun for three minutes at 100 eV and then the connectivity was checked again. It was observed that all the electrodes were connected. The open circuits were attributed to the formation of a thick Cr oxide layer when the sample was annealed at ~ 180 °C for 1 hour, which electrically insulated the pads from the probe electrodes. By using ion bombardment this native oxide is removed and electrical connection to the pads is again possible. Therefore, the previously fabricated MIMs were ion gunned and the I-V characteristics were measured again. It was observed that none of the fabricated devices reveal nonlinearity up to 500 mV and the junction resistance is ~ 13 k Ω . Considering that the resistance of each electrode is ~ 10 -12 k Ω , it can be concluded that the junction resistance is higher due to the presence of the oxide at the interface of the overlap between the two electrodes.

The effect of depositing the second electrode as described in (2) was investigated by eliminating the ALD step and depositing the second electrode directly onto the first electrode. The sample was exposed to the ion gun before the deposition of the second 65 nm thick Cr layer. After the lift-off process, the sample underwent a 2 minute ion bombardment process to eliminate the native oxide present on the electrodes. Both arms were electrically connected illustrating that the connectivity of the electrodes are preserved after the deposition of the second electrode. The I-V characteristic of the fabricated devices revealed an ohmic relationship corresponding to a junction resistance of ~ 17 k Ω . Considering that the resistance of each electrode is ~ 6 -12 k Ω , it can be concluded that, once again, the resistance of the junction is higher due to the interface of the overlap between the two electrodes.

For the next stage, the research was focused on improving the fabrication process in the following ways: (1) The current fabrication procedure for the second electrode has resulted in a low yield ($\sim 50\%$) such that modifications to the process flow are necessary and (2) the edge smoothness of the first electrode is still not ideal, even though the damascene lift-off process has been incorporated into the fabrication

procedure. It was concluded that the protrusions present on the edges are not completely covered by the oxide.

4.4.2 Phase two

At the start of this phase, the deposition of the first electrode was altered from sputtering to evaporation. Owing to the directionality of deposition in an evaporation technique, the side coverage is much less compared to the sputtering technique. To test this, while keeping all the fabrication steps the same, the first electrode consisting of 65 nm of Cr was deposited using an electron beam evaporator in the University of Alberta's NanoFab. The MIM junction was inspected using SEM and it is illustrated in Figure 4-8.

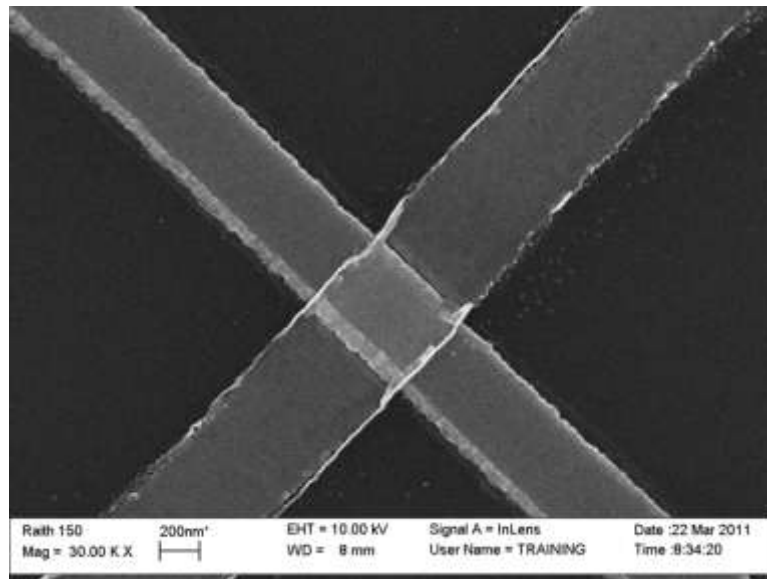


Figure 4-8 SEM image of Cr/Al₂O₃/Cr junction having 3 nm of oxide deposited using ALD. The first Cr electrode was deposited by evaporation technique.

It is illustrated that the rough edges of the first Cr electrode are eliminated using this process. Cr/Al₂O₃/Cr, MIMs having oxide thicknesses of 3 and 6 nm were fabricated using this modified procedure. After testing it was revealed that both devices exhibited an ohmic I-V characterization. This revealed that there must exist

another step in the process that would damage the diode junction. To ensure the ALD procedure for depositing Al_2O_3 is not defective, MIM diodes consisting of HfO_2 were fabricated. Similar, ohmic I-V characteristics were observed for these MIM devices as well. The next fabrication step that was questioned in the process flow of the MIM devices was the ion gun cleaning step.

In parallel experiments, the effect of ion gun cleaning was investigated on fabrication of MIM diodes using the shadow mask technique (Chapter 3). The MIM diodes that underwent an ion gun cleaning procedure prior to the oxide deposition step all possessed an ohmic I-V characteristic. It was concluded that this device failure was correlated to the roughening of the electrode surface via ion bombardment during the cleaning stage. Thus, ion gun cleaning was eliminated from the process flow and further MIM diodes were fabricated for qualifying the modified procedure. For this, MIM diodes having junction area of $120 \text{ nm} \times 120 \text{ nm}$ and $400 \text{ nm} \times 400 \text{ nm}$ were fabricated. After performing the final lift-off process step, the Cr layer deposited for the second electrode was completely lifted off with the resist. This failure in the device fabrication step was associated to the sputtering deposition of the second electrode. Since the step coverage in the sputtering technique is appreciable, it was proposed that the Cr layer deposited on the resist is connected to the Cr layer deposited onto the substrate. Thus, through the lift-off execution, the Cr layer is peeled off as a whole. To test this proposal, the deposition for the second electrode was switched to evaporation. Surprisingly, the second layer electrode was still completely removed as a result of the lift-off step.

The process flow was further modified to overcome the failure in the MIM device fabrication mentioned above.

4.4.3 Phase three

After carefully overviewing the fabrication process, it was realized that depositing the oxide layer using ALD after the deposition of the first electrode is a potential concern in process failure. The process flow has been schematically illustrated in Figure 4-9. Figure 4-9 (a) illustrates a cross-sectional schematic of the

junction where the first Cr electrode has been deposited and the second electrode has been patterned by means of EBL. Other than the junction area, the rest of the chip is coated by the resist layer here, a bilayer of PMMA. Next, through the deposition of the oxide layer by means of ALD, all areas of the chip are covered by the oxide layer (Figure 4-9 (b)).

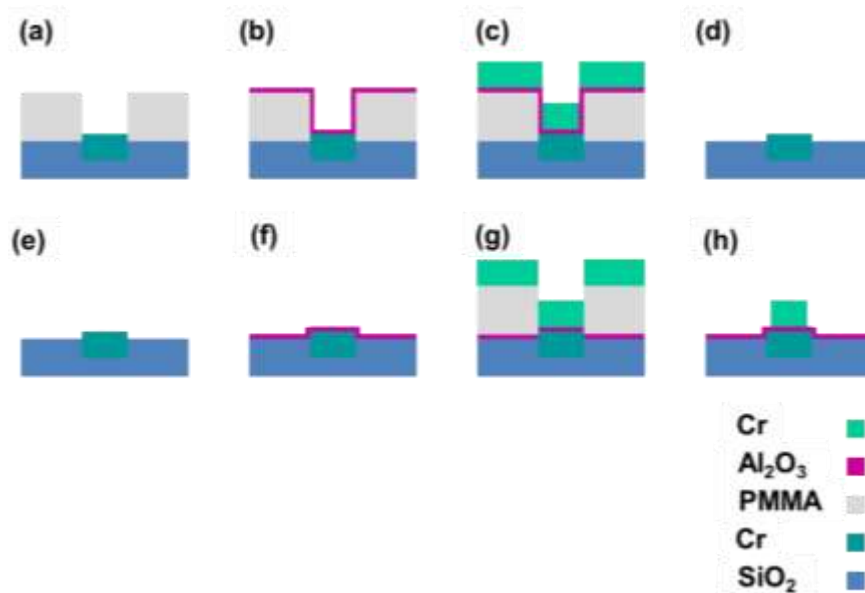


Figure 4-9 Process steps for the fabrication of MIM diodes: (a) first electrode is deposited and the second electrode is patterned; (b) oxide deposition via ALD; (c) metal deposition; (d) lift-off. Revised process flow: (e) first electrode is deposited; (f) oxide deposition via ALD; (g) resist coated, EBL patterned, and material deposition of second electrode; (h) lift-off.

This is associated with the conformal property of the ALD technique. For fabricating the second electrode, Cr is deposited on the chip as shown in Figure 4-9 (c). Finally, the chip undergoes a lift-off process at which the resist layer is stripped for removing excess material other than the patterned area. There is an issue in this step as shown in Figure 4-9 (d). Since the oxide has coated the entire area of the chip, in the course of a lift-off process all the deposited material (oxide and Cr for second electrode) is removed. Thus, this process flow results in a catastrophic failure of device fabrication.

To eliminate this problem, the process flow was further modified in phase three. For this, after the fabrication of the first electrode (Figure 4-9 (e)), the oxide

was deposited by means of ALD with no prior lithography step (Figure 4-9 (f)). In this process, the overall surface of the chip is coated since there is no resist present. Next, the electron beam resist (PMMA) is coated, the second electrode is patterned, and finally, the Cr material for the second electrode is deposited (Figure 4-9 (g)). As the last step, lift-off is performed on the chip and the final MIM junction is obtained (Figure 4-9 (h)).

To validate this process and to finalize the fabrication process flow for the fabrication of MIM devices having an integrated antenna, this modified process was tested on three chips. The diode junction consisted of Cr/Al₂O₃/Cr where the thickness of Al₂O₃ was set to 4 nm for all devices. Chip #1 and chip #2 had junction areas of 400nm × 400 nm and 150nm × 150nm, respectively. SEM images of the fabricated diode junctions are shown in Figure 4-10.

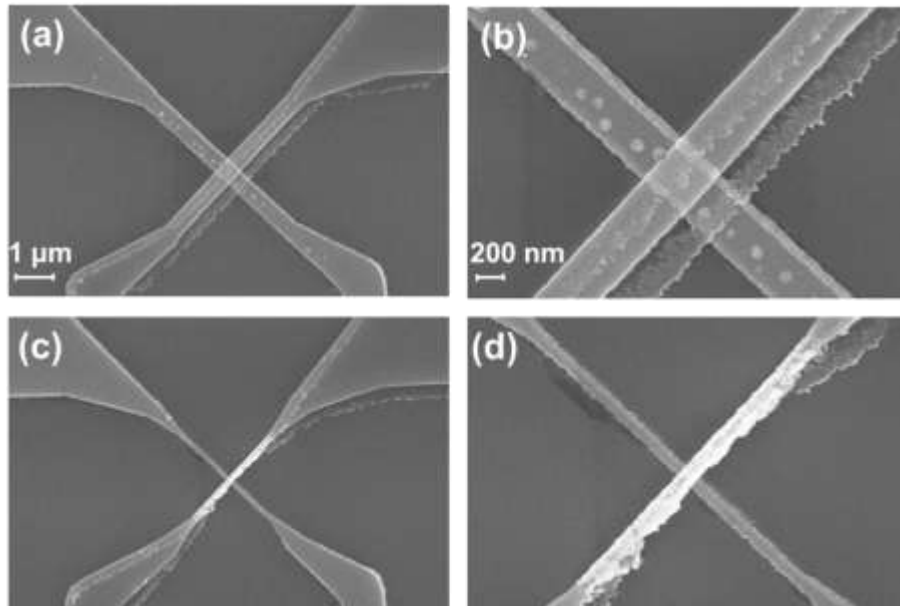


Figure 4-10 SEM images of diode junctions of: (a) chip #1, and (c) chip #2 at 10Kx magnification. Zoomed in (30×10^3 times) SEM images of (b) chip#1, and (d) chip#2.

Figure 4-10 (a, b) illustrates the diode junction having an area of 400 nm × 400 nm at 10 and 30 30×10^3 magnification. Similarly, Figure 4-10 (c, d) depicts the diode junction having an area of 150 nm × 150 nm at 10 and 30 30×10^3 magnifications. From Figure 4-10 (b),(d) it is clear that the first electrode possesses smooth edges.

The roughness observed on the second electrode as shown in Figure 4-10 (d) is not affecting the device as it is the top layer. Interestingly, the grains of Cr formed on the first electrode during the evaporation procedure are clearly visible for the chip #1. These grains seem to disappear when the junction electrode width is reduced (Figure 4-10 (d)). I-V characteristics of these diodes are shown in Figure 4-11.

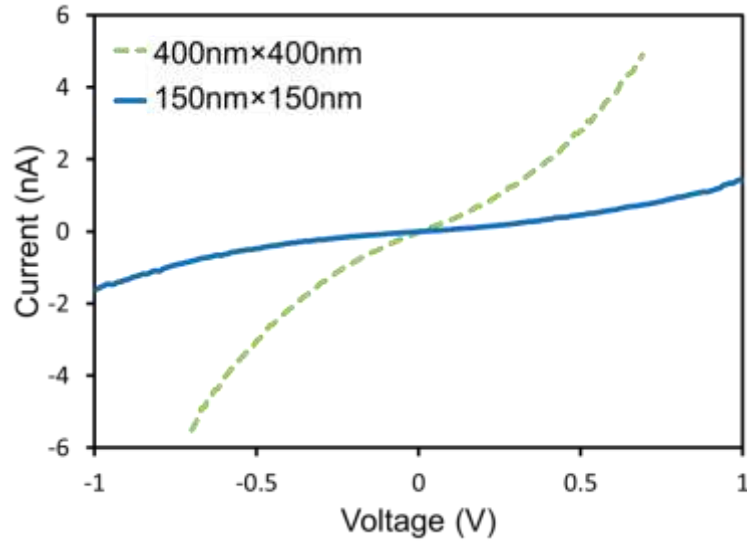


Figure 4-11 Current versus voltage characteristic curves for the Cr/Al₂O₃/Cr devices having junction areas of 400nm×400nm (chip #1) and 150nm×150nm (chip #2).

Since chip#1 possesses a larger junction area the tunneling current resulting from this chip is higher compared to that of chip #2 (~6 times). This is in good agreement with the junction area ratio of chip #1: chip #2 (~7 times). However, due to the operation at low biases, the asymmetry of the I-V curve is ~1.

Finally, the effect of sputter deposition of the two metallic electrodes on the device performance was investigated. For this, chip #3 was fabricated where the diode junction was 400nm × 400nm and the material and thickness of the oxide was similar to chip #1. It was realized that none of the devices were operational. SEM images of the two junctions for chip #3 are illustrated in Figure 4-12.

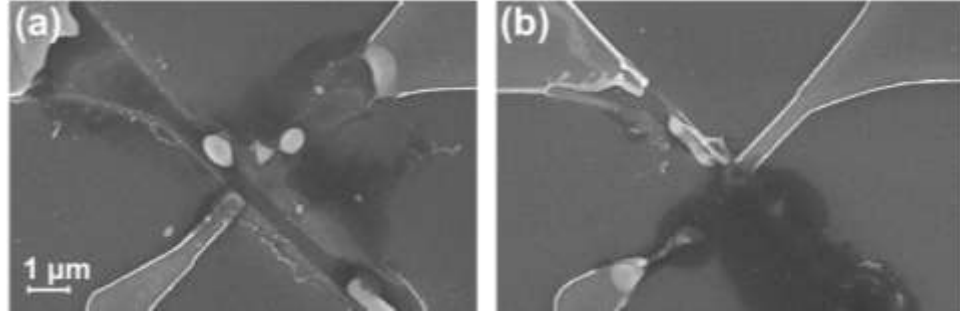


Figure 4-12 SEM image of two devices on chip #3.

When the electrode was deposited via sputtering technique, the diode junction is completely lifted-off. From these findings, the final process recipe for fabrication of the MIM diode having an integrated antenna was obtained.

4.4.4 Final device fabrication and characterization

The final stage of fabricating the electron tunneling THz detectors consisted of having five MIM diodes at the center of a 1 cm × 1cm chip. The MIM diodes having integrated antennas were positioned vertically. While keeping the diode structure the same, *fractal antennas* are incorporated into the detector as the integrated antenna. The overall design pattern is illustrated in Figure 4-13.

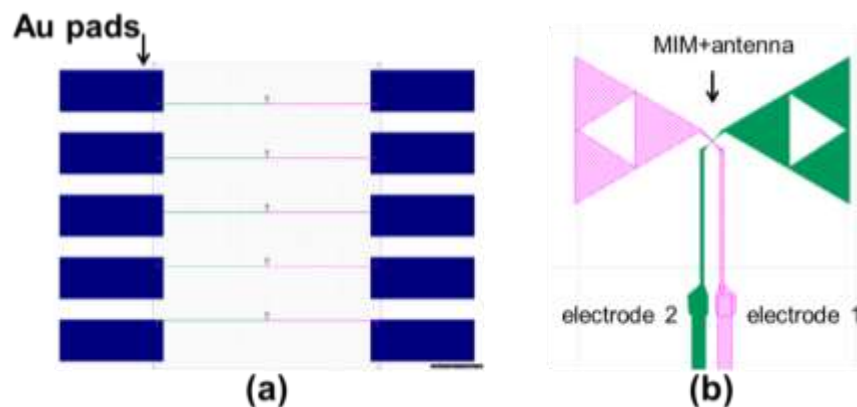


Figure 4-13 Design pattern for the final MIM diodes having integrated antennas. (a) The overall design consists of a 5x1 array of MIMs. (b) Zoomed in image of (a). The junction geometry is identical to that illustrated in section 4.3.1. The design areas in purple and green are electrode 1 and 2 respectively.

To facilitate testing of the devices under THz illumination, large pads made from gold were initially patterned on the SiO₂ substrate. A shadow mask made of aluminum was used for this purpose. Next, the finalized recipe was used to fabricate the first electrode, the oxide, and finally the second electrode. In this design, due to the presence of long transmission lines, the fixed beam moving stage (FBMS) capability of the EBL system was utilized. This is to facilitate problems such as stitching at the boundaries of write fields and minimizing drift in the lithography.

It is noteworthy that due to the exposure of the Cr layer to atmosphere the oxide layer is not purely Al₂O₃ but Cr₂O₃-Al₂O₃. In addition, during the plasma ALD the bottom electrode undergoes further oxidation due to the presence of O₂ plasma. It has been measured, using the ellipsometry technique that the total Cr₂O₃ oxide thickness is ~2nm. For this, the MIM discussed in this section and previous sections all have a Cr₂O₃ layer formed on the first electrode.

Three chips (chip #4, chip #5, and chip #6) were fabricated where each contained 5 detectors. The properties of each diode are summarized in Table 4-1.

Table 4-1 Summary of the properties of the fabricated MIM detectors.

Chip #	Oxide Material	Oxide Thickness (nm)
4	Cr ₂ O ₃ -Al ₂ O ₃ -HfO ₂	5
5	Cr ₂ O ₃ -Al ₂ O ₃	6
6	Cr ₂ O ₃ -Al ₂ O ₃ -HfO ₂	6

A SEM image of chip # 6 is shown in Figure 4-14. In this design a first order Sierpinski fractal is utilized as an integrated antenna for the MIM device. The goal is to have detectors that can detect low THz radiation power and it has been shown in section 2.5 that such fractal antennas are well suited for this purpose.

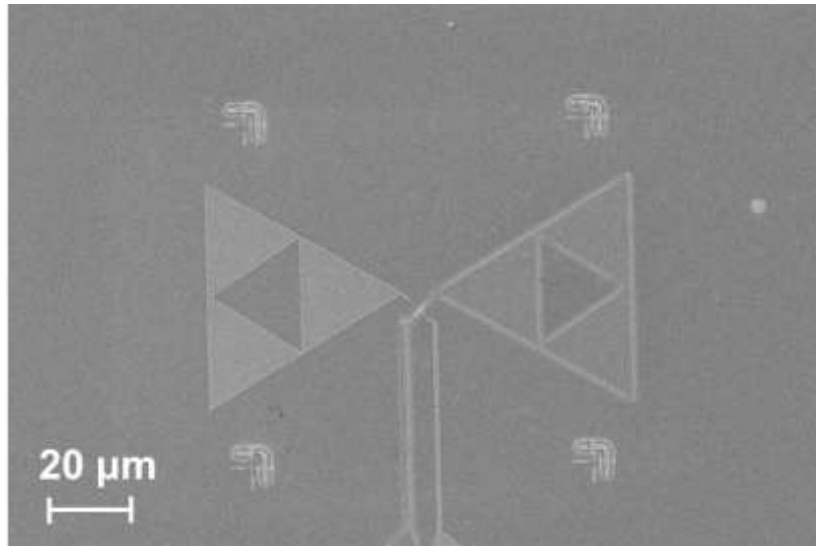


Figure 4-14 SEM image of an MIIM diode having an integrated fractal antenna.

Next, the characteristics of MIMs were characterized by performing I-V measurements on couple of the devices. This was limited to one or two devices in case I-V measurements would affect the junction properties. I-V curves of chip #4 and 5 are illustrated in Figure 4-15.

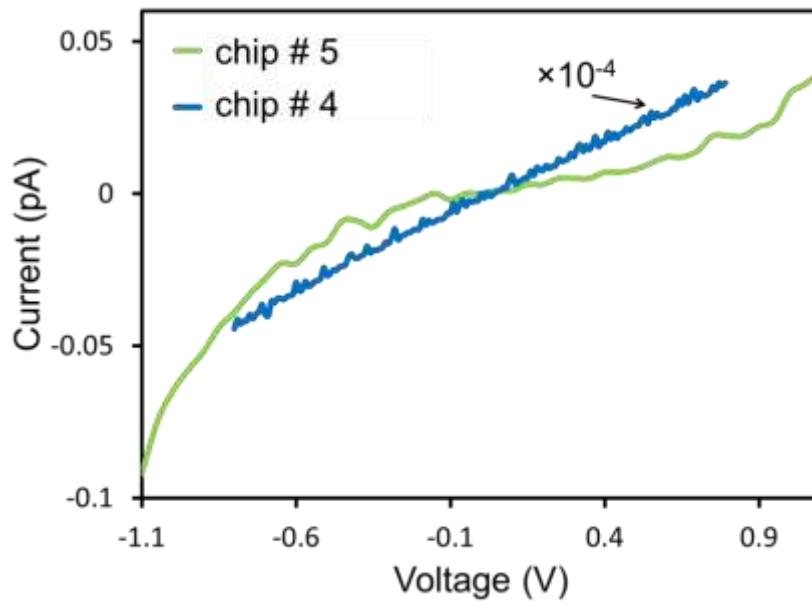


Figure 4-15 Current versus voltage characteristic curves for the chip #5 and chip #4. The curve for chip#4 is multiplied by 10^{-4} .

While chip #5 possesses a nonlinear I-V curve, Chip #4 shows an ohmic contact. This clearly illustrates that the minimum oxide thickness for the MIM to act as a tunnel diode is $\sim 6\text{nm}$. The asymmetry of the I-V curve for the chip #5 is ~ 2 at 1 V. Compared to the value of asymmetry value reported for MIIM devices (section 3.4) this value is not significant. This is because the asymmetry starts to increase at high biasing voltages ($>1\text{V}$). The fabricated devices would fail and undergo device breakdown at high voltages.

4.5 A Novel Nanofabrication Damascene Lift-off Technique

Lift-off is a well-known fabrication technique often used in defining very fine features in either a micro- or nano-fabrication process [115-117]. A lift-off process is an additive process which requires a sacrificial material layer to act as a temporary mask. In this process, after defining the desired pattern - for example, by means of lithography - the target material is deposited on the entire sample surface, which includes the desired structure on top of the substrate as well as on top of the sacrificial layer. Next, by introducing the sample to the sacrificial layer solvent, the deposited materials on this layer are washed away (lifted off) as this layer is dissolved, and the deposited material on the defined structure remains as it is, adhered to the substrate surface.

While the conventional lift-off process is widely used, its yield is low [118] and fabricated fine features of nanoscale structures often exhibit undesirable rough edges (rabbit-ear-shaped or overhangs [119]). There are two main reasons for the failure of the conventional lift-off process. Either the surface of the exposed area of the substrate is/becomes contaminated prior to material deposition, or the deposited material does not strongly adhere to the substrate by virtue of its chemistry and surface conditions. It should be noted that while the former can be caused by resist residuals, which can be eliminated by ashing the resist using oxygen plasma [120], the latter can be overcome by using adhesion layers in some materials such as Cr for Au deposition. Both of these issues, if not eliminated, can result in low adhesion of

the deposited material to the substrate, and thus, failure of the lift-off process. Ultimately, this leads to structure failure with or without the implementation of ultrasonic agitation. Additionally, there is an inherent limitation to the conventional lift-off process which arises when the thickness of the resist film is less than three or four times the thickness of the deposited material. In this situation, the residual material around the desired feature cannot be completely removed by the solvent during the lift-off process. Notably, in extreme cases, the deposited resist film is continuous across the substrate where it can result in complete removal of the desired feature, and potentially a catastrophic failure of the lift-off process. To eliminate this scenario, a thick resist film is usually utilized; however, not without imposing other constraints on the outcome of the process itself. A simple technique to increase the thickness of the resist is to spin the resist at lower round per minute (RPM) during the coating process. Although- simple, not many resists can be coated uniformly at low RPM, which in turn causes further process failures due to the lack of resist uniformity. In addition, by employing a thick resist the resolution of the smallest nanoscale features produced by lithographic processes is significantly compromised during the developing phase of the resist.

In particular, low process yield, process irreproducibility (due to the lack of strong adhesion of the deposited material), and low reliability (i.e., line edge roughness and overhangs) are often experienced when different materials are used within the same process. To improve the outcome of the residual deposition and to accelerate the conventional lift-off process, in certain circumstances it is necessary to agitate the sample in an ultrasonic bath filled with a solvent solution. However, such a procedure can lead to the removal not only of the residual material, but also the fabricated structure, especially when the desired features are very delicate and of nanoscale dimensions [121]. Hence, the lift-off process is often considered to be a trial and error technique, in which optimum process parameters identified with one particular material may not work for another.

In order to overcome these limitations, modifications to the conventional lift-off process have been introduced in fabricating Micro Electro Mechanical Systems (MEMS) devices [122-124]. Damghanian et al. [122], have modified the lift-off

process to overcome the pattern following effect by obtaining a final flat surface in result of the lift-off procedure. Using micrometer thick resist, and by etching the sample prior to material deposition, feature sizes from 20-500 μm have been fabricated using their modified lift-off process. However, not much attention was devoted to eliminate edge roughness. In addition, Wijngaards et al. [123] and Tong et al. [124] have utilized wet-etching in their lift-off process to improve their MEMS fabrication procedure.

While the results from the modified lift-off process were reported as satisfactory for specialized applications, all the results were reported for microfabrication of MEMS, which involves large scale features. Furthermore, performing a lift-off process is more tolerant for such large features, especially when dealing with few micrometer thick resists. In such a case, the edge roughness (which would be on the order of nanometers) is not crucial for the fabricated element and, in fact, not even noticeable to the feature sizes. Finally, the disadvantage of the methods reported in references [123, 124] is that wet-etching cannot be utilized in fabricating nanometer features such as nanofabrication of Nano Electro Mechanical Systems (NEMS) due to the isotropic characteristics of this etching process.

Here, a novel *damascene* lift-off process is described. This technique has been shown to solve the inherent problems associated with the conventional lift-off process mentioned above for fabricating nanoscale as well as microscale devices.

4.5.1 Experimental Details

The samples used for testing the damascene lift-off process were fabricated on a Si wafer that was diced into $1\text{ cm} \times 1\text{ cm}$ chips. A schematic diagram illustrating the fabrication process flow of the lift-off technique is presented in Figure 4-16.

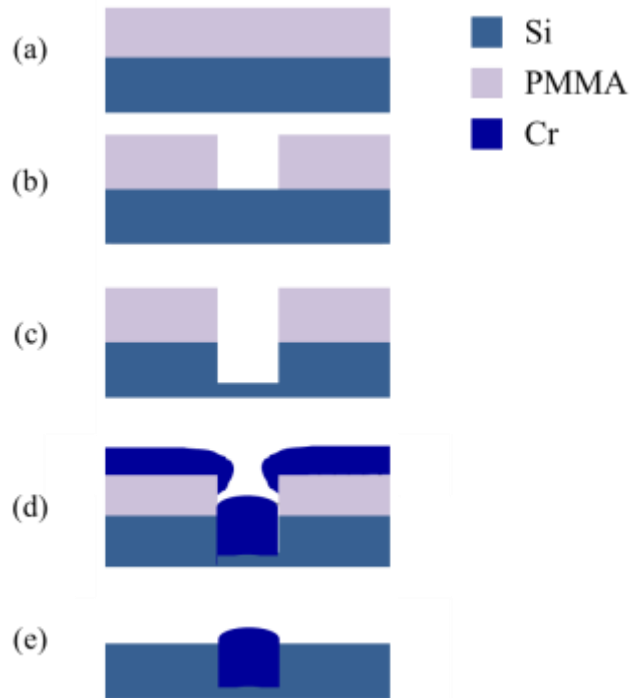


Figure 4-16 Process steps for the damascene lift-off process: (a) surface of the substrate is coated by resist; (b) after pattern transfer and development; (c) etching of pattern; (d) metal deposition; (e) final result after lift-off.

The resist used on these samples is Polymethyl methacrylate A2 (PMMA) (MicroChem). As schematically shown in Figure 4-16(a), the resist is spin coated on sample Si chips using Specialty Coating System Inc (Model P6700 Series). Shortly after pouring the resist (PMMA (A2 495)) on the chip's surface, the resist is spread by spinning the Si chip at 500 rpm for 5 seconds followed by additional spinning at 2000 rpm for 30 seconds. The resist is dehydrated for 25 minutes in ambient conditions by placing it on heating plate held at a constant temperature of 190 °C. Next, a second layer of PMMA (A2 950) is layered onto the sample, using the previous procedure, to form a bi-layer resist. It should be noted that the thickness of the resist must be such that a considerable amount of resist survives the etching process. In addition, the bi-layer PMMA has been shown to result in an undercut profile after resist development. The overall resist thickness using this procedure is 175 nm.

The desired pattern is transferred onto the prepared samples by means of electron beam lithography (EBL). The employed EBL apparatus was a Raith 150 system having an electron beam energy of 10 keV and 20- μm electron aperture. An area dose value of 120 $\mu\text{C}/\text{cm}^2$ is shown to be optimum for patterning $\leq 200\text{-nm}$ feature sizes on the bi-layer resist. After the pattern exposure, the sample is developed for 60 seconds in methyl isobutyl ketone: isopropyl alcohol (MIBK:IPA) (1:3), 20 s in IPA and 20 s in DI water. It is after the completion of this step that the samples having the desired pattern are prepared for testing using the novel damascene lift-off process (this step is schematically shown in Figure 4-16(b)).

The key aspect of the lift-off process is having the patterned feature introduced to an appropriate etching procedure prior to the deposition of the desired material. In this case, Inductively Coupled Plasma Reactive Ion Etching (ICP-RIE) is employed to expose the surface pattern to the chemically reactive plasma. The ICP-RIE etching process was performed using STS MESC Multiplex ICP ASE for 6 seconds. This etching process results in the removal of 53 nm of Si at the patterned features, as schematically shown in Figure 4-16(c). Due to the different chemical reactions of ions with the resist material versus the substrate material, the resist and the substrate are etched at different rates. The ratio, in the present case, of PMMA-to-Si etching rates is $\sim 1:2$. The target materials are deposited onto the sample chip by means of Physical Vapor Deposition (PVD) techniques, such as magnetron sputtering or electron beam evaporation. To demonstrate the capabilities of the damascene lift-off process, we used Cr as a target material. An 80-nm thick Cr film is sputtered on the surface of the sample chip at an Ar gas pressure of 1 mTorr and at a 300 W DC plasma power level (step shown in Figure 4-16(d)). Next, the sample is placed in the resist solvent (acetone) to perform the damascene lift-off process (Figure 4-16(e)). The deposited material is expected to strongly adhere to the substrate, while the excess deposited materials are removed along with the sacrificial layer.

4.5.2 Results and discussions

The application of this nanofabrication process to various structures having different features has resulted in $> 90\%$ yield. A typical Scanning Electron Microscope (SEM) image of a cross-shaped pattern fabricated using the damascene lift-off process is shown in Figure 4-17(a). As illustrated in the process flow diagram, this lift-off technique introduces an etching step *prior* to the material deposition, in contrast to the conventional lift-off process. The role of this etching process is to perform efficient cleaning away of contaminants (such as organic resist residuals) at the patterned areas, prior to material deposition. Since few nanolayers are removed from the substrate surface, an atomically fresh surface is introduced to the deposited material. In addition, the etching step roughens the substrate via ion bombardment [43, 125], thus significantly improving the adhesion of the deposited material to the substrate, and therefore the lift-off yield. It should be noted that in the damascene lift-off process the removal of the material takes only 2-3 minutes and requires no ultrasonic solvent agitation. For comparison, the conventional lift-off process was performed on the same material system (Cr, PMMA, Si) and it took 1-2 hours accompanied by ultrasonic agitation.

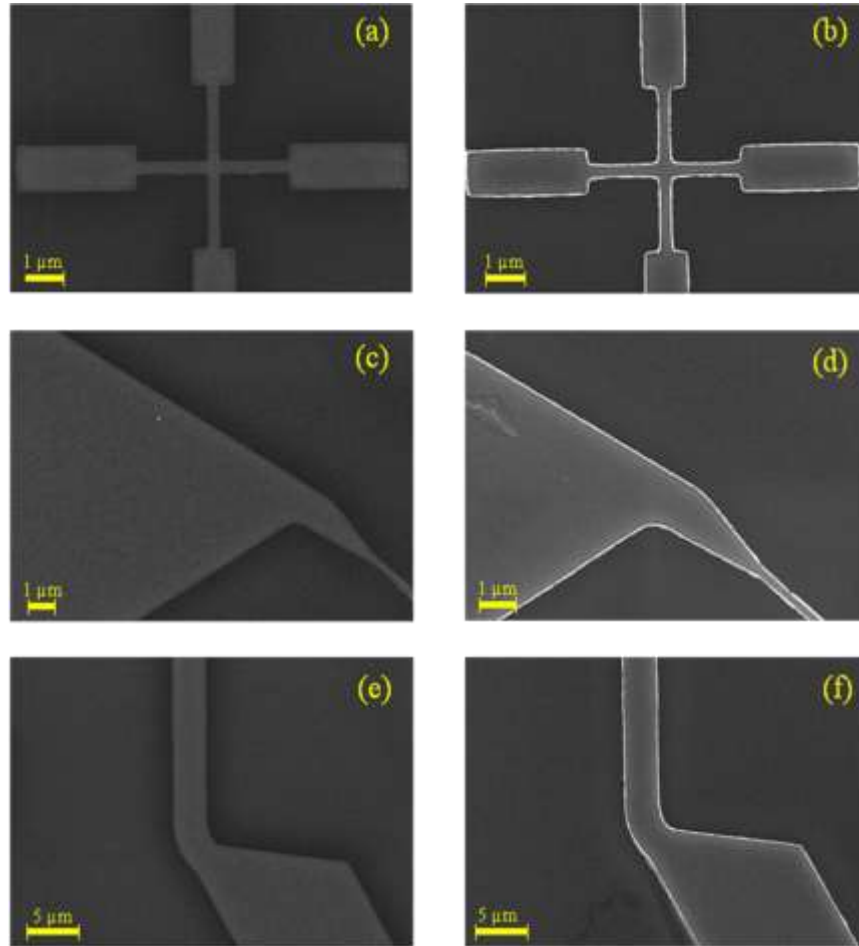


Figure 4-17 SEM images of various features resulting from the damascene lift-off process (a), (c) and (e). The same features fabricated using a conventional lift-off process are shown in panels (b), (d) and (f). Note that the conventional lift-off process results in rougher edges as indicated by the bright borders around the perimeter of the structures.

Furthermore, unlike the conventional lift-off process, it is important to realize that the elimination of the ultrasonic agitation is essential, as this is the reason that the damascene lift-off process preserves delicate nanoscale features.

Apart from the improved adhesion and very high process yield, fabrication of nanoscale structures via the damascene lift-off process results in features having minimal line edge roughness. To quantify this important advantage, edges from features fabricated via the conventional lift-off process are compared to those fabricated using the damascene lift-off process, for different feature shapes and sizes. It should be noted that for fabricating the sample using the conventional lift-off process, samples having the same resist as the one discussed above were used and the

same amount of Cr was deposited on the sample (the fabricate samples had 80 nm of Cr lying on the substrate). As shown in Figure 4-17, features abruptly varying in dimensions from 10 μm down to 200 nm are easily achieved. The choice of this large-to-small transition is used to testify to the quality of the fabricated structures under the same processing conditions.

It is evident that the structures fabricated via the damascene lift-off process without ultrasonic agitation exhibit superior feature quality. In particular, the edges of the fabricated features are significantly smoother over all dimensions, as shown in the zoomed-in SEM images of cross-shaped features in Figure 4-18.

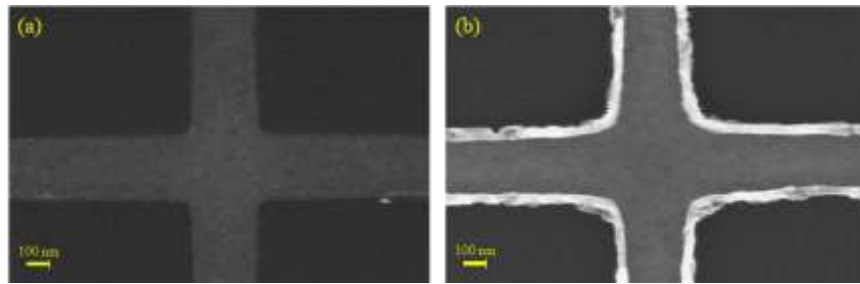


Figure 4-18 Zoomed-in SEM images of the same features resulting from: (a) damascene lift-off process and (b) conventional lift-off process. It is clearly visible that the edges of the deposited Cr are much smoother in comparison to the conventional lift-off process when the damascene lift-off process is utilized.

To further quantify the differences in line edge roughness resulting from the conventional lift-off process compared to this innovative process, topographic images of the samples were acquired using Atomic Force Microscopy (AFM) as shown in Figure 4-19. Figure 4-19 (a,c,e) are images obtained at various magnification levels of the cross-shaped feature resulting from the conventional lift-off process. Figure 4-19 (c, e) are zoomed-in AFM images of the top arm of the cross. It can be observed that the edges of the features resulting from this process are very rough compared to the features typical of the damascene lift-off process (i.e., Figure 4-19 (b,d,f)). It is worth noting that this scenario is true for features ranging from the microscale to the nanoscale.

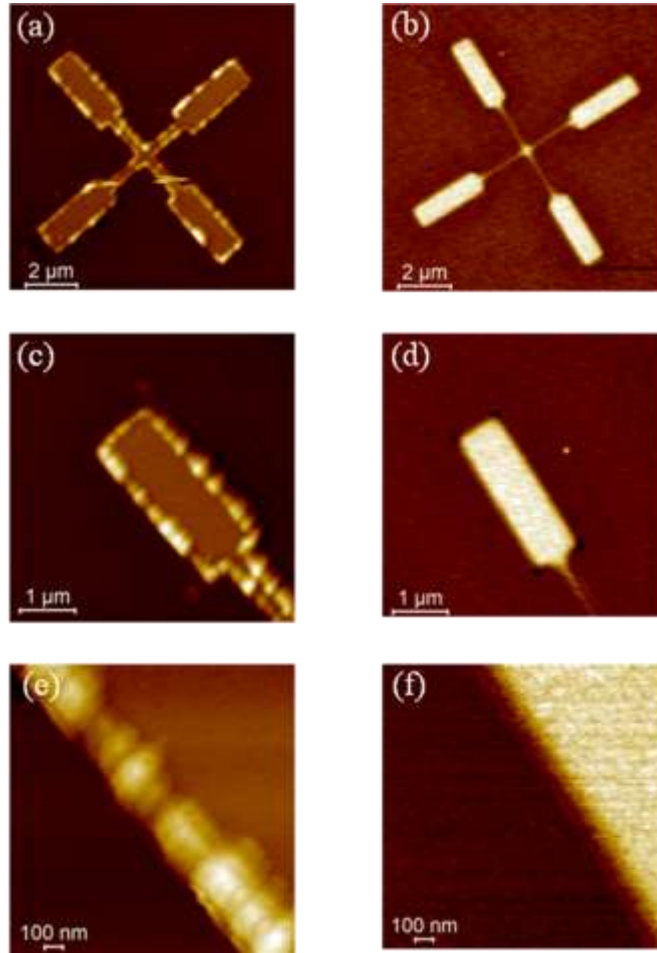


Figure 4-19 AFM images of the cross-shaped feature (a,b). Sequentially zooming in on the top arm (c,d & e,f). Results of the conventional lift-off process are shown in (a), (c) and (e). The same feature fabricated using the innovative lift-off process is shown in panels (b), (d) and (f).

Cross-sectional graphs of the steps shown in Figure 4-19 (e,f) were acquired, and are presented in Figure 4-20. Several topographic cross-sections, spaced out along the edge, are shown (displaying 3 line scans for the damascene process and 4 line scans for the conventional lift-off process). Remarkably, from the plateau present on the top level (feature height) in the topographic line scan shown in Figure 4-20 (a) it is evident that there is no protrusion present on the feature edges resulting from the damascene lift-off process. On the contrary, the line scans in Figure 4-20 (b) clearly show there is significant edge roughness resulting from the conventional lift-off process. The vertical roughness observed at the edges of the features (protrusions) in Figure 4-20 (b) vary from 15 nm (line 2) to 100 nm (line 4) above the feature height.

The other undesirable property of such protrusions on the edges is that their width varies along the lateral length of the boundary from 300 nm (line 2) to 500 nm (line 4). Such edge protrusions are problematic in the fabrication of multilayer devices, since they can cause undesirable multi-layer connections.

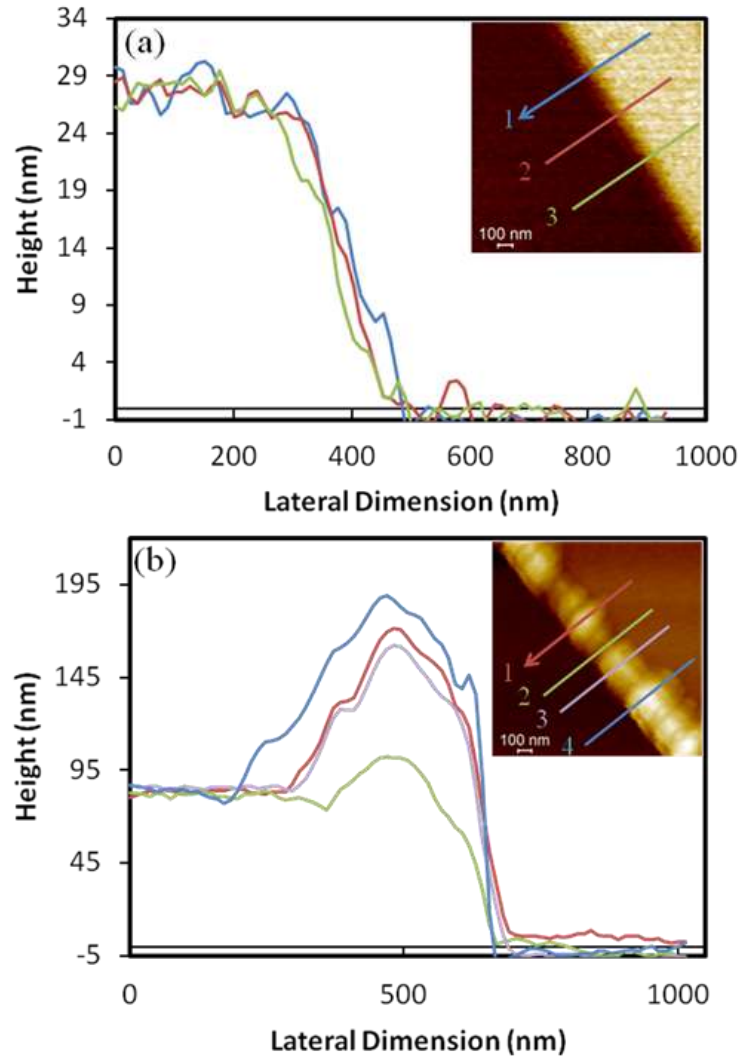


Figure 4-20 Cross-sectional topographic representation of the edges obtained from: (a) the damascene lift-off process, showing three cross-sections, and (b) the conventional lift-off process, showing four cross-sections, at different locations along the edge. The lines in the inset image show the location and direction of the cross-section on the edge.

The improvements that the damascene lift-off process provides over the standard lift-off process can be explained by considering the effect of etching on the

whole process. When the thickness of the resist film is less than three or four times the thickness of the deposited material, the edges of the deposited material inside the features' vias have a weak mechanical connection to the rest of the deposited material on the top layer, as illustrated in Figure 4-21(a). Hence, when the sample is placed in the resist solvent, due to removal of the resist, the deposited material on the top layer (resist) is mechanically torn from the material deposited in the feature vias, thus resulting in roughening on the edges, as shown in Figure 4-21(c). To eliminate this problem, the standard approach is to increase the resist thickness in order to reduce the degree of connectivity of the material deposited within the via with the top layer. By introducing the substrate to etching prior to the deposition of the material, the ratio of the resist thickness to that of the exposed deposited material is increased. To clarify this, the above-mentioned mechanism is schematically illustrated in Figure 4-21.

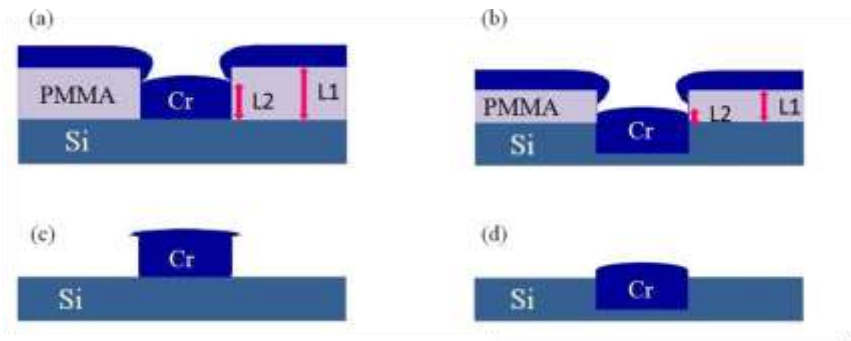


Figure 4-21 Schematic representation for: (a) the conventional lift-off process after metal deposition, (b) the damascene lift-off process after metal deposition, (c) conventional process after lift-off, and (d) damascene process after lift-off. L1 is the thickness of the resist and L2 is the thickness of the exposed material in contact with the resist.

Evidently, by etching the substrate a significant portion of the deposited material is embedded within the substrate (Figure 4-21(b) and 6(d)). For this reason, the amount of deposited material in contact with the resist walls (L2) is much less in comparison to the conventional lift-off process. In the fabrication process used to make the sample shown in Figure 4-19, the ratio $L2/L1$ (where L1 is the resist thickness and L2 is the thickness of the deposited material in contact with the resist

walls), is 3 for the damascene process and 9 for the conventional process. Therefore, in this novel lift-off process, deposited material in the feature area is far more easily separated from excess material deposited on the resist layer, which results in elimination of edge roughness. To quantify the process yield, this process was performed on 100 chips each containing six structures, which results in a total of 600 structures. Utilizing the same fabrication process, 550 structures were successfully fabricated. It should be pointed out that by utilizing this technique, it becomes feasible to deposit thicker amount of materials with minimal resist thickness, while obtaining more reliable and reproducible features at a fabrication yield significantly greater than 90%.

As shown, the deposited materials can be partially or completely inlaid in the substrate using this technique. This reduction in topography has the advantage that further fabrication steps such as deposition can be performed at higher yield, since feature steps are more uniformly coated at low compared to high topographies. For this reason, the process is well suited for fabricating multi-level structures. The innovative technique presented in this paper is stress-free and is capable of producing nanostructures with high yield.

4.6 Summary

In this chapter, the design parameters for a MIM diode having an integrated antenna utilized as a THz detector have been investigated. The fabrication flow for obtaining an operational detector has been comprehensively explained. This involved three phases of modifications to the initially proposed process. Through SEM inspection and I-V characterization of the fabricated devices the fabrication process flow was validated.

Finally, a proposed modified lift-off technique required for the fabrication of the detectors is demonstrated. This innovative damascene lift-off process results in high yield and high reproducibility process.

5. CHAPTER 5⁴

THz spectroscopy for characterization and imaging

5.1 Introduction

THz spectroscopy has gained a lot of attention in the field of imaging, spectroscopy, and sensing during the past few years. The main advantage of THz spectroscopy is the capability of being able to directly measure the transient electric field of the THz radiation rather than only its intensity (like Fourier-transform infrared spectroscopy, for example). This is advantageous because the amplitude and phase of each spectral component contained in the pulse can be directly determined, which eliminates the need for complicated mathematical analysis.

The goal of this chapter is to research the capabilities of THz spectroscopy for characterizing and studying the time dynamic of devices and complicated systems. To accomplish these tasks, a versatile optical setup for all-THz time resolved pump-probe spectroscopy was designed and tested. This THz setup will be used to potentially characterize the temporal and spectral response of the fabricated antenna coupled MIIM, and MIIIM diodes. For this, the optical system was first put into test to study the spectral response of THz particle plasmons. The THz particle plasmons were chosen as a test system since its underlying physics are well studied by our research group. Through a comprehensive time resolved studied, (1) the capabilities of the constructed THz pump-THz probe system was investigated; (2) the time dynamics of the induced surface charges was examined. This research was of great value since it revealed the interaction and effect of induced surface charges on the propagation of THz radiation.

⁴ This work has been published by P. Maraghechi et al. in, *Optics Express*, **17** (19), 2009, *Optics Express*, **17** (2), 2009, and *Review of Scientific Instruments*, **83**, 2012.

This knowledge can be further applied in application of THz in characterizing composite media consisting metallic media as well as imaging inside metallic media. As the next step, the THz-TDS was utilized for comprehensive characterization of complex media such as composite materials. For pushing the imaging capabilities of THz-TDS to the next step, terahertz radiation is required to be utilized in imaging not only dielectric materials but also composite materials. The knowledge gained through this series of experiments, was applied in utilizing THz-TDS for imaging dielectric objects embedded inside metallic media. This advancement of THz-TDS was successfully accomplished. It is important to note that these experiments are for justifying the concept of THz imaging inside complex materials. Super resolution image process has been also incorporated into the THz-TDS imaging to further increase the resolution of the acquired images. It is envisioned that through the utilization of the fractal THz emitters (Chapter 2) and the THz detectors (Chapter 4) fabricated in the course of this thesis, more sensitive and higher speed THz imaging systems (having higher SNR) are realized.

This chapter is outlined as follows: The first section introduces a versatile optical setup for all-terahertz (THz) time resolved pump-probe spectroscopy. The setup is utilized for studying the time dynamics of THz particle plasmons. In the second section, using the new THz spectroscopy system, the time dynamics of THz particle plasmons are thoroughly investigated. The third section is devoted to characterizing a material composite consisting of randomly oriented elements governed by non-resonant interactions using conventional THz-TDS. By exploiting near-field plasmonic interactions in a dense ensemble of subwavelength-sized dielectric and metallic particles, it is revealed that the group refractive index of the composite can be increased to be larger than the effective refractive indices of the constituent metallic and dielectric *parent* composites. Finally, the application of THz plasmonics in imaging dielectric objects embedded in metal-filled media is investigated using conventional THz-TDS. By exploiting the time-domain information from the transmitted pulse, signatures of embedded objects are observed.

5.2 All THz pump, THz probe characterization setup

Conventional ultrafast time-resolved spectroscopy techniques employ temporally-delayed ultrashort light pulses, referred to as pump or probe pulses, to sweep the ultrashort time interval of interest [126]. For an experiment in the optical regime, a single ultrashort seed pulse, generated from an ultrafast laser source, is split into two pulses (or more for specialized experiments) via passive optical components (e.g. reflection, polarizing, fiber, lamellar mirrors, and grating type beam splitters). These pulses are referred to as the pump and probe pulses. As the pump and probe pulses follow different optical paths, one pulse is directed along a variable path length to vary the relative timing between the two pulses. The pump pulse, which is typically the more intense pulse, is used to initiate the time-dependent phenomenon on a sample. The spatial extent of the ultrafast event is then probed, at a predefined temporal delay, by a much weaker probe pulse. Thus, the instantaneous response of the physical phenomenon can be detected at a particular temporal delay. By repeatedly probing the excited location at different time delays and recording the probe pulse response, the underlying time-resolved dynamics in a sample can be mapped out as a function of the time delay between the pump and probe pulses [127]. A fraction of a femtosecond time resolution is easily achieved as it is limited only by the duration of the optical seed pulse and the degree of the spatial overlap between the pump and probe pulses.

Similarly, in optical pump, terahertz (THz) probe or THz pump, THz probe time-resolved spectroscopy, the intense optical or THz radiation pulse serves to disturb the sample to create the ultrafast event and a synchronically-generated THz radiation pulse is directed and focused on the same spot probing the phenomenon of interest [128, 129]. Precise time delays can be produced with optical path length differences between the pump and probe pulses, thus enabling high precision time-resolved investigation of temporal response at THz frequencies.

A common method of producing two synchronized THz radiation pulses is by dividing a single THz radiation pulse by the use of a reflective dielectric beam splitter [130]. However, for THz-pump, THz-probe time-domain spectroscopy (THz-

PP-TDS), such an implementation is cumbersome, as it often requires positioning the beam splitter in the collimated and expanded portion of the THz beam [131]. This in turn necessitates the use of large diameter beam splitters (usually a few inches in diameter), to divide and superimpose the THz radiation pump and probe pulses, and exceedingly larger reflective optics to ensure complete interception of the THz radiation. Another disadvantage in using a beam splitter for such an experimental configuration, especially for co-linear arrangements, is the fact that 50% of the THz radiation intensity is removed and not utilized in the experiment. This arises due to secondary transmissions through the beam splitter since the THz pump and probe pulses are recombined. The loss of half of the THz radiation intensities can be detrimental especially when the seed THz radiation pulse intensity is very weak to start. Other limitations imposed in using THz beam splitters for THz-PP-TDS experiments are: the lack of the ability to precisely adjust the splitting ratio between the THz radiation pump and probe pulses as such requires the use of a different beam splitter for each ratio, lack of low loss ultrawide bandwidth THz radiation beam splitters [132], and THz radiation interference effects within the beam splitter especially for ultrashort THz radiation pulses where multiple reflections occur at the dielectric-air interfaces within the beam splitter. Initially, a THz pump probe setup employing a beam splitter was constructed and tested. The schematic of this setup is shown in Figure 5-1.

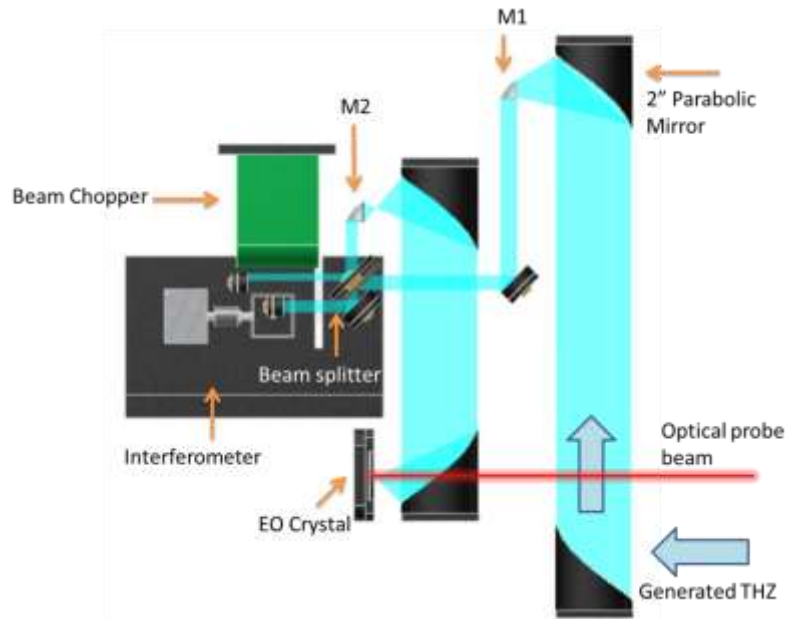


Figure 5-1 First THz pump-probe setup that was operated by splitting the THz radiation pulses.

Here, the THz beam is sent to a 45 degree mirror by means of a 0.5" diameter and 0.5" focal length parabolic mirror (M1) placed in front of the 2" diameter and 2" focal length parabolic mirror. The 45 degree flat mirror directs the THz radiation to the interferometer where, by means of a beam splitter, the THz pulse is split into two pulses and one pulse is delayed with respect to the other. Both THz pulses are made to pass through a mechanical chopper and are spaced such that they pass through the two different slits (inner and outer) of the chopping wheel. In this design the two THz pulse trains are chopped at different frequencies of f_1 and f_2 . By doing this, one can use the f_1-f_2 (i.e. difference frequency) as the reference frequency for the lock-in detection since the detected signal occurs at this frequency only when both beams are present. Since the THz radiation is not visible to the eye, a collinear beam from a HeNe laser was used to help align the THz optical components. To check the presence of THz at the focus of the last parabolic mirror, a femtosecond probe pulse was sent through the back of the parabolic mirror and an EO crystal is placed at its focus. Unfortunately, due to the inability of precise optical alignment and the significant (1/4) THz radiation power lost due to the presence of the beam splitter and

the small parabolic mirrors, no THz signal was detected using this setup. This THz pump-probe setup was soon decommissioned.

In the following section, we demonstrate a versatile THz-TDS system that can be configured for either a traditional THz-TDS or a THz-PP-TDS arrangement. The setup overcomes the abovementioned inherent constraints and limitations in traditional THz-PP-TDS systems.

5.2.1 Setup design

In all pump-probe type experiments, a crucial factor is precise synchronization between the pump and probe pulses. Thus, our THz-PP-TDS design setup takes advantage of the THz generation process from the PC emitters. The basic principle behind the THz-PP-TDS is as follows. Since the PC THz radiation pulse generation mechanism is sensitive to the shape of the envelope, not phase, of the excitation optical pulse, synchronized THz radiation pulses can be generated from identical optical pulses which are phase-locked and accurately timed. That is, if two identical PC emitters are placed in very close proximity to each other (i.e. at the collection point of the THz-PP-TDS setup as shown in Figure 5-2(a)), and are excited by two femtosecond optical pulses (i.e. optical pump 1 and optical pump 2) driven from the same femtosecond laser pulse source, two synchronously phase-locked and amplitude stable THz radiation pulses can be generated. In this situation, one of the THz radiation pulses serves as a pump pulse and the other serves as a probe pulse. By varying the time delay between the two femtosecond optical pump pulses (t_{d2}), the two THz radiation pulses follow the same relative time delay. Thus, for the THz-PP-TDS experiments, instead of scanning the time delay between the pump and probe THz radiation pulses, one can simply delay the femtosecond optical pump pulses exciting the PC emitters and achieve a precise time-resolved response from the THz radiation probe pulse. Clearly, such a design eliminates the use of an optical beam splitter and the cumbersome THz optics often required to redirect the THz radiation pulses. Furthermore, precise control of the relative electric magnitudes of the THz pump and probe pulses can be simply achieved by either independently varying the

bias voltage on the PC THz emitters or by changing the amount of optical energy fluence exciting the PC THz radiation emitters.

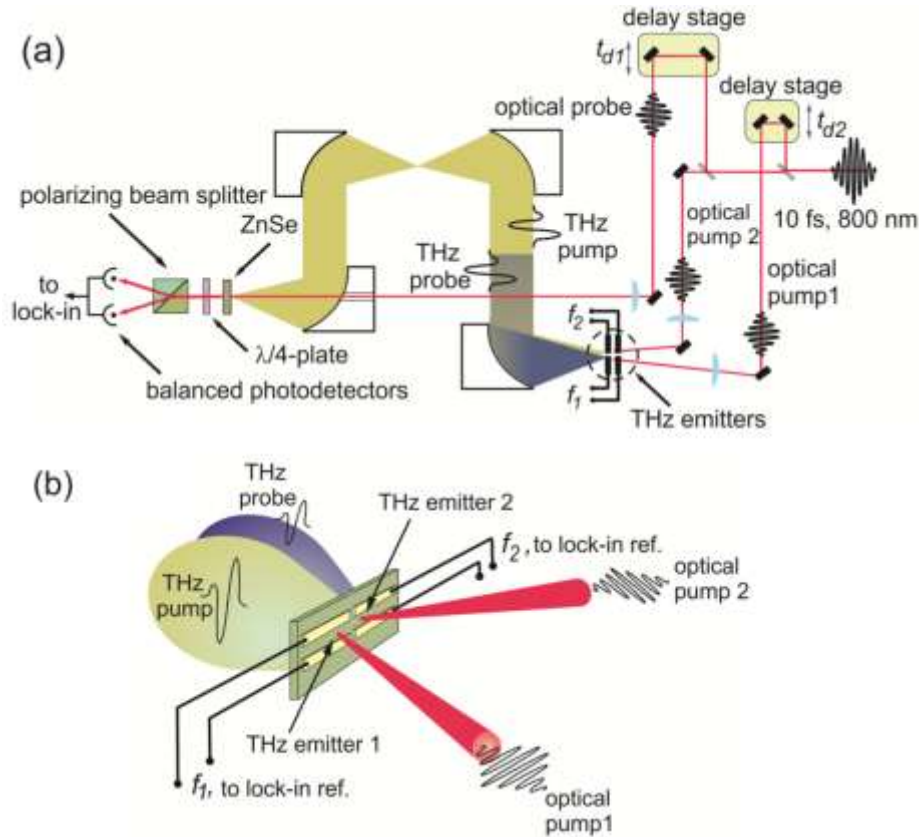


Figure 5-2 (a) Schematic of the THz-PP-TDS system. The 10 fs, 800 nm laser pulse train is split into three pulse trains: An optical probe (20 mW), an optical pump 1(60 mW, generating THz pump pulse) and an optical pump 2 (30 mW, generating THz probe pulse). The THz-PP-TDS system consists of four 90° off-axis gold-coated parabolic mirrors, two PC THz emitters, and an electro-optic sampling setup. The generated THz radiation pump pulse and THz radiation probe pulse were collected and co-linearly focused along with the optical probe pulse onto a 500 μm thick <111> ZnSe electro-optic crystal. The THz radiation-induced polarization modulation of the optical probe was extracted via a balanced detection arrangement, and lock-in detection was carried out at the bias voltage modulation frequency. (b) Schematic of the THz emitters. The two PC THz emitters were placed near each other at a separation of 200 μm. The bias voltages of the PC THz emitters 1 and 2 were modulated at frequencies f_1 and f_2 , respectively. Through phase-locking at the modulation frequency of the biasing voltage, this configuration allows locking at and detecting the THz radiation due to the THz pump signal, or the THz probe signal, or both.

Central to the implementation of this THz-PP-TDS design is the ability to independently address the two PC THz emitters. However, having the two PC THz emitters integrated on a common semiconductor substrate and being placed in very

close proximity to each other, results in a non-linear coupling between the PC transient currents. In this situation, the two PC THz emitters' response can strongly couple due to photogeneration and diffusion of carriers in the semiconductor substrate. To eliminate current cross-talk and improve the THz radiation pulses' amplitude stability, the two PC THz emitters must be both spatially and electrically isolated from each other.

The THz-PP-TDS system presented here consists of two identical and independent PC THz emitters. Each PC THz emitter is a 2 mm long coplanar transmission line type consisting of two 10 μm wide transmission lines and a 70 μm gap. The emitters were fabricated by means of photolithography on a 500 μm thick semiconductor (100) GaAs substrate having a resistivity of $2.5 \times 10^7 \Omega \text{ cm}$. Thin layers (20nm/100nm) of Cr/Au were sputtered and the coplanar transmission line metallic pattern was transferred to the substrate via a lift-off process. A schematic of the two PC THz emitters' configuration is illustrated in Figure 5-2 (b). While the two PC THz emitters were fabricated on the same semiconductor substrate, they are physically and electrically isolated from each other as shown in Figure 5-2 (b). This is accomplished by cleaving each PC THz emitter chip and placing them in close proximity of each other (to within 200 μm). This arrangement guarantees that no transient current flows between the two PC THz emitters. Each PC THz emitter was biased independently via a 20 Vpp sinusoidal voltage waveform delivered from a waveform synthesizer. To eliminate the relative electrical waveform drift between PC THz emitters, the two waveforms' frequencies (f_1 and f_2) were phase-locked to each other.

Depicted in Figure 1(a) is the THz-PP-TDS system consisting of a four 90° off-axis gold-coated parabolic mirror arrangement each of 2.5 cm focal length. The PC THz emitters were illuminated by Ti:sapphire laser pulses having durations of 20 fs, a central wavelength of 800 nm and a repetition rate of 80 MHz. For generating the THz radiation pump and the THz radiation probe pulses, and for probing the time-resolved electric fields, the 110 mW pulse train from the femtosecond laser was split into three pulse trains. A 20 mW pulse train was used to probe the THz pulses (referred to as an optical probe pulse train) and the other two (30 mW and 60mW) were used to generate the THz radiation pump and probe pulses. The angle between

these two optical pulse trains was set to 20° . To provide the temporal sampling scan of the THz pump pulse, the 60 mW optical pulse laser train was made to traverse a 15 fs resolution optical delay line driven by a stepper motor. Both the 30 mW and the 60 mW laser pulse trains were focused by two 5cm focal length lenses to spot sizes of 10 μm each between the co-planar transmission line arms.

To perform the electro-optic sampling of the THz radiation electric fields, the generated THz radiation pump pulse and THz radiation probe pulse were collected and co-linearly focused along with the optical probe pulse onto a 500 μm thick $\langle 111 \rangle$ ZnSe electro-optic crystal [26, 27]. The THz radiation-induced polarization modulation of the optical probe was extracted via a balanced detection arrangement, and lock-in detection was carried out at the bias voltage modulation frequency. Through phase-locking at the modulation frequency of the biasing voltage, this configuration allows locking at and detecting the THz radiation due to the THz pump signal, or the THz probe signal, or both. Complete information on the time-domain THz electric field amplitude and its phase were obtained by means of this setup.

5.2.2 Results and discussions

Typical electric fields from the THz radiation pump and probe pulses generated and detected by the abovementioned system are presented in Figure 5-3. Clearly, the presence of the electro-optic signature indicates that there is a good degree of spatial overlap between the two pulses and the femtosecond optical probe pulse. Here, the modulating frequencies of bias voltages applied to both PC THz emitters were set to 81 KHz and the delay between the THz radiation pump and the THz radiation probe pulses was fixed at 5.5 ps. For the purpose of performing THz-PP-TDS experiments, the energy fluence of the femtosecond optical laser pulse train illuminating the two THz PC emitters was set so that the ratio of the electric fields between the two THz radiation pulses is 3:1. This ratio could be varied to any desired value by varying the energy fluence illuminating the emitters or by varying

the biasing voltage applied to the emitters. In this THz-PP-TDS system, THz radiation field ratios of 1:1 down to 10:1 have been achieved.

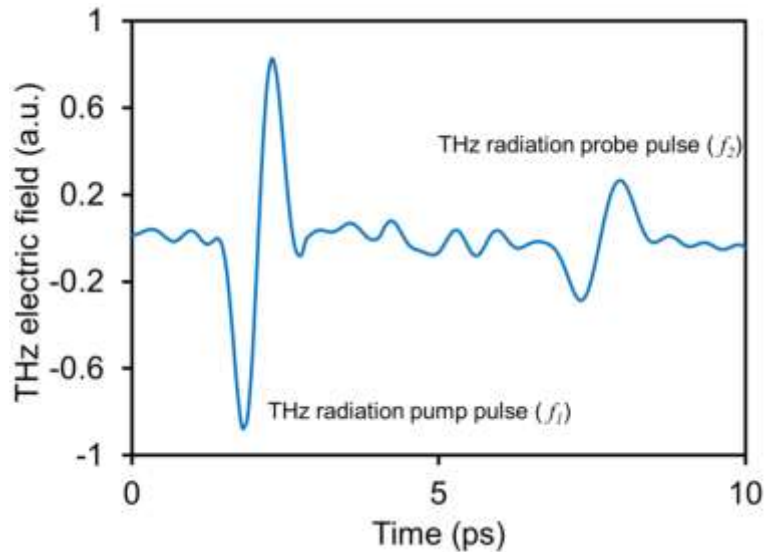


Figure 5-3 Electric fields of the THz radiation pump and probe pulses as generated and detected by the abovementioned THz-PP-TDS system. The THz probe pulse is delayed by 5.5 ps with respect to the THz pump pulse. The modulating frequencies (f_1 and f_2) of bias voltages applied to both PC THz emitters were set to 81 KHz. The ratio of the THz pump to THz probe was set to 3:1 in this experiment.

Since the two PC THz emitters were separated by $\sim 200 \mu\text{m}$, a major concern was the degree of spatial overlap between the THz radiation pulse and probe pulse. Using the knife edge technique, both THz radiation pulse spatial profiles were characterized at the focal plane located between the two parabolic mirrors. Here, the edge of a sharp blade was scanned vertically and horizontally, at a $50 \mu\text{m}$ resolution and the transmitted THz radiation fields were measured as a function of the spatial translations. Using this technique, the spot sizes of both the THz radiation pump and probe pulses were mapped out. As shown in Figure 5-4 (a,b), the overall full width at half maximum (FWHM) spatial extent of the THz radiation focal region was found to be $510 \mu\text{m}$ and $740 \mu\text{m}$ along the x - and y -directions, respectively. Clearly, the spot size was slightly asymmetric due to the lateral displacement of the PC THz emitters. In the x -direction, both the THz radiation pump spot and the THz radiation probe spot

were overlapped, whereas along the y -direction, the centers of the focal spots were displaced by $200\ \mu\text{m}$ with a 90% overlap.

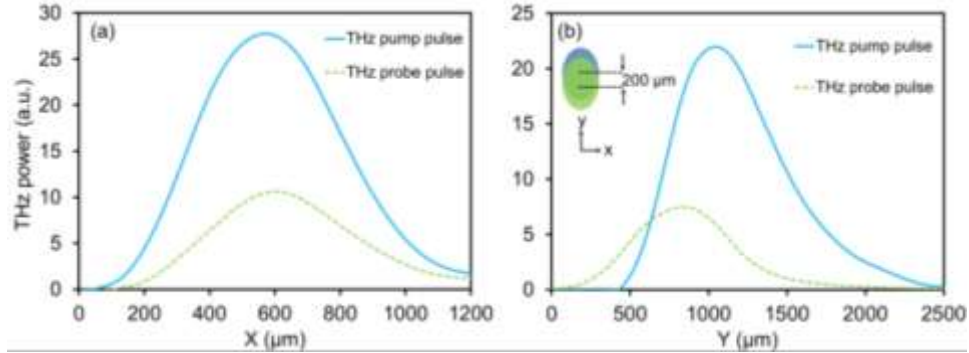


Figure 5-4 The spot sizes of both the THz radiation pump and probe pulses were mapped out using the knife edge technique in the (a) x - direction and (b) y - direction. The FWHM spatial extent of the THz radiation focal region was found to be $510\ \mu\text{m}$ and $740\ \mu\text{m}$ along the x - and y -directions, respectively. In the x -direction, both the THz radiation pump pulse and the THz radiation probe pulse overlapped and along the y -direction, the centers of the focal spots were displaced by $200\ \mu\text{m}$ with a 90% overlap. The x - and y - directions are depicted in the inset of (b).

It should be noted that the present THz-PP-TDS setup offers an additional capability to the time-resolved THz experiments, namely a control over the relative polarity between the THz radiation pump and THz radiation probe pulses. Figure 5-5 illustrates such a feature where by simply advancing the relative phase of the biasing voltages between the two PC THz emitters by 180° , the THz radiation probe pulse reverses its polarity. Such a feature is important for phase sensitive investigations.

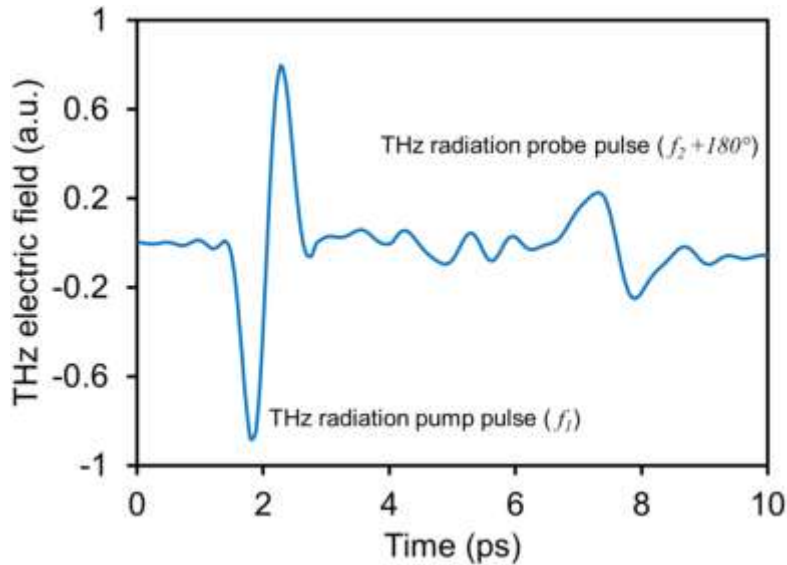


Figure 5-5 Electric fields of the THz radiation pump and probe pulses where the polarity of the THz probe pulse is reversed by 180° with respect to the THz pump pulse. The THz probe pulse is delayed by 5.5 ps with respect to the THz pump pulse and the modulating frequencies (f_1 and f_2) of bias voltages applied to both PC THz emitters were set to 81 KHz. The ratio of the THz pump to THz probe was set to 3:1 in this experiment.

Moreover, one of the challenges for THz-PP-TDS is the ability to perform THz time-resolved investigations at various THz radiation probe pulse polarizations. The ability to control the relative polarization angle between the THz radiation pump and probe pulses is essential for most all-THz pump-probe spectroscopy. Without sacrificing any THz radiation pulse power or employing of any optical components, this can be easily achieved with the current setup. The relative polarization state of the THz radiation pulses was attained by rotating one PC THz emitter while keeping the other fixed. The relative polarization state follows this rotation angle and, thus, any desired linear polarization can be set.

Using such a setup for THz-PP-TDS investigations requires illuminating a sample under study by the THz radiation pump pulse for excitation and studying the corresponding response on the THz radiation probe pulse as function of relative time delay. Thus, it is essential to modulate the biasing voltages of both PC THz emitters at different frequencies and phase-lock on one of the PC THz emitter's modulation frequency. Such a requirement is easily met with the present THz-PP-TDS. Figure 5-6 illustrates such an application where the PC THz emitter generating the THz

radiation pump pulse is modulated at $f_1=81$ kHz while the PC THz emitter generating the THz radiation probe pulse is modulated at $f_2= 40.5$ kHz.

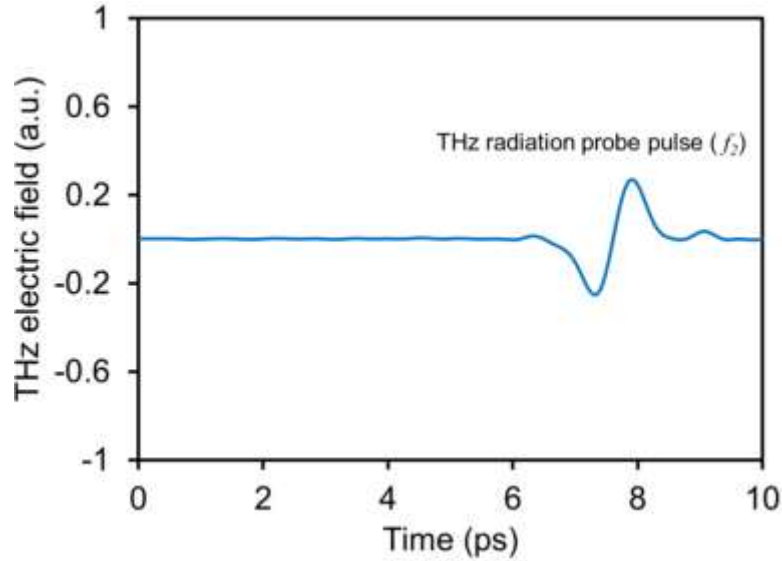


Figure 5-6 The THz-TDS probe signal pulse acquired at 40.5 kHz . Here, the PC THz emitter generating the THz radiation pump pulse was modulated at $f_1=81$ kHz while the PC THz emitter generating the THz radiation probe pulse was modulated at $f_2= 40.5$ kHz.

Notably, the choice of these frequencies represents the worst case scenario since f_1 is the second harmonic frequency of f_2 . This situation is intended to test the performance capability of the THz-PP-TDS under unfavorable conditions. It can be clearly observed from Figure 5-6 that by phase locking at f_2 , only the THz radiation probe signal is detected. This capability is especially essential for investigating phenomena for which the THz radiation pump pulse and the THz radiation probe are infinitesimally delayed in time or around zero time overlap.

This THz setup is to potentially characterize the temporal and spectral response of the fabricated antenna coupled MIIM, and MIIM diodes. The THz pump-Probe TDS system was initially used to study the spectral response of THz particle plasmons. This revealed the capabilities of the setup and prepared us for the next step of investigation (spectral response of MIIM). As mentioned earlier the THz particle plasmons were chosen as a test system since its underlying physics are well understood. Through a comprehensive time resolved studied the time dynamics of

the induced surface charges was examined. The importance of this research is in revealing the interaction and effect of induced surface charges on the propagation of THz radiation.

5.3 Time-resolved study of THz particle plasmons

Plasmonics, due to the ability to confine and enhance the electric field, is suitable for controlling electromagnetic propagation when interacting with matter [133]. In contrast to the plasmons excited at visible frequencies, which have been vastly studied, terahertz (THz) plasmons remain relatively unexplored. It has been illustrated that the THz electromagnetic field can be transported through a dense collection of metallic particles via the near-field coupling of non-resonant particle plasmon oscillations [134-136]. This provides a stimulating domain for studying the interaction of electromagnetic radiation with mesoscopic metallic structures, which is one of the fundamental investigations from the existence of Maxwell's equations. In addition, by exploiting the parameters of such transport, unique photonic behavior such as magnetic dependent transmission mediated by magnetoresistance [137] or spin injection [138] in ferromagnetic particles has been reported [ref]. While this coherent propagation process has been utilized for different experiments, to date no comprehensive study has described the dynamics of the particle-particle THz plasmon interaction.

In this section, a time resolved study of the effect of particle plasmons on the transmission of a THz probe pulse using THz-TDS is investigated. As mentioned earlier, understanding the effect of induced charges on the propagation of THz radiation in complex media is of great importance. A pump THz pulse is utilized to excite the metallic ensemble (via near-field coupling of nonresonant particle plasmons) and the transient of the charge oscillations (particle plasmons) is probed at various delay times by means of a THz probe pulse.

5.3.1 Experimental details

Using an all THz-Pump-Probe (THZ-PP) technique, the effect of particle plasmons on the transmission of a THz probe pulse was studied. The particle plasmons are excited in randomly distributed Au metallic microparticles having a mean diameter of ~ 100 nm. The ensemble was illuminated by a THz radiation pulse (acting as a pump) and the effect of excited particle plasmons on the transparency of the ensemble to a second THz radiation pulse (acting as a probe) was investigated as function of pump-probe relative time delay. For this experiment, a plastic sample holder 300 μm thick was filled with Au particles and was placed at the focal spot of the THZ-PP setup.

The THZ-PP system described in section 5.2 was used to perform this experiment. The ratio of the electric fields between the two THz radiation pulses (pump:probe) was set to 3:1 so that the THz probe pulse acts as solely a probe and does not over excite the metallic ensemble. To focus on the modification to the probe pulse, the biasing voltages of both PC THz emitters were modulated at different frequencies and the THz-TDS signal was acquired at the modulation frequency of the probe pulse via a lock-in amplifier. In the course of the experiment, the PC THz emitter generating the THz radiation pump pulse was modulated at $f_1=81$ kHz while the PC THz emitter generating the THz radiation probe pulse was modulated at $f_2=40.5$ kHz. The transmitted THz probe pulse was studied at delay times of $\Delta t=0, 1, 2, 3, 5$ and 7 ps with respect to the THz pump pulse. The schematic of the experiment is illustrated in Figure 5-7.

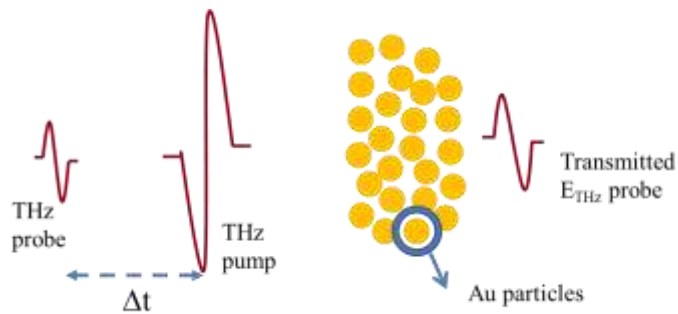


Figure 5-7 Schematic of the proposed THZ-PP experiment on Au sub-wavelength particles.

A total of four probe time-domain THz electric field signals were acquired and averaged for each time delay to obtain the final results.

5.3.2 Results and discussions

Figure 5-8 (a) depicts the time-domain electric field of the THz probe pulse transmitted through the Au particles at various time delays (Δt). In addition to all the time-resolved data, at $\Delta t = 0$, the pump pulse was blocked and only the probe beam was transmitted through the sample (shown as “pump blocked” in Figure 5-8 (a)). The variation of the transmitted probe THz electric field as a function of Δt can be better observed by exploring the change in the pulse’s spectral power density through the evaluation of the Fourier transform of each signal presented in Figure 5-8 (a). These spectral power plots for the pump blocked signal as well as $\Delta t = 0, 1,$ and 2 ps are illustrated in Figure 5-8 (b).

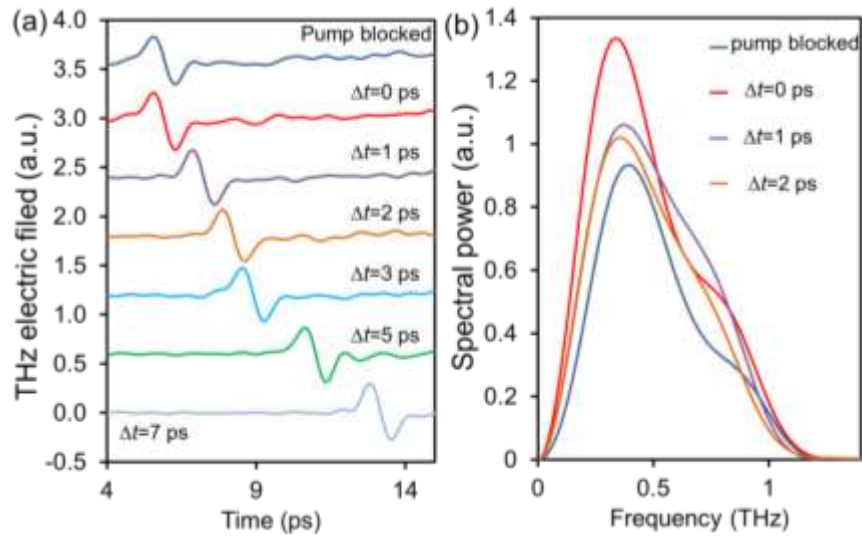


Figure 5-8 (a) Time-domain THz probe signals transmitted through Au particle sample at various delay times (Δt), and (b) their corresponding spectral power plots.

Note that the apparent resonance frequency at 0.4 THz of the transmitted probe pulse at the illustrated delay times arises from the inter-particle geometry of the Au particles [139]. It is evident from Figure 5-8 (b) that the transmitted probe THz

pulse power is lowest when the probe pulse is transmitted through the sample while the pump pulse is being blocked. On the other hand, the transmitted THz probe pulse power is the highest when the probe pulse is transmitted through the sample at the same time as the pump pulse ($\Delta t = 0$). For better comparison of the probe pulse transmitted power, the total integrated spectral power, $\int E_{THz}(\omega) E_{THz}^*(\omega) d\omega$, of each of the spectral power densities will be utilized for further analysis.

To further investigate the dynamics of the THz propagation through metallic ensemble the THz electric field phase of the probe beam was shifted by π (i.e. opposite polarity or out of phase) with respect to that of the THz pump pulse. Figure 5-9 (a) depicts the time-domain electric field of the transmitted THz probe pulse through the Au particles at various time delays (Δt). The spectral power plots for the pump blocked signal as well as $\Delta t = 0, 1$, and 2 ps are also illustrated in Figure 5-9 (b).

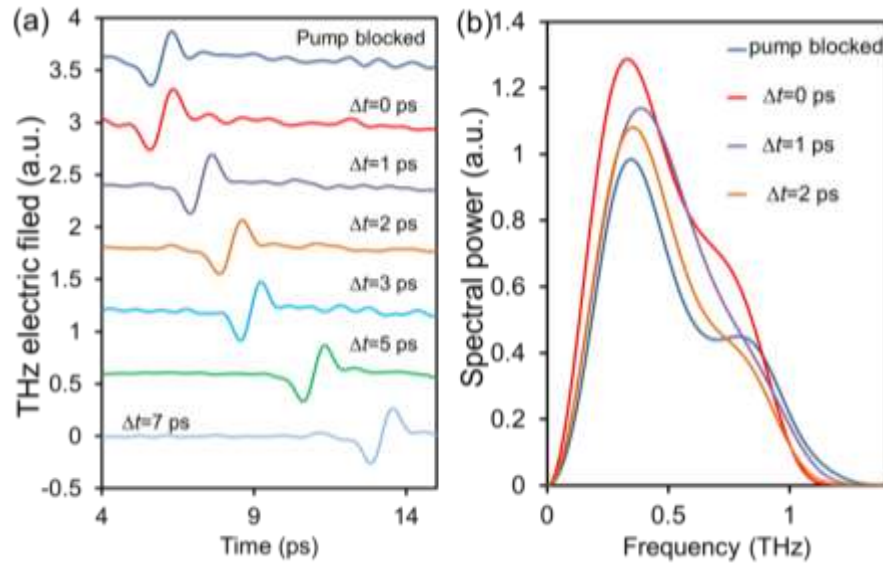


Figure 5-9 (a) Time-domain THz probe signals transmitted through Au particle sample at various delay times (Δt), and (b) their corresponding spectral power plots. The THz probe pulse electric field is out-of-phase with respect to the THz pump pulse.

Similar to the case when the THz pump and probe were in-phase, at $\Delta t = 0$ and when the pump beam is blocked the transmitted THz probe pulse has the maximum and minimum power, respectively. However, the THz transmission

enhancement in this configuration is not as significant as for the situation when the pump and the probe were in-phase. For better comparison of the probe pulse transmitted power, the total integrated spectral power of each of the spectral power densities was calculated. The percent change of the transmitted THz pulse compared to the transmitted THz probe in the absence of the THz pump pulse (P-P) has been plotted in Figure 5-10.

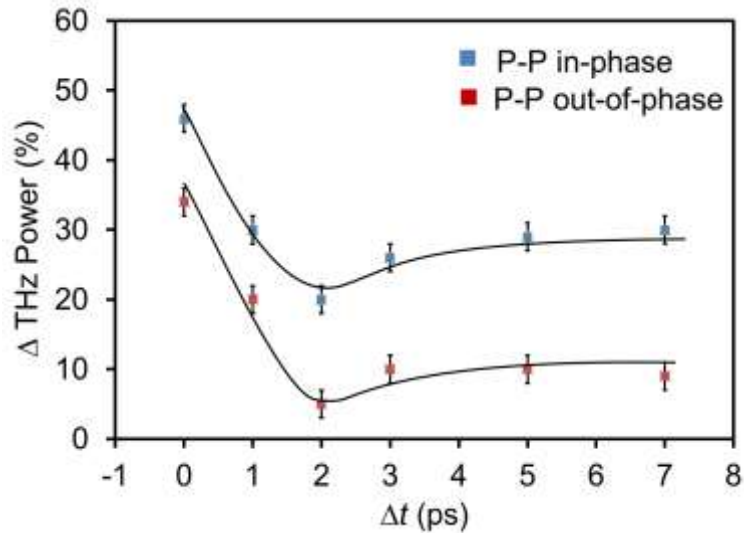


Figure 5-10 The percent change of the total integrated spectral power for the transmitted THz probe pulse compared to the transmitted THz probe when the THz pump pulse is blocked. P-P states for pump-probe in the legend. The solid lines in the figure are fitted curves.

In the case when the pump and probe are *in-phase* (*P-P in-phase*): (1) the probe pulse power for $\Delta t = 0$ is enhanced by $\sim 46\%$ when compared to the situation when the THz pump beam is blocked. This enhancement is reduced at $\Delta t = 1$ ps and it reaches a minimum at $\Delta t = 2$ ps. Beyond this time, for $\Delta t = 3, 5,$ and 7 the enhancement of the transmitted THz probe reaches a constant value of $\sim 30\%$.

On the other hand, when the pump and probe are *out-of-phase* (*P-P out-of-Phase*): (1) the probe pulse power for $\Delta t = 0$ is enhanced by $\sim 30\%$ when compared to the situation when the THz pump beam is blocked. This enhancement is reduced at $\Delta t = 1$ ps and it reaches a minimum at $\Delta t = 2$ ps. Beyond this time, for $\Delta t = 3, 5,$ and 7 the enhancement of the transmitted THz probe reaches a constant value of $\sim 10\%$.

The propagation of THz radiation via the particle plasmon mechanism (particle-particle coupling) is a surface dependent process and the condition of the particles' surfaces has a major influence on the transmitted THz pulse [140]. Therefore, surface condition modification can be the only explanation for the observed enhancement of the transmitted THz probe power. The transmitted THz probe for the case when the THz pump pulse is blocked represents the typical THz propagation through the ensemble of metallic particles. Essentially, the THz electric field is transformed into particle plasmons at the beginning of the metallic particle collection, propagated through THz plasmons and reradiated outside the collection of particles from where it is detected. However, with the presence of a THz pump pulse at $\Delta t=0$, the metallic ensemble is excited as the probe pulse is probing the sample. Thus, this enhancement is attributed to the effect of the THz pump pulse, which initially excites the particle plasmons. In this scenario, the surface impedance of the Au particles are altered by the coupled THz electric field that penetrates into the metal surface [141] as the sub-wavelength metallic particles are exposed to the illuminated THz electric field (THz pump pulse). Through the coupling of the THz field to the sub-wavelength particles, the particles are polarized where negative and positive charges are induced on the surface of the particle. These induced charges are responsible for altering the surface conductivity of the Au particles when compared to the unexcited particle. The schematic of this mechanism is presented in Figure 5-11.

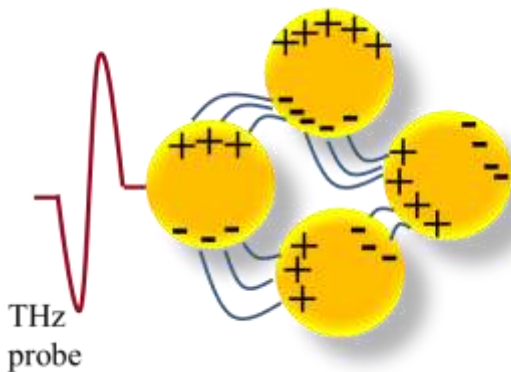


Figure 5-11 Schematic of the situation when the THz pump pulse has been coupled into THz particle plasmons and the THz probe pulse is been illuminated onto the Au ensemble at a later time.

Through this mechanism, the transmission enhancement of the probe pulse with the presence of the THz pump pulse is described. The minimum enhancement located at $\Delta t = 2\text{ps}$ is attributed to the pump THz pulse leaving the sample. This can be confirmed through considering the thickness of the ensemble ($\sim 500\ \mu\text{m}$) and the effective speed of light through the ensemble ($0.6c$). At $\Delta t > 2\text{ps}$, the charge distribution introduced by the THz pump pulse is spread in the metallic ensemble and thus the induced charge density induced on each particle is decreased compared to the case when $\Delta t < 2\text{ps}$ where the particle plasmons were localized. Beyond $\Delta t = 2\text{ps}$, the THz probe is probing the dynamics of the particle plasmons that are circulating in the ensemble (remnant of the pump THz electric field inside the ensemble) and thus, the enhancement reaches a constant value.

Notably, the two plots shown in Figure 5-10 follow the same trend, but there exists an offset between them. This is explained as follows: when the THz pump and the THz probe are in-phase, the polarity of the induced surface charges (ρ) by the pump THz pulse is in-phase with the induced charges introduced by the probe pulse and thus the overall induced charges on the particles are increased ($\rho_{\text{in-phase}} > \rho_{\text{pump-blocked}}$). However, when the pump and the probe are out-of-phase, The polarity of the induced surface charges by the pump THz pulse is out-of-phase with the induced charges introduced by the probe pulse and thus, the overall induced charges are lower compared to in-phase situation ($\rho_{\text{in-phase}} > \rho_{\text{out-of-phase}} > \rho_{\text{pump-blocked}}$).

To further study the effects of the THz pump on the transmitted THz probe and reveal more insight to the particle plasmon propagation mechanism, the phase of the transmitted THz electric field was investigated. Any change associated with the imaginary part of the impedance of the system is contained in the phase of the transmitted THz pulse. Thus, the phase of the transmitted electric field for $\Delta t = 0, 1, 2\ \text{ps}$ where compared to that of when the THz pump pulse was blocked as shown in Figure 5-12.

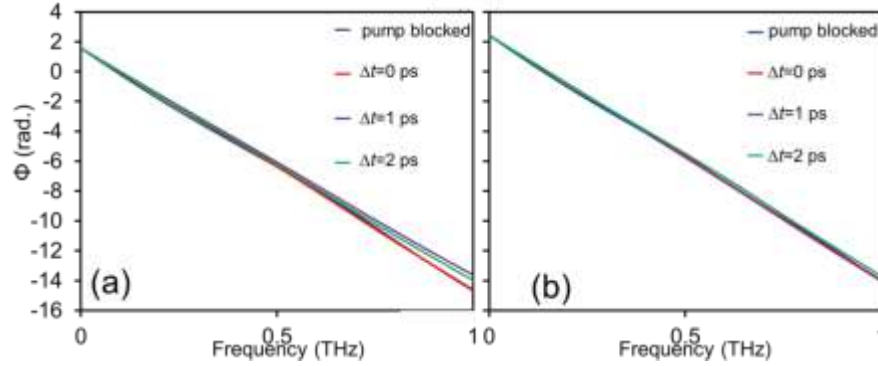


Figure 5-12 Phase of the transmitted THz probe electric field for $\Delta t=0, 1, 2$ ps of when pump-probe are: (a) in-phase, and (b) out-of-phase.

It is illustrated in Figure 3 (a) that the phase of the transmitted probe THz electric field compared to that of transmitted THz electric field with the THz pump pulse blocked is unchanged for frequencies up to ~ 0.6 THz. Beyond this point, there are slight differences between the phases of the transmitted THz probe pulse for different delay times. However, in the case of the THz pump and probe being out-of-phase, it is revealed that through the particle plasmon propagation mechanism, the phases of the transmitted THz probe field are identical for all delay times. Thus, it is evident that unlike the electric field amplitude of the propagated THz probe pulse; the phase content is independent of the relative phase of the pump and the probe.

Interestingly, change in conductivity of metallic surfaces has been illustrated through inducing charges at the surface by applying large external field on metallic surfaces [142, 143]. The reason for this change has been described by illustrating that at high external field the induced electron charge density has been increased considerably. This further supports our explanation for the observation of THz transmission enhancement phenomenon thorough sub-wavelength metallic ensemble. It can be concluded that the Au ensemble acts as an ultrafast modulator for THz radiation.

The knowledge gained from dynamics of THz plasmons can be further applied in application of THz in characterizing composite media consisting metallic ensembles. For this, the THz-TDS was utilized for comprehensive characterization of complex media such as composite materials. The further advancement of THz

application for imaging complex media, demands a thorough understanding of THz radiation propagation through complex materials.

5.7 Characterizing a plasmonic random composite

As already discussed, while much literature regarding plasmons excited at visible frequencies can be found, terahertz plasmons remain relatively unexplored. In this section, THz-TDS is utilized for characterizing the properties of plasmonic random composites. As mentioned earlier, this information is later employed for utilizing THz-TDS in imaging inside metallic media.

It was discussed that THz electromagnetic energy is transported across a dense collection of metallic particles via the near-field coupling of non-resonant particle plasmon oscillations [134]. In this section, we demonstrate a new terahertz plasmonic composite that is random in nature and exhibits an atypical refractive index [144]. In describing the permittivity and the permeability of a homogenized composite random media, Burghmann's effective medium theory (EMT) is widely utilized [145, 146]. Within the theory's framework, the electromagnetic response of a particulate composite medium is described by a set of average constitutive parameters, such as effective permittivity (ϵ_{eff}) and permeability (μ_{eff}), representing a weighted average of the constitutive. However, this homogenization formalism is valid only for ensembles composed of subwavelength-scale dielectric media and/or *nano*-scale metallic media, where the size of the metallic inclusions, a , is less than the radiation skin depth, α [147]. It is important to realize, however, that for random composites comprising metallic elements where $a \gg \alpha$, EMT does not capture the essence of the electromagnetic interaction. In this regime, a formalism describing mutual particle plasmon interactions within and between metallic elements is required [134, 140].

5.7.1 Results and discussion

The random composite employed in this work consists of a 4 mm thick mixture of Co metallic microparticles having a mean dimension of $a = 74 \pm 25 \mu\text{m}$ and spherical sapphire dielectric microparticles having $a = 100 \pm 15 \mu\text{m}$ [Figure 5-13(a)].

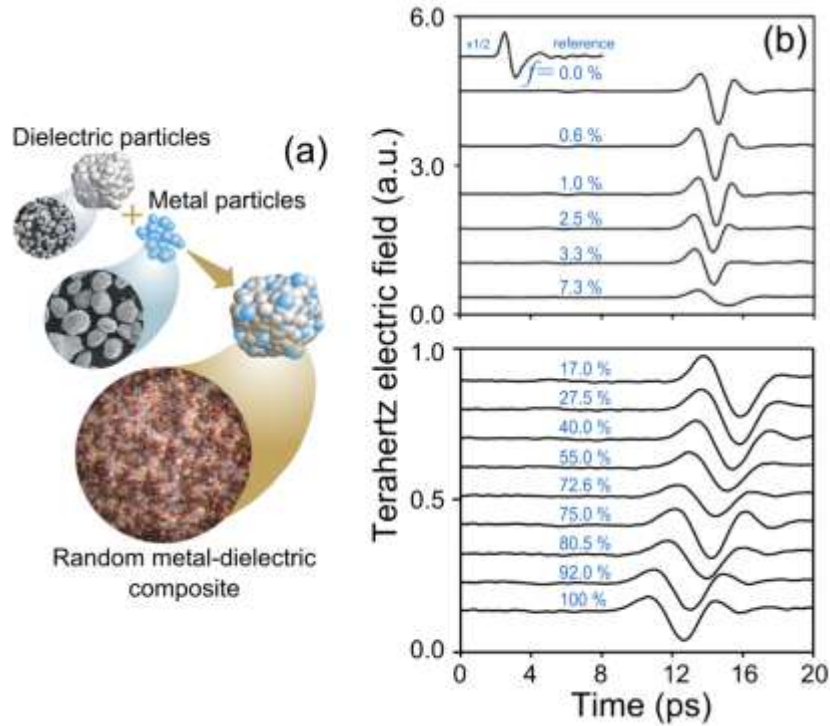


Figure 5-13 (a) Schematic diagram illustrating the random composite consisting of polydispersed metallic and dielectric particles. The circled images depict scanning electron microscope images of the dielectric and metal particles and an optical image of the composite. (b) Time-domain terahertz waveforms transmitted through an empty sample cell (reference) and 4.0 mm thick Co/sapphire particle mixtures for Co particles volume fraction, f , varying from 0.0 % to 100 %.

The *intrinsic* relative permittivities of the Co and sapphire particles at 1 THz are $-8 \times 10^3 + 10^4 i$ [148] and $10.5 + 0.02 i$ [149], respectively. We conduct our experimental observation in the terahertz (THz) regime where we access the time-domain electric field waveforms and their polarization states. Since α for Co at 1 THz is $\sim 100 \text{ nm}$ [148], which is much less than a , the ϵ_{eff} of the composite metal-dielectric random medium cannot be described as an effective medium. The electromagnetic behavior of ϵ_{eff} is depicted in the group refractive index or the group velocity of a

THz pulse propagating through the composite. By incorporating an increasing metallic particles volume fraction, f , into the dielectric random particles ensemble, we show evidence of a transition where there is a marked range of f where the refractive index is higher than the independent refractive indices of metallic and dielectric particle ensembles.

The TDS system utilizing EO detection described in section 1.3 was used for conducting this study. Shown in Figure 5-13 (b) are representative time-domain THz electric field waveforms transmitted through the composite where f is increased from 0.0 % (dielectric particles) to 100 % (metal particles). It is important to note that for representative particle ensembles with $f = 0\%$, $f = 17\%$, $f = 27\%$, and $f = 100\%$, the packing fraction (ρ) is measured to be 0.60 ± 0.01 , 0.61 ± 0.01 , 0.58 ± 0.01 , and 0.58 ± 0.02 , respectively. From these values, it is clear that the ρ remains fairly consistent over the full range of f . The electric fields shown in the figure are polarized parallel to the incident polarization. The most notable feature is that as f is increased greater than 17 %, an appreciable *advancement* of the pulse arrival time is observed. This extraordinary behavior is quantified by assigning the pulse arrival time as the temporal position of the peak pulse intensity (corresponding to the time when the greatest number of photons are detected), T [Figure 5-14 (a)]. Figure 5-14 (b) plots the time-dependent intensity profiles of the transmission electric field components polarized parallel, E_{\parallel} , and perpendicular, E_{\perp} , to the incident polarization for various f . For $f = 0.6\%$, the electric field is polarized along the incident polarization, since the majority of the pulse energy is in the parallel component. The small perpendicularly-polarized field component is attributed to small angle scattering from the dielectric constituents. When f increases to 40 %, T is delayed by 1 ps. This delay is a result of the THz pulse propagating a longer optical path due to increased scattering from both the dielectric and metallic particles, and the equal intensity of the parallel and perpendicular field components indicates that the transmitted electromagnetic pulse is unpolarized. Such polarization-randomizing scattering events impair the coherence of the electromagnetic energy transport. However, at $f = 100\%$ the transmitted pulse arrives 2 ps earlier than the transmitted pulses measured at $f = 0.6\%$. The high polarization purity of the THz electric field suggests coherent electromagnetic energy

propagation, and such marked transmission through the metallic Co particles is attributed to the recently demonstrated plasmonic enhanced propagation [134, 140]. Effectively, the addition of opaque, metallic particles to the composite in this regime *reduces* the optical path length.

To shed light on the frequency dependence of this phenomenon, the transmission power spectra is explored as shown in Figure 5-14 (c). The main features of this data are the frequency-dependent attenuation for $f < 17.0\%$ and the frequency-independent attenuation for $f > 17.0\%$. The transmission through the dielectric ensemble ($f = 0\%$) encompasses frequency components from 0.1 THz to 0.8 THz. However, as f increases to 7.2%, nearly all the frequency components above 0.4 THz are extinguished. Preferential attenuation of the higher frequency components is ascribed to the frequency-dependent Rayleigh scattering from the metallic particles [150], where shorter wavelength radiation is more readily scattered from the on-axis direction relative to larger wavelength radiation. It should be noted that scattering events from the individual metallic particles cannot account for the frequency-independent attenuation that is observed for f between 17.0 % and 72.6 %.

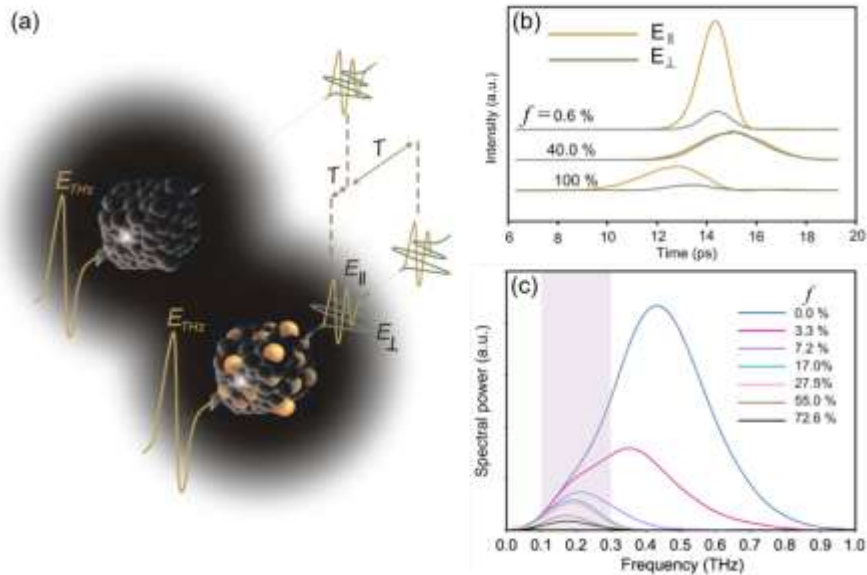


Figure 5-14 (a) Illustrative diagram depicting the THz electric field (E_{THz}) transmitted through the random metallic-dielectric composite with components polarized parallel ($E_{||}$) and perpendicular (E_{\perp}) to the incident polarization and temporal position shifted by a time T relative to the transmission through a dielectric particle sample (upper left). (b) Time-dependent THz pulse intensity envelopes through a 4.0 mm thick sample having various f values for both parallel

and perpendicular polarization states. Here, the time axis is measured relative to a 4.0 mm thick pure dielectric ensemble. (c) Power spectra of a THz pulse transmitted through mixtures of metallic and dielectric particles for varying f . The band marks the frequency range which is shared among all the samples of different f .

To illustrate the observed behaviour of the composite, we extract the effective refractive index, n_{eff} , as a function of f . Figure 5-15 (a) displays the change in the effective refractive index, Δn_{eff} , (measured relative to that of a sample having $f = 0\%$) versus f over the frequency range of interest. Within the 0.1- 0.3 THz bandwidth, the refractive index can be significantly altered by the addition of the metallic particles; and more interestingly, n_{eff} can be made higher than the refractive indices of *parent* dielectric (n_{eff}^d) or metallic (n_{eff}^m) constituents. This behavior is further illustrated in Figure 5-15 (b) for a representative n_{eff} versus f plot at a frequency of 0.23 THz. Within the range $0 < f < 20\%$, n_{eff} is shown to increase from 1.81 to 1.91 ($\Delta n_{eff} > 0$); however, beyond $f = 20\%$, n_{eff} displays a marked decrease, yet the refractive index is higher (ie: $\Delta n_{eff} > 0$) than either $n_{eff}^d = 1.81$ or $n_{eff}^m = 1.66$ (Note that the *intrinsic* index of individual opaque Co particles and transparent sapphire particles at 0.23 THz are $170+200i$ [148] and 3.25 [149], respectively).

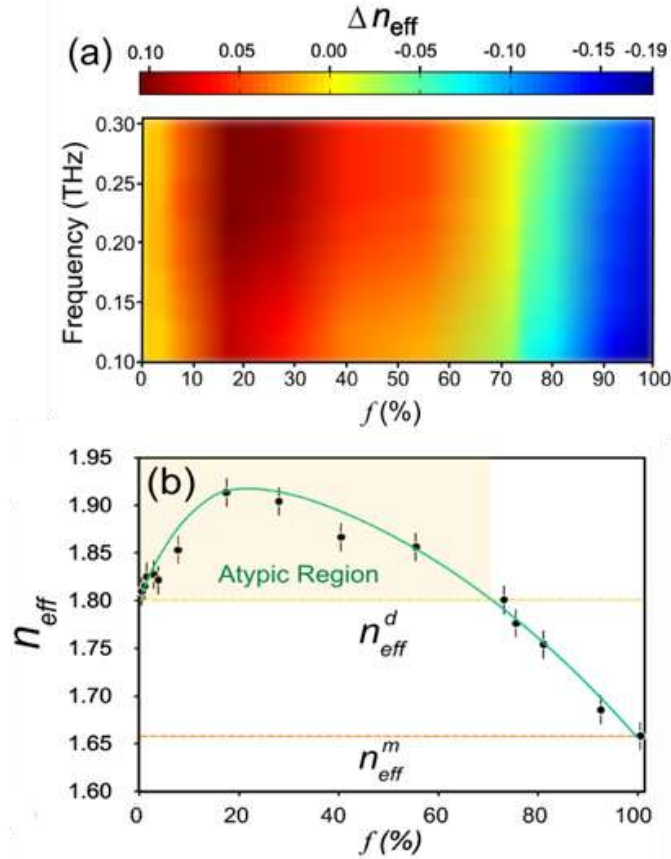


Figure 5-15 (a) Plot of the change (relative to a dielectric ensemble) of the effective refractive index of the random composite as a function of f and frequency. (b) Effective refractive index of the random metallic-dielectric composite measured at 0.23 THz and various f . Notably, within the atypic range the refractive index is larger than either the dielectric (n_{eff}^d) or metallic (n_{eff}^m) ensembles refractive indices.

Surprisingly, despite the high volume fraction of opaque metallic particles, at $f = 70\%$ $\Delta n_{eff} = 0$. That is, the dielectric-metal random composite has the same refractive index ($n_{eff}^d = 1.81$) as a dielectric particle ensemble. Beyond $f = 70\%$, $\Delta n_{eff} < 0$ and approaches a value of $\Delta n_{eff} = -0.15$ at $f = 100\%$. Notably, for a metallic particle ensemble ($f = 100\%$), n_{eff}^m is 8.3% lower than that of a pure dielectric particle ensemble (n_{eff}^d).

It is evident that the group refractive index is strongly dependent on the effective optical path which is related to f , or alternatively, the metallic particle separation. The average inter-particle separation, s_{ave} , between metallic particles is estimated by approximating the metallic particles as isotropically distributed random

spheres, as shown in the inset of Figure 5-16. The average radius, r_{ave} , occupied by a single metallic particle in a volume, V_{ave} , is $r_{ave} = (3V_{ave}/4\pi)^{1/3}$, and thus the average physical separation between nearest neighbor metallic particles from the surface of the particles is $s_{ave} = 2r_{ave} - a$.

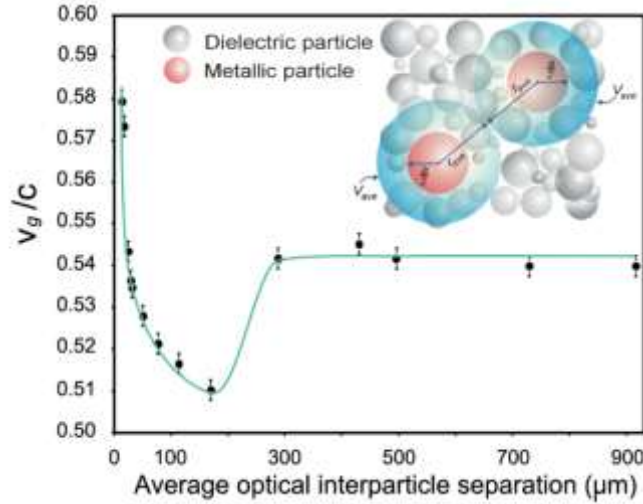


Figure 5-16 Group velocity (normalized to c) versus the average optical separation between metallic particles. The inset illustrates the average optical separation of metallic particles immersed in a background of a dielectric particle ensemble, where r_{ave} is the average radius occupied by a single metallic particle in a volume V_{ave} and a is the average diameter of a metallic particle.

Since the addition of metallic particles displaces a volume otherwise occupied by dielectric particles, the effective optical inter-particle separation, $s_{ave,opt} = s_{ave} n_s$, must account for the weighted refractive index, n_s , of the dielectric particles surrounding the metallic particles. Here, n_s is calculated using a Beer effective medium description [147],

$$n_s = \frac{\rho V_d n_d}{V_t} + \left(1 - \frac{f V_d}{V_t}\right) \quad (5.1)$$

where $n_d \approx 3$ is the refractive index of sapphire at 1 THz [12], V_t is the total volume occupied by the composite, and V_d is the total volume of sapphire in the composite. It is instructive to analyze the group velocity, v_g , of the light pulse versus

$s_{ave,opt}$. As depicted in Figure 5-16, for $s_{ave,opt} > 288 \mu\text{m}$, v_g is relatively constant at $\sim 0.54c$. In this regime, the metallic particles are separated by distances greater than the diameter of the dielectric particles and, on average, the spacing between metallic particles is occupied by several dielectric particles. Thus, mutual plasmonic coupling between metallic particles is inhibited and the metallic particles act like independent scatterers removing electromagnetic energy from the incident beam via Rayleigh scattering. Since the transmission in this regime is highly polarized, the pulse transmission through the composite arises mainly from direct propagation through the transparent dielectric particles (ballistic transmission) and small angle scattering. At $s_{ave,opt} \sim 170 \mu\text{m}$, v_g reaches a minimum of $0.51c$, which is lower than the group velocity in either constituent. The reduction in v_g over the range $170 \mu\text{m} < s_{ave,opt} < 288 \mu\text{m}$ is attributed to augmented scattering by the metallic and dielectric particles. Here, the ballistic transmission efficiency diminishes, and a greater portion of the transmitted pulse is mediated by scattered electromagnetic waves that must propagate within the gaps between the opaque metallic particles. Scattered photons following such a "zig-zag" path thus results in an increased propagation path-length and, accordingly, a decreased v_g and increased n_{eff} . However, for $s_{ave,opt} < 170 \mu\text{m}$ v_g begins to increase and approaches $0.58c$ at $s_{ave,opt} \sim 14 \mu\text{m}$. It is noteworthy that the inflection in v_g at $s_{ave,opt} \sim 170 \mu\text{m}$ corresponds to a physical separation of $s_{ave} \sim 95 \mu\text{m}$, similar to the diameter of one dielectric particle ($100 \pm 15 \mu\text{m}$). At this inflection value of $s_{ave,opt}$, the metallic particles become close enough to each other, on average, such that near-field particle-plasmon interaction between metallic particles begins to govern the propagation of electromagnetic energy across the ensemble. As such, the increasing v_g as $s_{ave,opt}$ decreases from $170 \mu\text{m}$ to $14 \mu\text{m}$ is attributed to increased particle-plasmon coupling. Note that the narrow band of the transmitted pulses for $s_{ave,opt} < 170 \mu\text{m}$ (i.e. $f > 17\%$) supports this claim, since near-field particle-plasmon transport is supported only over a relatively narrow band [134]. As the average spacing between metallic particles becomes significantly less than the diameter of the dielectric particles, the absence of straight-line trajectories through the dielectric particles precludes ballistic electromagnetic pulse propagation. Accordingly, nearly all transmission is mediated by near-field particle-plasmon interaction between

metallic particles for $s_{ave,opt}$ near 14 μm . Note that we can also identify the inflection point at $s_{ave,opt} \sim 170 \mu\text{m}$ as the particle plasmon transport percolation threshold, separating regimes where the electromagnetic behavior in the composite is governed by dielectric scattering and plasmonic interaction. At the plasmonic percolation threshold, the material exhibits atypical photonic transport that is mediated by contributions from both ballistic scattering and near field plasmonic coupling.

The knowledge gained through this series of experiments, are employed in performing THz-TDS imaging inside metallic media. As mentioned earlier, the application of THz-TDS in imaging inside metallic media is required for further advancing THz imaging technology. In the next section, the application of THz-TDS is extended to performing imaging inside metal-filled media. It is envisioned that through the utilization of the more efficient THz sources and the detectors fabricated in the course of this thesis, higher speed THz imaging systems having higher sensitivity are realized.

5.8 Terahertz imaging inside metal-filled media

Since Hu and Nuss' first pioneering experiments in 1995 [151], Terahertz (THz) imaging has evolved into one of the most practical applications of THz time-domain spectroscopy (THz-TDS). The reason for this continuing success is due to its broadband, sub-picosecond temporal resolution and phase sensitive coherent detection combined with the innate properties of a variety of dielectric materials, which are transparent in the THz regime.

Most of today's terahertz imaging systems employ sub-picosecond pulsed [152] radiation sources and construct images based on the coherent detection of the transmission and/or reflection spectrum of the object to be imaged. This technique has been shown to provide the capability of two-dimensional [153] real-time imaging [154], as well as the ability to reconstruct three-dimensional tomographic images [155] over a broad range of THz frequencies. A comprehensive review on the field of THz imaging can be found in [153, 155]. An equally important implementation of THz-TDS to imaging is the detection of objects buried within a host material. In such

an imaging modality, the average collected THz power, the degree of polarization contrast, or the arrival time of the THz pulse transients are collected and analyzed to reconstruct an image of the hidden object. Owing to the opacity of metals in the THz regime, this method has been used extensively to image metallic objects hidden deep within dielectric packages. However, because of this fact, it is impossible to probe dielectric matter or voids buried within a metallic host. This is the case only when the thickness of the metallic layer is greater than the THz radiation skin depth (i.e. ~ 100 nm) since the metallic layer possesses very high reflectivity (i.e. is perfectly conducting) and no radiation can interact with the dielectric object.

In this section, a potential application of pulsed terahertz imaging in which dielectric objects embedded inside a random collection of metallic particles are studied. Here, is the outline of the principles of this imaging process: In this configuration, a small dielectric object is immersed in a random collection of sub-wavelength metallic particles. A THz pulse incident on the sample excites localized, non-resonant surface plasmons on the metallic particles which coherently couple and propagate throughout the sample via near-field particle-particle oscillations [140, 144]. Notably, even though the host material is made up of metallic particles having large negative real permittivity, the media collectively transports the THz electromagnetic energy via near-field particle plasmon coupling. This makes the media partially transparent to the THz radiation implying that it possesses an effective positive real permittivity. Basically, the random collection of metallic particles appears dielectric rather than metallic to the THz radiation. In this regard, imaging a dielectric object buried inside the metallic particle collection is akin to the THz transmission imaging experiments used to detect power attenuation signatures from a dielectric embedded inside a dissimilar dielectric host. Embedding dielectric objects having sufficient thickness (i.e. much larger than the THz radiation wavelength) between adjacent metallic particle collections impedes the near-field particle-particle coupling. Under this circumstance, the particle plasmons in the vicinity of the front surface of the dielectric object reradiate the THz electric field. After the THz radiation propagates through the dielectric object, this far-field radiation is again captured by the metallic particles on the opposite side from where it continues to

propagate via near-field particle plasmon oscillations. Essentially, the THz electric field is transformed into propagating particle plasmons at the entrance of the metallic particle collection, re-radiated through the dielectric object, and then collected by the randomly placed metallic particles at the other face of the object and propagated outside the collection of particles from where it is detected. This fact manifests itself as an innate difference in the THz pulse arrival time, phase, and attenuation of the electric field when the pulse is incident on a location containing only metallic particles versus a location containing metallic particles with embedded dielectric.

5.8.1 Results and discussion

In this experiment, dielectric objects have been placed inside a metallic media composed of close-packed, poly-disperse Cu microparticles having a mean dimension of $\sim 70 \mu\text{m}$ and a packing fraction of 0.6. The dielectric objects were cut from Teflon sheets into triangular and polygon geometries having different sizes and thicknesses. In preparing the samples, a 3 mm thick and 1.5 cm wide plastic container transparent to THz radiation was filled with the Cu particles. The Teflon triangular- and polygon-shaped objects were then fully embedded in the middle of the Cu particle collection. The target was raster scanned by an x - y translation stage with a resolution of 0.6 mm/pixel over a $9.6 \times 7.8 \text{ mm}^2$ area, corresponding to $16 \times 13 = 208$ pixels for the triangular-shaped object and a $6 \times 7.2 \text{ mm}^2$ area, corresponding to $10 \times 12 = 120$ pixels for the polygon-shaped object.

In order to image the sample, the THz-TDS described in section 1.3 was employed to perform the two-dimensional scans. EO detection was utilized for this experiment. Using this setup, THz-TDS of the sample was obtained for each point over the two-dimensional grid, and images of the shapes of the Teflon objects were successfully constructed. It should be noted that no signal averaging schemes have been performed in this experiment. The data acquired at each point are the result of a single transmitted THz temporal pulse.

Figure 5-17 illustrates the THz electric field time domain signal, $E_{\text{THz}}(t)$, transmitted through a single location on the sample containing only Cu particles. In

comparison to the free-space propagating $E_{THz}(t)$ signal, the amplitude of the transmitted electric field is attenuated by $\sim 98\%$ due to the high reflectivity of the host Cu particles. Also shown is the THz electric field time domain signal transmitted through a single location on the sample where the Teflon object is embedded.

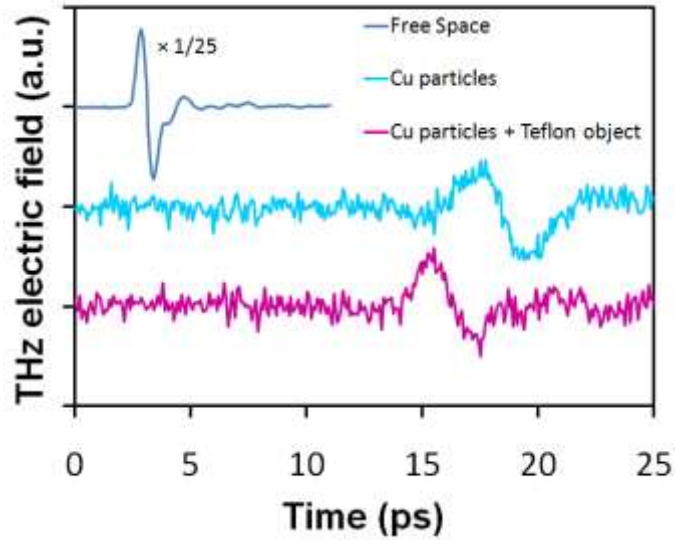


Figure 5-17 Transmitted THz electric field through the metallic ensemble. (blue) free space time domain signal, (light blue) time domain signal through the Cu and (purple) time domain signal through Cu and Teflon.

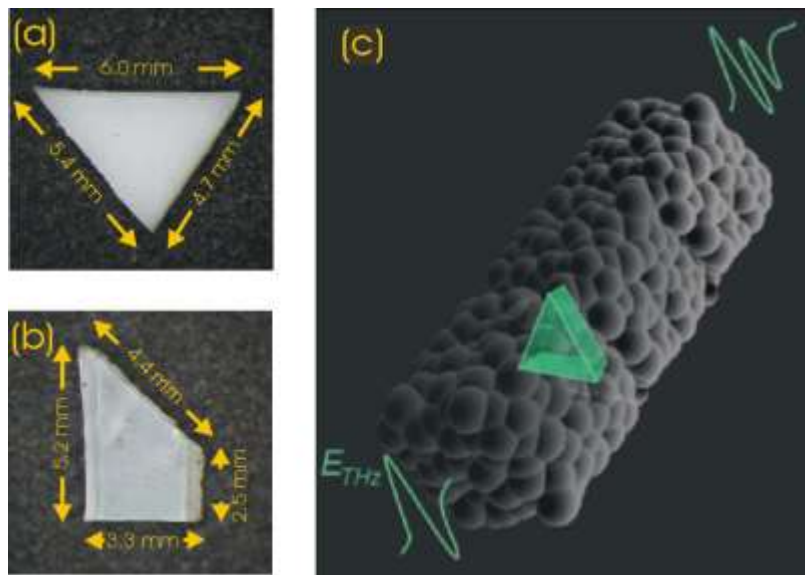


Figure 5-18 (a,b) Pictures of the Teflon objects used in the experiment. (c) An illustration depicting the THz electric field (E_{THz}) transmitted through the samples.

In order to obtain an unambiguous representative image of the embedded Teflon test object, a time-domain electric field scan was performed on samples containing a 0.8 mm thick triangular-shaped and 1.1 mm thick polygon-shaped Teflon objects shown in Figure 5-18 (a,b). An illustrative diagram depicting the transmission of the THz electric field through these samples is given in Figure 5-18 (c). Since small changes in the transmitted THz signal are of interest, contrasts in the arrival times and slight differences in the electric field amplitudes can be better registered by evaluating the instantaneous power, $|E_{THz}(t)|^2$, and the spectral power, $|E_{THz}(\omega)|^2$, respectively. $|E_{THz}(t)|^2$ and $|E_{THz}(\omega)|^2$ are acquired at every pixel in the grid by utilizing Hilbert and Fourier transforms on the time domain signals, respectively. The Hilbert transform, H , produces the original signal plus the transformed (imaginary) part of the signal $H(E_{THz}(t)) = E_{THz}(t) + E_{THz}^*(t)$, where $E_{THz}(t)$ is the original and $E_{THz}^*(t)$ contains the complex conjugate of the signal). To obtain the integrated instantaneous power, we calculate $|E_{THz}(t)E_{THz}^*(t)|$ and integrate it over the pulse duration. Henceforth, “instantaneous power integrated over the pulse duration” refers to “instantaneous power” for brevity.

Figure 5-19 illustrates a 2D image of the total transmitted instantaneous power $\int E_{THz}(t)E_{THz}^*(t)dt$ integrated over the duration of the pulse for both the triangular- and polygon-shaped objects. The raw images appear very noisy and smeared out beyond the actual size of the physical objects. This is due to the nature of the multiple, indirect random paths taken by the THz radiation as it is channeled via particle plasmons through the sample as well as the non-directional collection of the THz electric field by the receiving particle plasmons in the vicinity of the embedded dielectric object. The low contrast of the images is due to the fact that the Teflon samples are thin (~1 mm), resulting in only a small observable difference in absorption between the embedded Teflon object and the Cu background; however, thicker Teflon objects can produce much higher image contrast. Nevertheless, there are subtle enough differences in the detected instantaneous powers to discern the region where the Teflon objects are located.

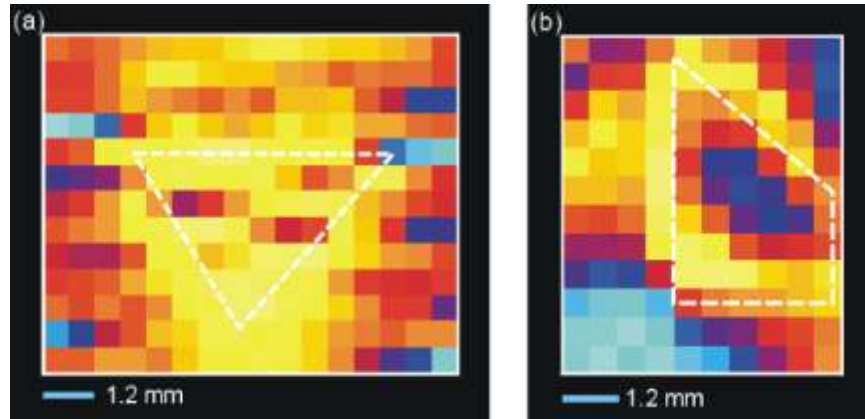


Figure 5-19 Acquired raw transmitted instantaneous power images of the embedded integrated over the duration of the pulse (a) 0.8 mm thick triangular-shaped object at a resolution of (16×13) pixels and (b) 1.1 mm thick polygon-shaped object at a resolution of (10×12) pixels. The dashed lines indicate the location of the embedded object.

While such low contrast might not be obvious, the signature of the objects on the THz pulse power can be enhanced if sophisticated digital image processing techniques are applied to the acquired low resolution images. In particular, the spatial resolution of the objects can be improved by enhancing the original images using the super-resolution through neighbor embedding technique [156]. This super-resolution algorithm is used to produce high resolution enlargements from low resolution images, which helps overcome the limitations of the low pixel image acquisition system. However, prior to its application some preprocessing steps are adopted to suppress noise and increase the image contrast.

Since the raw data contains background noise from the random nature of the excitation and propagation of THz particle plasmons, a 3×3 median filter [157] is employed. This filter replaces the value of a given pixel by the median of the intensity levels in a neighborhood centered on that pixel. Furthermore, to eliminate image blurring a threshold is set to select noisy pixels to which filtering is selectively applied. Finally, to bring out the object of interest from the background and make it more distinguished, the method of contrast stretching [157] is applied to the filtered images.

The neighbor embedding based super-resolution technique is then applied to the preprocessed low resolution images to enhance the spatial resolution of the

embedded objects. This algorithm requires learning from an object training set [156] generated using a set of 7 high resolution images. First, a 3×3 averaging filter is applied to the high resolution images to model the blurring effect introduced during image acquisition. Next, the blurred images are down-sampled by a factor of three in both the horizontal and vertical directions. Each high resolution image is then divided into patches having dimensions of 9×9 pixels, and for each patch in the high resolution image the corresponding 3×3 pixel patch is generated for the low resolution image. This step provides a set of 16157 pairs of low resolution and high resolution patches used to reconstruct the acquired images. This super-resolution image processing was applied to the two acquired raw THz images depicted in Figure 5-19. Figure 5-20 illustrates the resultant 9-fold increase in the spatial resolution of the images. It is evident that there is significant image enhancement in the post processed images compared to the originally acquired ones.

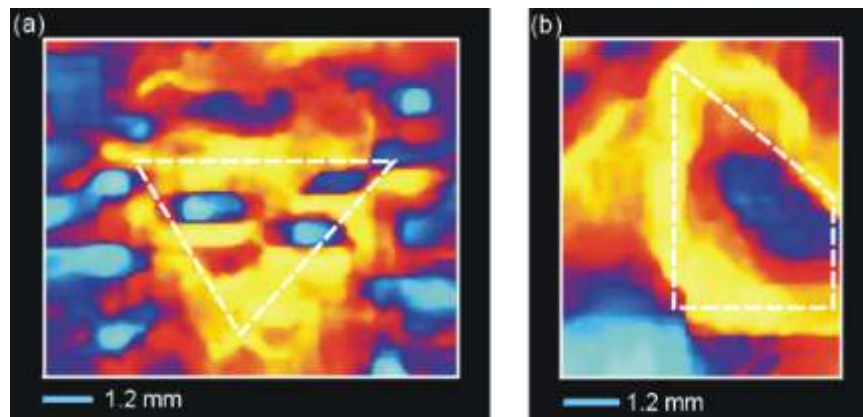


Figure 5-20 The super-resolved images of those presented in Fig. 3. The high-resolution images are based on total transmitted instantaneous power with a 9-fold increase in spatial resolution for the original (a) (16×13) pixel triangular-shaped and (b) (10×12) pixel polygon-shaped Teflon objects. The dashed lines indicate the location of the embedded object.

However, it can be observed that even though the resolution and contrast of the images has been enhanced, the exact shapes of the embedded objects are indistinguishable from such instantaneous power maps. As mentioned earlier, this is attributed to the fact that the Teflon samples are thin, resulting in only a small observable difference in absorption between the embedded dielectric object and the

metallic particle environment. This makes it very challenging to detect the hidden objects by only observing the transmitted THz power.

To further study the THz plasmonic imaging technique, other property maps of the transmitted THz pulse, such as arrival time and phase magnitude were studied. Using the time domain electric field of the transmitted THz pulse, the temporal position of the peak pulse intensity was acquired from the centroid of $|E_{THz}(t)|^2$ for each detected pixel. The peak intensity corresponds to the time at which the maximum number of photons is detected. Considering that the pulse arrival time varies as the THz pulse travels from the metallic region through the dielectric region of thickness L , the time difference can be represented by $\Delta t = (L/c)(n_d - n_m)$, where n_d and n_m are the refractive index of the dielectric and the effective refractive index of the metallic mediums, respectively. Consequently, Δt is dependent on the location of the dielectric object within the sample; therefore, the location and shape of the embedded object can be mapped by acquiring such time differences as shown in Figure 5-21.

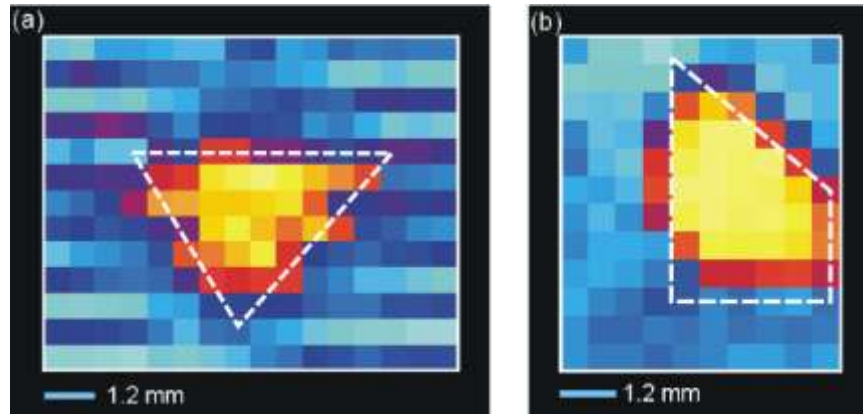


Figure 5-21 Acquired raw 2D maps of the THz pulse arrival time of (a) 0.8 mm thick triangular-shaped object at a resolution of (16×13) pixels and (b) 1.1 mm thick polygon-shaped object at a resolution of (10×12) pixels. The dashed lines indicate the location of the embedded object.

Using this image representation, it is evident from the figure that both the embedded triangular- and polygon-shaped Teflon objects are clearly distinguishable from the background metallic media. Unlike the transmitted pulse instantaneous power, which is based on the average power loss due to near field interactions

between the particles along the propagation path, the time arrival representation shows higher contrast. However, the exact boundaries of the objects are not well defined. The low resolution on the edges is attributed to the spatial spread of the particle plasmons' coupling radiation as discussed earlier.

Since the THz radiation transport through the random metallic media was previously reported to be a coherent phenomenon, it is only natural to investigate the phase magnitude of the transmitted THz pulse for potential phase contrast imaging. In this study, the phase magnitude at a frequency of 0.15 THz (corresponding to the maximum pulse power when the signal travelled only through metallic particles) was selected at each pixel. Shown in Figure 5-22 are the phase magnitude images for both the triangular- and polygon-shaped Teflon objects. It is evident from the figure that the raw phase contrast images are less distinctive compared to the arrival time images; nevertheless, they show features of the embedded objects. The phase magnitude of the transmitted pulse depends on the refractive index of the media in which the pulse has traveled. The reason behind this high contrast is the near field particle-particle plasmon which propagates the THz electric field inside the metallic particle sample. In areas of the sample with pure metallic particles, these near field particle-particle plasmons travel through the sample continuously, whereas in areas where the dielectric object is present, these near fields have to be reradiated and coupled back to particle-particle plasmons in the vicinity of the dielectric object. Clearly, there is a difference in the phase accumulated in the two regions as a result of refractive index difference (high contrast) at different locations within the sample.

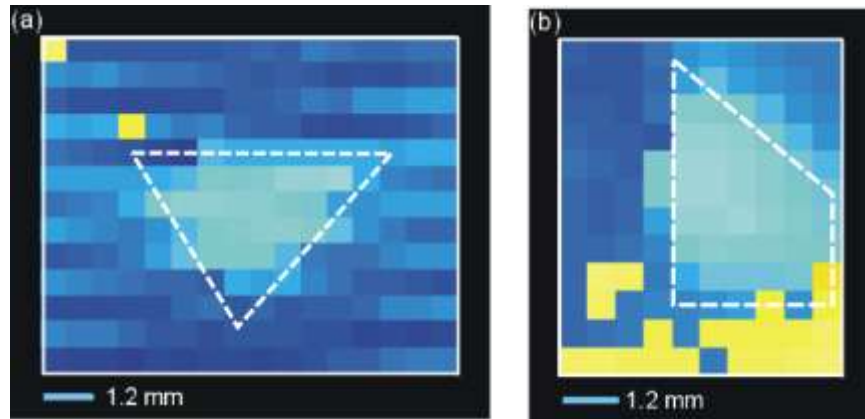


Figure 5-22 Acquired raw 2D maps of the phase magnitude taken at 0.15 THz for the (a) 0.8 mm thick triangular-shaped object at a resolution of (16×13) pixels and (b) 1.1 mm thick polygon-shaped object at a resolution of (10×12) pixels.

To enhance the resolution of the arrival time and phase contrast images, the aforementioned super-resolution algorithm was applied to the raw data. Figure 5-23 illustrates the post processed high resolution images resulting from this technique. In all cases, the visual quality is improved as the resolution level increases, and from the enhanced images more details of the embedded dielectric objects are visually recognizable.

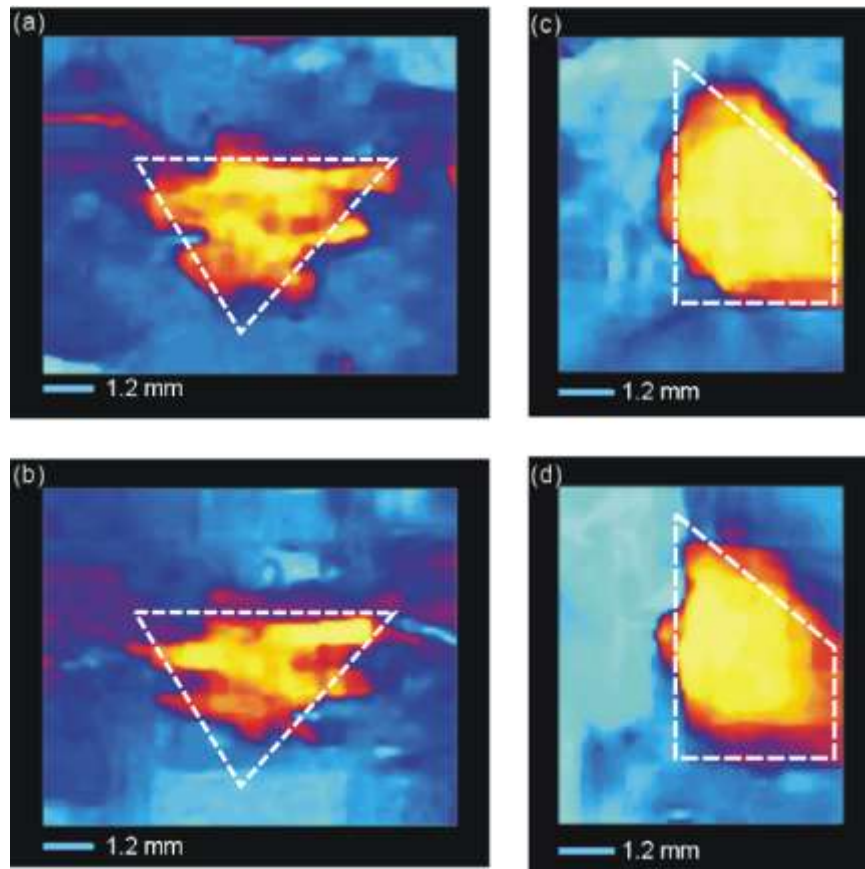


Figure 5-23 The super-resolved images with a 9-fold increase in resolution for the acquired (a,c) pulse arrival time images and for (b,d) phase magnitude images. The dashed lines indicate the location of the embedded object.

More specifically, sharper edges make the objects of interest more distinguishable from the background metallic media. According to the information known about the shape of the objects, pulse arrival time gives the most informative depiction of the objects. Phase magnitude basically conveys similar information, but the edges are not as clear as that of the pulse arrival time images. This demonstrates that super resolution can be effectively implemented to produce more detailed information from low quality images acquired via THz plasmonic imaging of dielectric objects embedded in metallic media.

5.9 Summary

In this chapter THz-TDS has been utilized as both a characterization as well as an imaging tool. For this, a versatile THz-TDS system that can be configured for either a traditional THz-TDS or a THz-PP-TDS arrangement is introduced. The setup overcomes the abovementioned inherent constraints and limitations in traditional THz-PP-TDS systems. The setup utilizes a dual pulse generator module based on semiconductor photoconductive emitters to generate two independent but synchronized THz radiation pump and probe pulses. Since the present THz-PP-TDS setup eliminates the use of a beam splitter, it allows for 100% utilization of the THz radiation pulses generated at the source for time-resolved experiments. The THz setup allows for precise control of the splitting ratio between the THz radiation pump and probe pulses by independently controlling the level of optical excitation of the PC THz emitters. Without the use of additional components, the system has the added capabilities of providing both in-phase and out-of-phase THz-PP-TDS experiments as well as polarization-dependent THz-pump/THz-probe measurements. The setup has a compact footprint, is easy to align, does not require specialized THz radiation optical components, and can be implemented in any THz-TDS system.

Next, the time resolved dynamics of THz particle plasmons have been investigated using the above mentioned setup. The effect of induced charges on the THz propagation is studied. It has been shown that the surface conductivity of metals is modified via induced charges.

Next, the characterization of a material composite consisting of randomly oriented sub-wavelength particles was conducted. By exploiting near-field plasmonic interaction in a dense ensemble of subwavelength-sized dielectric and metallic particles, it was revealed that the group refractive index of the composite can be increased to be larger than the effective refractive indices of constituent metallic and dielectric *parent* composites. These findings introduce a new class of engineered photonic materials having customizable and atypical optical constants.

Finally, THz-TDS was utilized for imaging dielectric objects embedded in metal-filled media. By exploiting the time domain information from the transmitted

pulse, signatures of the objects were observed. To enhance the low quality images acquired through THz time domain spectroscopy, a super-resolution image processing technique was applied. It was shown that pulse arrival time and phase magnitude information compared to the integrated instantaneous power of the transmitted pulse provides more detailed images of the embedded object.

CHAPTER 6

Conclusions

In Chapter 2, a new class of PC THz emitters using fractal geometry has been presented and thoroughly investigated. While the characteristics of fractal antennas at GHz frequencies have been vastly studied, little is known about their emission properties in the terahertz regime. In this work a new class of plasmonic photoconductive THz emitters based on complementary Sierpinski gasket fractal geometry was presented. By engineering the antenna surface to have perforations of dimensions less than the wavelength of the excited radiation, the THz generated from the PC gap is coupled to the sub-wavelength structures through surface plasmons. Through utilizing THz-TDS, photoconductive THz emitters exhibiting ~80% increase in the emitted THz radiation power to conventional bow-tie and Sierpinski gasket THz emitters are demonstrated. It is shown that the self-similar current distribution is the key in the observed enhanced THz emission. Due to their higher radiation power and better signal to noise (S/N) ratios, these emitters are ideal for situations when higher THz signals (S/N) are required such as in THz-TDS systems. In addition, we presented on a special class of plasmonic THz dipole emitters based on Apollonian fractal geometry. By utilizing the Apollonian spatial distribution of plasmonic surface current, we have shown that higher order fractal THz emitters exhibit improved performance over their lower order counterparts. The complementary second-order Apollonian fractal provided up to ~60% enhancement of THz radiation power in comparison to all other fractals and the circular THz dipole emitters. Finally, the effect of self-similarity in THz fractal photoconductive THz emitters has been studied in detail. For this, new classes of PC THz emitters and non-fractal emitters have been proposed and their radiation properties have been compared to the bow-tie and fractal PC THz emitters. It is shown that self-similarity of the antenna

surface of the PC THz emitters is a key factor in enhancing the emitted THz radiation power.

In Chapter 3, the improved metal-insulator-metal diodes has been presented and thoroughly investigated. It is shown that the asymmetry and nonlinearity characteristics of these rectifiers outperform the conventional MIM design. In this chapter a metal-insulator-insulator-metal quantum tunneling device having superior I-V characteristics in comparison to conventional metal-insulator-metal devices was presented. Through the introduction of a cascaded potential barrier, different mechanisms for electron tunneling under forward and reverse bias were realized. A high I-V nonlinearity, up to 10 times that of conventional MIM devices, was obtained for identical metal electrodes. Finally, through the incorporation of resonant tunneling mechanism, a new class of electron tunneling devices consisting of a metal-insulator-insulator-insulator-metal (MIIM) was demonstrated. These electron tunneling devices are shown to exhibit extreme asymmetry and high non-linearity that is sought after for tunneling devices. It is shown that modification of the order of the ultrathin oxide layers modifies the form of the potential barrier, and thus alters the conduction of electrons across the junction. Through material selection of appropriate oxide materials, potential barriers having cascaded ($\text{Cr}_2\text{O}_3\text{-HfO}_2\text{-Al}_2\text{O}_3$) and non-cascaded ($\text{Cr}_2\text{O}_3\text{-Al}_2\text{O}_3\text{-HfO}_2$) profiles were fabricated and successfully characterized. The MIIM devices are demonstrated to possess superior properties compared to the MIM ones. The importance of the present demonstration lies in enhancing the characteristics of electron tunneling devices through potential barrier material-engineering. These findings are significant in the development of future electron tunneling devices in many disciplines for either high or low voltage operations. Specifically, this MIIM diode is suitable for the improved ultrafast terahertz radiation detectors.

In Chapter 4, the design parameters for an antenna coupled, MIM diode utilized as a THz detector has been investigated. In addition, the fabrication procedure required for obtaining an operational detector has been comprehensively explained. Utilizing the finalized process, three detectors were fabricated and tested. Finally, a proposed modified lift-off technique required for the fabrication of the

detectors is demonstrated. An innovative damascene lift-off process with high yield and high reproducibility is introduced. It has been shown that the features resulting from this lift-off process strongly adhere to the substrate, and that resultant edge roughness is minimal. In this way, some of the disadvantages of the conventional lift-off process are overcome. This novel lift-off technique can be utilized in fabrication processes from microscale down to nanoscale, as well as in a standard base process for inlaid fabrication.

In Chapter 5, THz-TDS has been utilized as both a characterization as well as an imaging tool. For this, a versatile all-THz pump-probe spectroscopy system, which is suitable for studying picosecond time scale phenomena, is introduced. By utilizing two independent photoconductive THz emitters, the need for any specialized THz optical components, such as beam splitters, phase shifters, and polarization rotators were eliminated. This setup can be easily implemented with minimal alteration to a conventional THz time domain spectroscopy (THz-TDS) system. The purpose of this setup was to test the temporal and spectral response of the fabricated antenna coupled MIIM, and MIIIM diodes. This system was initially tested on characterizing the time resolved dynamics of THz particle plasmons. In this research the interaction and effect of induced surface charges on the propagation of THz radiation was investigated. In the next step, the interaction of THz radiation with composite media was investigated. This was to extend the application of THz in characterizing composite media consisting metallic media as well as imaging inside metallic media. Finally, THz-TDS was utilized for imaging dielectric objects embedded in metal-filled media. By exploiting the time domain information from the transmitted pulse, signatures of the objects were observed. To enhance the low quality images acquired through THz time domain spectroscopy, a super-resolution image processing technique was applied. It is important to note that these experiments were for justifying the concept of THz imaging inside complex materials.

6.1 Future work

Some directions for the future research in this area are as follows:

(1) Employ the fractal THz emitters and the THz detectors fabricated in the course of this thesis, for constructing more sensitive and high speed THz imaging, sensing and spectroscopy systems.

(2) Utilize chemical mechanical polishing (CMP) in the fabrication of antenna coupled MIIM and MIIIM diodes. The CMP can be used to for fabricating the first electrode fully inlaid into the substrate. For this, after the damascene lift-off process, the chip undergoes a CMP process step. CMP causes the surface as well as the edges of the deposited electrode to be ultra-smooth independent of the material deposition technique. As mentioned in the section on fabrication of MIM diodes, the most critical factors in the fabrication of such diodes are the quality of the sandwich oxide as well as the surface roughness of the electrodes. Through incorporating CMP process into fabricating arrays of antenna coupled MIIM and MIIIM diodes, the yield and reproducibility of the fabrication process is significantly improved.

(3) Here antenna coupled MIIM and MIIIM diodes have been utilized as single detectors. Furthermore, by having an array of such detectors, one can detect the presence of THz radiation and directly perform THz imaging. The object desired will be irradiated by a THz source and the reflected/transmitted radiation will be introduced to the array of THz detectors. Depending on the intensity that each element receives, a signal will be sent to a multiplexing system. The multiplexing system will then output a contrast difference map of the object. Using image process techniques, an image will be reconstructed from the contrast map captured by the multiplexing system. Due to the properties of THz radiation, there has been an increasing interest in utilizing terahertz (THz) radiation for imaging, spectroscopy, and sensing. Therefore, the proposed THz imaging device could replace traditional imaging systems due to its fast response and potentially high resolution.

References

1. Dexheimer, S.L., *Terahertz Spectroscopy: Principles and Applications*. 2008, Boca Raton, FL: Taylor & Francis Group (CRC Press).
2. Mittleman, D., *Sensing with Terahertz Radiation*. 2003: Springer.
3. X. C. Zhang, J.X., *Introduction to THz Wave Photonics* 2010, New York: Springer.
4. Jansen, C., et al., *Terahertz imaging: applications and perspectives*. Applied Optics, 2010. **49**(19): p. E48-E57.
5. Siegel, P.H., *Terahertz technology*. Microwave Theory and Techniques, IEEE Transactions on, 2002. **50**(3): p. 910-928.
6. Doi, Y., et al., *Large-format and compact stressed Ge : Ga array for the ASTRO-F (IRIS) mission*, in *New Results in Far Ir and Sub-Mm Astronomy*, R. Szczerba, Editor. 2002, Pergamon-Elsevier Science Ltd: Oxford. p. 2099-2104.
7. Fujiwara, M., et al., *Development of a gallium-doped germanium far-infrared photoconductor direct hybrid two-dimensional array*. Applied Optics, 2003. **42**(12): p. 2166-2173.
8. Fischer, B.M., et al., *Terahertz time-domain spectroscopy and imaging of artificial RNA*. Optics Express, 2005. **13**(14): p. 5205-5215.
9. Son, J.H., *Terahertz electromagnetic interactions with biological matter and their applications*. Journal of Applied Physics, 2009. **105**(10).
10. Chen, J.Y., et al., *Large oxidation dependence observed in terahertz dielectric response for cytochrome c*. Physical Review E, 2005. **72**(4).
11. Kawase, K., et al., *Non-destructive terahertz imaging of illicit drugs using spectral fingerprints*. Optics Express, 2003. **11**(20): p. 2549-2554.
12. Karpowicz, N., et al., *Compact continuous-wave subterahertz system for inspection applications*. Applied Physics Letters, 2005. **86**(5): p. 054105.
13. Morita, Y., et al., *Terahertz technique for detection of microleaks in the seal of flexible plastic packages*. Optical Engineering, 2005. **44**(1): p. 019001.
14. Auston, D.H., K.P. Cheung, and P.R. Smith, *Picosecond photoconducting Hertzian dipoles*. Applied Physics Letters, 1984. **45**(3): p. 284-286.
15. Fattinger, C. and D. Grischkowsky, *Terahertz beams*. Applied Physics Letters, 1989. **54**(6): p. 490-492.
16. Fattinger, C. and D. Grischkowsky, *Point-source terahertz optics*. Applied Physics Letters, 1988. **53**(16): p. 1480-1482.
17. Lee, Y.S., *Principles of Terahertz Science and Technology*. 2008, New York: Springer.
18. Jepsen, P.U., D.G. Cooke, and M. Koch, *Terahertz spectroscopy and imaging - Modern techniques and applications*. Laser & Photonics Reviews, 2011. **5**(1): p. 124-166.
19. Tani, M., et al., *Emission characteristics of photoconductive antennas based on low-temperature-grown GaAs and semi-insulating GaAs*. Applied Optics, 1997. **36**(30): p. 7853-7859.

20. Maraghechi, P. and A.Y. Elezzabi, *Enhanced THz radiation emission from plasmonic complementary Sierpinski fractal emitters*. Optics Express, 2010. **18**(26): p. 27336-27345.
21. Richards, P.L., *Bolometers for infrared and millimeter waves*. Journal of Applied Physics, 1994. **76**(1): p. 1-24.
22. Golay, M.J.E., *The Theoretical and Practical Sensitivity of the Pneumatic Infra-Red Detector*. Review of Scientific Instruments, 1949. **20**(11): p. 816-820.
23. Sze, S.M., *Physics of Semiconductor Devices*. 2nd ed. 1981, New York: John Wiley & Sons.
24. Otani, C., et al. *Terahertz direct detector using superconducting tunnel junctions*. 2004. SPIE.
25. Vardoulakis, G., et al., *Superconducting kinetic inductance detectors for astrophysics*. Measurement Science & Technology, 2008. **19**(1).
26. Nahata, A., et al., *Coherent detection of freely propagating terahertz radiation by electro-optic sampling*. Applied Physics Letters, 1996. **68**(2): p. 150-152.
27. Wu, Q. and X.C. Zhang, *Free-space electrooptic sampling of terahertz beams*. Applied Physics Letters, 1995. **67**(24): p. 3523-3525.
28. Holzman, J.F., *Ultrafast photonic applications for terahertz waveform generation*, in *Electrical and Computer Engineering 2003*, University of Alberta: Canada.
29. Trager, F., *Springer Handbook of Lasers and Optics*. 2007, New York: Springer.
30. Siebert, K.J., et al., *Continuous-wave all-optoelectronic terahertz imaging*. Applied Physics Letters, 2002. **80**(16): p. 3003-3005.
31. Miyamaru, F., et al., *Dependence of emission of terahertz radiation on geometrical parameters of dipole photoconductive antennas*. Applied Physics Letters, 2010. **96**(21): p. 211104.
32. Shen, Y.C., et al., *Ultrabroadband terahertz radiation from low-temperature-grown GaAs photoconductive emitters*. Applied Physics Letters, 2003. **83**(15): p. 3117-3119.
33. Mendis, R., et al., *Tunable CW-THz system with a log-periodic photoconductive emitter*. Solid-State Electronics, 2004. **48**(10-11): p. 2041-2045.
34. Vanexter, M., C. Fattinger, and D. Grischkowsky, *High-brightness terahertz beams characterized with an ultrafast detector*. Applied Physics Letters, 1989. **55**(4): p. 337-339.
35. Tani, M., et al., *Novel Terahertz Photoconductive Antennas*. International Journal of Infrared and Millimeter Waves, 2007. **27**(4): p. 531-546.
36. Awad, M., et al., *Characterization of low temperature GaAs antenna array terahertz emitters*. Applied Physics Letters, 2007. **91**(18).
37. Miyamaru, F., et al., *Emission of terahertz radiations from fractal antennas*. Applied Physics Letters, 2009. **95**(22): p. 221111.
38. Anguera, J., et al., *Small and high-directivity bow-tie patch antenna based on the Sierpinski fractal*. Microwave and Optical Technology Letters, 2001. **31**(3): p. 239-241.

39. Mandelbrot, B.B., *The Fractal Geometry of Nature*. 1983, New York: W. H. Freeman and Company
40. H. O. Peitgen, H.J., and D. Saupe, *Chaos and Fractals: New Frontiers of Science*. 1990, New York: Springer-Verlag.
41. Jaggard, D.L., *On Fractal Electrodynamics*. Recent Advances in Electromagnetic Theory ed. H.N.K.a.D.L. Jaggard. 1990, New York: Springer-Verlag.
42. Jaggard, D.L. and T. Spielman, *TRIADIC CANTOR TARGET DIFFRACTION*. Microwave and Optical Technology Letters, 1992. **5**(9): p. 460-466.
43. Kim, Y. and D.L. Jaggard, *The fractal random array*. Proceedings of the IEEE, 1986. **74**(9): p. 1278-1280.
44. Jaggard, D.L. and X.G. Sun, *Reflection from fractal multilayers*. Optics Letters, 1990. **15**(24): p. 1428-1430.
45. Werner, D.H. and S. Ganguly, *An overview of fractal antenna engineering research*. Antennas and Propagation Magazine, IEEE, 2003. **45**(1): p. 38-57.
46. C. Puente, J.R., A. Cardama, *Fractal-Shaped Antennas*, in *Frontiers in Electromagnetics*, R.M. D. H. Werner, Editor. 1999, Wiley-IEEE Press. p. 48-93.
47. Puente, C., et al., *Fractal multiband antenna based on the Sierpinski gasket*. Electronics Letters, 1996. **32**(1): p. 1-2.
48. Puente-Baliarda, C., et al., *On the behavior of the Sierpinski multiband fractal antenna*. Ieee Transactions on Antennas and Propagation, 1998. **46**(4): p. 517-524.
49. Puente, C., *Fractal Antennas*, in *Department of Signal Theory and Communications 1997*, Universitat Plitecnica de Catalunya
50. Gonzalez, J.M., et al., *Active zone self-similarity of fractal-Sierpinski antenna verified using infra-red thermograms*. Electronics Letters, 1999. **35**(17): p. 1393-1394.
51. Puente, C., et al., *Small but long Koch fractal monopole*. Electronics Letters, 1998. **34**(1): p. 9-10.
52. Breden, R. and R.J. Langley, *Printed fractal antennas*. IEE Conference Publications, 1999. **1999**(CP461): p. 1-4.
53. Liu, J.C., et al., *Relationship between Sierpinski gasket and Apollonian packing monopole antennas*. Electronics Letters, 2006. **42**(15): p. 847-848.
54. Harde, H. and D. Grischkowsky, *Coherent transients excited by subpicosecond pulses of terahertz radiation*. Journal of the Optical Society of America B-Optical Physics, 1991. **8**(8): p. 1642-1651.
55. Katzenellenbogen, N. and D. Grischkowsky, *Efficient generation of 380 fs pulses of thz radiation by ultrafast laser-pulse excitation of a biased metal-semiconductor interface*. Applied Physics Letters, 1991. **58**(3): p. 222-224.
56. Vanexter, M. and D.R. Grischkowsky, *Characterization of an optoelectronic terahertz beam system*. IEEE Transactions on Microwave Theory and Techniques, 1990. **38**(11): p. 1684-1691.

57. Smith, P.R., D.H. Auston, and M.C. Nuss, *Subpicosecond photoconducting dipole antennas*. IEEE Journal of Quantum Electronics, 1988. **24**(2): p. 255-260.
58. Rutledge, D.B., D.P. Neikirk, and D.P. Kasilingam, *Integrated-Circuit Antennas*, in *Infrared and Millimeter Waves*, K.J. Button and J.C. Wiltse, Editors. 1983, Academic Press. p. 1.
59. Frankel, M.Y., et al., *Terahertz attenuation and dispersion characteristics of coplanar transmission-lines*. Ieee Transactions on Microwave Theory and Techniques, 1991. **39**(6): p. 910-916.
60. G.H. Brown and O.M. Woodward, *Experimentally determined radiation characteristics of conical and triangular antennas* RCA Rev., 1952. **13**.
61. Fumeaux, C., et al., *Nanometer thin-film Ni-NiO-Ni diodes for detection and mixing of 30 THz radiation*. Infrared Physics & Technology, 1998. **39**(3): p. 123-183.
62. Maraghechi, P. and A. Elezzabi, *Experimental Confirmation of Design Techniques for Effective Bow-Tie Antenna Lengths at THz Frequencies*. Journal of Infrared, Millimeter and Terahertz Waves, 2011. **32**(7): p. 897-901.
63. Karlsson, M. and S.F. Gong, *Circular Dipole Antenna for Mode 1 UWB Radio With Integrated Balun Utilizing a Flex-Rigid Structure*. IEEE Transactions on Antennas and Propagation, 2009. **57**(10): p. 2967-2971.
64. Graham, R.L., et al., *Apollonian circle packings: Geometry and group theory I. The Apollonian group*. Discrete & Computational Geometry, 2005. **34**(4): p. 547-585.
65. Maraghechi, P. and A. Elezzabi, *The Role of Self-Similarity in Fractal Photoconductive THz Emitters*. Journal of Infrared, Millimeter and Terahertz Waves, 2011. **32**(11): p. 1285-1290.
66. Mazumder, P., et al., *Digital circuit applications of resonant tunneling devices*. Proceedings of the IEEE, 1998. **86**(4): p. 664-686.
67. Wolf, S.A., et al., *The Promise of Nanomagnetism and Spintronics for Future Logic and Universal Memory*. Proceedings of the IEEE, 2010. **98**(12): p. 2155-2168.
68. Berggren, K.K., *Quantum computing with superconductors*. Proceedings of the IEEE, 2004. **92**(10): p. 1630-1638.
69. Prober, D.E., et al., *Ultrasensitive quantum-limited far-infrared STJ detectors*. Ieee Transactions on Applied Superconductivity, 2007. **17**(2): p. 241-245.
70. Meng, X.F., et al., *Micron and submicron Nb/Al-AlO_x/Nb tunnel junctions with high critical current densities*. Ieee Transactions on Applied Superconductivity, 2001. **11**(1): p. 365-368.
71. Esaki, L., *New Phenomenon in Narrow Germanium p-n Junctions*. Physical Review, 1958. **109**(2): p. 603-604.
72. Moagar-Poladian, G., *Theory of the basic optoelectronic behavior of a tunnel diode*. Applied Optics, 2001. **40**(33): p. 6086-6097.
73. Tsu, R. and L. Esaki, *Tunneling in a finite superlattice*. Applied Physics Letters, 1973. **22**(11): p. 562-564.
74. Chang, L.L., L. Esaki, and R. Tsu, *Resonant tunneling in semiconductor double barriers*. Applied Physics Letters, 1974. **24**(12): p. 593-595.

75. Shewchuk, T.J., et al., *Resonant tunneling oscillations in a GaAs-AlxGa1-xAs heterostructure at room-temperature*. Applied Physics Letters, 1985. **46**(5): p. 508-510.
76. Ng, K.K., *Complete Guide to Semiconductor Devices*. 2002: Wiley-IEEE Press.
77. Brown, E.R., et al., *High-speed resonant-tunneling diodes made from the In_{0.53}Ga_{0.47}As material system*. High-Speed Electronics and Device Scaling, ed. L.F. Eastman. Vol. 1288. 1990, Bellingham: Spie - Int Soc Optical Engineering. 122-135.
78. Sanchez, A., et al., *MOM tunneling diode - theoretical estimate of its performance at microwave and infrared frequencies*. Journal of Applied Physics, 1978. **49**(10): p. 5270-5278.
79. Wilke, I., et al., *Nanometer thin-film Ni-NiO-Ni diodes for 30 THz radiation*. Applied Physics a-Materials Science & Processing, 1994. **58**(4): p. 329-341.
80. Kale, B.M., *Electron-tunneling devices in optics*. Optical Engineering, 1985. **24**(2): p. 267-274.
81. Badri Tiwari, et al., *Controlled etching and regrowth of tunnel oxide for antenna-coupled metal-oxide-metal diodes*. J. Vac. Sci. Technol. B, 2009. **27**.
82. Esfandiari, P., et al., *Tunable antenna-coupled metal-oxide-metal (MOM) uncooled IR detector*, in *Infrared Technology and Applications XXXI*, B.F. Andresen and G.F. Fulop, Editors. 2005, SPIE: Bellingham. p. 470-482.
83. Hobbs, P.C.D., R.B. Laibowitz, and F.R. Libsch, *Ni-NiO-Ni tunnel junctions for terahertz and infrared detection*. Applied Optics, 2005. **44**(32): p. 6813-6822.
84. Wilke, I., W. Herrmann, and F.K. Kneubuhl, *Integrated nanostrip dipole antennas for coherent 30 thz infrared radiation*. Applied Physics B-Lasers and Optics, 1994. **58**(2): p. 87-95.
85. Corkish, R., M.A. Green, and T. Puzzer, *Solar energy collection by antennas*. Solar Energy, 2002. **73**(6): p. 395-401.
86. Bean, J., et al., *Nanoantenna Infrared Detectors*, in *Cellular Nanoscale Sensory Wave Computing*, C. Baatar, W. Porod, and T. Roska, Editors. 2010, Springer. p. 27-86.
87. Hauge, E.H. and J.A. Stovneng, *Tunneling times - a critical-review*. Reviews of Modern Physics, 1989. **61**(4): p. 917-936.
88. Simmons, J.G., *Generalized formula for electric tunnel effect between similar electrodes separated by a thin insulating film*. Journal of Applied Physics, 1963. **34**(6): p. 1793-&.
89. Simmons, J.G., *Electric tunnel effect between dissimilar electrodes separated by a thin insulating film*. Journal of Applied Physics, 1963. **34**(9): p. 2581-&.
90. Heiblum, M., et al., *Characteristics of integrated mom junctions at dc and at optical frequencies*. Ieee Journal of Quantum Electronics, 1978. **14**(3): p. 159-169.
91. Carelli, G., et al., *On the work mechanism of MIM point contact diodes*. International Journal of Infrared and Millimeter Waves, 1992. **13**(8): p. 1099-1114.

92. Dees, J.W., *Detection and harmonic generation in the submillimeter wavelength region*. Microwave J., 1966. **9**: p. 48-55.
93. Gustafso.Tk, R.V. Schmidt, and J.R. Perucca, *Optical detection in thin-film metal-oxide-metal diodes*. Applied Physics Letters, 1974. **24**(12): p. 620-622.
94. Elchinger, G.M., et al., *Mechanism of detection of radiation in a high-speed metal-metal oxide-metal junction in visible region and at longer wavelengths*. Journal of Applied Physics, 1976. **47**(2): p. 591-594.
95. Wiesendanger, E. and F. Kneubuhl, *Thin-film MOM-diodes for IR detection*. Applied Physics, 1977. **13**(4): p. 343-349.
96. Krishnan, S., E. Stefanakos, and S. Bhansali, *Effects of dielectric thickness and contact area on current-voltage characteristics of thin film metal-insulator-metal diodes*. Thin Solid Films, 2008. **516**(8): p. 2244-2250.
97. Berland, B., *Photovoltaic Technologies Beyond the Horizon: Optical Rectenna Solar Cell*, 2003, NREL.
98. Krishnan, S., et al., *Design and development of batch fabricatable metal-insulator-metal diode and microstrip slot antenna as rectenna elements*. Sensors and Actuators a-Physical, 2008. **142**(1): p. 40-47.
99. Cowell, E.W., et al., *Advancing MIM Electronics: Amorphous Metal Electrodes*. Advanced Materials, 2011. **23**(1): p. 74-+.
100. Eliasson, B.J., *Metal-Insulator-Metal Diodes For Solar Energy Conversion*, in *Electrical and Computer Engineering*2001, University of Colorado.
101. Puurunen, R.L., *Surface chemistry of atomic layer deposition: A case study for the trimethylaluminum/water process*. Journal of Applied Physics, 2005. **97**(12): p. 121301.
102. Maraghechi, P., et al., *Enhanced rectifying response from metal-insulator-insulator-metal junctions*. Applied Physics Letters, 2011. **99**(25): p. 253503.
103. Periasamy, P., et al., *Fabrication and Characterization of MIM Diodes Based on Nb/Nb(2)O(5) Via a Rapid Screening Technique*. Advanced Materials, 2011. **23**(27): p. 3080-+.
104. Di Ventra, M., et al., *Indented barrier resonant tunneling rectifiers*. Journal of Applied Physics, 1996. **80**(7): p. 4174-4176.
105. Maraghechi, P., et al., *Observation of resonant tunneling phenomenon in metal-insulator-insulator-insulator-metal electron tunnel devices*. Applied Physics Letters, 2012. **100**(11): p. 113503.
106. Schulz, P.A. and C. Dasilva, *Two-step Barrier Diodes*. Applied Physics Letters, 1988. **52**(12): p. 960-962.
107. Esfandiari P. , e.a. *Tunable Antenna-Coupled Metal-Oxide-Metal (MOM) Uncooler IR Detector*. in *Proc. SPIE*. 2005.
108. Small, J.G., et al., *Ac Electron Tunneling at Infrared Frequencies - Thin-Film M-O-M Diode Structure with Broad-Band Characteristics*. Applied Physics Letters, 1974. **24**(6): p. 275-279.
109. Wang, S.Y., T. Izawa, and T.K. Gustafson, *Coupling Characteristics of Thin-Film Metal-Oxide-Metal Diodes at 10.6 Mum*. Applied Physics Letters, 1975. **27**(9): p. 481-483.
110. H. C. Torrey and C.A. Whitmer, *Crystal Rectifiers*. 1984, New York: McGraw Hill.

111. Fisher, J.C. and I. Giaever, *Tunneling through thin insulating layers*. Journal of Applied Physics, 1961. **32**(2): p. 172-&.
112. Maraghechi, P., K. Cadien, and A.Y. Elezzabi, *A Novel Nanofabrication Damascene Lift-Off Technique*. IEEE Transactions on Nanotechnology, 2011. **10**(4): p. 822-826.
113. Maraghechi, P. and A.Y. Elezzabi, *The design of a reversible wafer holder for uniform photoresist coatings of deeply etched cavities*. Measurement Science & Technology, 2008. **19**(8).
114. P. Maraghechi, A.Y. Elezzabi, and K. Cadien, *Damascene Lift-Off Process* U.o. Alberta, Editor 2009.
115. Halverson, R.M., M.W. MacIntyre, and W.T. Motsiff, *The Mechanism of Single-Step Liftoff with Chlorobenzene in a Diazo-Type Resist*. IBM Journal of Research and Development, 1982. **26**(5): p. 590-595.
116. Hatzakis, M., B.J. Canavello, and J.M. Shaw, *Single-Step Optical Lift-Off Process*. IBM Journal of Research and Development, 1980. **24**(4): p. 452-460.
117. Liang, J., et al., *Improved bi-layer lift-off process for MEMS applications*. Microelectronic Engineering, 2008. **85**(5-6): p. 1000-1003.
118. West, P.R., K.J. Polasko, and C.L. Fasoldt, *A metal liftoff process facilitated by the use of contrast enhanced photolithography*. Journal of Vacuum Science & Technology B: Microelectronics and Nanometer Structures, 1987. **5**(1): p. 449-453.
119. Hwang, S.Y., et al., *Fabrication of nano-sized metal patterns on flexible polyethylene-terephthalate substrate using bi-layer nanoimprint lithography*. Thin Solid Films, 2009. **517**(14): p. 4104-4107.
120. Macintyre, D.S., et al., *Resist residues and transistor gate fabrication*. Journal of Vacuum Science & Technology B: Microelectronics and Nanometer Structures, 2009. **27**(6): p. 2597-2601.
121. Jebril, S., et al., *Integration of Thin-Film-Fracture-Based Nanowires into Microchip Fabrication*. Small, 2008. **4**(12): p. 2214-2221.
122. Damghanian, M. and B.Y. Majlis. *A modified lift-off technique to prevent pattern following effect in microfabrication*. in *Semiconductor Electronics, 2008. ICSE 2008. IEEE International Conference on*. 2008.
123. Wijngaards, D., M. Bartek, and R.F. Wolffenbuttel, *Silicon ic process compatible thin metal film post-processing module*. Sensors and Actuators A: Physical, 1998. **68**(1-3): p. 419-428.
124. Tong, H.D., et al., *Platinum patterning by a modified lift-off technique and its application in a silicon load cell*. Sensors and Materials, 2001. **13**(4): p. 235-246.
125. Brault, P., P. Dumas, and F. Salvan, *Roughness scaling of plasma-etched silicon surfaces*. Journal of Physics-Condensed Matter, 1998. **10**(1): p. L27-L32.
126. Shah, J., *Ultrafast spectroscopy of semiconductors and semiconductor nanostructures*. 1999, New York: Springer.
127. Gloskovskii, A., et al., *Electron emission from films of Ag and Au nanoparticles excited by a femtosecond pump-probe laser*. Physical Review B, 2008. **77**(19).

128. Schmuttenmaer, C.A., *Exploring dynamics in the far-infrared with terahertz spectroscopy*. Chemical Reviews, 2004. **104**(4): p. 1759-1779.
129. Hoffmann, M.C., et al., *THz-pump/THz-probe spectroscopy of semiconductors at high field strengths Invited*. Journal of the Optical Society of America B-Optical Physics, 2009. **26**(9): p. A29-A34.
130. You, D., et al., *Generation of high-power sub-single-cycle 500-fs electromagnetic pulses*. Optics Letters, 1993. **18**(4): p. 290-292.
131. Greene, B.I., et al., *Interferometric characterization of 160 fs far-infrared light-pulses*. Applied Physics Letters, 1991. **59**(8): p. 893-895.
132. Homes, C.C., et al., *Silicon beam splitter for far-infrared and terahertz spectroscopy*. Applied Optics, 2007. **46**(32): p. 7884-7888.
133. Maier, S.A. and H.A. Atwater, *Plasmonics: Localization and guiding of electromagnetic energy in metal/dielectric structures*. Journal of Applied Physics, 2005. **98**(1).
134. Chau, K.J., G.D. Dice, and A.Y. Elezzabi, *Coherent plasmonic enhanced terahertz transmission through random metallic media*. Physical Review Letters, 2005. **94**(17).
135. Chau, K., *Terahertz electromagnetic wave interaction with mesoscopic media*, in *Department of Electrical and Computer Engineering 2008*, University of Alberta: Canada.
136. Straatsma, C.J.E., *An Investigation of Magnetically Active Terahertz Devices*, in *Department of Electrical and Computer Engineering 2011*, University of Alberta: Canada.
137. Chau, K.J. and A.Y. Elezzabi, *Photonic anisotropic magnetoresistance in dense Co particle ensembles*. Physical Review Letters, 2006. **96**(3).
138. Chau, K.J., M. Johnson, and A.Y. Elezzabi, *Electron-spin-dependent terahertz light transport in spintronic-plasmonic media*. Physical Review Letters, 2007. **98**(13).
139. Straatsma, C., M. Startsev, and A. Elezzabi, *An Investigation of Terahertz Particle Plasmons: Affect of Particle Size on the Transparency of a Metallic Particle Ensemble*. Journal of Infrared, Millimeter and Terahertz Waves, 2010. **31**(6): p. 659-666.
140. Chau, K.J. and A.Y. Elezzabi, *Terahertz transmission through ensembles of subwavelength-size metallic particles*. Physical Review B, 2005. **72**(7): p. 075110.
141. Wang, K.L. and D.M. Mittleman, *Dispersion of surface plasmon polaritons on metal wires in the terahertz frequency range*. Physical Review Letters, 2006. **96**(15).
142. Bonfiglioli, G., E. Coen, and R. Malvano, *Modulation of Conductivity by Surface Charges in Metals*. Physical Review, 1956. **101**(4): p. 1281-1284.
143. Bonfiglioli, G. and R. Malvano, *Surface States in Metals*. Physical Review, 1959. **115**(2): p. 330-335.
144. Elezzabi, A.Y., et al., *A plasmonic random composite with atypical refractive index*. Optics Express, 2009. **17**(2): p. 1016-1022.

145. Mujumdar, S., K.J. Chau, and A.Y. Elezzabi, *Experimental and numerical investigation of terahertz transmission through strongly scattering sub-wavelength size spheres*. Applied Physics Letters, 2004. **85**(25): p. 6284-6286.
146. Choy, T.C., *Effective medium theory: principles and applications*. 1999, New York: Oxford University Press.
147. Vollmer, U.K.a.M., *Optical Properties of Metal Clusters*. Vol. 25. 1995, Berlin: Springer-Verlag.
148. Ordal, M.A., et al., *Optical-properties of 14 metals in the infrared and far infrared - AL, CO, CU, AU, FE, PB, MO, NI, PD, PT, AG, TI, V, and W*. Applied Optics, 1985. **24**(24): p. 4493-4499.
149. Grischkowsky, D., et al., *Far-infrared time-domain spectroscopy with terahertz beams of dielectrics and semiconductors*. Journal of the Optical Society of America B-Optical Physics, 1990. **7**(10): p. 2006-2015.
150. C. F. Bohren, D.R.H., *Absorption and Scattering of Light by Small Particles*. 1983, New York: Willey.
151. Hu, B.B. and M.C. Nuss, *Imaging with terahertz waves*. Optics Letters, 1995. **20**(16): p. 1716-&.
152. Hoshina, H., et al., *Terahertz pulsed imaging of frozen biological tissues*. Applied Physics Letters, 2009. **94**(12): p. 123901.
153. Chan, W.L., J. Deibel, and D.M. Mittleman, *Imaging with terahertz radiation*. Reports on Progress in Physics, 2007. **70**(8): p. 1325-1379.
154. Behnken, B.N., et al., *Real-time imaging using a 2.8 THz quantum cascade laser and uncooled infrared micrometer camera*. Optics Letters, 2008. **33**(5): p. 440-442.
155. Wang, S. and X.C. Zhang, *Pulsed terahertz tomography*. Journal of Physics D-Applied Physics, 2004. **37**(4): p. R1-R36.
156. Hong, C., Y. Dit-Yan, and X. Yimin. *Super-resolution through neighbor embedding*. in *Computer Vision and Pattern Recognition, 2004. CVPR 2004. Proceedings of the 2004 IEEE Computer Society Conference on*. 2004.
157. R. C. Gonzalez, a.R.E.W., *Digital Image Processing*. Second ed. 2002, NJ: Prentice Hall.
158. Cimalla, V., J. Pezoldt, and O. Ambacher, *Group III nitride and SiC based MEMS and NEMS: materials properties, technology and applications*. Journal of Physics D-Applied Physics, 2007. **40**(20): p. 6386-6434.
159. Walker, J.A., *The future of MEMS in telecommunications networks*. Journal of Micromechanics and Microengineering, 2000. **10**(3): p. R1-R7.
160. Sun, Y. and B.J. Nelson, *MEMS capacitive force sensors for cellular and flight biomechanics*. Biomedical Materials, 2007. **2**(1): p. S16-S22.
161. Yong-Kyu, Y., P. Jung-Hwan, and M.G. Allen, *Multidirectional UV Lithography for Complex 3-D MEMS Structures*. Microelectromechanical Systems, Journal of, 2006. **15**(5): p. 1121-1130.
162. Han, M., et al., *3D microfabrication with inclined/rotated UV lithography*. Sensors and Actuators A: Physical, 2004. **111**(1): p. 14-20.
163. Rooks, M.A.M.a.M.J.P., *Handbook of Microlithography, Micromachining, and Microfabrication*, ed. P. Rai-Choudhury. Vol. 1. 1997, Bellingham: SPIE.

164. Matsui, S. and Y. Ochiai, *Focused ion beam applications to solid state devices*. Nanotechnology, 1996. **7**(3): p. 247-258.
165. Grogg, D., N. Badila-Ciressan, and A. Ionescu, *Focussed ion beam based fabrication of micro-electro-mechanical resonators*. Microsystem Technologies, 2008. **14**(7): p. 1049-1053.
166. Kutchoukov, V.G., J.R. Mollinger, and A. Bossche, *New photoresist coating method for 3-D structured wafers*. Sensors and Actuators A: Physical, 2000. **85**(1-3): p. 377-383.
167. Kutchoukov, V.G., et al., *Patterning of polyimide and metal in deep trenches*. Sensors and Actuators A: Physical, 2001. **92**(1-3): p. 208-213.
168. Choi, C.H. and C.J. Kim, *Fabrication of a dense array of tall nanostructures over a large sample area with sidewall profile and tip sharpness control*. Nanotechnology, 2006. **17**(21): p. 5326-5333.
169. O'Brien, J., et al., *Advanced photoresist technologies for microsystems*. Journal of Micromechanics and Microengineering, 2001. **11**(4): p. 353-358.

APPENDIX A

Allowed energy levels in potential wells

As shown in Figure 3-18 at certain voltages at the interface of two oxides, a potential well forms. As described by quantum mechanics, there are allowed energy levels associated with a potential well. For example, the potential well formed between the Cr_2O_3 - HfO_2 interface in a $\text{Cr}/\text{Al}_2\text{O}_3$ - HfO_2 - $\text{Cr}_2\text{O}_3/\text{Cr}$ structure at +2.6 V is shown in Figure A-1. The actual potential well formed in this device is shown in the solid black line. For calculating the allowed energies, of such potential well, the well is approximated by a rectangular well shown in dashed black lines in Figure A-1.

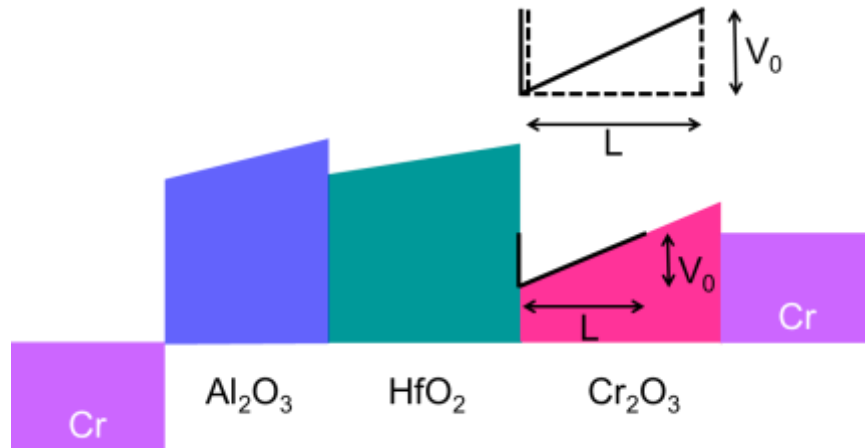


Figure A-1 Energy band diagram of the $\text{Cr}/\text{Cr}_2\text{O}_3$ - HfO_2 - $\text{Al}_2\text{O}_3/\text{Cr}$ device. The solid black lines depict the potential well. The inset on top depicts the approximated potential well profile (the dashed black line).

Here V_0 and L are the depth and the width of the potential well, respectively. V_0 and L for this structure are 0.8 eV and 1 nm at +2.7 V, respectively. The allowed energies of the quantum well is obtained by solving the Schrodinger equation of a finite square well in one dimension. This results in a transcendental equation:

$$\tan z = \sqrt{\frac{z_0^2}{z^2} - 1} \quad (\text{A.1})$$

here z is the single variable, and

$$\begin{aligned} z_0^2 &= \frac{mL^2V_0}{2\hbar^2} \\ z &= \frac{L\sqrt{2m(E+V_0)}}{2\hbar} \end{aligned} \tag{A.2}$$

where m is the mass of electron and E is the allowed potential well energy. Substituting, the values for V_0 and L and solving equation (A.1) numerically, the value of z is obtained (=1.3). Using equation (A.2) the value for E is -0.5 eV from the top of the potential well.

Numerical simulation of I-V curve characteristics of MIIM diodes has also been investigated. For this, the transmission coefficient is required to be calculated numerically. Due to the limitation of WKB approximation, transfer matrix formulation of quantum tunneling was utilized. In this approach the barrier is divided into a series of infinitesimally small sections and the transfer matrix is calculated for each interface. The transmission of the total barrier is then calculated by multiplying all of the individual transfer matrices from each interface. It is from the total transfer matrix that the tunneling probability of an electron is calculated. However, the tunneling probability calculated using this technique depicted singularities due to the special shape of the potential barrier profile in the MIIM structures.

APPENDIX B

MIM cut-off frequency

The cut-off frequency for the equivalent circuit for the diode with an integrated antenna (Figure B-1) is calculated in this appendix.

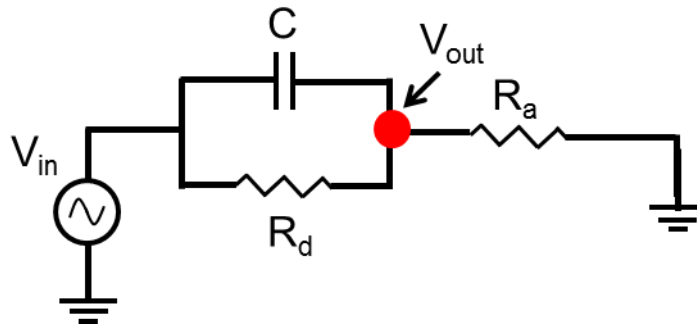


Figure B-1 The equivalent circuit for the MIM diode with an integrated antenna.

The ration between V_{out} (voltage across the diode) and V_{in} (voltage across the circuit) is defined as:

$$V_{out} = \frac{\frac{R_d}{R_d C_S + 1}}{\frac{R_d}{R_d C_S + 1} + R_a} V_{in} \quad (\text{B.1})$$

which can be simplified to:

$$V_{out} = \frac{R_d}{R_d + R_a (R_d C_S + 1)} V_{in} \quad (\text{B.2})$$

The transfer function for this circuit is:

$$H_c(s) = \frac{V_{out}}{V_{in}} \quad (\text{B.3})$$

The magnitude of the transfer function is:

$$|H(\omega)| = \frac{R_d}{\sqrt{(R_d + R_a)^2 + (R_d + R_a C \omega)^2}} \quad (\text{B.4})$$

At cut-off frequency (ω_c) the magnitude of the transfer function ($|H(\omega = \omega_c)|$) by definition reduces to $\frac{1}{\sqrt{2}}$ of its maximum value ($|H(\omega = 0)|$). This results in:

$$\omega_c = \frac{1}{C} \left(\frac{R_d + R_a}{R_d R_a} \right) \quad (\text{B.5})$$

In the case where $R_d \gg R_a$ this expression is reduced to:

$$\omega_c = \frac{1}{R_a C} \quad (\text{B.6})$$

APPENDIX C⁵

The design of a reversible wafer holder for uniform photoresist coating of deeply etched cavities

With the current development of complex microelectro-mechanical systems (MEMS) for a variety of device applications [158-160], it is often necessary to pattern small features situated deep within and especially near the sidewalls of etched vias. These fabrication processes require sophisticated micro/nanofabrication techniques, such as UV-photolithography [161, 162], electron beam lithography [163] or focused ion beam (FIB) milling [164]. While the latter technique is successful in fabricating deep sub-micron gaps [165] it is expensive to implement, and it requires a high level of expertise. Thus, it is desirable to develop a simple, inexpensive and fast process to fabricate micro or nanoscale features located at the bottom of cavities or trenches at various elevations using conventional lithographic techniques. However, there is a major challenge in that both UV and electron beam lithography require a uniform photoresist layer on the surface of the substrate to pattern and develop the desired features. In applying the photoresist layer, it is important to cover the wafer's surface evenly. When the thickness of the photoresist is variable across the wafer, the energy absorbed by the photoresist from either photons or electrons is nonuniformly distributed. In this case, only the top surfaces where the photoresist is thicker get lithographically exposed, and the consistency and the spatial dimensions of the exposed pattern are significantly degraded.

In order to satisfy the requirement for uniform photoresist coating, spin coating has been commonly employed for coating flat surfaces and surfaces having shallow 3D features. Here, the photoresist is dispensed on the surface and the wafer is

⁵ This work has been published by P. Maraghechi and A. Y. Elezzabi in, *Meas. Sci. Technol.*, **19**, 2008.

first slowly spun in order to spread the photoresist on the surface. This step is followed by a fast spin cycle to thin and dry the photoresist. The thickness of the photoresist layer is dependent on the spinning rate and the viscosity of the applied photoresist. However, this process is not suitable for patterning micro/nano features situated deep within or near the sidewalls of etched cavities.

To date, two techniques have been demonstrated for coating surfaces having nonplanar topography. (1) The spray coating technique: this method involves dispensing of a chemically diluted photoresist in the form of micrometer- sized droplets. During the spraying process, the spray head, which consists of an ultrasonic spray nozzle, is scanned across the wafer surface while the wafer is spun at 30–60 rpm. By slowly spinning the wafer, the centrifugal force acting on the photoresist droplets on the surface of the substrate is minimized; therefore, the surface of the wafer is perpendicularly impinged by the photoresist microdroplets and all topographic features on the wafer are evenly coated by the photoresist regardless of their elevation and location. Unfortunately, while spray coating has been shown to be an adequate method for coating 3D structures, there is no exact recipe for photoresist preparation; therefore, obtaining an applicable photoresist composition having both proper viscosity and solvent evaporation rate requires numerous empirical trials. (2) The electrodeposition coating technique. Here, prior to electrodeposition coating, the surface of interest is covered with a conductive layer. Then the wafer is positioned facing a metallic anode that is placed inside a cataphoretic photoresist emulsion cell in close proximity to wafer's surface. By applying a potential difference between the conductive wafer and the anode, the surface of the wafer is coated with the photoresist. The electrodeposition process is short and self-terminating where the thickness of the photoresist depends on the voltage applied and the bath temperature. It should be noted that this method results in better coating uniformity compared to the spray and spin coating methods. On the other hand, having to cover the wafer with a conductive layer and to use a special type of photoresist are disadvantageous.

Although spray coating and electrodeposition have been used for coating surfaces having nonplanar topography, a procedure that can be performed by minimally modifying the commonly available spin coating system is more desirable.

Kutchoukov *et al* [166] demonstrated a method for coating using a standard photoresist by spinning a semiconductor wafer having through holes from both sides. In addition, Kutchoukov *et al* [167] applied this method to spin coat and pattern polyimide in anisotropically wet-etched deep grooves. In their method, the wafer is spin coated in a conventional way. Then the wafer is flipped upside down, and spun again, to improve the uniformity of the coated photoresist layer. This procedure resulted in a uniform coverage of photoresist layer on the corners and sidewalls of an inclination of 54.7° . However, applying the same process for coating at the bottom and near-vertical sidewalls of deeply etched recesses was not demonstrated.

C1. Design of the wafer holder

The material used in fabricating the wafer holder is Teflon. The main attachment of the wafer holder is a 6 mm thick disc of 113.8 mm in diameter. As shown in Figure C-1, at the bottom face of the disc, a small 10 mm long cylindrical protrusion of an outer radius of 19 mm attaches the wafer holder to the spinner's rotating shaft (Specialty Coating System Inc. Model P6700 series). At the perimeter of the top surface of the disc, three 4.5 mm radius vertical posts are located at equidistance from the center, as shown in Figure C-1 [113]. Two of the posts are 10 mm long, and at a distance of 7 mm from their base attachment point, a 0.7 mm wide slit is cut such that it traverses to the center of the post. The slits serve as insert grooves that hold the wafer. The third post is 7 mm long where an 8-32 nylon thumbscrew is attached to its top surface. The thumbscrew is used to fasten the wafer to the post and, thus, prevents it from slipping out from the slits during the spinning process. By having one screw for fastening the wafer, the time necessary for flipping the wafer between stages of process (flipping from upside down to upside up) is greatly minimized to ~ 5 s. All the posts are fixed to the bottom of the attachment disc using 8-32 countersunk flat head nylon screws.

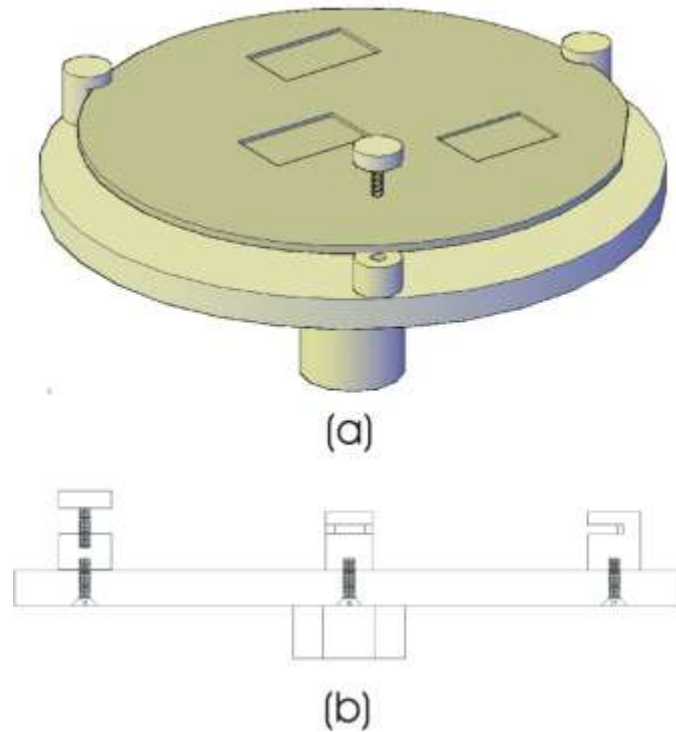


Figure C-1 (a) A schematic of the wafer holder with a mounted wafer showing a face up mounting arrangement. (b) Side view of the wafer holder used in the photoresist coating.

In order to produce photoresist uniform coating on a wafer having nonplanar topography, the photoresist is dispensed on the wafer's surface where the 3D features are located. The wafer is then turned over and inserted and secured to the wafer holder such that the surface containing features is faced down. This allows the excess photoresist to drain under the force of gravity from vias, cavities or trenches. After performing the spinning cycles, the thumbscrew is loosened and the wafer is flipped so that the surface of the wafer having the deep features faces up. Then the wafer is fastened back in the wafer holder post and spun again to evenly distribute the photoresist on the wafer's uppermost surface. This face down/face up spin coating process is expected to produce better and more uniform coverage compared to the conventional face up spin coating process. In contrast to the method by Kutchoukov *et al* [166, 167], where the wafer is spun face up in the first stage, in our method the wafer is spun face down in the first stage. It should be noted that spinning the wafer, faced down in the first stage (our procedure) allows the fresh and moist excess photoresist to drain down easily under the force of gravity. This results in less

accumulation of photoresist in close proximity to near-vertical sidewalls of deeply etched recesses. Thus, photoresist coating required for patterning small features situated deep within and especially near the sidewalls of etched cavities and recesses is obtained. Another major difference between the present work and the work reported by Kutchoukov *et al* is the fact that their coating process is suited for inclined walls rather than vertical ones. In their work, the sidewall angle of an anisotropically wet-etched groove is 54.7° , thus the access photoresist can up flow the wall much easier compared to a vertically deeply etch cavity. For this reason, our reported procedure is suitable for uniform photoresist coating at the bottom and near the vertical sidewalls of deeply etched cavities.

C2. Photoresist coating procedure

For our investigation of the above-mentioned design, we utilized a silicon wafer having deeply etched recesses. Here, 4 inch wafers were Piranha cleaned prior to the coating process. Using UV optical lithography (AB-M Contact Mode Mask Alignment System), a mask comprising $2\text{ mm} \times 3\text{ mm}$ rectangular features was used to pattern the wafers. The wafers were dry-etched using an inductively coupled plasma-reactive ion etch (STS MESC Multiplex ICP ASE) using a Bosch process [168] to produce two sets of $110\ \mu\text{m}$ and $300\ \mu\text{m}$ deep $2\text{ mm} \times 3\text{ mm}$ rectangular cavities.

A positive photoresist, AZ P4620 (AZ Electronic Materials), was used throughout our experiments. The coating procedure starts by pouring the photoresist on the prepared wafer and mounting the wafer upside down on the wafer holder. In order to slow down the photoresist drying rate, the wafer with its holder assembly is transferred into a sealed enclosure that is filled with a solvent vapor (ethyl lactate (98%, Aldrich)). The sealed enclosure is formed using a bowl with covering. Ethyl lactate is poured at the bottom of the bowl where the solvent vapor (ethyl lactate) slows down the photoresist drying rate. Figure C -2 shows a picture of the Teflon holder and the bowl.



Figure C -2 Image of the Teflon wafer holder in the bowl.

During the first spinning stage (features are faced down), the assembly is spun at 500 rpm for 11 s in order for the photoresist to spread on the wafer's surface. This is followed by a second spinning cycle of 29 s at 3500 rpm. Immediately after, the wafer is turned over (features are faced up) within ~5–7 s and the same spinning procedure is repeated. In order to remove the water and solvents present in the photoresist, the wafers are baked on a hot plate (Solitec Vacuum hot plate) at 102 ° C for 2.5 min after the completion of the spinning stage. The process flow is tabulated in Table C-1.

Table C-1 Process flow of the photoresist coating procedure.

Spin speed	Time	Soft bake	Exposure dose	Develop time	Hard bake
Face up		102 ° C for 2.5 min	620 mJ cm ⁻²	40 s	120 ° C for 3.5 min
500 rpm	11 s				
Spin 3500 rpm	29 s				
Face down					
500 rpm	11 s				
Spin 3500 rpm	29 s				

Parameters such as spin speed and the duration of spinning determine the thickness and dryness of the coated photoresist layer, respectively. The fast spin

speed determines the thickness of the coated photoresist layer. The fast spin speed in our experiments was chosen 3500 rpm since it results in a $\sim 2 \mu\text{m}$ thick photoresist layer. As mentioned earlier, the purpose of the fast spin is to thin and dry the photoresist. In the outlined procedure, the duration of the fast spin is reduced to 29 s so that in the presence of the solvent vapor, the photoresist does not completely dry while thinning.

C3. Results

The photoresist coverage was characterized using a scanning electron microscope (SEM) (LEO 1430). Figure C-3(a) shows a typical cross-sectional SEM image of a $110 \mu\text{m}$ deep cavity coated using the conventional face up spin coating process. Clearly, the photoresist accumulation region extends to a distance of $145 \mu\text{m}$, followed by a sloping region that monotonically increases in thickness, starting at $2.2 \mu\text{m}$ at a position $145 \mu\text{m}$ away from the corner point. In comparison, Figure C-3 (b) depicts a cross-sectional SEM image of the same cavity using the above-mentioned wafer holder and the face down/face up spin coating process. This process produces a photoresist layer of uniform thickness beyond a distance of $107 \mu\text{m}$.

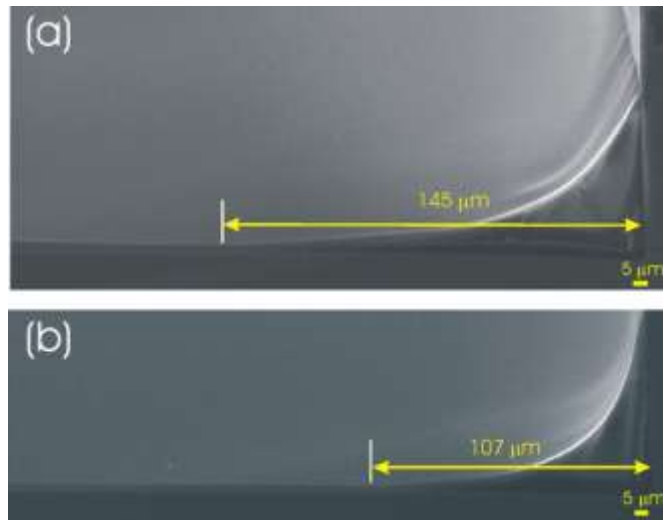


Figure C-3 Cross-sectional SEM images (500 \times) near the edge of a $110 \mu\text{m}$ deep cavity and photoresist coating using: (a) the face up spin coating process. Here, the photoresist accumulation extends to a distance of $145 \mu\text{m}$, followed by a sloping region that monotonically increases in thickness, starting at $2.2 \mu\text{m}$ at a position $145 \mu\text{m}$ away from the corner point. (b) The face down/face up spin coating process. This process produces a photoresist layer of uniform thickness beyond a distance of $107 \mu\text{m}$.

It is evident from the images that the photoresist layer obtained using the face down/face up spin coating process is more uniform than the one obtained using the conventional face up spin coating process. Beyond a distance of $107\ \mu\text{m}$ from a corner point of the cavity, the face down/face up spin coating produces a $1.7\ \mu\text{m}$ thick uniform photoresist coating at the bottom of these cavities, as shown in Figure C-4. To ensure a more uniform photoresist coating closer to the vertical edge, the accumulation of photoresist near the vertical corner of the cavity must be further minimized. This can be accomplished by reducing the viscosity of the applied photoresist, thus allowing it to drain away during the face down spin process.

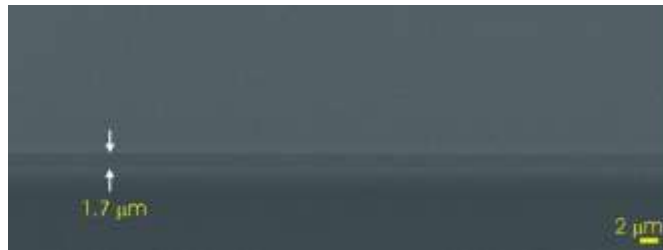


Figure C-4 A cross-sectional SEM image ($1700\times$) of a photoresist layer at the bottom of a $110\ \mu\text{m}$ cavity. A uniform thickness of $1.7\ \mu\text{m}$ was achieved using the face down/face up spin coating process beyond a distance of $107\ \mu\text{m}$.

To test the consistency of this method, similar experiments were performed on deeper cavities. Unfortunately, due to the scalping effect inherent in the Bosch process [168], the deeply-etched silicon walls were not exactly vertical. However, such cavity edges are sufficient for performing our comparative experiments. Figure C-5 (a) depicts a typical cross-sectional SEM image of a $300\ \mu\text{m}$ deep coated cavity using only the conventional face up spin coating procedure. Notably, the photoresist nonuniformity is similar to that observed in the $110\ \mu\text{m}$ deep cavity (Figure C-3 (a)) having a photoresist accumulation extent of $166\ \mu\text{m}$. Interestingly, although this cavity is very deep, by using the face down/face up spin coating process, as shown in Figure C-5 (b), the uniformity of the photoresist beyond a distance of $104\ \mu\text{m}$ is excellent, maintaining a constant layer thickness of $1.6\ \mu\text{m}$.

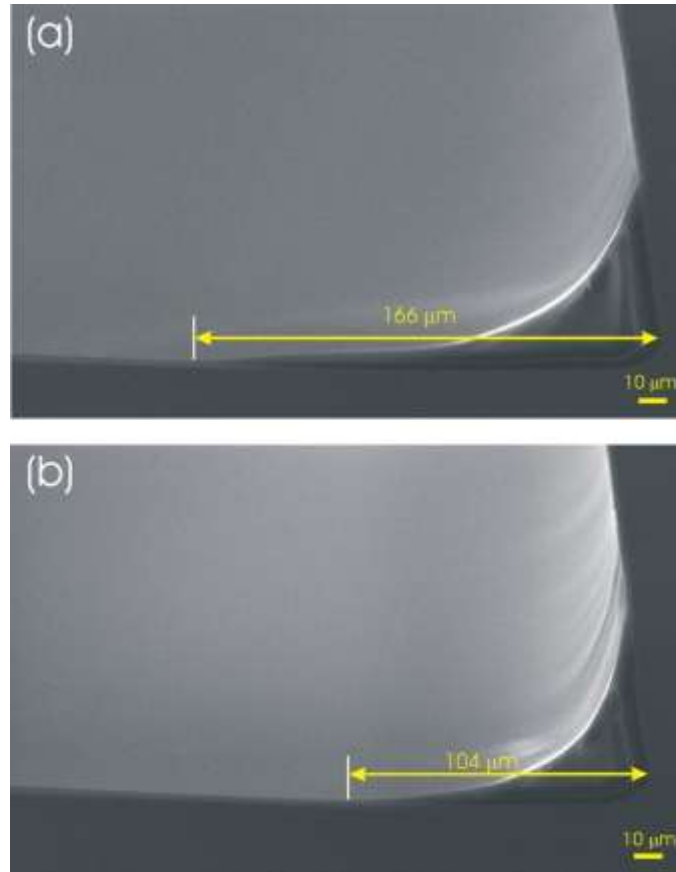


Figure C-5 Cross-sectional SEM images (500 \times) near the edge of a 300 μm deep cavity and photoresist coating using (a) the face up spin coating process. Here, the photoresist accumulation extends to a distance of 166 μm , followed by a sloping region that monotonically increases in thickness, starting at 1 μm at a position 166 μm away from the corner point. (b) The face down/face up spin coating process. This process produces a photoresist layer of uniform thickness beyond a distance of 104 μm .

These experiments indicate that the face down/face up spin coating process results in a more uniform photoresist coating near the edges of deep cavities as compared to the conventional face up spin coating process. In addition to the near-edge uniformity of the face down/face up spin coating method of deep cavities, it was observed that the top step layer of the cavity (elevated wafer surface away from the edge) was also uniformly coated. Furthermore, this method has been tested on 3 wafers each having 72 rectangular cavities (a total of 216 cavities). It was observed that the repeatability of this method is excellent.

It should be noted that when the wafer is rotating, depending on the location of the cavities on the wafer relative to the center of rotation, photoresist coverage on

the edges of the cavities would be different. Consequently, for cavities that are located off the rotational axis, the photoresist will pile up less at the edge closer to the axis of rotation compared to the opposite edge. As shown in the illustration in Figure C-6, the fact that the centrifugal force on the photoresist points in the radially outward direction, it is expected that the photoresist at the bottom of the cavity will flow more toward the left edge. This causes the photoresist to pile up more on the left edge. The consequence of this effect is that the photoresist reaches a uniform coating in a longer distance, L_1 (measured from the left edge), compared to the distance, L_2 (measured from the right edge), where a uniform coating is obtained. The average value of the ratio of L_1/L_2 obtained from our experiments was ~ 1.3 for both cavities.

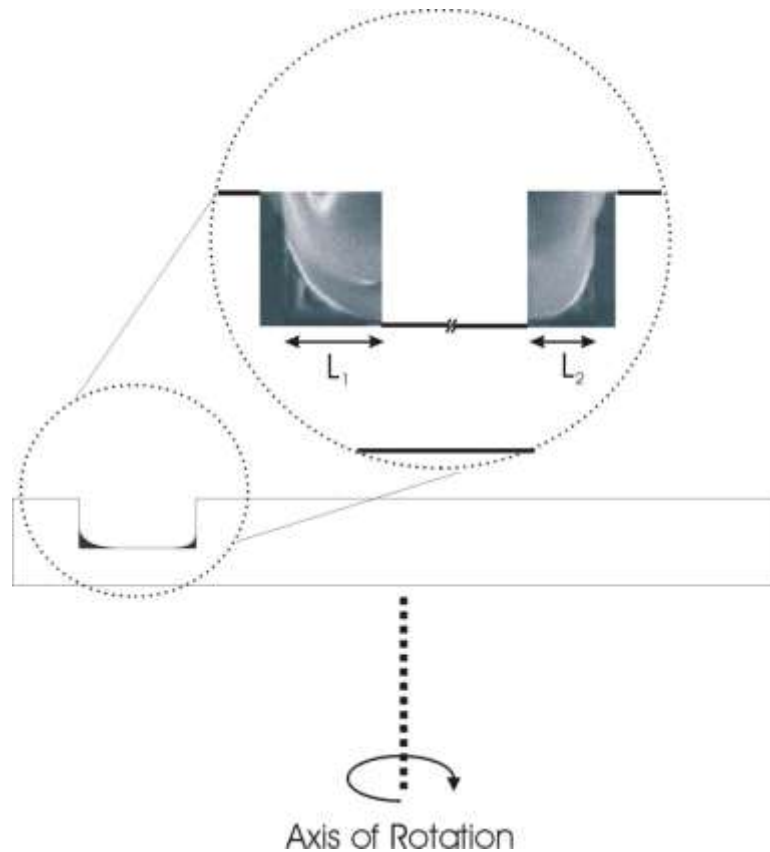


Figure C-6 An illustration (not to scale) of a cross-sectional view of a rotating wafer having a cavity etched on the left side. Due to centrifugal force, the accumulation of photoresist at the opposite edges of this cavity is asymmetric.

In summary, a wafer holder for coating photoresist on a wafer having deep 3D structures was designed and tested. Using a simple construction of a wafer holder and a two-step face down/face up spin coating procedure, a uniform photoresist coating was achieved. This device is ideally suited for photoresist coating that is required for patterning small features situated deep within and especially near the sidewalls of etched cavities and recesses. The implementation of this tool to commercial spin coating systems requires minimal modifications; therefore, it is fast and inexpensive, and it does not require any special photoresist [169].